uOttawa

L'Université canadienne
Canada's university

FACULTÉ DES ÉTUDES SUPÉRIEURES ET POSTOCTORALES

uOttawa

L'Université canadienne
Canada's university

FACULTY OF GRADUATE AND POSDOCTORAL STUDIES

Jeffrey Wheeldon
AUTEUR DE LA THÈSE / AUTHOR OF THESIS

Ph.D. (Physics)
GRADE / DEGREE

Department of Physics
FACULTÉ, ÉCOLE, DÉPARTEMENT / FACULTY, SCHOOL, DEPARTMENT

Group Theoretic Expressions of Optical Singularities in Photonic Crystals

TITRE DE LA THÈSE / TITLE OF THESIS

Henry Schriemer
DIRECTEUR (DIRECTRICE) DE LA THÈSE / THESIS SUPERVISOR

Trevor Hall
CO-DIRECTEUR (CO-DIRECTRICE) DE LA THÈSE / THESIS CO-SUPERVISOR

EXAMINATEURS (EXAMINATRICES) DE LA THÈSE / THESIS EXAMINERS

Serge Desgreniers

Kevin Graham

Stephen Hughes

Gary W. Slater
Le Doyen de la Faculté des études supérieures et postdoctorales / Dean of the Faculty of Graduate and Postdoctoral Studies

GROUP THEORETIC EXPRESSIONS OF OPTICAL SINGULARITIES IN PHOTONIC CRYSTALS

by

Jeffrey F. Wheeldon

A thesis submitted in partial fulfillment of the
requirements for the degree of

Doctorate of Philosophy

Department of Physics
University of Ottawa
Ottawa, Ontario, Canada

Your file Votre référence
ISBN: 978-0-494-51824-3
Our file Notre référence
ISBN: 978-0-494-51824-3

ABSTRACT

Fundamental theoretical insights into the fine structure of electromagnetic fields in photonic crystals are developed, by examining the singular nature of field representations in linear systems, and fundamental design paradigms are established in this meta-material system. Photonic crystals are optical meta-materials that permit the transport of electromagnetic energy that can be tailored by modifying the underlying periodically structured dielectric profile. Propagation is characterized by the dispersion surface through the Bloch states, where frequency wave vector relations characterize system response. A renewed appreciation for the richness of the dispersion relations has led to a deeper consideration of the modal structure itself and its inherent relationship to symmetry. This has led to a group theoretic treatment of the fundamental system space symmetries expressed through local representations of the singular character of the Bloch mode and its vortex states.

Central to this study is an analysis of the local energy transport, which has uncovered the existence of optical vortices centered about phase singularities. Further investigation into the energy transport properties at the local level (i.e., far below the scale of the wavelength) reveals optical features never before explicated in the photonic crystal community. It is shown that the electromagnetic mode structure bears the hallmarks of singular optics, whereby the field becomes characterized by singularities – that is, spatial locations where mathematical descriptions of optical properties become undefined. Optical vortices, revealed by energy circulation about a singular point, are expressed by global system space symmetries and the particular character of the dispersion surface. Vortices are the local field magnitude response to their associated phase singularities. In this study, the locations of optical vortices in real space are determined using phasor geometry, and the symmetry rules for their existence are established with group theory. They are categorized into symmetry and accidental singularities, constraining their locations in reciprocal space.

Further research on the vectorial character of the local electromagnetic field has uncovered the rich nature of polarization singularities in these periodic microstructures. A group theory representation is used to express its complementarity polarization singularity representation, where fundamental transformation operations permitted by the system's space group are quantified. As a result, the entire electromagnetic field may be determined from the fundamental domain of the system's space group, using derived transformation properties of the local state of polarization. Furthermore, it is shown that local symmetry requires the electromagnetic field to become singular at particular points, known as Wyckoff positions. The reduction of the electromagnetic field to a fundamental domain, the location of the optical singularities, and the transformation properties of the local state of the electromagnetic field allow one to determine the major features of the sub-wavelength structure of the electromagnetic field from fundamental symmetry principles.

In each the case, these fundamental principles were applied to Bloch modes derived in the vanishing dielectric contrast limit. Additional confirmation of theoretical predictions is supported by simulations of high-dielectric-contrast, purely two-dimensional, photonic crystal Bloch modes, in which Maxwell's equations are solved directly using the Finite Element Method (FEM). Finally, studies of optical vortices and polarization singularities within dimensionally confined photonic crystal slabs are studied with three-dimensional FEM simulations, in order to inform the design and fabrication of such structures for future experimental confirmation of the phenomena and possible photonic crystal optical singularity applications.

STATEMENT OF ORIGINALITY

In accordance with the guidelines for a Ph.D. thesis in the Department of Physics, University of Ottawa, the author declares that, to best of his knowledge, this body of research represents original work in the field of physics, except where otherwise noted. These results were obtained during the period of the author's Ph.D. research project under the supervision of Dr. H. P. Schriemer and the co-supervision of Dr. T. J. Hall.

The following papers are on work directly covered in this thesis:

1. **J. Wheeldon** and H. Schriemer, "Application of first-order group theory methods to photonic crystals", (Drafted).
2. **J. Wheeldon** and H. Schriemer, "Group theoretic transformations of Bloch modes at special Wyckoff positions within photonic crystals", (Drafted).
3. **J. Wheeldon** and H. Schriemer, "Self-consistent effective index method applied to photonic band structures", (Drafted).
4. **J. Wheeldon** and H. Schriemer, "Symmetry transformation properties express polarization singularities in Bloch mode systems", Opt. Express (Submitted).
5. **J. Wheeldon** and H. Schriemer, "Polarization Singularities and Local Field Symmetries in Photonic Crystals.", IEEE LEOS Optical MEMS and Nanophotonics, Freiburg, Germany (2008).
6. **J. Wheeldon** and H. Schriemer, "Photonic crystals as a novel structure to generate optical vortices", CAP Congress 2008, Quebec City, Canada (2008).
7. **J. Wheeldon**, T. Hall, and H. Schriemer, "Symmetry constraints and the existence of Bloch mode vortices in linear photonic crystals", Opt. Express **15**, 3531 (2007).

The following papers were produced during the thesis but are not directly related to the topics covered in the thesis:

8. H. Schriemer, **J. Wheeldon**, and T. Hall, "Transport Properties of Nonlinear Photonic Crystals", Photonics North 2005, Toronto, Canada (2005).
9. **J. Wheeldon**, H. Schriemer, and T. Hall, "A nanoscale perspective of nonlinear optical tunability in two-dimensional photonics crystals in the superprism regime, Modelling", Simulation and Design of Dielectrics, Cambridge, UK (2005).
10. R. Millett, **J. Wheeldon**, T. Hall, and H. Schriemer, "Towards Modelling Semiconductor Heterojunctions", COMSOL Conference 2006, Boston, USA (2006).

TABLE OF CONTENTS

LIST OF FIGURES

ACKNOWLEDGMENTS

I would like to express my deepest gratitude to my supervisor, Dr. Henry P. Schriemer, who spent countless hours with me in deep theoretical discussions regarding the nature and meaning of my research and without whose help I would not be the physicist I am today. I thank him for his perseverance, which involved reading every multiple page group theoretic derivation I gave him, and always sending me back to the drawing board when he could sense there was more to uncover. Most of all, I appreciated Henry's enthusiasm for the subject matter. When I needed to push through a difficult theorem, Henry would always energize me and keep me going. I would also like to sincerely thank my co-supervisor, Dr. Trevor J. Hall, who has been my silent partner (or fairy-godfather, as he would say) since I started at the University of Ottawa. Trevor has given me financial support, and more important, countless insights into what it means to be a scientist in a world community. Furthermore, he has always been there for me, directing me from behind the scenes and ensuring I had a place to continue my chosen research, even when old research groups dissolved and new ones formed. Additionally, I would like to thank the National Science and Engineering Research Council and the Ontario Graduate Scholarship for their financial support of this Ph.D. research project.

To my parents, thanks for letting that weird kid of theirs, who wasn't even supposed to finish high school, pursue his dreams and trust his instincts. I want to thank my mom who taught me how to dream, and I want to thank my dad for teaching me that success comes from paying attention to the details.

Lastly, I would like to try to express the inexpressible (a singularity in the field of gratitude and love which influences everything around it), namely my feelings for my partner Jody. She has given me constant love, support and editing, without which I would have not been able to complete my Ph.D.

CHAPTER 1 – INTRODUCTION

1.1 Photonic crystals and optical singularities

The control and manipulation of light is a subject of great interest, in many fields and applications, where the interaction of light with matter is the fundamental concern. Until recently, the optical properties of materials were thought to be structurally invariant. E. Yablonovitch [1] and S. John [2], [3] were the first to propose that the properties of photons could be controlled in the same manner as electrons in crystalline semiconductor materials. They suggested that structures with periodic variations in the dielectric profile can control the radiative properties of materials by modifying the photonic modes. Such periodic dielectric structures are known as photonic crystals, which are part of a larger group of new optical materials called meta-materials. The essential feature of a photonic crystal is that the transport of light is renormalized by means of distributed Bragg reflections. In a photonic crystal, the dielectric interfaces of the periodic structure act as the Bragg scatterers for the photons, in the same way as the layers of atoms within a crystalline semiconductor interact with electrons. For sufficient dielectric contrast, photons within a photonic crystal will exhibit many of the same properties as electrons within a semiconductor, most notable forbidden energy gaps. A forbidden energy gap, also known as the photonic band gap, is a range of frequencies (energy) where the photon is not allowed to propagate within the photonic crystal. In a complete photonic band gap the spontaneous emission rate is completely suppressed [1]. The photonic band gap is a result of the periodic spacing of the Bragg scatterers, whereby light constructively or destructively interferes [4]. Figure 1 reveals the photonic band structure (in a reduced zone scheme) of a typical two-dimensional photonic crystal, formed from a square array of dielectric columns in an air background (see Section 4.3 for this calculation). Here, we can see a photonic band gap for the TM optical mode (orange region). In this region, photons (polarized to match the TM case) will not be allowed to propagate in the photonic crystal.

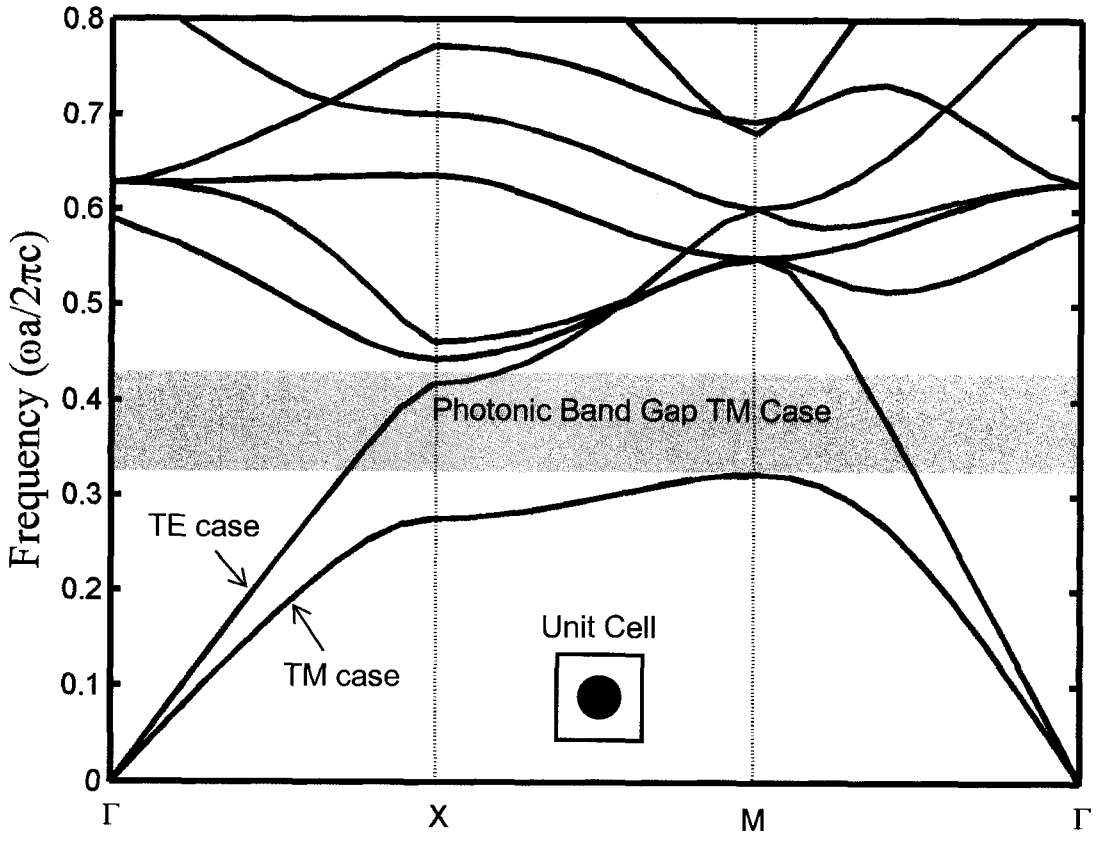

Figure 1. Two-dimensional photonic crystal, square lattice of dielectric columns $\varepsilon = 8.9$ in an air background $\varepsilon = 1$; Photonic band structure TE bands (red), TM bands (blue) and TM case photonic band gap (orange). The axes of the photonic band structure are normalized frequency $\omega a/2\pi c$ and normalized wave vector $ka/2\pi$, where a is the lattice constant and c is the speed of light in a vacuum.

However, this is not a complete photonic band gap, because light is allowed to propagate in the TE direction.

Equally important, and related to the photonic band gap, is the fact that the transport of electromagnetic energy within a photonic crystal can be tailored by modifying the underlying periodically-structured dielectric profile. The global transport properties of the optical modes are characterized by their net energy velocity. Averaged over the lossless photonic crystal, the energy velocity can be shown to be equivalent to the group velocity, which is the velocity of a propagating wave packet, given by the standard definition

$$\mathbf{v}_g = \partial\omega/\partial\mathbf{k}, \tag{1.1}$$

([5], pp. 30-32). Propagation of the optical modes is then characterized by the slope of the dispersion surfaces, where the photonic band structure characterizes the system response (see Figure 1). The complex dispersion surfaces of the photonic crystal optical modes can lead to interesting and new energy transport phenomena not found in ordinary optical materials, such as: the slow light effect [6]-[8]; negative index of refraction [9]-[14]; the superprism effect [15]-[17]; and self-collimation [18]-[20]. Many of the applications of photonic crystals have focused on these new global transport phenomena and the photonic band gap. This has resulted in a large number of publications concerning the design and measurement of the overall transport properties of photons in photonic crystals and the photonic band gap, in many different configurations [6]-[44].

A renewed appreciation for the richness of the dispersion relations has led to a deeper consideration of the modal structure itself for applications, such as: nano-scale transport properties of photonic crystals in the superprism regime [45]-[46]; improving the performance of photonic crystal waveguiding [47]-[48]; manipulation of sub-wavelength dielectric particles within photonic crystals [49]-[51]; laser cooling of atoms within photonic crystals [52], [53]; photonic crystals as a method to generate light that contains

orbital angular momentum [4] [54]-[57]; and fabrication of photonic crystals in self-assembled colloidal systems [58]-[59]. Inherent to each of these studies is an interest in the properties of light within photonic crystals at length scales smaller than the lattice constant. Investigation into the energy transport properties at the local level (i.e., far below the scale of the wavelength) reveals optical features never before explicated in the photonic crystal community: The electromagnetic mode structure bears the hallmarks of singular optics, whereby the field becomes characterized by singularities – that is, spatial locations where mathematical descriptions of optical properties become undefined.

In the general discipline of optics, the structure of the electromagnetic field at length scales smaller than its wavelength is an exciting topic of study [60]-[89]. Since Huygens published his *Treatise on Light*, over 300 years ago, we have known light can be treated as a wave phenomenon. However, it was not until the mid-1970's that the optics community realized that the sub-wavelength features of electromagnetic waves could be systematically described by examining the singular points within the electromagnetic field [85]. Optical singularities are locations in the electromagnetic field where a particular description of the electromagnetic field becomes undefined. In each case, the singular points are major features that greatly impact the behaviour of the electromagnetic field around the singular point. In electromagnetic fields that are adequately described using scalar waves (i.e., light which is linear polarized in a single direction), the singular points take the form of phase singularities. Unambiguous definition of the local phase of the optical mode is achieved through the relation between real and imaginary parts of a complex field description. Examination of the local flow of energy close to a phase singularity reveals that these singular points are the centers of optical flux, which form optical vortices. These singular points, while a zero in the optical intensity, are also the terminus of a dislocation in the phase of the optical mode [77]. The phase behavior in the vicinity of the singularity quantifies the optical vorticity, which is necessarily related to the orbital angular momentum of the optical mode [56], and thus a primary motivator for research into such states [78]-[79]. Furthermore, when one considers complex vector fields, one must also consider the state of polarization. The

state of polarization of the electromagnetic field is one of its most fundamental properties, quantifying the vector character of the optical response of systems ranging from the simple to the complex. In general, it is a spatially-dependent quantity, represented by an ellipse extracted at every point by mapping the modulation of the field vector over a temporal period. The polarization state is circumscribed by three distinct types of singularities: pure circular polarization (indeterminate ellipse rotation angle); pure linear polarization (indeterminate polarization handedness); and disclinations (indeterminate polarization due to zero field intensity in all polarization directions). Polarization singularities in transverse electromagnetic fields were first discussed in depth by Hajnal [87]. A generalization to random vector fields was performed by Berry and Dennis [88].

To this point, there has been no formal treatment of group theoretic principles to the study of singular optics in systems of high symmetry, such as photonic crystals. As a result, the major goal of this thesis is a systematic application of group theoretic methods to the optical modes of photonic crystals as a means of establishing fundamental relationships linking the symmetry of an optical system to the singular points of its electromagnetic field. This will allow us to advance a set of intuitive design parameters that can not only be used to analyze existing optical systems, but also to create new optical systems that require specific local electromagnetic field characteristics. Previous group theoretic studies focused on the global optical response of photonic crystals. Here, the purpose is to understand the sub-wavelength characteristic of the electromagnetic field. As a consequence, we are the first to apply the concept of site (local) symmetry to the optical response of a photonic crystal (Chapter 3), which was critical to understanding the properties of the local state of polarization. Confirmation of group theoretic predications are supported by simulations of photonic crystals by solving Maxwell's equation for the Bloch modes using the Finite Element Method (FEM), studying optical singularities within purely two-dimensional photonic crystals and in dimensionally confined photonic crystal slabs (Chapter 4). Photonic crystal fabrication poses many technological challenges; a single mistake could cost a significant percentage of a

research budget (the fabrication techniques will not be considered here, but the interested reader may consult [24], [27]-[29], [31]-[33], [43], [59], ([90] Ch. 5-9), [91]- [95]). Our secondary goal was the development of the simulation software, which will inform future experimental realizations and photonic crystal applications (see Appendix D), and which highlights a dramatic improvement to the standard effective index method. Two types of optical singularities were studied within the optical modes of photonic crystals: phase singularities that formed optical vortices, and polarization singularities. The optical vortices are the local field magnitude response to their associated model phase singularities; their location in real space and the symmetry rules for their existence are determined by using group theory and phasor geometry. Phase singularities are categorized into symmetry and accidental singularities, which constrain their locations in reciprocal space (Chapter 5). Polarization singularities reveal the complex nature of the vector character of the local state of the electromagnetic field in photonic crystals. A group theoretic representation is used to express its complementary polarization singularity representations, where fundamental transformation operations permitted by the system's space group are quantified. As a result, the entire electromagnetic field is determined from the fundamental domain of the system's space group, using derived transformation properties of the local state of polarization. Furthermore, it is found that local symmetry requires the electromagnetic field to become singular at particular Wyckoff positions (Chapter 6).

1.2 Thesis outline

The main body of the thesis begins in Chapter 2, which first defines the periodicity of a photonic crystal by establishing its Bravais lattice, reciprocal lattice and the first Brillouin zone. Section 2.3 introduces the optical modes of a photonic crystal as solutions of an eigenvalue problem formulated using Maxwell's equations; we show the solutions are optical Bloch modes. The rest of Chapter 2 is dedicated to examining the optical Bloch modes of purely two-dimensional photonic crystals and two-dimensional photonic crystal slabs. It is in these sections that the derivation of the optical Bloch modes in the

vanishing dielectric contrast limit is introduced. Chapter 3 reviews the application of group theory to the optical Bloch modes determined in Chapter 2. In Chapter 3, it is shown that the optical Bloch modes are the partner functions of the irreducible representations of the symmetry transformation operators. In Section 3.4, we complete the derivation of the optical Bloch modes in the vanishing dielectric contrast limit, in which the partner functions of a reducible representation are shown to decompose into linear combinations of the optical Bloch modes in the vanishing dielectric contrast limit. Furthermore, in Section 3.5, the concepts of site (local) symmetry are applied to the transformation properties of the optical Bloch modes. The finite element method (FEM) numerical models are presented in Chapter 4, where we begin with the derivation of the scalar model. The scalar model is applied to the purely two-dimensional photonic crystal problem and later used during the application of the effective index method to the photonic crystal slab problem. Section 4.4 details the application of a novel self-consistent effective index method to determine the photonic band structure of a photonic crystal slab and the results are compared to solutions based on the standard effective index method and the full vector FEM solutions. It is in Chapters 5 and 6 that optical singularities are investigated using the tools established in Chapters 3 and 4. Chapter 5 starts with defining phase singularities and optical vortices in the general case. Examining the analytical form of the optical Bloch modes in the vanishing dielectric contrast limit, the locations of phase singularities are determined and the symmetry rules for their existence are established. These symmetry insights are confirmed by examining FEM simulations of optical Bloch modes in low and high dielectric contrast photonic crystals. Chapter 6 is the final chapter in the main body of the thesis, where polarization singularities are examined. The elliptical form of the local state of polarization is established, where polarization singularities are identified as locations where the elliptical description becomes undefined. These polarization singularities are explicitly identified in photonic crystals by examining the local state of polarization in the analytical forms of the optical Bloch modes in the vanishing dielectric contrast limit. Application of site symmetry to the local state of polarization reveals it is constrained to a subset of all possible polarization states. These theoretical findings are compared to FEM simulations

of the optical Bloch modes of high dielectric contrast photonic crystals. The central findings of the thesis are summarized in Chapter 7. Appendix A details the derivation of the Poynting vector field within a two-dimensional photonic crystal Bloch mode. In Appendix B, we apply the plane wave expansion method to the two-dimensional photonic crystal eigenvalue problem as a means of justifying the vanishing dielectric contrast approximation from Section 2.4.2. Appendix C adds details to the derivation of the partner functions of the E irreducible representation from Section 3.4.4. Appendix D is a preliminary study of the optical forces within an optical Bloch mode that contains optical vortices, which is a potential future application of this research. Appendix E is a second preliminary study examining how to excite an optical Bloch that contains optical singularities using an electromagnetic source located outside of a photonic crystal.

CHAPTER 2 – EIGENMODES OF PHOTONIC CRYSTALS

2.1 Introduction

In this chapter, we formally state the photonic crystal eigenvalue problem: It describes the fundamental interaction of an electromagnetic field with the periodic dielectric structure known as a photonic crystal. From this eigenvalue problem we can determine the photonic band structure and, more importantly for our research, we can determine its eigenmodes. The photonic crystal eigenmodes are the fundamental forms of the electromagnetic field that are allowed to exist within a photonic crystal, where any electromagnetic field can be described as a linear combination of these eigenmodes. In many cases, there are a finite number of eigenmodes for a given direction of propagation, polarization, and frequency, and usually the electromagnetic field is merely a single eigenmode. As a result, it suffices to study the eigenmodes themselves, to understand the sub-wavelength optical properties of a photonic crystal.

We model a photonic crystal as an infinite periodic dielectric structure. As a result, we can describe the periodicity of the dielectric permittivity by a Bravais lattice and a reciprocal lattice. Real photonic crystals are not infinite, but if the system includes a sufficient number of repeated units, and one is only interested in phenomena not influenced by the edges of the photonic crystal, an infinite photonic crystal is a sufficient approximation. Once the dielectric structure is defined, then Maxwell's equations are employed to generate the photonic crystal eigenvalue problem. We explore the form of the photonic crystal eigenmodes by applying Bloch theorem. This allows the eigenmodes to be identified as photonic crystal Bloch modes. This is similar to the application of Bloch's theorem to electron wave functions of solid state physics ([96] chapter 8). We describe the transport of energy within a photonic crystal by examining the Poynting vector of a Bloch mode.

The focus of this study will be on the two types of photonic crystals in which the periodicity is limited to the *x-y* plane: the purely two-dimensional (2D) photonic crystal, and the 2D photonic crystal slab. The purely 2D photonic crystal is periodic in the *x-y* plane and continuous in the $\hat{\mathbf{z}}$ direction. The 2D photonic crystal slab is also periodic in the *x-y* plane, but is of limited extent in the $\hat{\mathbf{z}}$ direction. This region of space is on the order of the wavelength of the light and the average dielectric permittivity of the photonic crystal is larger than the surrounding medium (index guiding). There is an extensive body of literature devoted to 2D photonic crystals and photonic crystal slabs ([5]-[37], [40], [43]-[48], [52]-[55], [90]-[95], [100]-[101], [105]-[106], [108], and [110]-[112]) because they are significantly easier to fabricate using existing planar waveguide fabrication technology than are three-dimensional (3D) photonic crystals. Furthermore, the analytical and numerical analysis of two-dimensional periodic photonic crystals is also simpler than in a three-dimensional periodic structure, but the systems still retain the novel defining characteristics we wish to study.

In this study, optical singularities in photonic crystals will be studied with an array of analytical and numerical techniques. The most fundamental of these techniques is the vanishing dielectric contrast limit approximation, in which the photonic crystal Bloch modes can be approximated as a linear combination of eigenmodes of a similar non-periodic structure ([5], pp. 5-11), ([5], pp. 50-54), ([5], pp. 179-181), and ([90] pp. 79-81). Based on this approximation, the photonic band structure can be determined and an analytic form of the photonic crystal Bloch modes can be derived (the exact values of the coefficients for the linear combinations are determined in Chapter 3 using symmetry arguments). The vanishing dielectric contrast approximation is analogous to the weak periodic potential approximation used to find electron wave functions in a crystalline solid ([96], pp.152-156). In subsequent chapters, such analytical forms of the Bloch modes are used to determine the locations and types of optical singularities that must appear in photonic crystals, and they are compared to their high dielectric contrast counterparts.

2.2 Photonic crystals as periodic dielectric structures

2.2.1 Periodic dielectric structures

Photonic crystals are structures composed of arrays of materials with different refractive indices. These arrays are periodic in one, two or three dimensions. The simplest example is a one-dimensional photonic crystal. In Figure 2(a), we see a multi-layered dielectric stack that alternates between two different dielectric materials, with a spatial period of a. The spatial period a is known as the lattice constant and is on the order of the relevant wavelength of light for the photonic crystal. As an illustration of a typical lattice constant, we assume light incident upon a multi-layered dielectric stack light is parallel to the direction of periodicity. The total reflected light for the relevant wavelength is maximum when the lattice constant is $a = \lambda_0/(2n_1) + \lambda_0/(2n_2)$, where λ_0 is the free space wavelength of the light, and n_1 and n_2 are refractive indices of the two dielectric materials ([76], p.100). For a photonic crystal that is periodic in two or three dimensions, a single scalar lattice constant is no longer suitable, but lattice vectors must be defined. As in the case of the one-dimensional photonic crystal, the lattice vectors will be on the order of the relevant wavelengths of the photonic crystals. In Figure 2(b) and Figure 2(c), we see examples of a two-dimensional photonic crystal, and a three-dimensional photonic crystal, respectively. To fundamentally describe the multi-dimensional periodicity, we review the Bravais lattice, which defines the lattice vectors and the reciprocal lattice, in the following two sections.

2.2.2 Bravais Lattice

The Bravais lattice quantifies the periodicity of a photonic crystal, as in the crystalline solids of solid state physics ([96], pp.64-82). It is an infinite array of discrete points that specifies the locations of the repeated units of the photonic crystal, given by the set of position vectors

$$\mathbf{R} = n_1\mathbf{a}_1 + n_2\mathbf{a}_2 + n_3\mathbf{a}_3, \tag{2.1}$$

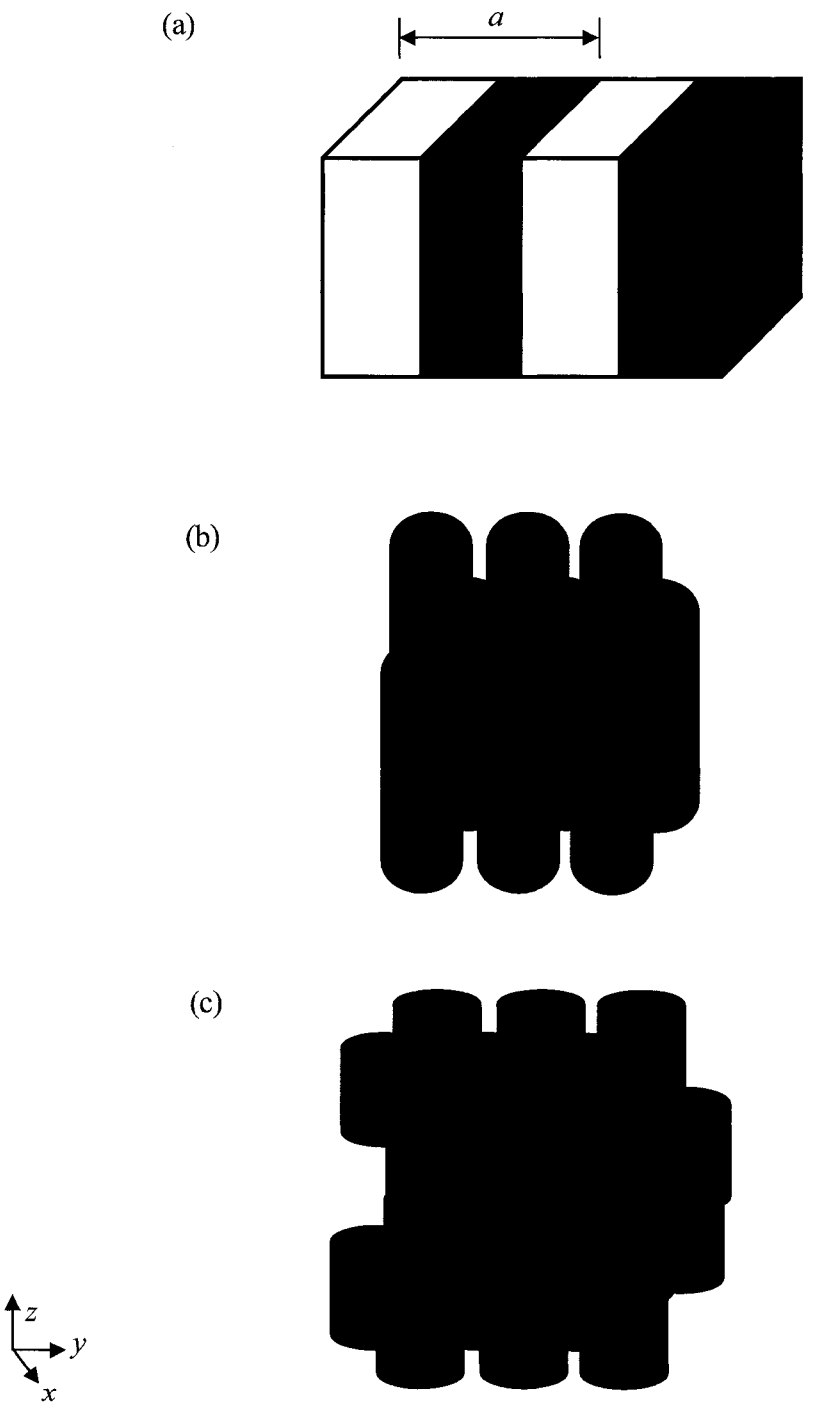

Figure 2. Photonic crystals with (a) one-dimensional periodicity, (b) two-dimensional periodicity, and (c) three-dimensional periodicity.

where $\mathbf{a}_i$ is an elementary lattice vector, n_i is any integer, and i runs over the dimension of the system (here, 3). Using Eq. (2.1), the photonic crystal as a periodic array of materials with different refractive indices can be written as

$$\varepsilon(\mathbf{r}+\mathbf{R})=\varepsilon(\mathbf{r}), \tag{2.2}$$

where $\varepsilon(\mathbf{r})$ is the spatially dependent relative dielectric constant. The repeated units of the photonic crystals are called the unit cell, which is a volume of space that, when translated by the vectors of the Bravais lattice, will cover all space. There are several methods to determine the unit cell of a crystal; we focus on the primitive unit cell. The primitive unit cell contains only one lattice point and is the minimum volume of space required to define the crystal structure. It can be described by two methods: first a parallelepiped is formed by the elementary lattice vectors $\mathbf{a}_1$, $\mathbf{a}_2$, $\mathbf{a}_3$, yielding a volume of $V=\mathbf{a}_1\cdot(\mathbf{a}_2\times\mathbf{a}_3)$ (see Figure 3(a)); or second, by the Wiger-Seitz primitive cell, which is the volume of space defined by placing the origin at a lattice point and drawing planes that bisect the lines joining the nearest neighbours (see Figure 3(b)). The first definition is typically used in reference to a dielectric profile, and the presentation of Eq. (2.2) may vary depending on where the origin of the lattice is located. As an example, two possible unit cells are defined in a two-dimensional hexagonal photonic crystal (top view), which is composed of an infinite array of dielectric cylinders that are infinitely tall in the $\hat{\mathbf{z}}$ direction (see Figure 3(a)). Since the structure of Figure 3(a) has two-dimensional periodicity, the unit cell extends to infinity in the $\hat{\mathbf{z}}$ direction, and the elementary lattice vectors are $\mathbf{a}_1=a\hat{x}$ and $\mathbf{a}_2=\hat{\mathbf{x}}a/2+\hat{\mathbf{y}}\sqrt{3}a/2$, where a is the lattice constant. When using numerical techniques to determine the eigenmodes of a photonic crystal, the solution space can be limited to the unit cell with periodic boundary conditions; this reduces an infinite crystal to a tractable finite solution space (see Chapter 4). The second representation, the Wiger-Seitz primitive cell, is the standard when viewing the possible photonic crystal eigenmodes in reciprocal space (see the next section for a discussion of reciprocal space).

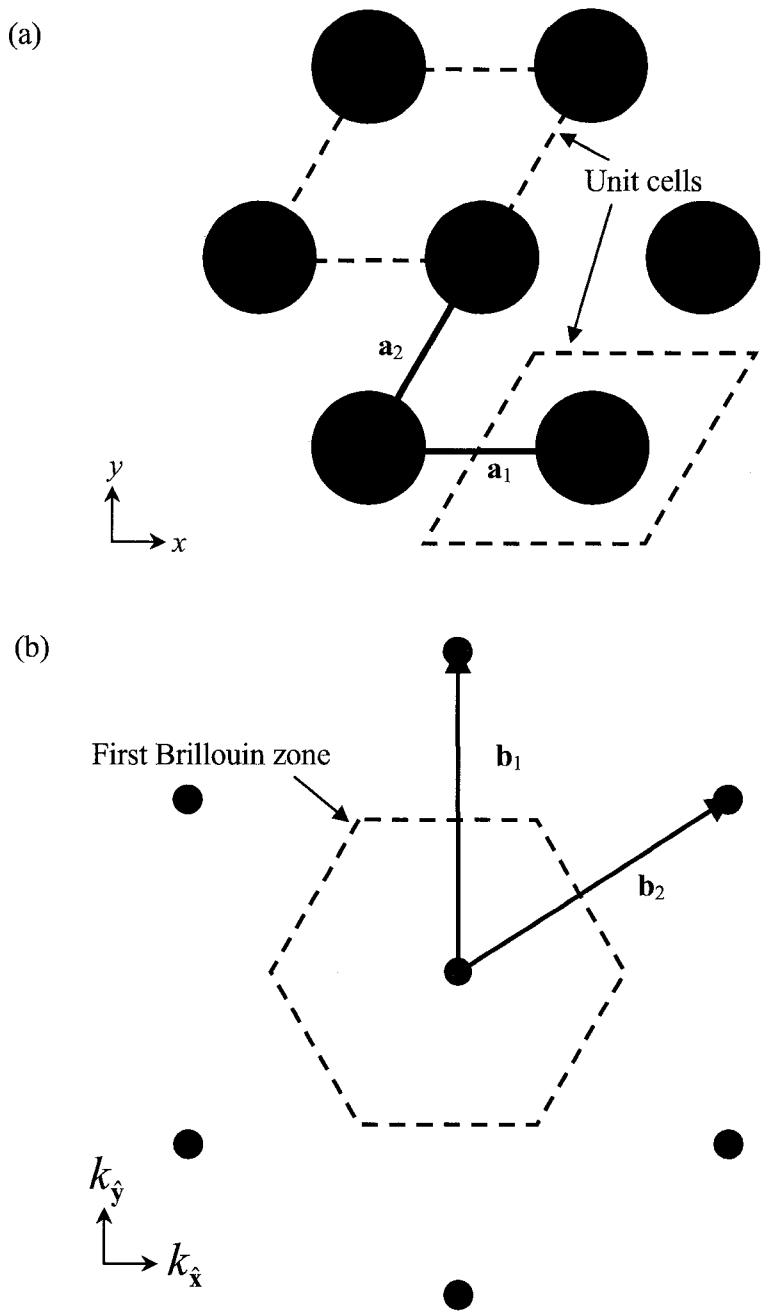

Figure 3. Top down view of a two-dimensional hexagonal lattice photonic crystal, where two examples of possible unit cells are outlined (dashed lines), and the elementary lattice vectors are $\mathbf{a}_1 = \hat{\mathbf{x}}a$ and $\mathbf{a}_2 = \hat{\mathbf{x}}a/2 + \hat{\mathbf{y}}\sqrt{3}a/2$. (b) First Brillouin zone (dashed lines) and reciprocal lattice vectors (black arrows) $\mathbf{b}_1 = \hat{\mathbf{x}}2\pi/a - \hat{\mathbf{y}}2\pi/\left(\sqrt{3}a\right)$ and $\mathbf{b}_2 = \hat{\mathbf{y}}4\pi/\left(\sqrt{3}a\right)$, and points in the reciprocal lattice (aqua circles).

2.2.3 Reciprocal lattice vectors

The second fundamental description of the periodicity of a photonic crystal is the reciprocal lattice. In the following sections, the reciprocal lattice will allow us to establish the Brillouin zone (primitive unit cell in reciprocal space), which defines the set of unique Bloch wave vectors **k** of the photonic crystal eigenmodes (wave vectors for plane waves and Bloch modes are described in Section 2.3.2). Furthermore, the reciprocal lattice also describes the elements of the Fourier series expansion of the photonic crystal eigenmodes (described in Section 2.3.2). The reciprocal lattice is the set of wave vectors **k** that yield plane waves $e^{i\mathbf{k}\cdot\mathbf{r}}$ with the same periodicity as the Bravais lattice, i.e.

$$e^{i\mathbf{G}\cdot(\mathbf{r}+\mathbf{R})} = e^{i\mathbf{G}\cdot\mathbf{r}}, \tag{2.3}$$

where $\mathbf{G} = \mathbf{k}$ is a reciprocal lattice vector, and the wave vector **k** has the units of radians per meter. Equation (2.3) implies $e^{i\mathbf{G}\cdot\mathbf{R}} = 1$, and the reciprocal lattice is defined as the set of points

$$\mathbf{G} = l_1\mathbf{b}_1 + l_2\mathbf{b}_2 + l_3\mathbf{b}_3, \tag{2.4}$$

where $\mathbf{b}_1 = 2\pi\frac{\mathbf{a}_2\times\mathbf{a}_3}{\mathbf{a}_1\cdot(\mathbf{a}_2\times\mathbf{a}_3)}$, $\mathbf{b}_2 = 2\pi\frac{\mathbf{a}_3\times\mathbf{a}_1}{\mathbf{a}_1\cdot(\mathbf{a}_2\times\mathbf{a}_3)}$, $\mathbf{b}_3 = 2\pi\frac{\mathbf{a}_1\times\mathbf{a}_2}{\mathbf{a}_1\cdot(\mathbf{a}_2\times\mathbf{a}_3)}$ are the reciprocal lattice vectors, and l_i, $(i=1,2,3)$, is any integer. These reciprocal lattice vectors have dimensions of radians per reciprocal length, due to $2\pi/\mathbf{a}_1\cdot(\mathbf{a}_2\times\mathbf{a}_3)$, and the reciprocal lattice vectors lie in reciprocal space spanned by the axes $k_{\hat{\mathbf{x}}}$, $k_{\hat{\mathbf{y}}}$ and $k_{\hat{\mathbf{z}}}$. In reciprocal space, a unit cell is defined by the Wigner-Seitz primitive cell and is called the first Brillouin zone. The first Brillouin zone of a two-dimensional hexagonal lattice photonic

crystal is a hexagon in $k_{\hat{x}}$-$k_{\hat{y}}$ plane, of infinite extent in the $k_{\hat{z}}$ direction. The reciprocal lattice vectors are $\mathbf{b}_1 = \hat{\mathbf{x}}\,2\pi/a - \hat{\mathbf{y}}\,2\pi/\left(\sqrt{3}a\right)$ and $\mathbf{b}_2 = \hat{\mathbf{y}}\,4\pi/\left(\sqrt{3}a\right)$ (see Figure 3(b)).

2.3 Maxwell's equations and the eigenvalue problem

2.3.1 The eigenvalue problem

Photonic crystals are periodic dielectric structures, similar to the crystalline structures of solid state physics that modify the electromagnetic field. The fields are described in the form of a photonic crystal eigenvalue problem derived from Maxwell's equations. The solutions of the photonic crystal eigenvalue problem are the energy eigenmodes of the system that propagate harmonically in the time domain. To derive the photonic crystal eigenvalue equation, we start with Maxwell's equations, the most basic description of the classical behaviour of the electromagnetic field, where matter is incorporated through the constitutive relation. When free charges and the electric current are absent, Maxwell's equations in MKS units are as follows ([5] pp.13-14):

$$\nabla \cdot \mathbf{D}(\mathbf{r},t) = 0, \tag{2.5}$$

$$\nabla \cdot \mathbf{B}(\mathbf{r},t) = 0, \tag{2.6}$$

$$\nabla \times \mathbf{E}(\mathbf{r},t) = -\frac{\partial}{\partial t}\mathbf{B}(\mathbf{r},t), \tag{2.7}$$

$$\nabla \times \mathbf{H}(\mathbf{r},t) = \frac{\partial}{\partial t}\mathbf{D}(\mathbf{r},t), \tag{2.8}$$

where $\mathbf{E}(\mathbf{r},t)$ is the electric field, $\mathbf{D}(\mathbf{r},t)$ is the electric displacement, $\mathbf{H}(\mathbf{r},t)$ is the magnetic field, and $\mathbf{B}(\mathbf{r},t)$ is the magnetic induction. In addition to Maxwell's equations, we require the constitutive equations

$$\mathbf{D}(\mathbf{r},t)=\varepsilon_0\varepsilon(\mathbf{r})\mathbf{E}(\mathbf{r},t), \tag{2.9}$$

$$\mathbf{B}(\mathbf{r},t)=\mu_0\mathbf{H}(\mathbf{r},t), \tag{2.10}$$

to relate the electric field to the electric displacement, Eq. (2.9), and the magnetic field to the magnetic induction, Eq. (2.10); ε_0 is the permittivity of free space, $\varepsilon(\mathbf{r})$ is the relative dielectric permittivity, and μ_0 is the permeability of free space. We assume the dielectric permittivity is isotropic and frequency independent, with the permeability being equal to free space, and the solutions having a harmonic time dependence of $e^{-i\omega t}$. Using these assumptions, Maxwell's equations and the constitutive relationships may be solved for $\mathbf{E}(\mathbf{r},t)=\mathbf{E}(\mathbf{r})e^{-i\omega t}$ and $\mathbf{H}(\mathbf{r},t)=\mathbf{H}(\mathbf{r})e^{-i\omega t}$, and we obtain the following eigenvalue equations:

$$\mathsf{L}_E\mathbf{E}(\mathbf{r})\equiv\frac{1}{\varepsilon(\mathbf{r})}\nabla\times\{\nabla\times\mathbf{E}(\mathbf{r})\}=\frac{\omega^2}{c^2}\mathbf{E}(\mathbf{r}), \tag{2.11}$$

$$\mathsf{L}_H\mathbf{H}(\mathbf{r})\equiv\nabla\times\left\{\frac{1}{\varepsilon(\mathbf{r})}\nabla\times\mathbf{H}(\mathbf{r})\right\}=\frac{\omega^2}{c^2}\mathbf{H}(\mathbf{r}), \tag{2.12}$$

where $c=1/\sqrt{\varepsilon_0\mu_0}$ is speed of light in free space. $\mathbf{E}(\mathbf{r})$ and $\mathbf{H}(\mathbf{r})$ are the eigenmodes of the Maxwell operators, L_E and L_H, and ω^2/c^2 is the associated eigenvalue where ω is the angular frequency. To determine the eigenmodes of a photonic crystal either Eq. (2.11) or Eq. (2.12) can be solved, because the solutions are identical (i.e., if Eq. (2.11) is solved, Eq. (2.7) and Eq. (2.10) would be used to determine the associated magnetic field $\mathbf{H}(\mathbf{r})$, which is identical to the eigenmodes obtained directly from Eq. (2.12)). All of the fields are written in complex notation for ease of manipulation, but the final electric and magnetic fields are assumed to be the real part of these complex fields as

$$\mathbf{E}(\mathbf{r},t)=\mathrm{Re}\left[\mathbf{E}(\mathbf{r})e^{-i\omega t}\right], \tag{2.13}$$

$$\mathbf{H}(\mathbf{r},t) = \mathrm{Re}\left[\mathbf{H}(\mathbf{r})e^{-i\omega t}\right]. \tag{2.14}$$

The complex conjugate of a field is denoted as $\mathbf{E}^*(\mathbf{r},t)$, where the complex conjugate is defined as $\left(a(\mathbf{r})+ib(\mathbf{r})\right)^* = \left(a(\mathbf{r})-ib(\mathbf{r})\right)$.

2.3.2 Bloch's theorem

In section 2.1, the periodicity of the photonic crystals is defined by Eq. (2.2), which permits the application of Bloch's theorem. This is analogous to the application of Bloch's theorem when determining the electron wave functions of solid state physics ([96], Chapter 8). Bloch's theorem indicates that the electric and magnetic eigenmodes can be expressed as vector wave functions in the following form:

$$\mathbf{E}(\mathbf{r}) = \mathbf{E}_{\mathbf{k}n}(\mathbf{r}) = \mathbf{u}_{\mathbf{k}n}(\mathbf{r})e^{i\mathbf{k}\cdot\mathbf{r}}, \tag{2.15}$$

$$\mathbf{H}(\mathbf{r}) = \mathbf{H}_{\mathbf{k}n}(\mathbf{r}) = \mathbf{v}_{\mathbf{k}n}(\mathbf{r})e^{i\mathbf{k}\cdot\mathbf{r}}, \tag{2.16}$$

where the Bloch modes $\mathbf{E}_{\mathbf{k}n}(\mathbf{r})$ and $\mathbf{H}_{\mathbf{k}n}(\mathbf{r})$ are labeled by their wave vector $\mathbf{k}$ in the first Brillouin zone (the significance of $\mathbf{k}$ is discussed below), and by their frequency (energy) band index n (see [5], pp. 18-19 for a proof of Bloch's theorem applied to electromagnetic phenomena). Although we typically focus on the electric or the magnetic field, the electric and magnetic fields are both in the form of a Bloch mode for a given electromagnetic field because the solutions of Eq. (2.11) and Eq. (2.12) are identical (a complete argument is presented in Chapter 3, where it is shown that both of the Maxwell operators L_E and L_H have periodic symmetry). The Bloch mode is composed of two parts: a periodic part that has the periodicity of the Bravais lattice, given by

$$\mathbf{u}_{\mathbf{k}n}(\mathbf{r}+\mathbf{R}) = \mathbf{u}_{\mathbf{k}n}(\mathbf{r}), \tag{2.17}$$

$$\mathbf{v}_{\mathbf{k}n}(\mathbf{r}+\mathbf{R}) = \mathbf{v}_{\mathbf{k}n}(\mathbf{r}), \tag{2.18}$$

and a space harmonic term $e^{i\mathbf{k}\cdot\mathbf{r}}$, where $\mathbf{k}$ is the Bloch wave vector. The Bloch wave vector $\mathbf{k}$ should not be confused with the wave vector $\mathbf{k}$ of a plane wave $\mathbf{E}(\mathbf{r}) = \mathbf{A}e^{i\mathbf{k}\cdot\mathbf{r}}$. In an isotropic medium, the wave vector of a plane wave $\mathbf{k}$ defines the propagation direction, and the velocity of the equi-phase surfaces. In contrast, the Bloch mode does not have rigorously defined equi-phase surfaces, since it is a superposition of plane waves (see the Fourier expansion below). Equally important, the direction of energy propagation, defined by the time-averaged Poynting vector as

$$\mathbf{S}(\mathbf{r}) = \frac{1}{2}\mathrm{Re}\left[\mathbf{E}(\mathbf{r}) \times \mathbf{H}^*(\mathbf{r})\right], \tag{2.19}$$

is not necessarily parallel to the Bloch wave vector $\mathbf{k}$ (see Section 2.4.1 and Chapters 4 and 5 for an example of the Poynting vector within a two-dimensional photonic crystal, or [5] pp.30-34 and [45]-[46] for more in-depth discussion). To investigate the properties of the Bloch wave vector $\mathbf{k}$, we allow it to take on any value and relabeled $\mathbf{q}$. The central property of the Bloch mode (focusing on the electric field, but equally applicable to the magnetic) is the following relationship to the periodic translational symmetry of the Bravais lattice:

$$\mathbf{E}_{\mathbf{q}n}(\mathbf{r}+\mathbf{R}) = \mathbf{u}_{\mathbf{q}n}(\mathbf{r}+\mathbf{R})e^{i\mathbf{q}\cdot(\mathbf{r}+\mathbf{R})} = e^{i\mathbf{q}\cdot\mathbf{R}}\mathbf{E}_{\mathbf{q}n}(\mathbf{r}), \tag{2.20}$$

where we have used Eqs. (2.15) and (2.17). Equation (2.20) defines $\mathbf{q}$ as the Bloch wave vector, where the significance of the periodic translational symmetry becomes clear in the context of irreducible representations discussed in Chapter 3. The Bloch wave vector $\mathbf{q}$ can be written equivalently as $\mathbf{q} = \mathbf{k} + \mathbf{G}$, where $\mathbf{k}$ is a wave vector in the first Brillouin zone and $\mathbf{G}$ is the appropriate reciprocal lattice vector. Placing this equivalent form into Eq.(2.20), and using $e^{i\mathbf{G}\cdot\mathbf{R}} = 1$, we find

$$\mathbf{E}_{kn}(\mathbf{r}+\mathbf{R}) = \mathbf{u}_{kn}(\mathbf{r}+\mathbf{R})e^{i(\mathbf{k}+\mathbf{G})\cdot(\mathbf{r}+\mathbf{R})} = e^{i\mathbf{k}\cdot\mathbf{R}}e^{i\mathbf{G}\cdot\mathbf{R}}\mathbf{E}_{kn}(\mathbf{r}) = e^{i\mathbf{k}\cdot\mathbf{R}}\mathbf{E}_{kn}(\mathbf{r}). \quad (2.21)$$

That is, we cannot distinguish between **q** and **k** based on the translational symmetry, and thus Eq. (2.20) and (2.21) are equivalent Bloch modes. Thus any wave vector **q** can be mapped back into the first Brillouin zone. Furthermore, any two wave vectors **k** and $\mathbf{k}'$ are consider equivalent when

$$\mathbf{k}' = \mathbf{k} + \mathbf{G}. \quad (2.22)$$

Equation (2.22) is known as the conservation of crystalline momentum ([5] p.10). As a result of Eq.(2.22), the first Brillouin zone is the volume in reciprocal space that identifies all of the unique Bloch wave vectors, **k,** and hence all the possible unique Bloch modes. Due to this relationship, the convention in the field is to identify each Bloch mode by its Bloch wave vector **k** in the first Brillouin zone and its frequency (energy) band index *n*.

The vector Bloch modes can be expanded in a Fourier series, as follows ([5] p. 15):

$$\mathbf{E}_{kn}(\mathbf{r}) = \sum_{\mathbf{G}} \mathbf{E}_{kn}(\mathbf{G})e^{i(\mathbf{k}+\mathbf{G})\cdot\mathbf{r}} = e^{i\mathbf{k}\cdot\mathbf{r}}\sum_{\mathbf{G}} \mathbf{E}_{kn}(\mathbf{G})e^{i\mathbf{G}\cdot\mathbf{r}} \quad (2.23)$$

$$\mathbf{H}_{kn}(\mathbf{r}) = \sum_{\mathbf{G}} \mathbf{H}_{kn}(\mathbf{G})e^{i(\mathbf{k}+\mathbf{G})\cdot\mathbf{r}} = e^{i\mathbf{k}\cdot\mathbf{r}}\sum_{\mathbf{G}} \mathbf{H}_{kn}(\mathbf{G})e^{i\mathbf{G}\cdot\mathbf{r}}. \quad (2.24)$$

Equation (2.23) and Eq. (2.24) are summed over all the reciprocal lattice vectors given by Eq.(2.4), and the Fourier coefficients, $\mathbf{E}_{kn}(\mathbf{G})$ and $\mathbf{H}_{kn}(\mathbf{G})$, are determined using numerical or analytical techniques. For this body of research, the Fourier expansion is used to determine an analytic form of the Bloch mode in the vanishing dielectric contrast limit, consisting of the first order elements of the Fourier series expansion.

2.3.3 Orthogonality of the Bloch modes

The Maxwell operator of Eq. (2.12) is Hermitian (see [5] pp. 16-18 for a full proof and definition of a Hermitian operator). As a consequence, the magnetic photonic crystal eigenmodes of Eq. (2.16) will be orthogonal to each other, as indicated by

$$\int_V \mathbf{H}^*_{\mathbf{k}n} \cdot \mathbf{H}_{\mathbf{k}'n'} d\mathbf{r} = V \delta_{\mathbf{k}\mathbf{k}'} \delta_{nn'}, \tag{2.25}$$

where the integral is over the volume V of the photonic crystal ([5] p.17). However, the Maxwell operator of Eq. (2.11) is a non-Hermitian operator and the electric photonic crystal eigenmodes of Eq. (2.15) are not necessarily orthogonal to each other. An orthogonality relationship can be established between the electric field and the electric displacement; a new eigenvalue equation can be developed, where the operator is Hermitian and the eigenmodes are $\mathbf{Q}_{\mathbf{k}n}(\mathbf{r}) = \sqrt{\varepsilon_0 \varepsilon(\mathbf{r})}\mathbf{E}_{\mathbf{k}n}(\mathbf{r})$. This leads to the ED orthogonality given by

$$\int_V \mathbf{E}^*_{\mathbf{k}n} \cdot \mathbf{D}_{\mathbf{k}'n'} d\mathbf{r} = V \delta_{\mathbf{k}\mathbf{k}'} \delta_{nn'}, \tag{2.26}$$

where the integral is again over the volume V of the photonic crystal ([5], p. 36).

2.4 Two-dimensional photonic crystals

2.4.1 The eigenvalue problem and scalar Bloch modes

The two-dimensional photonic crystal is represented by a dielectric structure that is periodic in the *x-y* plane and infinite in the $\hat{\mathbf{z}}$ direction, such as the dielectric columns in Figure 2(b) and Figure 3(a). In practice, this theoretical structure is suited to model any two-dimensional periodic photonic crystal where h (the height of the dielectric structure

perpendicular to the periodicity) is such that $h \gg a$ or λ, where a is the lattice constant and λ is the wavelength of light ([90], p. 119). Assuming the dielectric profile has no $\hat{\mathbf{z}}$ dependence and the Bloch wave vectors $\mathbf{k}$ of the photonic crystal eigenmodes are restricted to the *x-y* plane, the eigenvalue problems of Eq. (2.11) and Eq. (2.12) reduce to the following:

$$\mathsf{L}_E^{(TM)} E_z(\mathbf{r}) \equiv -\frac{1}{\varepsilon(\mathbf{r})}\left(\frac{\partial^2}{\partial x^2}+\frac{\partial^2}{\partial y^2}\right) E_z(\mathbf{r}) = \frac{\omega^2}{c^2} E_z(\mathbf{r}), \tag{2.27}$$

$$\mathsf{L}_E^{(TE)} H_z(\mathbf{r}) \equiv -\left(\frac{\partial}{\partial x}\frac{1}{\varepsilon(\mathbf{r})}\frac{\partial}{\partial x}+\frac{\partial}{\partial y}\frac{1}{\varepsilon(\mathbf{r})}\frac{\partial}{\partial y}\right) H_z(\mathbf{r}) = \frac{\omega^2}{c^2} H_z(\mathbf{r}). \tag{2.28}$$

The eigenmodes of Eq. (2.27) and Eq. (2.28) are $E_z(\mathbf{r})$ and $H_z(\mathbf{r})$, which are independent of the $\hat{\mathbf{z}}$ coordinate, polarized in the $\hat{\mathbf{z}}$ direction, and propagate in the *x-y* plane. The solutions of Eq. (2.27) are called TM modes (transverse magnetic), where the electric field of the photonic crystal eigenmodes are of the form $\mathbf{E}(\mathbf{r}) = \hat{\mathbf{z}} E_z(\mathbf{r})$, and the associated magnetic field is found using Eq. (2.7), given by $\mathbf{H}(\mathbf{r}) = \hat{\mathbf{x}} H_x(\mathbf{r}) + \hat{\mathbf{y}} H_y(\mathbf{r})$. The solutions of Eq. (2.28) are called TE modes (transverse electric), where the magnetic field of the photonic crystal eigenmodes are of the form $\mathbf{H}(\mathbf{r}) = \hat{\mathbf{z}} H_z(\mathbf{r})$, and the associated electric field is found using Eq. (2.8), given by $\mathbf{E}(\mathbf{r}) = \hat{\mathbf{x}} E_x(\mathbf{r}) + \hat{\mathbf{y}} E_y(\mathbf{r})$. The eigenmodes of Eq. (2.27) and Eq. (2.28) are

$$\mathbf{E}_{\mathbf{k}n}(\mathbf{r}) = \hat{\mathbf{z}} E_{\mathbf{k}n}(\mathbf{r}) = \hat{\mathbf{z}} u_{\mathbf{k}n}(\mathbf{r}) e^{i\mathbf{k}\cdot\mathbf{r}}, \tag{2.29}$$

$$\mathbf{H}_{\mathbf{k}n}(\mathbf{r}) = \hat{\mathbf{z}} H_{\mathbf{k}n}(\mathbf{r}) = \hat{\mathbf{z}} v_{\mathbf{k}n}(\mathbf{r}) e^{i\mathbf{k}\cdot\mathbf{r}}, \tag{2.30}$$

where $E_{\mathbf{k}n}(\mathbf{r})$ and $H_{\mathbf{k}n}(\mathbf{r})$, called the scalar Bloch modes for the TM and TE case respectively, are labeled by their Bloch wave vector $\mathbf{k}$ in the first Brillouin zone and their frequency band index n. They are called the scalar Bloch modes because the fields are

only polarized the $\hat{\mathbf{z}}$ direction. This allows the rigorous reduction of the vector eigenvalue problem to a scalar eigenvalue problem, significantly reducing the complexity of analytical and numerical models.

The Poynting vectors for the TE and TM cases are found by substituting the Bloch modes Eq. (2.29) or Eq. (2.30), and their associated magnetic or electric field into Eq. (2.19):

$$\mathbf{S}_{kn}^{TE}(\mathbf{r}) = \frac{1}{2\omega\varepsilon_0\varepsilon(\mathbf{r})}\left[\mathbf{k}\left|v_{kn}(\mathbf{r})\right|^2 - \mathrm{Im}\left[\left(v_{kn}^*(\mathbf{r})\nabla v_{kn}(\mathbf{r})\right)\right]\right], \tag{2.31}$$

$$\mathbf{S}_{kn}^{TM}(\mathbf{r}) = \frac{1}{2\omega\mu_0}\left[\mathbf{k}\left|u_{kn}(\mathbf{r})\right|^2 - \mathrm{Im}\left[\left(u_{kn}^*(\mathbf{r})\nabla u_{kn}(\mathbf{r})\right)\right]\right], \tag{2.32}$$

(see Appendix A, for a full derivation). The explicit form of the Poynting vector for the TE and TM cases allows us to examine the relationship between the Bloch wave vector **k**, and the direction of energy flow in greater detail than previously seen in Section 2.3.2. Equation (2.31) and Eq. (2.32) both have the same form, where the Poynting vector is a sum of two parts. Focusing on the TE case, the first part is $\mathbf{k}\left|v_{kn}(\mathbf{r})\right|^2$, where the direction is determined by the Bloch wave vector **k**. The second part is $-\mathrm{Im}\left[\left(v_{kn}^*(\mathbf{r})\nabla v_{kn}(\mathbf{r})\right)\right]$, where the direction is determined by the gradient of the periodic part of the Bloch mode $\nabla v_{kn}(\mathbf{r})$. Since the Bloch wave vector **k** and the periodic part of the Bloch mode are independent of the $\hat{\mathbf{z}}$ axis, the direction of the Poynting vector will be limited to the *x-y* plane. Moreover, we can see that the direction of energy flow is clearly influenced by the Bloch wave vector **k** due to the first part of the sum, but it is only one of two factors, where the second depends on the spatial variation of the periodic part of the Bloch mode $v_{kn}(\mathbf{r})$. Examples of the Poynting vector field of a Bloch mode can be seen in Chapter 5, where Poynting vortices are discussed.

The Fourier expansion of the Bloch mode for the TE and TM cases may be simplified to a sum of plane waves polarized in the $\hat{\mathbf{z}}$ direction, as

$$\mathbf{E}_{kn}(\mathbf{r}) = \hat{\mathbf{z}} e^{i\mathbf{k}\cdot\mathbf{r}} \sum_{\mathbf{G}} E_{kn}(\mathbf{G}) e^{i\mathbf{G}\cdot\mathbf{r}}, \tag{2.33}$$

$$\mathbf{H}_{kn}(\mathbf{r}) = \hat{\mathbf{z}} e^{i\mathbf{k}\cdot\mathbf{r}} \sum_{\mathbf{G}} H_{kn}(\mathbf{G}) e^{i\mathbf{G}\cdot\mathbf{r}}, \tag{2.34}$$

due to the scalar form of the eigenmodes Eq. (2.29) and Eq. (2.30).

2.4.2 Two-dimensional photonic crystal eigenmodes in the vanishing dielectric contrast limit

In the vanishing dielectric contrast, the Fourier expansion of the Bloch modes is limited to its first order terms, and we can obtain an analytical form for the Bloch mode. We express the vanishing dielectric contrast eigenmode with a set of degenerate basis functions. The photonic band structure is found by folding the dispersion curves of the basis functions into the first Brillouin zone. A two-dimensional photonic crystal is typically composed of two materials with relative dielectric permittivities of ε_1 and ε_2. If $\varepsilon_1 = \varepsilon_2$, the solutions of the Maxwell operators Eq. (2.27) and Eq. (2.28) are plane waves given by

$$\mathbf{E}(\mathbf{r}) = E_z e^{i\mathbf{q}\cdot\mathbf{r}} \hat{z}, \tag{2.35}$$

$$\mathbf{H}(\mathbf{r}) = H_z e^{i\mathbf{q}\cdot\mathbf{r}} \hat{z}. \tag{2.36}$$

The plane wave dispersion relationship is $\omega(\mathbf{q}) = v_{ph}|\mathbf{q}|$, where $\mathbf{q}$ is the wave vector, $v_{ph} = c/\sqrt{\varepsilon}$ is the phase velocity and c is the speed of light. If the dielectric permittivity of one of the two materials is increased infinitesimally, so that $\varepsilon_1 \approx \varepsilon_2$, the structure is then periodic, and the eigenmodes now have the form of a Bloch mode. The wave vector $\mathbf{q}$ can be mapped into the first Brillouin zone using Eq. (2.22) and the dispersion

relationship becomes $\omega(\mathbf{k}) \approx v_{ph}|\mathbf{q}| = v_{ph}\sqrt{(\mathbf{k}+\mathbf{G})\cdot(\mathbf{k}+\mathbf{G})}$, where the frequency $\omega(\mathbf{k})$ is a function of the Bloch wave vector $\mathbf{k}$ (see Figure 22 and Figure 25 in chapter 5 for examples) ([5], pp. 5-11). Comparing the forms of the Bloch modes Eq. (2.33) and Eq. (2.34), to Eq. (2.35) and Eq. (2.36) requires $E_{\mathbf{k}n}(\mathbf{G}) \approx H_{\mathbf{k}n}(\mathbf{G}) \approx 1$ and $E_{\mathbf{k}n}(\mathbf{G}') \approx H_{\mathbf{k}n}(\mathbf{G}') \approx 0$ for $\mathbf{G}' \neq \mathbf{G}$, where $\mathbf{G}$ is defined by $\mathbf{q} = \mathbf{k} + \mathbf{G}$. By contrast, for higher bands and/or the edge of the zone, there may be multiple coefficients $E_{\mathbf{k}n}(\mathbf{G})$ and $H_{\mathbf{k}n}(\mathbf{G})$ that give rise to the same frequency

$$\omega(\mathbf{k}) = v_{ph}|\mathbf{q}| = v_{ph}\sqrt{(\mathbf{k}+\mathbf{G})\cdot(\mathbf{k}+\mathbf{G})} = v_{ph}\sqrt{(\mathbf{k}+\mathbf{G}')\cdot(\mathbf{k}+\mathbf{G}')} = v_{ph}\sqrt{(\mathbf{k}+\mathbf{G}'')\cdot(\mathbf{k}+\mathbf{G}'')} = \ldots \tag{2.37}$$

for $\mathbf{G} \neq \mathbf{G}' \neq \mathbf{G}'' \neq \ldots$. For the degenerate case, the Bloch mode approximates the sum of the appropriate plane waves as (see Appendix B)

$$\mathbf{E}_{\mathbf{k},n}(\mathbf{r}) \approx e^{i\mathbf{k}\cdot\mathbf{r}}\left(E_{\mathbf{k},n}(\mathbf{G})e^{i\mathbf{G}\cdot\mathbf{r}} + E_{\mathbf{k},n}(\mathbf{G}')e^{i\mathbf{G}'\cdot\mathbf{r}} + E_{\mathbf{k},n}(\mathbf{G}'')e^{i\mathbf{G}''\cdot\mathbf{r}} + \ldots\right)\hat{\mathbf{z}}, \tag{2.38}$$

$$\mathbf{H}_{\mathbf{k},n}(\mathbf{r}) \approx e^{i\mathbf{k}\cdot\mathbf{r}}\left(H_{\mathbf{k},n}(\mathbf{G})e^{i\mathbf{G}\cdot\mathbf{r}} + H_{\mathbf{k},n}(\mathbf{G}')e^{i\mathbf{G}'\cdot\mathbf{r}} + H_{\mathbf{k},n}(\mathbf{G}'')e^{i\mathbf{G}''\cdot\mathbf{r}} + \ldots\right)\hat{\mathbf{z}}. \tag{2.39}$$

In Chapter 5, the two-dimensional photonic crystal eigenmodes in the vanishing dielectric contrast approximation will be used to analyze Poynting vortices. In Chapter 3, we will develop the method to determine the coefficients, $E_{\mathbf{k},n}(\mathbf{G})$ and $H_{\mathbf{k},n}(\mathbf{G})$, based on symmetry arguments, where they are known as symmetry adapted plane waves ([90] pp. 79-81).

2.5 Photonic crystals slabs

2.5.1 Eigenmodes of photonic crystal slabs

The photonic crystal slab is a dielectric structure that is periodic in the x-y plane, but confines the light in the $\hat{\mathbf{z}}$ direction, such as the dielectric profile of Figure 4(b). The confinement of the light in the $\hat{\mathbf{z}}$ direction is accomplished by guiding light in a dielectric which is on average of higher dielectric permittivity (refractive index) than the surround medium (index guiding) and of a thickness d on the order of λ, the relevant wavelength of light. In an infinite dielectric slab, this would be called index guiding by total internal reflection. The eigenmodes of the photonic crystal slab are the solutions of the vector wave equations Eq. (2.11) and Eq. (2.12), which are difficult to determine directly, requiring time-consuming full vector numerical techniques (see Chapter 4). Alternate approximation techniques have been developed, such as the effective index method [34], and the expansion of the eigenmodes as a sum of dielectric slab eigenmodes ([5], p.180). The effective index method approximates the photonic band structure of a photonic crystal slab by solving the two-dimensional photonic crystal eigenvalue problem, where the dielectric permittivity (index) of the background medium is replaced by an effective dielectric permittivity of the guided modes of the unperturbed dielectric slab. The effective index method is discussed in Section 4.4.2 under numerical methods. To address the index guiding, the expansion of the eigenmodes as a sum of dielectric slab modes replaces the Fourier plane wave expansion when the eigenmodes are determined approximately in the vanishing dielectric contrast limit. In the following sections, we develop the analytical forms of the photonic crystal slab eigenmodes in the vanishing dielectric contrast approximation in three stages: first, we examine the eigenmodes of a dielectric slab, which are the basis modes of the expansion (Section 2.5.2); second, we establish the photonic band structure, where we identify the region in reciprocal space that has tractable photonic crystal slab Bloch modes (below the single mode cutoff frequency of the dielectric slab and outside of the light cone), and we resolve the degenerate basis modes (Section 2.5.3); third,

(a)

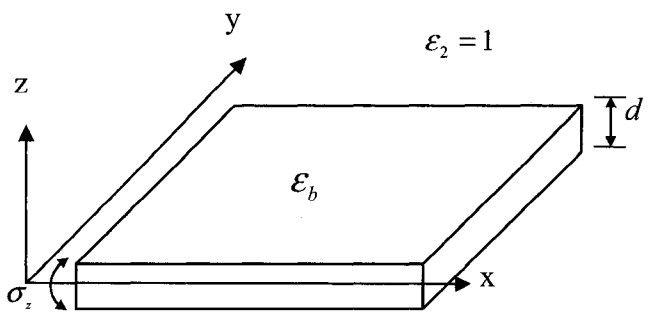

(b)

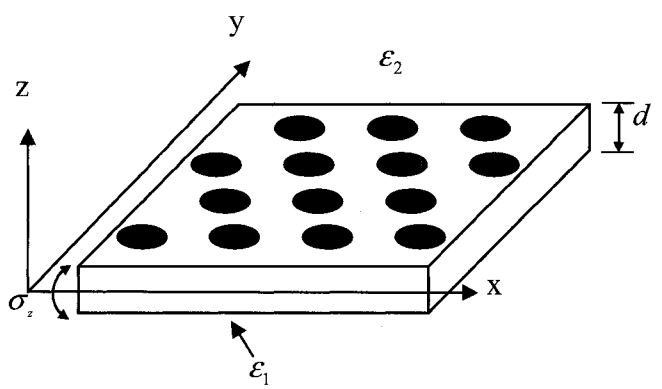

Figure 4. (a) Dielectric slab, finite thickness d in the z direction and infinite in the x-y plane; (b) photonic crystal slab, finite thickness $d = a/2$ in the z direction, infinite in the x-y plane, air hole radius of $r = 0.25a$, background dielectric permittivity of $\varepsilon_1 = 11.56$ (GaAs).

we determine the exact form of the symmetry adapted basis modes (i.e. derive the coefficients of the expansion) based on the symmetry of the photonic crystal Bloch mode (Section 3.4.4).

2.5.2 Eigenmodes of dielectric slabs

The propagating modes of a dielectric slab are in the form of a traveling wave in the *x-y* plane. They are confined within the dielectric slab by index guiding (total internal reflection) according to the degree of index contrast between the slab and the surroundings. The dielectric slab has a finite thickness of d in the $\hat{\mathbf{z}}$ direction and is infinite in the $\hat{\mathbf{x}}$ and $\hat{\mathbf{y}}$ directions (see Figure 4(a)). The relative dielectric permittivity of slab structure is ε_b, which is presumed greater than the dielectric permittivity of the surrounding medium (assumed air, $\varepsilon_0 = 1$). Since the dielectric structure is infinite in the *x-y* plane, Maxwell's equation may be separated into two eigenmode equations, a TE case and a TM, as

$$\frac{1}{\varepsilon(\mathbf{r})}\left(\frac{\partial^2}{\partial z^2} - k_x^2\right) E_y(z) = -\frac{\omega^2}{c^2} E_y(z), \tag{2.40}$$

$$\left(\frac{\partial}{\partial z}\left(\frac{1}{\varepsilon(\mathbf{r})}\frac{\partial}{\partial z}\right) - \frac{k_x^2}{\varepsilon(\mathbf{r})}\right) H_y(z) = -\frac{\omega^2}{c^2} H_y(z), \tag{2.41}$$

where we assume that the eigenmodes propagate in the $\hat{\mathbf{x}}$ direction (i.e., $\mathbf{k} = \hat{\mathbf{x}} k_x$) ([97], p.15). The *x-y* plane is located at the mid-plane inside the dielectric slab, and thus the dielectric structure has mirror symmetry, σ_z, about this plane. The mirror symmetry allows the classification of the modes (TE or TM) as even or odd. The core concepts are explored through the even TE modes, but the extension to the other case is straightforward. The even TE electric field eigenmode inside the dielectric slab, $-d/2 \le z \le d/2$, is given by

$$\mathbf{E}_1 = \begin{pmatrix} 0 \\ E_{1y} \\ 0 \end{pmatrix} \exp\{i(k_x x - \omega t)\} \cos(k_z z), \tag{2.42}$$

where $c^2/\varepsilon(\mathbf{r})(k_z^2 + k_x^2) = \omega^2$, and outside of the dielectric slab, $|\mathbf{z}| > d/2$, is given by

$$\mathbf{E}_2 = \begin{pmatrix} 0 \\ E_{2y} \\ 0 \end{pmatrix} \exp(ik_x x - \kappa z - i\omega t), \tag{2.43}$$

where $\omega^2 = c^2(k_x^2 - \kappa^2)$ ([5], p.176). The related magnetic field can be obtained using Maxwell's equations: inside the dielectric slab, $-d/2 \le z \le d/2$,

$$\mathbf{H}_1 = \frac{E_{1y}}{i\omega\mu_0} \begin{pmatrix} k_z \sin(k_z z) \\ 0 \\ ik_x \cos(k_z z) \end{pmatrix} \exp\{i(k_x x - \omega t)\}, \tag{2.44}$$

and outside of the dielectric slab, $|\mathbf{z}| > d/2$

$$\mathbf{H}_2 = \frac{E_{2y}}{i\omega\mu_0} \begin{pmatrix} \kappa \\ 0 \\ ik_x \end{pmatrix} \exp(ik_x x - \kappa z - i\omega t). \tag{2.45}$$

The x-y plane dependence of the electric field is in the form of a traveling wave, moving parallel to its wave vector $\mathbf{k} = \hat{\mathbf{x}}k_x$. In general, the wave vector $\mathbf{k}$ of the eigenmodes of a dielectric slab may appear any direction in the x-y plane $\mathbf{k} = \hat{\mathbf{x}}k_x + \hat{\mathbf{y}}k_y$; this is due to the infinite translation symmetry in this plane. The state of polarization $\mathbf{E} = \hat{\mathbf{y}}E_{1y}$ is perpendicular to wave vector $\mathbf{k} = \hat{\mathbf{x}}k_x$, parallel to the $\hat{\mathbf{y}}$ axis. The wave vector $\mathbf{k} = \hat{\mathbf{x}}k_x$

and the state of polarization $\mathbf{E} = \hat{\mathbf{y}} E_{1y}$ are orthogonal, $\mathbf{k} \cdot \mathbf{E} = 0$. This orthogonality relationship satisfies the constitutive relationship $\nabla \cdot \mathbf{D}(\mathbf{r}, t) = 0$, where in general $\mathbf{k} \cdot \mathbf{E} = 0$ for any wave vector $\mathbf{k} = \hat{\mathbf{x}} k_x + \hat{\mathbf{y}} k_y$. The $\hat{\mathbf{z}}$ dependence of the electric field is a cosine function within the dielectric slab, $-d/2 \le z \le d/2$, and outside the slab, $|\mathbf{z}| > d/2$, the electric field is evanescent. The electric field is therefore confined to the slab region. The magnetic field given by Eqs. (2.44) and (2.45) has a very similar spatial dependence in the *x-y* plane to the electric field, but the $\hat{\mathbf{z}}$ dependence is different depending on the state of polarization. In general, the electric field of the TE mode has its polarization restricted to the *x-y* plane (i.e., $\mathbf{E}_1 = \hat{\mathbf{x}} E_x(\mathbf{r}) + \hat{\mathbf{y}} E_y(\mathbf{r})$). In contrast, the magnetic field as given by Eqs. (2.44) and (2.45) may be polarized in any direction. Similarly for the TM modes, the polarization of the magnetic field will be restricted to the *x-y* plane and the electric field may be polarized in any direction.

The dispersion relationship of a dielectric slab can be found numerically using a root-finding technique ([97] pp.19-22) (see Figure 5). As an example, we examine a dielectric slab with a core dielectric permittivity of $\varepsilon_b = 8.18$ surrounded by air $\varepsilon_2 = 1$ (in the following section we will see that $\varepsilon_b = 8.18$ is the average dielectric permittivity of an example photonic crystal slab structure). Figure 5 displays the first two TE dielectric slab eigenmodes (red lines), the first two TM dielectric slab eigenmodes (blue lines), and the light cone (green area with the edge given by the blue dashed line). The surface of the light cone is defined by the dispersion relationship for the bulk medium $\varepsilon_2 = 1$ surrounding the dielectric slab $\omega = |\mathbf{k}| c / \sqrt{\varepsilon_2}$, where c is the speed of light. Each of the bands in the dispersion relationship is labeled by its mirror symmetry as either even $\sigma_z = 1$ or odd $\sigma_z = -1$. One of the main characteristics of dielectric slab eigenmodes is that only the first two modes (TE $\sigma_z = 1$ and TM $\sigma_z = -1$) have dispersion relationships that start at $(\omega d / \pi c) = 0$.

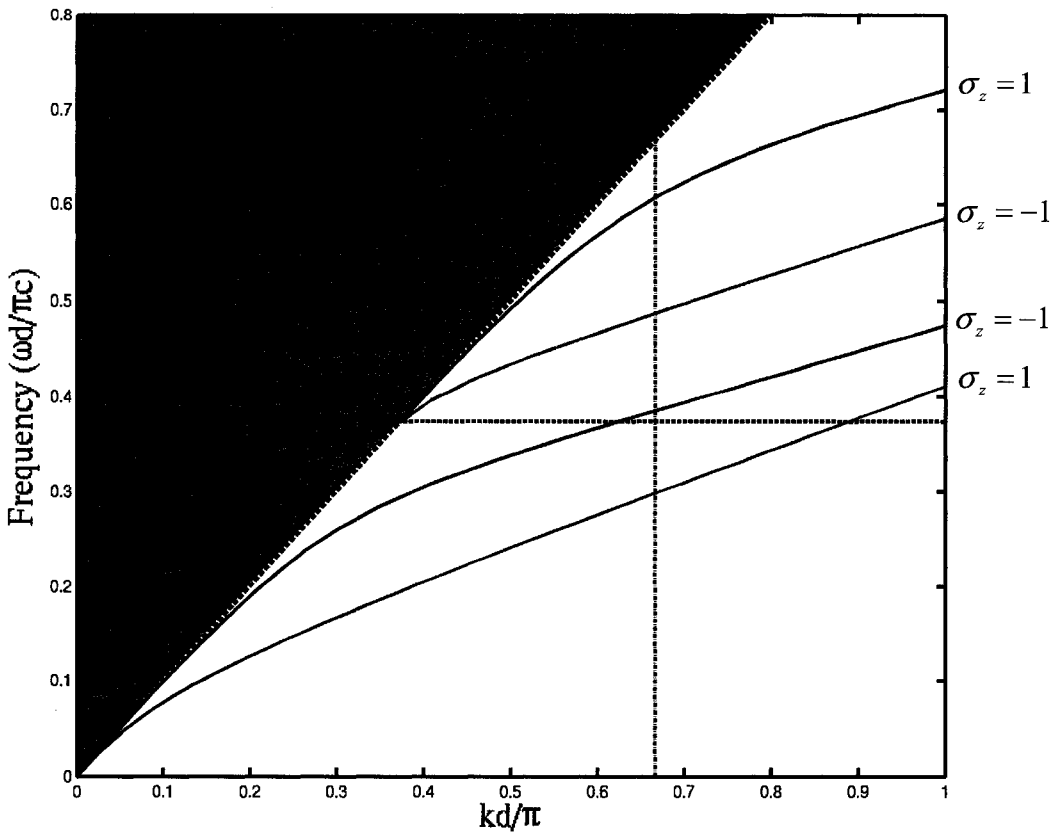

Figure 5. Uniform dielectric slab with core, $\varepsilon = 8.18$, surrounded by air, $\varepsilon = 1$, dispersion relationship: TE modes (red lines) and TM modes (blue lines); dielectric slab light cone (blue dashed line and green area); TE and TM single mode cutoff frequency (horizontal black dashed line); and mode symmetry about the center of the slab indicated as $\sigma_z = 1$ or $\sigma_z = -1$. The axes are in normalized frequency $\omega d/\pi c$ and normalized wave vector kd/π, where d is the thickness of the slab. When $a = d/2$, the K point of the photonic band structure appears at $kd/\pi = 2/3$ (vertical black dashed line).

All of the other dielectric slab modes have cutoff frequencies larger than $(\omega d/\pi c)=0$; in this case, the single mode cutoff for both the TE and TM modes is $(\omega d/\pi c)_{cf}=0.373$.

2.5.3 Photonic crystal slab eigenmodes in the vanishing dielectric contrast limit

The photonic crystal slab eigenmodes have the form of a Bloch mode in the *x-y* plane (due to the periodicity in the *x-y* plane), and are index-guided in the $\hat{\mathbf{z}}$ direction. A photonic crystal slab has the same spatial dimensions as a similar dielectric slab: finite thickness d in the $\hat{\mathbf{z}}$ direction, and mirror symmetry about the *x-y* plane; additionally, it is also periodic in the *x-y* plane. In Figure 4(b), we see an example of a photonic crystal slab that has a hexagonal lattice of periodic air holes, $\varepsilon_2=1$, in a dielectric slab with relative dielectric permittivity ε_1. For illustration, we take the radius of the air holes as $r=0.25a$, and the slab thickness as $d=0.5a$. The relative dielectric permittivity of the dielectric slab is set to $\varepsilon_1=11.56$ (GaAs), and the surround medium is air $\varepsilon_2=1$, which is an example of air-bridge type photonic crystal slab. In the same manner as the two-dimensional photonic crystals, photonic crystal slab eigenmodes are parameterized by the Bloch wave vector **k** and (frequency) band index *n*.

In the previous section, we described the eigenmodes of a uniform dielectric slab, where the dielectric permittivity of the slab ε_b was greater than the surrounding medium $\varepsilon_0=1$. If the dielectric slab is perturbed by the inclusion of holes that have a dielectric permittivity ε_{per} that is infinitesimally smaller than ε_b, the structure is now periodic; this is the vanishing dielectric contrast limit approximation for a photonic crystal slab. In the vanishing dielectric contrast limit, the photonic crystal slab Bloch modes can be expanded as a linear combination of a few terms, similar to the case of the two-dimensional photonic crystal scalar Bloch modes. Now, the optimum set of basis modes is no longer a plane wave set, but the set of dielectric slab eigenmodes of the same dimensions as the photonic crystal slab ([5] pp.179-181). In general, TE and TM dielectric slab modes may mix to form the set of the basis modes, but they must have the

same mirror symmetry either even $\sigma_z = 1$, or odd $\sigma_z = -1$; the reason being that the photonic crystal slab eigenmodes are also classified as even or odd, thus the basis modes must have the same symmetry (see Section 3.3.3 for a more in-depth discussion, where it is shown that the photonic crystal slab eigenmodes are the partner functions of the irreducible representations of the C_{1h} group; and Section 3.4.4 regarding symmetry adapted basis modes). Below the single mode cutoff frequency of a dielectric slab, there are only two modes, the even TE mode and the odd TM mode (see Figure 5). In the vanishing dielectric contrast limit, any photonic crystal slab eigenmode, whose frequency lies below the single mode cutoff frequency of the dielectric slab, will be a linear combination of either even TE modes or odd TM modes, due to the symmetry restrictions on the basis set. To maintain the tractability of the analytical forms of the Bloch modes, we will focus on deriving eigenmodes with frequencies below the single mode cutoff frequency. This also allows a direct comparison between the results obtained using the vanishing dielectric contrast limit approximation and the photonic band structures determined using the effective index method, where only a single effective index can be chosen (see Section 4.4.2).

In Appendix B, in the vanishing dielectric contrast limit, we show the dominant Fourier basis modes of the 2D photonic crystal eigenmodes are plane waves that have a frequency given by the average dielectric perimittivity of the photonic crystal. In the same manner, the dominant Fourier basis modes of the photonic crystal slab eigenmodes are the eigenmodes of a dielectric slab that has the average dielectric permittivity ε_b of the photonic crystal slab ([5], pp. 179-181). For the above-mentioned hexagonal photonic crystal slab, the average dielectric permittivity is $\varepsilon_b = 8.18$ surrounded by air $\varepsilon_2 = 1$, where the slab has a thickness of $d = 0.5a$ (a is the lattice constant). The dispersion relationship of the corresponding dielectric slab was examined in Section 2.5.2 (see Figure 5). Similar to the purely two-dimensional photonic crystal, we can find the photonic band structure of the hexagonal photonic crystal slab in the vanishing dielectric contrast limit by folding the dispersion relationship of the dielectric slab into the first

Brillouin zone using Eq. (2.22) ([5], p.179). For example, at the edge of the Brillouin zone, the K point, the Bloch wave vector is $\mathbf{k} = \hat{\mathbf{x}} 4\pi/(3a)$ (see Figure 6 for the first Brillouin zone of a hexagonal lattice); when $d = 0.5a$, the K point in normalized dielectric slab units is $kd/\pi = 2/3 = ka/2\pi$ (see Figure 5). At $kd/\pi = 2/3 = ka/2\pi$, the even or odd modes are mapped back into the first Brillouin zone using a reduced zone scheme ([96], pp. 159-161). The result is the photonic band structure of the even photonic crystal slab Bloch modes, which appear below the single mode cutoff frequency (see Figure 7). Note that bands 2 and 3, labeled *A* and *B* (labeling to be explained in Section 3.4.3), in the $\Gamma \rightarrow \mathrm{K}$ direction are degenerate in the vanishing dielectric contrast limit (outside of this approximation they are not degenerate due to symmetry, see Section 3.4.3), thus superimposed. In Figure 7, the TE single mode cutoff frequency is labeled by a dashed line and the light cone is the green area. The surface of the light cone is defined by the dispersion relationship for the bulk medium $\varepsilon_2 = 1$ surrounding the photonic crystal slab, $\omega = |\mathbf{k}| c/\sqrt{\varepsilon_2}$, where c is the speed of light, just as for the dielectric slab. The photonic crystal slab eigenmodes that are located inside of the light cone may couple energy to the medium outside of the slab. These Bloch quasi-modes only have finite lifetimes, but are very important for certain applications, such as guided resonance in photonic crystal slabs (see [35] for a more in-depth discussion of these Bloch quasi-modes). Bloch modes that appear outside of the light cone are guided within the slab structure, which have infinite lifetimes. For this body of research, we focus on the guided modes outside of the light cone, although the finite lifetime Bloch modes are an important area for future applications of this research. Note that the photonic band gaps are infinitesimal in the vanishing dielectric contrast limit, because the band gap is related to the dielectric contrast - in this case almost zero ([5], pp. 5-7). With the photonic band structure established, we continue to derive the analytical forms of the photonic crystal slab eigenmodes in the vanishing dielectric contrast limit, where we focus on the even ($\sigma_z = 1$) Bloch mode.

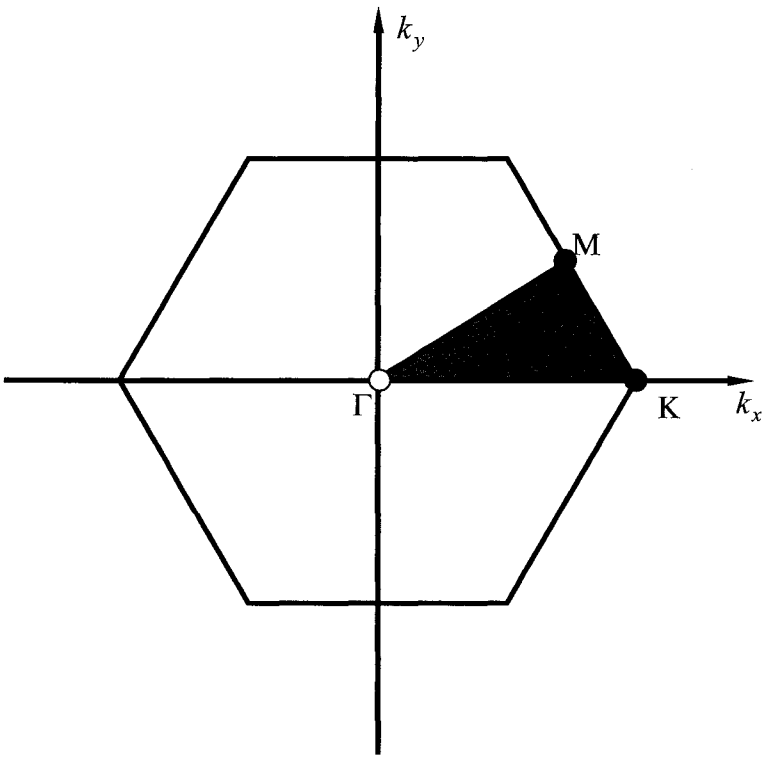

Figure 6. Hexagonal slab photonic crystal first Brillouin zone (black), and irreducible Brillouin zone (grey triangle).

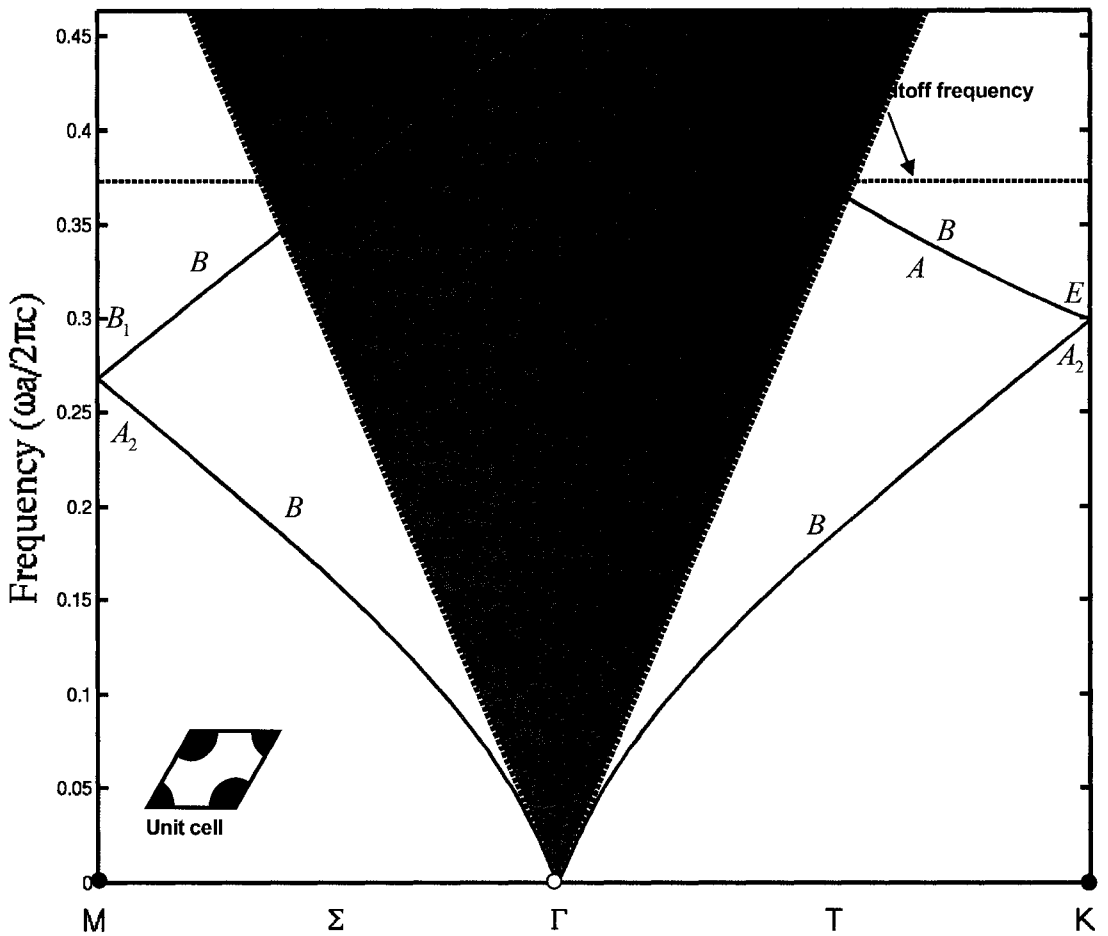

Figure 7. Hexagonal slab photonic crystal, photonic band structure in the vanishing dielectric contrast limit, band 1, 2 and 3 (red line, where 2 and 3 are superimposed); dielectric slab light cone (blue dashed line and green area); and single mode cutoff frequency (black dashed line). The axes are in normalized frequency $\omega a/2\pi c$ and normalized wave vector $ka/2\pi$, where $a = d/2$. Irreducible representation labels are for the electric field.

As previously mentioned, below the TE and TM single mode cutoff frequency, only the first even TE $(\sigma_z = 1)$ modes are the basis modes for the expansion of the even photonic crystal slab Bloch mode. As a result, the Fourier expansion of the even photonic crystal slab Bloch mode is reduced to a sum of degenerate even TE modes (Eq. (2.42)), which have wave vectors $\mathbf{k}+\mathbf{G}'$:

$$\mathbf{E}_{\mathbf{k}n}(\mathbf{r}) = \sum_{\mathbf{G}'} \mathbf{A}(\mathbf{G}') e^{i(\mathbf{k}+\mathbf{G}')\cdot\mathbf{r}} \cos(k_z z), \tag{2.46}$$

where $\mathbf{E}_{\mathbf{k}n}(\mathbf{r})$ represents the electric field within the photonic crystal slab $-d/2 \le z \le d/2$, and $\mathbf{A}(\mathbf{G}')$ are the vector Fourier coefficients of the expansion. Similar to the dielectric slab mode, k_z is determined by $c^2/\varepsilon(\mathbf{r})\left(k_z^2 + (\mathbf{k}+\mathbf{G}')^2\right) = \omega^2$, where now $k_x = \mathbf{k}+\mathbf{G}'$. The field outside of the photonic crystal slab is a summation of the same form as Eq. (2.46), but instead the evanescent electric field is the basis.

To determine the number of degenerate basis modes in Eq. (2.46), one can examine the photonic band structure. In the photonic band structure, the dielectric slab modes are folded back into the first Brillouin zone, where the original wave vector is mapped to its equivalent Bloch wave vector $\mathbf{k}$ in the first Brillouin zone using $\mathbf{k}' = \mathbf{k}+\mathbf{G}$, i.e., Eq. (2.22), (see Section 2.3.2 for more detail on equivalent Bloch wave vectors $\mathbf{k}$). When there are multiple dielectric slab modes with equivalent Bloch wave vectors $\mathbf{k}$ (due to Eq. (2.22)) and the same frequency ω, these modes form the degenerate basis set of Eq. (2.46). At a general point in reciprocal space $(\mathbf{k}, \omega)$, in the first band, the photonic band structure is nondegenerate, which means there is only a single basis mode and Eq. (2.46) reduces to

$$\mathbf{E}_{\mathbf{k}n}(\mathbf{r}) = \mathbf{A}(\mathbf{G}) e^{i(\mathbf{k}+\mathbf{G})\cdot\mathbf{r}} \cos(k_z z). \tag{2.47}$$

To determine $\mathbf{A}(\mathbf{G})$, we can apply the constitutive relation $\nabla \cdot \mathbf{D}(\mathbf{r},t) = 0$ to the electric field within the photonic crystal slab, Eq. (2.47):

$$\nabla \cdot \varepsilon_0 \varepsilon(\mathbf{r}) \mathbf{E}_{kn}(\mathbf{r}) = \nabla \cdot \varepsilon_0 \varepsilon(\mathbf{r}) \mathbf{A}(\mathbf{G}) e^{i(\mathbf{k}+\mathbf{G})\cdot\mathbf{r}} \cos(k_z z) = 0. \tag{2.48}$$

In the vanishing dielectric contrast limit $\varepsilon(\mathbf{r}) \to \varepsilon_{average}$, as a result, $\varepsilon(\mathbf{r})$ may be treated as a constant. Furthermore, the electric TE modes are polarized only in the *x*-*y* plane (see Section 2.5.2), and $\mathbf{k}+\mathbf{G}$ is restricted also to the *x*-*y* plane. Then we obtain the simple relationship

$$\mathbf{A}(\mathbf{G}) \cdot (\mathbf{k}+\mathbf{G}) = 0. \tag{2.49}$$

This relationship is applicable to every basis mode of Eq. (2.46).

Equation (2.47) is consistent with the vanishing dielectric contrast limit because the dielectric contrast is only infinitesimal, whereby the photonic crystal slab Bloch mode must reduce to a simple dielectric slab mode for the general case. This result is also consistent with effective medium theories, where at long wavelengths, λ, as compared to the lattice constant, *a*, the background medium can be approximated by an average effective index, in this case a uniform dielectric slab (see Section 4.4.2).

For higher bands and/or the edge of the zone, there may be multiple dielectric slab modes that are degenerate when mapped back into the first Brillouin zone. As an example, we chose the K point, at the edge of the Brillouin zone, where $(\omega a/2\pi a) = 0.299$ (see Figure 7). At the K point, bands 1, 2 and 3 are degenerate, whereby the three bands correspond to the three Bloch mode wave vectors,

$$\mathbf{k} = \hat{\mathbf{x}} 4\pi/(3a),$$

$$\mathbf{k}' = \mathbf{k} - \left(\hat{\mathbf{x}}\, 2\pi/a - \hat{\mathbf{y}}\, 2\pi/\left(\sqrt{3}a\right)\right) = -\hat{\mathbf{x}} 2\pi/(3a) + \hat{\mathbf{y}}\, 2\pi/\left(\sqrt{3}a\right), \tag{2.50}$$
$$\mathbf{k}'' = \mathbf{k} - \left(\hat{\mathbf{x}}\, 2\pi/a + \hat{\mathbf{y}}\, 2\pi/\left(\sqrt{3}a\right)\right) = -\hat{\mathbf{x}} 2\pi/(3a) - \hat{\mathbf{y}}\, 2\pi/\left(\sqrt{3}a\right),$$

which are equivalent wave vectors according to Eq. (2.22). This point in reciprocal space is well below the TE single mode cut-off frequency $(\omega a/2\pi a) = 0.373$, and outside of the light cone; therefore the Bloch modes are in the form of Eq. (2.46). Substituting the three equivalent wave vectors Eq. (2.50) into Eq. (2.46), and using Eq. (2.49) to determine the direction of polarization for each basis mode, we obtain

$$\mathbf{E}_{\mathbf{k},n}(\mathbf{r}) = \cos(k_z z)\left[\begin{pmatrix}0\\1\\0\end{pmatrix} A(\mathbf{k}-0) e^{i4\pi x/3a} + \begin{pmatrix}\sqrt{3}\\1\\0\end{pmatrix} A\left(\mathbf{k} - \left(\hat{\mathbf{x}}\, 2\pi/a - \hat{\mathbf{y}}\, 2\pi/\left(\sqrt{3}a\right)\right)\right) e^{-i2\pi\left(x/3a - y/\left(\sqrt{3}a\right)\right)}\right.$$
$$\left. + \begin{pmatrix}\sqrt{3}\\-1\\0\end{pmatrix} A\left(\mathbf{k} - \left(\hat{\mathbf{x}}\, 2\pi/a + \hat{\mathbf{y}}\, 2\pi/\left(\sqrt{3}a\right)\right)\right) e^{-i2\pi\left(x/3a + y/\left(\sqrt{3}a\right)\right)}\right]. \tag{2.51}$$

Equation (2.51) is the analytical form of the photonic crystal slab modes, in the vanishing dielectric contrast limit, for the first three Bloch modes at the K point in reciprocal space. The determination of the scalar coefficients $A(\mathbf{k}-\mathbf{G})$ will be explained in Section 3.4.

CHAPTER 3 – APPLICATION OF GROUP THEORY TO PHOTONIC CRYSTAL EIGENMODES

3.1 Introduction

In the previous chapter, we established the photonic crystal eigenvalue problem for the two-dimensional photonic crystal and the photonic crystal slab. In each case, we touched upon the form of the Bloch modes and used the vanishing dielectric contrast approximation to determine the photonic band structures. We were able to generally describe the photonic crystal eigenvalue problem by treatments based on the dominant symmetries of the photonic crystal, such as the application of Bloch's theorem due to periodic symmetry, and the separation of the fields into TE and TM cases due to mirror symmetry. A typical photonic crystal has other symmetries associated with the dielectric structure and its associated eigenmodes, which we have touched upon in developing Eq. (2.51). Therefore it is beneficial to seek further reductions based rigorously on symmetry before attempting to solve the photonic crystal eigenvalue problem. Throughout this study of optical singularities in photonic crystals, the resources of group theory will assist us in taking full advantage of the system symmetries. In this chapter, we establish the formal language of group theory applied to photonic crystals. The application to optical singularities is left to subsequent chapters.

Historically, group theory has been used to study the global optical response of photonic crystals, using analytical methods. This approach has clarified the sources of new and perplexing phenomena undiscovered during numerical and experimental studies. For example, it has been shown that certain photonic crystal eigenmodes cannot be excited by external plane waves due to a symmetry mismatch [91]-[92], and symmetry insights have led to the discovery of Brewster bands [98]-[99]. Group theory also has been used to determine additional selection rules for nonlinear photonic crystal optical processes ([5]

pp.100-123), and to explain the absence of diffraction loss within a photonic crystal ([5] pp.183-186). For approximate methods, group theory provides the method to choose first order functions of the correct symmetry ([5], pp. 5-11), ([5], pp. 50-54), ([5], pp. 179-181), and ([90] pp. 79-81).

This body of work focuses on the sub-wavelength properties of the electromagnetic field, which to this point have not received any formal treatment in the field of photonic crystals. Therefore, it is necessary to make explicit group theoretic methods that have only received special treatments, and to apply new local symmetry methods to the study of photonic crystals (where the group theory methods used are common to quantum mechanical problems [113]-[117]); these new applications of group theory form the second goal of this thesis. For each type of optical singularity, the group theoretic properties were investigated by examining Bloch modes analytically derived in the vanishing dielectric contrast limit. The vanishing dielectric contrast Bloch modes are explicitly derived using symmetry adapted basis functions, based on irreducible representation projection operator techniques. This work is inspired by preivous contributions: ([5], pp. 5-11), ([5], pp. 50-54), and ([5], pp. 179-181), in which a simplified group theorectic method is outlined to assign irreducible representations to photonic band structures; ([90] pp. 79-81), where Bloch modes are treated as symmetry-related polarized plane waves, although no explicit derivation is given; [115] and [116], in which rigorous group theoretic methods are applied to quantum mechanical systems. Additionally, the concept of site (local) symmetry has been applied to the transformation properties of the optical modes. In this case, the determination of the irreducible representations of the transformation operations has been generalized to any symmetry axis of the dielectric structure – not just the principal axis. To my knowledge, this is the first application of site symmetry to the optical response of photonic crystals.

Initially, we review abstract group theory, whereby we establish the characteristics of a group and group representation. In this context, reducible and irreducible representations of a group will be discussed. Next, we move to the application of abstract group theory

to photonic crystals. The primary symmetry of which we will take advantage of is the transformation properties of the photonic crystal eigenvalue problem given by Eq. (2.11) and Eq. (2.12). We show how to extract the modal characteristics encoded by the system symmetries given by the transformation properties of the dielectric profile, $\varepsilon(\mathbf{r})$, and the Bloch wave vector $\mathbf{k}$. Transformation operators cause a coordinate transformation in any mathematical entity that follows them. In this case, the mathematical entities will be points in Cartesian space, other operators, or functions. More specifically, we examine the group of transformation operators that leave the photonic crystal eigenvalue problem invariant; this is known as the photonic crystal space group, G. The exploration of the photonic crystal space group, G, is divided into two parts, part one global properties and part two local properties.

In part one, Section 3.3, we examine the symmetry properties related to the periodic translational symmetry operators and the photonic crystal point group. The photonic crystal point group is composed of all the transformation operators that leave the principal axis invariant, where the principal axis is the axis of highest symmetry in the photonic crystal ([113], p. 39). These transformation operators include rotations, mirror reflections, and inversions. The photonic crystal eigenmodes are classified by association with the irreducible representations of the above mentioned groups. The irreducible representations reveal the allowed symmetry transformation properties of their associated photonic crystal eigenmodes and identify frequency degeneracies in the photonic crystal eigenmodes. The irreducible representation associated with an eigenmode can be determined by examining the spatial transformations of the eigenmodes obtained by numerical simulation. However, there is another more fundamental analytical method to identify the irreducible representation associated with a photonic crystal eigenmode that we review in Section 3.4.3 ([5] pp. 52-54). Finally in Section 3.4.4, we describe fully the derivation of the photonic crystal eigenmodes in the vanishing dielectric contrast limit introduced in Chapter 2. Here the projection operators of the irreducible representations reveal symmetry adapted basis functions, which are the photonic crystal eigenmodes

(extending the work of ([5], pp. 5-11), ([5], pp. 50-54), ([5], pp. 179-181), and ([90] pp. 79-81)).

In part 2, Section 3.5, we develop the symmetry constraints on the local optical response of the photonic crystal via an analysis of its site (local) symmetry, crystallographic orbits and fundamental domain. This permits us to characterize the nature of the singularities that must arise as a consequence of system symmetries. To our knowledge, this is the first application of these concepts to photonic crystals, in which it was motivated by the local nature of optical singularities. The site symmetry group is the set of transformation operators that leave the photonic crystal eigenvalue problem invariant, where the transformation operators may be applied with respect to any point within the photonic crystal, not just the principal axis. These transformation operators include not only rotations, mirror reflections and inversions, but also translations that are fractions of a lattice vector. We show that the classification of the photonic crystal eigenmodes, according to their irreducible representations, changes when a non-principal axis is considered.

3.2 Abstract group theory fundamentals

3.2.1 Elements of a group

A group is an abstract mathematical entity consisting of a set G of elements g ($g \in G$) that may be of finite order (order is the number of elements g in the set G), or may be of infinite order. The group G must have a defined binary algebraic operation that associates any two elements with a third element (i.e., group multiplication). In addition, the group's binary algebraic operation must have the following four characteristics:

1. The product of any two elements of the set must be equal to another element in the same set:

$$g_i g_j = g_k, \quad g_i, g_j, g_k \in G, \tag{3.1}$$

that is, the group is closed under group multiplication.

2. The product of three or more elements is associative:

$$\left(g_i g_j\right) g_k = g_i \left(g_j g_k\right), \quad g_i, g_j, g_k \in G. \tag{3.2}$$

3. The group contains an identity element E, such that

$$E g_i = g_i E = g_i, \quad g_i \in G. \tag{3.3}$$

4. Every element g of the set G has an inverse (reciprocal) element g^{-1}, such that

$$g g^{-1} = g^{-1} g = E, \quad g \in G. \tag{3.4}$$

By establishing the defining characteristics of a group, we can also define subgroups, conjugate elements, and conjugacy classes. The set B of elements b are considered a subgroup of G, if B is a subset of the elements in G ($b \in B \subset G$), and B also forms a group according to the four characteristic given above. Two elements, g_i and g_j ($g_i, g_j \in G$), are considered conjugate to one another if there exists an operator q ($q \in G$), such that $g_i = q g_j q^{-1}$. In addition, if g_j and g_k are conjugate to g_i, then they are also conjugate to each other ([115], p. 12). All of the elements that are mutually conjugated form what is called a conjugacy class.

Finally, we note the relationships between groups, defined as group homomorphism and group isomorphism. If there are two groups G and G' that have a many-to-one correspondence between the group elements, then the two groups are considered

homomorphic. The most trivial example is the identity group (order equal to one, the set containing only the identity operator E), which is homomorphic to any other group because the group multiplication reduces to $EE = E$. If there are two groups G and G' with the same order that have a one-to-one correspondence between the elements, then the two groups are considered isomorphic. ($g_i \rightarrow g_i'$ and $g_i g_j = g_k \rightarrow g_i' g_j' = g_k'$)

3.2.2 Group representations

Any group G_D of concrete mathematical entities that is homomorphic to the original group G is a representation of the abstract group G. G_D is typically a set of linear operators $\hat{D}(g) = \hat{g}$ in a vector space L_m. The group multiplication of the set G_D is given by

$$\hat{D}(g_i)\hat{D}(g_j) = \hat{D}(g_i g_j), \tag{3.5}$$

which satisfies the four requirements in Section 3.2.1. The representation G_D has the same dimension m and the same basis e_i ($i = 1,2,\ldots m$) as the vector space L_m. The basis e_i ($i = 1,2,\ldots m$) of the space L_m may be a set of functions, denoted the partner functions of the representation. In the vector space L_m, the matrix $\ddot{D}^{(\nu)}(g)$ (ν is a representation label) defines the operator $\hat{D}(g)$ given by

$$\hat{D}(g)e_i = \sum_j D_{ji}^{(\nu)}(g)e_j, \tag{3.6}$$

where $D_{ji}^{(\nu)}(g)$ are the matrix elements of $\ddot{D}^{(\nu)}(g)$. The set of matrices $\Gamma^{(\nu)}$ (where $\Gamma^{(\nu)}$ is the set of $\ddot{D}^{(\nu)}(g)$, $g \in G_D$) is the matrix representation, ν, of the group G_D, in the basis e_i ($i = 1,2,\ldots m$). The binary algebraic operations of the set $\Gamma^{(\nu)}$ are matrix multiplications, where the elements, $\ddot{D}^{(\nu)}(g)$ ($g \in G_D$), satisfy the requirements of

Section 3.2.1. For this body of research, all the matrices defined by Eq. (3.6) will be unitary matrices, where the defining feature of a unitary matrix is $\left(\vec{\vec{D}}(g)\right)^{\dagger} = \left(\vec{\vec{D}}(g)\right)^{-1}$ (i.e. the inverse element g^{-1} is represented by the transpose of the matrix $\vec{\vec{D}}(g)$). An equivalent representation of the group G can be created by introducing a nonsingular unitary operator $\hat{A}$ and defining the elements of the equivalent set as

$$\hat{D}'(g) = \hat{A}\hat{D}(g)\hat{A}^{-1},\ g \in G_D. \tag{3.7}$$

The matrix representation of $\hat{D}'(g)$ is the set of matrices $\vec{\vec{A}}\vec{\vec{D}}^{(v)}(g)\vec{\vec{A}}^{-1}$, which is the equivalent matrix representation, in the new basis $\hat{A}e_i = \sum_j A_{ji}e_j$ in the space L_m. Since there are an infinite number of choices of the operator $\hat{A}$ and similarly for $\vec{\vec{A}}$, there is an infinite number of equivalent representations of the group G_D.

A representation can be considered an irreducible representation or a reducible representation. An irreducible representation is defined as a representation which cannot be expressed in a representation of lower dimensionality *m*. All other representations are considered reducible representations. In other words, for a representation, if there is a subspace L_p ($L_p \subset L_m$, $p < m$) that is also invariant when acted upon by the operators of the group $\hat{D}(g), g \in G_D$ (given by Eq. (3.6)) then the representation is reducible. The irreducible representations are very important because they are considered the fundamental representations of the group. The number of irreducible representations of a group is equal to the number of conjugacy classes of the group. For a given group *G*, the sum of the dimensions m_v^2 of the irreducible representations must be equal to the number of elements in the group h (i.e., $h = \sum_v m_v^2$); thus for a finite group, there will be a finite number of irreducible representations, each with a definite dimension. In the following

sections, we will show that each photonic crystal eigenmode is a partner function for a particular irreducible representation of a group of transformation operators. The irreducible representation provides the ideal symmetry label for the photonic crystal eigenmodes (in quantum mechanics, this is known as "a good quantum number" ([115], p. 36)). Furthermore, the dimension m_v of the irreducible representation associated with a photonic crystal eigenmode reveals the frequency degeneracy required by fundamental symmetry arguments.

The space L_m of a reducible representation can be decomposed into a direct sum of invariant sub spaces $L_{m_v}^{(v)}$ of the irreducible representations:

$$L_m = \sum L_{m_v}^{(v)}, \tag{3.8}$$

where v identifies the irreducible representation, and $m = \sum m_v$. Due to Eq. (3.8), the matrix representation of the reducible representation $\Gamma^{(red)}$ can also be decomposed into the direct sum of irreducible matrix representations:

$$\Gamma^{(red)} = \sum a_v \Gamma^{(v)}, \tag{3.9}$$

where a_i is the number of times $\Gamma^{(i)}$ appears in the direct sum. Note the direct sum of matrices is not simple matrix addition. For example, the set $\Gamma^{(red)} = \Gamma^{(v)} + \Gamma^{(w)}$ has matrix elements in the following form

$$\vec{D}^{(red)}(g) = \begin{pmatrix} \vec{D}^{(v)}(g) & \mathbf{0} \\ \mathbf{0} & \vec{D}^{(w)}(g) \end{pmatrix}, \tag{3.10}$$

where **0** represents a block of zeros. Many times, the reducible matrix representation $\vec{D}^{(red)}(g)$ will not appear in diagonal form such as Eq. (3.10). The rows and columns of $\vec{D}^{(red)}(g)$ must be unscrambled using a similarity transformation $\vec{A}$, the matrix representation of the nonsingular unitary operator $\hat{A}$. Since the matrix representation $\vec{D}^{(v)}(g)$ is defined by Eq. (3.6) in terms of the basis e_i $(i=1,2,\ldots m)$, we can conclude that the choice of basis determines the irreducibility or reducibility of a representation. In Section 3.4, we illustrate decomposition a reducible representation into its irreducible representations (Eq. (3.9)). This decomposition process will be used to determine the possible irreducible representations associated with each photonic crystal Bloch mode in a photonic band structure.

All equivalent matrix representations related by unitary transformations (Eq. (3.7)) have the same character, $\chi(g)$, where the character, $\chi(g)$, is defined as the trace of the matrix:

$$\chi(g)=Tr\left\{\vec{D}(g)\right\}=\sum_i D_{ii}(g). \tag{3.11}$$

Therefore, the set of characters (the set of $\chi(g)$, where $g\in G_D$) provides a way of identifying all the equivalent representations and characterizing the group independent of the basis. Furthermore, all the elements that belong to a particular conjugacy class will also have the same character, since these elements are related by unitary transformations (i.e., all the transformation operators of the symmetry groups are unitary transformations).

3.3 Periodic symmetry and the photonic crystal point group

3.3.1 Transformation operators

We here explore the symmetry properties of the photonic crystal eigenvalue problem with regards to the periodic translation symmetry group and the photonic crystal point group. These groups are both subgroups of the photonic crystal space group G. The transformation operators R will be the main tool to establish the symmetry transformation properties. Each operator R can be specified by a real orthogonal transformation of the coordinates; we first define the application of the operators to points in space and then to functions.

The photonic crystal point group transformation operators are: the rotational symmetry operator C_n, where n specifies the $2\pi/n$ rotation angle about the principal axis of symmetry; the mirror reflection operator σ_v, where v identifies the mirror plane through the principal axis; and the identity operator E, which leaves the system the same. Similarly, the transformation operators of the periodic symmetry subgroup are all the translations by lattice vectors $\mathbf{R}$ as defined by Eq. (2.1), where the operator is $T(\mathbf{R})$. In the next section, we will examine some of the typical point groups of two-dimensional photonic crystals and photonic crystal slabs and see how they can change depending on the choice of the Bloch wave vector $\mathbf{k}$.

In the Cartesian coordinate system, a point is described by a position vector $\mathbf{r} = (x, y, z)$. If the coordinate system is rotated about the principal axis (located at $(0,0,0)$ and parallel to the $\hat{\mathbf{z}}$ axis) by an angle φ, the position vector remains unchanged, but it has a different set of vector components $\mathbf{r} = (x', y', z')$ in the new rotated coordinate system (see Figure 8(a)). The old vector components are mapped to the new vector components by

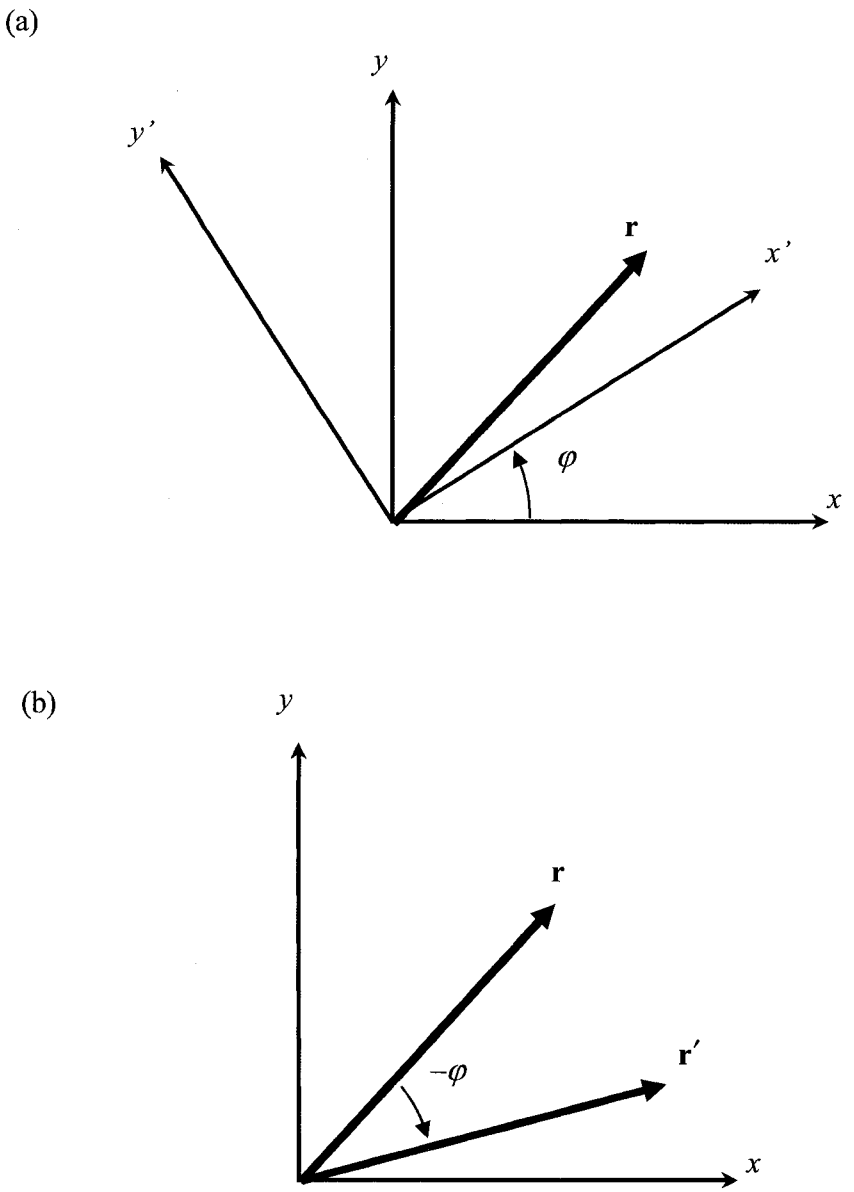

Figure 8. Rotation applied to a position vector **r** from the two points of view: (a) the vector r remains fixed and the coordinate system is rotated; (b) coordinate system remains fixed, and a new vector $\mathbf{r}'$ is created.

$$x' = x\cos\varphi + y\sin\varphi, \tag{3.12}$$

$$y' = -x\sin\varphi + y\cos\varphi, \tag{3.13}$$

$$z' = z. \tag{3.14}$$

If the position vector $\mathbf{r} = (x, y, z)$ is set as a column vector, then the relationships Eq. (3.12)-(3.14) can be written in matrix form as follows:

$$\begin{pmatrix} x' \\ y' \\ z' \end{pmatrix} = \begin{pmatrix} \cos\varphi & \sin\varphi & 0 \\ -\sin\varphi & \cos\varphi & 0 \\ 0 & 0 & 1 \end{pmatrix} \begin{pmatrix} x \\ y \\ z \end{pmatrix}, \tag{3.15}$$

where the rotation is represented as a real orthogonal matrix $\ddot{R}$. In fact, any coordinate transformation can be placed in the matrix form

$$\mathbf{r}' = \ddot{R}\mathbf{r}. \tag{3.16}$$

Since $\ddot{R}$ is an orthogonal matrix, the inverse of this operation is $\ddot{R}^{-1} = \ddot{R}^{\dagger}$, where $\ddot{R}^{\dagger}$ is the transpose of $\ddot{R}$, and $\ddot{R}\ddot{R}^{-1} = \ddot{E}$, where $\ddot{E}$ is the identity matrix. The transformation of a point by an orthogonal matrix is known as a similarity transformation. An alternate point of view has the vector $\mathbf{r}$ rotated by $-\varphi$ to create a new vector $\mathbf{r}'$, when it is transformed by $\ddot{R}$, and the coordinate axis remains fixed (see Figure 8(b)). This second point of view reduces the confusion of multiple sets of coordinates, and emphasizes the effect $\ddot{R}$ has on the object $\mathbf{r}$. It is this second point of view that will be used throughout this study for the transformation of any object in space, including scalar functions and vector fields. These two points of view have a direct equivalence to quantum theory. The first point of view is analogous to the Heisenberg picture, where the basis transforms in time but the state vector remains fixed. The second point of view is analogous to the

Schrödinger picture, where the basis is fixed and the state vector transforms in time ([114], pp.191-203). We can further develop this idea by writing Eq. (3.16) as the application of the rotation operator C_n to the point in space $\mathbf{r}$:

$$C_n\mathbf{r} \equiv \ddot{C}_n\mathbf{r} = \mathbf{r}'. \tag{3.17}$$

Comparing Eq. (3.17) to Eq. (3.6), we can see that $\ddot{C}_n$ is the matrix form of the operator C_n in the Cartesian coordinate system.

Any scalar function $f(\mathbf{r})$ may be transformed by an operator R, under fixed coordinate systems as

$$Rf\left(\ddot{R}\mathbf{r}\right) = f(\mathbf{r}), \tag{3.18}$$

equivalently

$$Rf(\mathbf{r}) = f'(\mathbf{r}) = f\left(\ddot{R}^{-1}\mathbf{r}\right), \tag{3.19}$$

([5], p. 46). That is the application of the transformation operator, R, to the scalar function, $f(\mathbf{r})$, produces a new scalar function $f'(\mathbf{r})$.

If this operator R transforms a vector field $\mathbf{F}(\mathbf{r})$, the scalar part is transformed as Eq. (3.19) while the vector portion transforms as Eq. (3.16), so that

$$R\mathbf{F}(\mathbf{r}) = \ddot{R}\mathbf{F}\left(\ddot{R}^{-1}\mathbf{r}\right), \tag{3.20}$$

([5], p. 62). Note that Eq. (3.20) can be written in Cartesian component form as

$$R\mathbf{F}(\mathbf{r}) = F_x\left(\vec{R}^{-1}\mathbf{r}\right)\left(\vec{R}\hat{\mathbf{x}}\right) + F_y\left(\vec{R}^{-1}\mathbf{r}\right)\left(\vec{R}\hat{\mathbf{y}}\right) + F_z\left(\vec{R}^{-1}\mathbf{r}\right)\left(\vec{R}\hat{\mathbf{z}}\right). \tag{3.21}$$

As an example, we rotate the vector field

$$\mathbf{E}(\mathbf{r}) = \begin{pmatrix} 1 \\ 0 \\ 0 \end{pmatrix} e^{-iky} + \begin{pmatrix} 0 \\ 1 \\ 0 \end{pmatrix} e^{-ikx} \tag{3.22}$$

by $\varphi = \pi/2$, where we have switched to column vector notation. The orthogonal matrix for a rotation by $\varphi = \pi/2$ is

$$\vec{C}_4 = \begin{pmatrix} 0 & -1 & 0 \\ 1 & 0 & 0 \\ 0 & 0 & 1 \end{pmatrix}, \tag{3.23}$$

and the inverse of the rotation is

$$\vec{C}_4^{-1} = \begin{pmatrix} 0 & 1 & 0 \\ -1 & 0 & 0 \\ 0 & 0 & 1 \end{pmatrix} \tag{3.24}$$

(For the second point of view, where the coordinates are fixed, the inverse of the matrix in Eq. (3.15) is used to derive Eq. (3.23) and Eq. (3.24)). When C_4 is applied to a scalar function, we obtain

$$C_4 f(x,y,z) = f\left(\vec{C}_4^{-1}(x,y,z)\right) = f(y,-x,z). \tag{3.25}$$

To transform the vector field Eq. (3.22), we apply the results of Eq. (3.25) to the scalar components and multiply the vector part by the matrix Eq. (3.23):

$$
\begin{aligned}
C_4\mathbf{E}(\mathbf{r}) &= \begin{pmatrix} 0 & -1 & 0 \\ 1 & 0 & 0 \\ 0 & 0 & 1 \end{pmatrix}\begin{pmatrix} 1 \\ 0 \\ 0 \end{pmatrix} e^{ikx} + \begin{pmatrix} 0 & -1 & 0 \\ 1 & 0 & 0 \\ 0 & 0 & 1 \end{pmatrix}\begin{pmatrix} 0 \\ 1 \\ 0 \end{pmatrix} e^{-iky} \\
&= \begin{pmatrix} 0 \\ 1 \\ 0 \end{pmatrix} e^{ikx} + \begin{pmatrix} -1 \\ 0 \\ 0 \end{pmatrix} e^{-iky}.
\end{aligned} \tag{3.26}
$$

3.3.2 Irreducible representations

A photonic crystal's point group is the set of transformation operators R, with respect to the principal axis, that leave the dielectric profile $\varepsilon(\mathbf{r})$ invariant:

$$
R\varepsilon(\mathbf{r}) = \varepsilon(\mathbf{r}). \tag{3.27}
$$

In a photonic crystal, there may be multiple axes of rotation and planes of mirror reflection symmetry that satisfy Eq. (3.27), but the principal axis will be the axis of highest rotational symmetry and it will be coincident with the largest number of mirror reflection planes ([113], p. 39). For two-dimensional photonic crystals, the dielectric structure is periodic in the x-y plane and infinite in the $\hat{\mathbf{z}}$ direction. Thus we focus on transformation operators acting in the x-y plane (the principal axis will be parallel to the $\hat{\mathbf{z}}$ axis). For a system that is periodic in two-dimensions, the only possible rotational symmetries in the x-y plane are C_n, $n = 1,2,3,4,6$. Due to this limitation on rotational symmetry, the two main lattice symmetries of interest are the hexagonal lattice and the square lattice. In the case of a hexagonal lattice, the set of symmetry operations R that leave the dielectric profile invariant are

$$
C_{6v} = \left\{E, C_6, C_6^{-1}, C_3, C_3^{-1}, C_2, \sigma_x, \sigma_x', \sigma_x'', \sigma_y, \sigma_y', \sigma_y''\right\}, \tag{3.28}
$$

(see Figure 9(a)). To label the point groups of two-dimensional systems, we use the Schoenflies notation C_{nv}, where n indicates the rotation angle $2\pi/n$ of the largest rotation operator, and v (h) indicates the presence of mirror reflection operators parallel (perpendicular) to the rotation plane ([115], pp. 53-61). Thus the hexagonal lattice point group is called the C_{6v}. For a square lattice, the set of symmetry operations R that leave the dielectric profile invariant are

$$C_{4v} = \left\{E, C_4, C_4^{-1}, C_2, \sigma_x, \sigma_y, \sigma_d', \sigma_d''\right\}, \tag{3.29}$$

(see Figure 9(b)). Both of these sets of symmetry operations, C_{6v} and C_{4v}, form mathematical groups because they satisfy the group requirements of section 3.2.1 when operating on the dielectric profile given by Eq. (3.16): first, any two subsequent symmetry operators are equivalent to a single operator within the same symmetry group, such as $\sigma_y\left(\sigma_x \varepsilon(\mathbf{r})\right) = C_2 \varepsilon(\mathbf{r})$; second, any three symmetry operators are associative, i.e. $E\left(C_2\sigma_y\right)\varepsilon(\mathbf{r}) = \left(EC_2\right)\sigma_y \varepsilon(\mathbf{r})$; third, the group contains the identity element E that leaves every element in the group unchanged when multiplied by it, $E\left(C_2\varepsilon(\mathbf{r})\right) = C_2\varepsilon(\mathbf{r})$; fourth, every element of the group R has an inverse R^{-1} that is also part of the group, such that $RR^{-1} = R^{-1}R = E$. In Figure 9, the principal axis is located at the center of a red column, for both the hexagonal lattice and the square lattice. Note that the location of the principal axis is unique only to within a reciprocal lattice vector **R**, because the center of each column is equivalent due to the periodic symmetry. The same groups of symmetry operators that leave the dielectric profile invariant also leave the Maxwell operators invariant. The application of a symmetry operator to the Maxwell operator takes the following form:

$$R\mathsf{L}_E^{(TM)}R^{-1} = \mathsf{L}_E^{(TM)}, \tag{3.30}$$

$$R\mathsf{L}_H^{(TE)}R^{-1} = \mathsf{L}_H^{(TE)}, \tag{3.31}$$

(a)

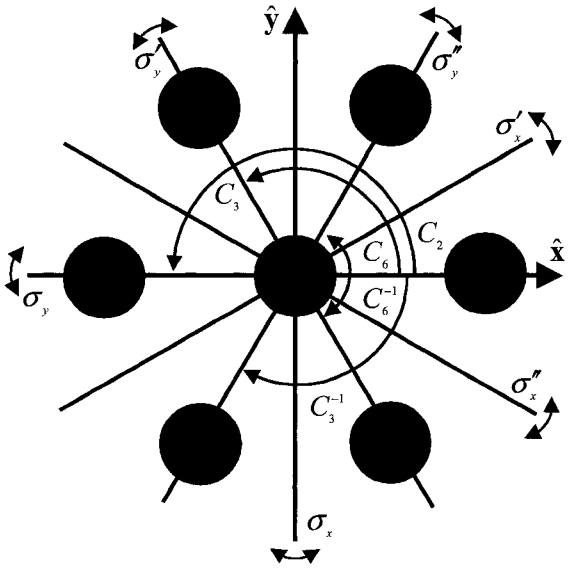

$$R\varepsilon(\mathbf{r}) = \varepsilon(\mathbf{r})$$

(b)

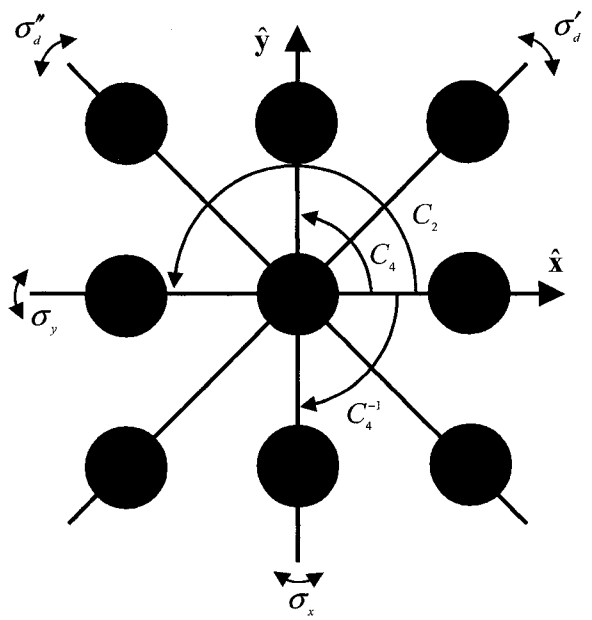

Figure 9. Two-dimensional photonic crystal lattices, top down view of the dielectric profile and the set of symmetry operators that leave the dielectric profile invariant: (a) hexagonal lattice, and (b) square lattice.

where we focus on the two-dimensional forms for the Maxwell operators given by Eq. (2.27) and Eq. (2.28). Equations (3.30) and Eq. (3.31) imply that the symmetry operator R commutes with the Maxwell operators, hence the operators have simultaneous eigenmodes (see [5] pp.46-47 for a full proof).

Substituting the scalar form of the TM Bloch mode Eq. (2.29) into Eq. (2.27), and applying the symmetry operator R to both sides (using $RR^{-1} = R^{-1}R = E$ and Eq. (3.30)), we obtain:

$$R\mathsf{L}_E^{(TM)}R^{-1}R\mathbf{E}_{\mathbf{k}n}(\mathbf{r}) = \mathsf{L}_E^{(TM)}Ru_{\mathbf{k}n}(\mathbf{r})e^{i\mathbf{k}\cdot\mathbf{r}} = \frac{\omega^2}{c^2}Ru_{\mathbf{k}n}(\mathbf{r})e^{i\mathbf{k}\cdot\mathbf{r}}. \tag{3.32}$$

We have suppressed the $\hat{\mathbf{z}}$ polarization because it is invariant under transformation operators R, and we focus on the TM case; these results are equally applicable to the TE case. From Eq. (3.32) it is clear that since $u_{\mathbf{k}n}(\mathbf{r})e^{i\mathbf{k}\cdot\mathbf{r}}$ is an eigenmode, $Ru_{\mathbf{k}n}(\mathbf{r})e^{i\mathbf{k}\cdot\mathbf{r}}$ must also be an eigenmode and has the same eigenvalue ω^2/c^2 (i.e., they are degenerate). In particular, the application of R to the eigenmode is

$$Ru_{\mathbf{k}n}(\mathbf{r})e^{i\mathbf{k}\cdot\mathbf{r}} = u_{\mathbf{k}n}\left(\vec{R}^{-1}\mathbf{r}\right)e^{i\mathbf{k}\cdot\vec{R}^{-1}\mathbf{r}} = u_{\mathbf{k}n}\left(\vec{R}^{-1}\mathbf{r}\right)e^{i\vec{R}\mathbf{k}\cdot\mathbf{r}} = u'_{\vec{R}\mathbf{k}n}(\mathbf{r})e^{i\vec{R}\mathbf{k}\cdot\mathbf{r}}, \tag{3.33}$$

where the invariance of the dot product (scalar quantity) to symmetry transformations is used (i.e., $\mathbf{k}\cdot\vec{R}^{-1}\mathbf{r} = R\mathbf{k}\cdot R\vec{R}^{-1}\mathbf{r} = R\mathbf{k}\cdot\mathbf{r}$). In general, the rotated degenerate eigenmode is a new mode, having the same band index n, but different wave vector $\vec{R}\mathbf{k}$ (also within the first Brillouin zone). This symmetry relationship allows the reduction of the solution space to an irreducible Brillouin zone when solving for the photonic band structure (ω versus $\mathbf{k}$), since the Bloch wave vectors $\mathbf{k}$ and $\vec{R}\mathbf{k}$ are frequency (ω) degenerate. In Figure 10(a), we see the Brillouin zone of a hexagonal lattice, its irreducible Brillouin zone is the grey triangle. This irreducible Brillouin zone will cover the first entire

Brillouin zone when it is transformed by the symmetry operator of C_{6v} and the eigenmodes will change from $u_{\mathbf{k}n}(\mathbf{r})e^{i\mathbf{k}\cdot\mathbf{r}}$ to $u'_{\vec{R}\mathbf{k}n}(\mathbf{r})e^{i\vec{R}\mathbf{k}\cdot\mathbf{r}}$ with each transformation. Similarly in Figure 10(b), we see the Brillouin zone of a square lattice; its irreducible Brillouin zone is grey equilateral triangle.

The action of the periodic symmetry operator $T(\mathbf{R})$ upon a function $f(\mathbf{r})$ is $T(\mathbf{R})f(\mathbf{r})=f(\mathbf{r}+\mathbf{R})$, where the operator $T(\mathbf{R})$ is part of the periodic symmetry subgroup. If we apply $T(\mathbf{R})$ to the eigenmode Eq. (2.29), we find

$$T(\mathbf{R})\mathbf{E}_{\mathbf{k}n}(\mathbf{r})=T(\mathbf{R})u_{\mathbf{k}n}(\mathbf{r})e^{i\mathbf{k}\cdot(\mathbf{r})}=e^{i\mathbf{k}\cdot\mathbf{R}}u_{\mathbf{k}n}(\mathbf{r})e^{i\mathbf{k}\cdot\mathbf{r}}. \tag{3.34}$$

Equation (3.34) has the same form as Eq. (3.6), in which the irreducible matrix representation of $T(\mathbf{R})$ is $e^{i\mathbf{k}\cdot\mathbf{R}}$ (matrix with dimension of one) and the one-dimensional basis is the function $u_{\mathbf{k}n}(\mathbf{r})e^{i\mathbf{k}\cdot\mathbf{r}}$. Next if we apply the same periodic operator $T(\mathbf{R})$ to the degenerate eigenmode with Bloch wave vector $\vec{R}\mathbf{k}$ (Eq. (3.33)) we obtain

$$T(\mathbf{R})u_{\mathbf{k}n}\left(\vec{R}^{-1}\mathbf{r}\right)e^{i\vec{R}\mathbf{k}\cdot(\mathbf{r})}=u_{\mathbf{k}n}\left(\vec{R}^{-1}\mathbf{r}+\vec{R}^{-1}\mathbf{R}\right)e^{i\vec{R}\mathbf{k}\cdot(\mathbf{r}+\mathbf{R})}=e^{i\vec{R}\mathbf{k}\cdot\mathbf{R}}u_{\mathbf{k}n}\left(\vec{R}^{-1}\mathbf{r}\right)e^{i\vec{R}\mathbf{k}\cdot\mathbf{r}}. \tag{3.35}$$

In this case $u_{\mathbf{k}n}\left(\vec{R}^{-1}\mathbf{r}+\vec{R}^{-1}\mathbf{R}\right)=u_{\mathbf{k}n}\left(\vec{R}^{-1}\mathbf{r}\right)$ because $\vec{R}^{-1}\mathbf{R}$ is a lattice vector and Eq. (3.33) is also a Bloch mode, where $u_{\mathbf{k}n}\left(\vec{R}^{-1}\mathbf{r}\right)$ is periodic in the unit cell ([115], p. 279). In the new basis $u_{\mathbf{k}n}\left(\vec{R}^{-1}\mathbf{r}\right)e^{i\vec{R}\mathbf{k}\cdot\mathbf{r}}$, the irreducible matrix representation of $T(\mathbf{R})$ is $e^{i\vec{R}\mathbf{k}\cdot\mathbf{R}}$. Any wave vector that satisfies

$$R\mathbf{k}=\mathbf{k}'=\mathbf{k}+\mathbf{G} \tag{3.36}$$

(a)

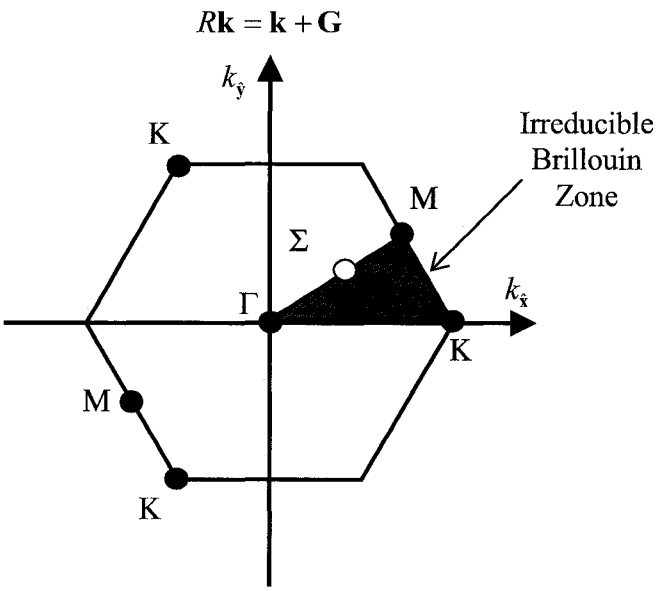

(b)

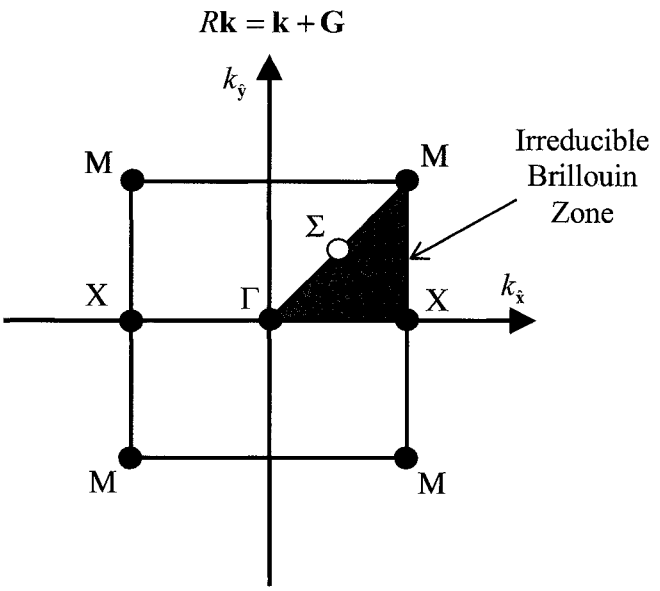

Figure 10. Reciprocal space description of the two-dimensional photonic crystal lattices, with the irreducible Brillouin zone and points of high symmetry labeled for the (a) hexagonal lattice, and (b) the square lattice.

is an equivalent wave vector due to Eq. (2.22). When Eq. (3.36) is satisfied, then $u_{\mathbf{k}n}(\mathbf{r})e^{i\mathbf{k}\cdot\mathbf{r}}$ and $u_{\mathbf{k}n}\left(\vec{R}^{-1}\mathbf{r}\right)e^{i\vec{R}\mathbf{k}\cdot\mathbf{r}}$ are associated with the same irreducible matrix representation of $T(\mathbf{R})$, because $e^{i\vec{R}\mathbf{k}\cdot\mathbf{R}} = e^{i(\mathbf{k}+\mathbf{G})\cdot\mathbf{R}} = e^{i\mathbf{k}\cdot\mathbf{R}}$. The irreducible matrix representation $e^{i\mathbf{k}\cdot\mathbf{R}}$ and the frequency identify the eigenmode (i.e., **k** and *n*). When **k** and *n* are the same, then $u_{\mathbf{k}n}(\mathbf{r})e^{i\mathbf{k}\cdot\mathbf{r}}$ and $u_{\mathbf{k}n}\left(\vec{R}^{-1}\mathbf{r}\right)e^{i\vec{R}\mathbf{k}\cdot\mathbf{r}}$ must be either an equivalent eigenmode of the Maxwell operator, or a linear combination of the degenerate eigenmodes also associated with the same irreducible representation. The set of point symmetry operators *R* that satisfy Eq. (3.36) is called the **k**-group of the eigenmodes ([5] pp. 46-47). The **k**-group is a subgroup of the point group associated with the Maxwell operator of the system (i.e., $\mathsf{L}_E^{(TM)}$), where the **k**-group determines the point group symmetry classification of the eigenmodes. It is the **k**-group that determines if the two eigenmodes are the same or degenerate due to symmetry. In Figure 10(a), several significant wave vectors and their equivalent points due to Eq. (3.36) are identified in the Brillouin zone of the hexagonal lattice. The point K, which has two other equivalent points, is associated with $C_{3v} = \{E, C_3, C_3^{-1}, \sigma_y, \sigma_y', \sigma_y''\}$. The point M has only one other equivalent point and is associated with $C_{2v} = \{E, C_2, \sigma_y'', \sigma_x''\}$. Finally, Σ has no other equivalent points and is associated with $C_{1h} = \{E, \sigma_x''\}$. Therefore, it is clear that the dielectric profile defines the maximum possible symmetry of the photonic crystal system, but it is the symmetry of the particular wave vector **k** that determines the symmetry classification of the individual eigenmodes (**k**-group).

So far, we have determined the irreducible matrix representations of the periodic symmetry group, but what about the irreducible matrix representations of the point group operators? When all the symmetry transformation operators of two subgroups commute with each other, then the operators of the two subgroups have simultaneous partner functions and their irreducible matrix representations can be considered independently.

To demonstrate that the periodic symmetry operators $T(\mathbf{R})$ and the point group transformation operators R commute, we apply R to both sides of Eq. (3.34):

$$RT(\mathbf{R})u_{\mathbf{k}n}(\mathbf{r})e^{i\mathbf{k}\cdot(\mathbf{r})} = Re^{i\mathbf{k}\cdot\mathbf{R}}u_{\mathbf{k}n}(\mathbf{r})e^{i\mathbf{k}\cdot\mathbf{r}} = e^{i\mathbf{k}\cdot\mathbf{R}}u_{\mathbf{k}n}\left(\vec{R}^{-1}\mathbf{r}\right)e^{i\vec{R}\mathbf{k}\cdot\mathbf{r}}. \tag{3.37}$$

If $R\mathbf{k} = \mathbf{k} + \mathbf{G}$, then the righthand sides of Eq. (3.35) and Eq. (3.37) are the same. This means that we can apply the operators $T(\mathbf{R})$ and R in any order ($T(\mathbf{R})R$ or $R\ T(\mathbf{R})$) and obtain the same result, which is the definition of commuting operators.

The irreducible matrix representations $\vec{D}^{(v)}(R)$ of the point group operators R are defined by

$$R\mathbf{E}^{(v)}_{\mathbf{k}ni}(\mathbf{r}) = \sum_j^l D^{(v)}_{ji}(R)\mathbf{E}^{(v)}_{\mathbf{k}nj}(\mathbf{r}), \tag{3.38}$$

where $D^{(v)}_{ji}(R)$ is a matrix component of $\vec{D}^{(v)}(R)$, v is the irreducible representation label, i is the degeneracy index, l is the total number of degenerate partner functions (which is determined by the dimension of the basis) ([115], pp. 34-37). This v is not the same v as in C_{nv}, context will make the distinction clear. Equation (3.38) is also consistent with Eq. (3.6), the basis functions being the photonic crystal eigenmodes $\mathbf{E}^{(v)}_{\mathbf{k}ni}(\mathbf{r})$ given by Eq. (2.29). Since there are an infinite number of frequency bands, but only a finite number of irreducible representations, many of the photonic crystal eigenmodes will be associated with the same irreducible representation. In the same way, there are many different irreducible matrix representations, as defined by Eq. (3.38), which are equivalent representations, as described in section 3.2.2. These equivalent representations have the same set of characters, defined by Eq. (3.11). Thus, the set of characters collectively identify all equivalent irreducible representations, i.e., it is the set of characters that is the meaningful label, but v is used for conciseness, since v maps uniquely to the character set. For each symmetry group, a character table can be defined

Table 1. C_{3v} character table

Γ	Conjugacy classes		
	E	$2C_3$	$3\sigma_v$
A_1	1	1	1
A_2	1	1	-1
E	2	-1	0

Table 2. C_{1h} character table

Γ	Conjugacy classes	
	E	σ_z
A	1	1
B	1	-1

that lists the characters for each irreducible representation. Table 1 is the character table of the C_{3v} point group. Three irreducible representations are listed: A_1 and A_2 (which are nondegenerate); and E (which is a doubly degenerate). Note that E as employed here is not the identity operator, context makes the choice clear. The degeneracy of an irreducible representation is equal to the character, $\chi_E^{(\nu)} = l$, of the identity operator, E, where E is always given in the first column of the character table. Note characters $\chi_R^{(\nu)}$ are always labeled as follows: the superscript identifies the representation label ν and the subscript the transformation operator R. Furthermore, the columns of the character table are organized under the set of operators which are conjugate with each other, where the number preceding the operator denotes the number of elements in the conjugacy class. The character tables of all two-dimensional point groups are well known and used to determine properties of eigenmodes associated with particular irreducible representations.

This becomes particularly transparent when dealing with nondegenerate eigenmodes because $\chi_R^{(\nu)} = \vec{D}^{(\nu)}(R)$ (i.e., the matrix is one-by-one) and hence we have all the symmetry transformation properties of a nondegenerate eigenmode. For degenerate eigenmodes, it is usually required that the eigenmodes be determined first, then $\vec{D}^{(\nu)}(R)$ be found using Eq. (3.38).

For photonic crystal slabs, there is another symmetry subgroup, in addition to the two-dimensional point group and the periodic symmetry subgroup (where the operators act with respect to the *x*-*y* plane). This is the group of symmetry transformations along the $\hat{\mathbf{z}}$ axis that leave the dielectric profile invariant. In Chapter 2, we considered a photonic crystal slab that possessed mirror symmetry about the *x*-*y* plane; this is associated with the C_{1h} point group. The C_{1h} point group has two irreducible representations that classify the photonic crystal slab eigenmodes as *A* (even) or *B* (odd) (see Table 2).

Once all the independent subgroups are examined, the irreducible labels from each are combined into an overall label for the photonic crystal eigenmode. The overall degeneracy of an irreducible representation is determined by

$$l_{(space)} = \left(l_{(periodic)}\right)\left(l_{(pointgroup)}\right)\ldots. \tag{3.39}$$

The irreducible representations of the periodic subgroup are $l_{(periodic)} = 1$, for all Bloch modes. Similarly, the irreducible representations associated with mirror symmetry about the *x*-*y* plane, C_{1h} group, are also one dimensional. Therefore, the overall degeneracy of the purely two-dimensional photonic crystal eigenmodes and photonic crystal slab eigenmodes will be entirely determined by the dimension of the irreducible representations of its **k**-group.

3.3.3 Irreducible representations of the related electric or magnetic fields

In the previous section we focused on the irreducible matrix representations, $\vec{D}^{(\nu)}(R)$, where the eigenmodes of Eqs. (3.30) and (3.31) were the partner functions. We now explicitly consider the irreducible matrix representations of the related electric or magnetic fields of the eigenmodes. As stated in Section 2.4, the eigenmodes of Eq. (3.30) (TM case) are the electric field functions, Eq. (2.29). The related magnetic field is determined using Eqs. (2.7), (2.10) and assuming harmonic time dependence $e^{-i\omega t}$:

$$\mathbf{H}_{\mathbf{k}n}(\mathbf{r}) = (-i/\mu_0\omega)\nabla\times\mathbf{E}_{\mathbf{k}n}(\mathbf{r}). \tag{3.40}$$

Similarly, the eigenmodes of Eq. (3.31) (TE case) are the magnetic field functions, Eq. (2.30), where the related electric field is determined using Eqs. (2.8)-(2.9) and, again assuming harmonic time dependence $e^{-i\omega t}$:

$$\mathbf{E}_{\mathbf{k}n}(\mathbf{r}) = \left(i/\omega\varepsilon_0\varepsilon(\mathbf{r})\right)\nabla\times\mathbf{H}_{\mathbf{k}n}(\mathbf{r}). \tag{3.41}$$

In both cases the related field is determined by taking the curl of the eigenmodes. If we now examine an arbitrary vector field $\mathbf{F}(\mathbf{r})$, we can consider the commutative properties of the curl operator, $\nabla\times$, and a **k**-group transformation operator, R. This commuting relationship is given by

$$R(\nabla\times)R^{-1}\mathbf{F}(\mathbf{r}) = \left(\det\vec{R}\right)\nabla\times\mathbf{F}(\mathbf{r}), \tag{3.42}$$

where $\det\vec{R}=1$ for proper transformations such as rotations, C_n, and $\det\vec{R}=-1$ for improper transformations such as mirror reflections, σ_v, (see [5], pp. 62-65). To obtain the irreducible matrix representation of the related field, we apply a **k**-group transformation operator R to Eq. (3.40):

$$R\mathbf{H}_{\mathbf{k}n}(\mathbf{r}) = (-i/\mu_0\omega) R(\nabla\times) R^{-1} R\mathbf{E}_{\mathbf{k}n}(\mathbf{r}), \tag{3.43}$$

where we have used $R^{-1}R = E$. Next we substitute Eq. (3.38) into Eq. (3.43) and using the results of Eq. (3.42) we obtain

$$\begin{aligned} R\mathbf{H}^{(w)}_{\mathbf{k}ni}(\mathbf{r}) &= \left(\det \ddot{R}\right)(-i/\mu_0\omega)\nabla\times\sum\nolimits_j^l D^{(v)}_{ji}(R)\mathbf{E}^{(v)}_{\mathbf{k}nj}(\mathbf{r}), \\ &= \left(\det \ddot{R}\right)\sum\nolimits_j^l D^{(v)}_{ji}(R)\mathbf{H}^{(w)}_{\mathbf{k}nj}(\mathbf{r}), \end{aligned} \tag{3.44}$$

where $(v),(w)$ are irreducible representation labels and i, j are degeneracy labels. Therefore, from Eq. (3.44), the irreducible matrix representation of the electric field is connected to the irreducible matrix representation of the related magnetic by

$$\ddot{D}^{(\mathbf{H}\to w)}(R) = \left(\det \ddot{R}\right)\ddot{D}^{(\mathbf{E}\to v)}(R). \tag{3.45}$$

In the same manner, we can determine that the irreducible matrix representations of the magnetic field and the related electric field. We apply a **k**-group transformation operator R to Eq. (3.41):

$$R\mathbf{E}_{\mathbf{k}n}(\mathbf{r}) = R\left(i/\omega\varepsilon_0\varepsilon(\mathbf{r})\right)R^{-1}R(\nabla\times)R^{-1}R\mathbf{H}_{\mathbf{k}n}(\mathbf{r}). \tag{3.46}$$

Next we substitute Eq. (3.38) (for the magnetic field) into Eq. (3.46) and using the results of Eq. (3.42) we obtain

$$\begin{aligned} R\mathbf{E}_{\mathbf{k}ni}(\mathbf{r}) &= \left(\det \ddot{R}\right)\left(i/\omega\varepsilon_0\varepsilon(\mathbf{r})\right)\nabla\times\sum\nolimits_j^l D^{(v)}_{ji}(R)\mathbf{H}^{(v)}_{\mathbf{k}nj}(\mathbf{r}), \\ &= \left(\det \ddot{R}\right)\sum\nolimits_j^l D^{(v)}_{ji}(R)\mathbf{E}^{(w)}_{\mathbf{k}nj}(\mathbf{r}). \end{aligned} \tag{3.47}$$

Finally from Eq. (3.47), the irreducible matrix representation of the electric field is connected to the irreducible matrix representation of the related magnetic by

$$\vec{D}^{(\mathbf{E}\to w)}(R)=\left(\det\vec{R}\right)\vec{D}^{(\mathbf{H}\to v)}(R). \tag{3.48}$$

Equations (3.45) and (3.48) confirm that the irreducible representation of the associated field may be obtain starting from the electric field or the magnetic field. As an example of the application of Eq. (3.45), we can assume the electric field photonic crystal eigenmode is the partner function of the nondegenerate A_2 irreducible matrix representation associated with the C_{3v} **k**-group. Since the representation is nondegenerate, $\vec{D}^{(\mathbf{E}\to A_2)}(R)=\chi_R^{(\mathbf{E}\to A_2)}$, and the character table provides the irreducible matrix representations (see Table 1). The first two conjugacy classes of the C_{3v} character table, E and C_3, are proper transformations, hence $\det\vec{R}=1$, and the irreducible representations remain the same, $\left(\det\vec{R}\right)\chi_{C_3}^{(\mathbf{E}\to A_2)}=(1)(1)=1=\chi_{C_3}^{(\mathbf{H}\to w)}$, for the magnetic field representation $\chi_{C_3}^{(\mathbf{H}\to w)}$. The last conjugacy class, σ_v, is an improper transformation, hence $\det\vec{R}=-1$, and the representation changes from $\chi_{\sigma_v}^{(\mathbf{E}\to A_2)}=-1$ to $\left(\det\vec{R}\right)\chi_{\sigma_v}^{(\mathbf{E}\to A_2)}=-1(-1)=1=\chi_{\sigma_v}^{(\mathbf{H}\to w)}$ for the magnetic field representation. The final result is that all of the irreducible matrix representations where the magnetic field is the partner function are $\chi_R^{(\mathbf{H}\to w)}=1$, $R\in C_{3v}$. Examining the C_{3v} character table, we see that $\chi_R^{(\mathbf{H}\to w)}=1$, $R\in C_{3v}$ must belong to the A_1 irreducible matrix representation. Therefore, the electric field is associated with the A_2 irreducible representation and the related magnetic field is associated with the A_1 irreducible representation, of the C_{3v} group. In general, although the electric field and the related magnetic field are associated with the same Bloch wave vector **k** and band index n, they are associated with different irreducible representations of the **k**-group.

3.3.4 The orthogonality of different irreducible representations

In Section 2.3.3, we reviewed the orthogonality of the electric and magnetic fields, showing that while, the magnetic fields form an orthogonal basis set the electric fields did not. Considering the irreducible representations, we can extend the orthogonality relationships of the electric and magnetic fields by noting that the partner functions of different irreducible representations are also orthogonal. For example, any two photonic crystal eigenmodes (electric or magnetic), the following relationship holds true

$$\int_V \left\{\mathbf{E}_{\mathbf{k}n}(\mathbf{r})\right\}^* \cdot \mathbf{E}_{\mathbf{k}'n}(\mathbf{r})\, d\mathbf{r} = 0 \tag{3.49}$$

when $\mathbf{k} \neq \mathbf{k}'$, where the integral is taken over the volume of the photonic crystal. For Eq. (3.49), the two eigenmodes belong to two different irreducible representations of the translational symmetry group, $e^{i\mathbf{k}\cdot\mathbf{r}}$ and $e^{i\mathbf{k}'\cdot\mathbf{r}}$; therefore they are orthogonal functions. This orthogonality relationship holds true for any of the symmetry groups associated with a photonic crystal. Furthermore, the orthogonality relationship, or vanishing inner product, holds true between any of the related fields of the photonic crystal eigenmode and any combination of them ([90], pp. 81-82). For example, the inner product of the electric field, from Section 3.3.3 (associated with the A_2 irreducible representation), with its related magnetic field (associated with the A_1 irreducible representation) would yield

$$\int_V \left\{\mathbf{E}_{\mathbf{k}n}^{(A_2)}(\mathbf{r})\right\}^* \cdot \mathbf{H}_{\mathbf{k}n}^{(A_1)}(\mathbf{r})\, d\mathbf{r} = 0, \tag{3.50}$$

because A_2 and A_1 are different irreducible representations of the C_{3v} **k**-group. The orthogonality of the partner functions associated with different irreducible representations is a very powerful tool that simplifies many of the analytical problems tackled in this thesis, such as determining analytical forms of the photonic crystal eigenmodes.

3.4 Photonic crystal eigenmodes in the vanishing dielectric contrast limit and decomposition of a reducible representation

3.4.1 Introduction

In Chapter 2, we showed that the Fourier expansions of the photonic crystal eigenmodes in the vanishing dielectric contrast limit are well approximated by a small number of degenerate basis modes. In each case, the basis modes of the Fourier expansions were solutions of less complex systems, such as plane waves for two-dimensional photonic crystals, and eigenmodes of a dielectric slab for photonic crystal slabs. In this section, we discuss further the photonic crystal eigenmodes in the vanishing dielectric contrast limit, but from a group theoretic perspective. Using the methods of group theory, we will determine the irreducible representation associated with a particular vanishing dielectric contrast eigenmode, i.e., we can determine which vanishing dielectric contrast eigenmodes may be a partner function to a given irreducible representation. The assignment of an irreducible representation to a particular vanishing dielectric contrast eigenmode also indicates the irreducible representations permitted in high dielectric contrast system, because the assignment is rigorously based on symmetry ([5], pp. 54). Furthermore, using projection operators, we will determine the exact form of the photonic crystal eigenmode in the vanishing dielectric contrast limit associated with a particular irreducible representation.

These group theoretic methods are based on decomposition of a reducible representation into its irreducible parts (see Section 3.2.2). In Section 3.4.2, we will show that the basis modes of the Fourier expansions are the partner functions of a reducible representation. Using the partner functions, the reducible matrix representations will be derived. In Section 3.4.3, we will perform a decomposition of the reducible matrix representation by comparing the character tables of the reducible and irreducible representations. This will determine the possible irreducible representations at a particular location in reciprocal space. Finally in Section 3.4.4, the projection operators of the irreducible representations will be applied to the Fourier expansions, i.e., the linear combinations of basis modes.

The result will be the partner functions for a given irreducible representation, where the partner functions are equal to the photonic crystal eigenmodes (as established in Section 3.3.2).

Our analytic approach is indebted to earlier contributions [115] and [116], in which the following group theoretic methods were adapted from their rigorous applications to quantum mechanical systems. Previous photonic crystal research that inspired this methodology is the following: ([5], pp. 5-11), ([5], pp. 50-54), and ([5], pp. 179-181), who were the first to use analytic techniques to assign irreducible representations to most common photonic band structures; and ([90] pp. 79-81), who treated Bloch modes as symmetry-related polarized plane waves. The group theoretic methods are derived using the photonic crystals slab as the example system, since this demonstrates the method applied to a full vector eigenmode.

3.4.2 Reducible representations

In Section 3.2.2, we classified group representations as irreducible or reducible, in which an irreducible representation is defined as a representation that cannot be expressed in a representation of lower dimensionality m. The partner functions of the irreducible representations were shown to be the photonic crystal eigenmodes, and the irreducible matrix representations were defined (see Section 3.3.2). However, any representation of a group can be constructed from partner functions of simpler systems, because any complete basis can be used to construct another. In this case, the best choice is to select the simplest meaningful partner functions that require the least number of terms. In the vanishing dielectric contrast limit, the degenerate basis modes of the Fourier expansions are the plane waves Eq. (2.35) for the two-dimensional photonic crystal and the dielectric slab eigenmodes Eq. (2.42) for the photonic crystal slab. These degenerate basis modes are the ideal partner functions to construct a reducible representation ([5], pp. 50-54) and ([5], pp. 179-181).

Similar to the irreducible matrix representation of the point group, we can define the reducible matrix representation, $\ddot{D}^{(red)}(R)$, in the basis of the degenerate partner functions $\mathbf{T}_1^{(red)}(\mathbf{r})\ldots\mathbf{T}_l^{(red)}(\mathbf{r})$:

$$R\mathbf{T}_i^{(red)}(\mathbf{r}) = \sum_j^l D_{ji}^{(red)}(R)\mathbf{T}_j^{(red)}(\mathbf{r}), \tag{3.51}$$

where $D_{ij}^{(red)}(R)$ is an element of the matrix $\ddot{D}^{(red)}(R)$, i denotes the degeneracy, l is the number of partner functions. As an example, we examine the photonic crystal slab eigenmodes associated with the C_{3v} point group, i.e., for $\mathbf{k} = \hat{\mathbf{x}}4\pi/(3a)$, applicable to the frequency bands $n = 1,2,3$. The partner functions of the reducible representation of the C_{3v} group are the elements of the sum shown in Eq. (2.51):

$$\begin{aligned}
\mathbf{T}_1^{(red)}(\mathbf{r}) &= \begin{pmatrix} 0 \\ 1 \\ 0 \end{pmatrix} e^{i4\pi x/3a}\cos(k_z z), \\
\mathbf{T}_2^{(red)}(\mathbf{r}) &= \begin{pmatrix} \sqrt{3} \\ 1 \\ 0 \end{pmatrix} e^{-i2\pi\left(x/3a - y/(\sqrt{3}a)\right)}\cos(k_z z), \\
\mathbf{T}_3^{(red)}(\mathbf{r}) &= \begin{pmatrix} \sqrt{3} \\ -1 \\ 0 \end{pmatrix} e^{-i2\pi\left(x/3a + y/(\sqrt{3}a)\right)}\cos(k_z z).
\end{aligned} \tag{3.52}$$

Note that the reducible partner functions Eq. (3.52) are only valid for the first three frequency bands $n = 1,2,3$, with the Bloch wave vector $\mathbf{k} = \hat{\mathbf{x}}4\pi/(3a)$. For bands $n = 4,5,6$, or any other point in reciprocal space, another set of partner functions would be required. In each case, the appropriate partner functions are determined by the dominant Fourier basis modes, as outlined in Appendix B.

Table 3. Transformation Properties of $R\mathbf{T}_m^{(red)}(\mathbf{r})$

	E	C_3	C_3^{-1}	σ_y	σ_y'	σ_y''
$\mathbf{T}_1^{(red)}$	$\mathbf{T}_1^{(red)}$	$\frac{1}{2}\mathbf{T}_3^{(red)}$	$-\frac{1}{2}\mathbf{T}_2^{(red)}$	$-\mathbf{T}_1^{(red)}$	$\frac{1}{2}\mathbf{T}_2^{(red)}$	$-\frac{1}{2}\mathbf{T}_3^{(red)}$
$\mathbf{T}_2^{(red)}$	$\mathbf{T}_2^{(red)}$	$-2\mathbf{T}_1^{(red)}$	$-\mathbf{T}_3^{(red)}$	$\mathbf{T}_3^{(red)}$	$2\mathbf{T}_1^{(red)}$	$-\mathbf{T}_2^{(red)}$
$\mathbf{T}_3^{(red)}$	$\mathbf{T}_3^{(red)}$	$-\mathbf{T}_2^{(red)}$	$2\mathbf{T}_1^{(red)}$	$\mathbf{T}_2^{(red)}$	$-\mathbf{T}_3^{(red)}$	$-2\mathbf{T}_1^{(red)}$

At higher frequency bands, such as beyond the single mode cutoff frequency, the determination of the partner functions will be more complex, because of contributions from both TE and TM modes, but the methodology is the same.

Since there are three degenerate partner functions, the reducible matrix representation of C_{3v} will be a set of three by three matrices $\Gamma^{(red)}$. We note that the three irreducible representations (A_1, A_2 and E) of the C_{3v} point group have dimensions of two or less, so $\Gamma^{(red)}$, with a dimension of three must, be reducible. To determine the matrix representation $\tilde{D}^{(red)}(R)$ in the basis of Eq. (3.52) there are two steps. First, we apply each symmetry operator R of the point group C_{3v} to each partner function of Eq. (3.52); the results are tabulated in Table 3. The first column lists the function $\mathbf{T}_m^{(red)}(\mathbf{r})$ to which the symmetry operator R is applied. The subsequent column lists the results of the application of the particular operator $R\mathbf{T}_m^{(red)}(\mathbf{r})$, where the operator R is listed at the top of the column. Second, the results of Table 3 are compared to Eq. (3.51) the definition of $\tilde{D}^{(red)}(R)$. As an example, we calculate $\tilde{D}^{(red)}(C_3)$. To determine the first row of the matrix $\tilde{D}^{(red)}(C_3)$, we substitute $R = C_3$ and $i = 1$ into Eq. (3.51), and expand the summation:

$$C_3\mathbf{T}_1^{(red)}(\mathbf{r}) = D_{11}^{(red)}(C_3)\mathbf{T}_1^{(red)}(\mathbf{r}) + D_{21}^{(red)}(C_3)\mathbf{T}_2^{(red)}(\mathbf{r}) + D_{31}^{(red)}(C_3)\mathbf{T}_3^{(red)}(\mathbf{r}). \quad (3.53)$$

The left-hand side of Eq. (3.53) must be equal to $C_3\mathbf{T}_1^{(red)}(\mathbf{r}) = \frac{1}{2}\mathbf{T}_3^{(red)}$ according to Table 3. Comparing the left-hand side to the right-hand of Eq. (3.53), we determine that $D_{31}^{(red)}(C_3) = \frac{1}{2}$ and all other elements are $D_{11}^{(red)}(C_3) = D_{21}^{(red)}(C_3) = 0$. To ascertain the second and third rows of the matrix $\ddot{D}^{(red)}(C_3)$, again we substitute into Eq. (3.51) $R = C_3$, but now $i = 2$

$$C_3\mathbf{T}_2^{(red)}(\mathbf{r}) = D_{12}^{(red)}(C_3)\mathbf{T}_1^{(red)}(\mathbf{r}) + D_{22}^{(red)}(C_3)\mathbf{T}_2^{(red)}(\mathbf{r}) + D_{32}^{(red)}(C_3)\mathbf{T}_3^{(red)}(\mathbf{r}), \quad (3.54)$$

and $i = 3$

$$C_3\mathbf{T}_3^{(red)}(\mathbf{r}) = D_{13}^{(red)}(C_3)\mathbf{T}_1^{(red)}(\mathbf{r}) + D_{23}^{(red)}(C_3)\mathbf{T}_2^{(red)}(\mathbf{r}) + D_{33}^{(red)}(C_3)\mathbf{T}_3^{(red)}(\mathbf{r}). \quad (3.55)$$

The left-hand side of Eq. (3.54) must be equal to $C_3\mathbf{T}_2^{(red)}(\mathbf{r}) = -2\mathbf{T}_1^{(red)}$ (see Table 3). Comparing the left-hand and the right-hand side of Eq. (3.54), we determine that $D_{12}^{(red)}(C_3) = -2$ and all other elements are $D_{22}^{(red)}(C_3) = D_{32}^{(red)}(C_3) = 0$. The left-hand side of Eq. (3.55) must be equal to $C_3\mathbf{T}_3^{(red)}(\mathbf{r}) = -\mathbf{T}_2^{(red)}$ (see Table 3). Comparing the left-hand side and the right-hand side of Eq. (3.55), we determine that $D_{23}^{(red)}(C_3) = -1$ and all other elements are $D_{13}^{(red)}(C_3) = D_{33}^{(red)}(C_3) = 0$. The final reducible matrix representation is

$$\ddot{D}^{(red)}(C_3) = \begin{pmatrix} 0 & -2 & 0 \\ 0 & 0 & -1 \\ 1/2 & 0 & 0 \end{pmatrix}. \quad (3.56)$$

Table 4. C_{3v} reducible representation character table

Γ	Conjugacy classes		
	E	$2C_3$	$3\sigma_v$
$\chi_R^{(red)}$	3	0	-1

Once all of the matrix elements $\vec{D}^{(red)}(R)$ are determined, we have completely defined the reducible representation $\Gamma^{(red)}$ of C_{3v}, in the basis of degenerate dielectric slab modes $\mathbf{T}_1^{(red)}(\mathbf{r})\ldots\mathbf{T}_l^{(red)}(\mathbf{r})$. In the next section, we will decompose the reducible representation $\Gamma^{(red)}$ into its irreducible parts $\Gamma^{(v)}$. This will be accomplished by comparing the character table of the reducible representation to the character table of the irreducible representations. In preparation, we calculate the C_{3v} reducible representation character table using Eq. (3.11), where the character of the example $\vec{D}^{(red)}(C_3)$ is given by

$$\chi_{C_3}^{(red)} = Tr\left\{\vec{D}^{(red)}(C_3)\right\} = 0+0+0 = 0, \tag{3.57}$$

and the characters, $\chi_R^{(red)}$, of the other matrices, $\vec{D}^{(red)}(R)$, $R \in C_{3v}$, are summarized in Table 4.

3.4.3 Decomposition of a reducible representation into its irreducible parts

By definition, any reducible matrix representation can be decomposed into a set of irreducible representations given by Eq. (3.9), restated for the reader:

$$\Gamma^{(red)} = \sum a_v \Gamma^{(v)}, \tag{3.58}$$

where v is the index identifying the irreducible representations. The coefficients a_v can be determined by the following relationship between the set of characters of the reducible representation $\chi^{(red)}(R)$ and a given irreducible representation $\chi^{(v)}(R)$:

$$a_v = 1/h \sum_R \chi_R^{(red)} \chi_R^{(v)}, \tag{3.59}$$

where h is the number of elements in the group and the summation is over all elements $R \in C_{nv}$ ([116] p. 158). The rows of the irreducible character table (the set $\chi_R^{(v)}$, $R \in C_{nv}$) form an orthogonal vector system ([115], p. 30). Therefore, Eq. (3.59) is an inner product between two vectors representing the reducible representation and the irreducible representation.

Returning to the example of the photonic crystal slab eigenmodes with the Bloch wave vector $\mathbf{k} = \hat{\mathbf{x}} 4\pi/(3a)$, we apply Eq. (3.59) for each of the irreducible representations A_1, A_2 and E of the C_{3v} symmetry group to the set of character of the reducible representation (see Table 4) and we find:

$$\begin{aligned} a_{(A_1)} &= 1/6 \sum_R \chi_R^{(red)} \chi_R^{(A_1)} = 1/6[3+0-3] = 0, \\ a_{(A_2)} &= 1/6 \sum_R \chi_R^{(red)} \chi_R^{(A_2)} = 1/6[3+0+3] = 1, \\ a_{(E)} &= 1/6 \sum_R \chi_R^{(red)} \chi_R^{(E)} = 1/6[6+0+0] = 1. \end{aligned} \tag{3.60}$$

Substituting the results of Eq. (3.60) into Eq. (3.58) indicates the reducible representation, $\Gamma^{(red)}$, is decomposed into

$$\Gamma^{(red)} = \Gamma^{(A_2)} + \Gamma^{(E)}. \tag{3.61}$$

This means that A_2 and E are the only possible irreducible representations, when $\mathbf{T}_m^{(red)}$ ($m=1,2,3$) are the partner functions of the reducible matrix representation. Since the partner functions of the irreducible representations are the photonic crystal eigenmodes and they are constructed using the basis modes $\mathbf{T}_m^{(red)}$ ($m=1,2,3$), it is only possible for the photonic crystal eigenmodes to be associated with either the A_2 irreducible representation or the doubly degenerate E irreducible representation. Even when the dielectric contrast is increased beyond the vanishing dielectric contrast limit, the irreducible assignments remains the same, because every eigenmode, regardless of the dielectric contrast, is a sum of basis modes with the same symmetry ([5], pp. 54). The knowledge of the allowed irreducible representations is very useful, because it indicates the symmetry properties of the eigenmodes and their allowed degeneracy at that point in reciprocal space. To determine the allowed irreducible representations at other points in reciprocal space, such as for the Bloch wave vector $\mathbf{k}=\hat{\mathbf{x}}4\pi/(3a)$ for frequency bands $n=4,5,6$, a new set of reducible representation partner functions must be determined. The reduction procedure is then repeated with the new set of partner functions, in which another set of possible irreducible representations will be determined. As an example, the irreducible labels have been assigned to all the even TE photonic crystal slab modes of the vanishing-dielectric-contrast, photonic band structure calculated in Section 2.5.3 (see Figure 7). In a photonic band structure determined in vanishing dielectric contrast limit, many of the eigenmodes are degenerate, such as at the K and M points and the second and third bands from $\Gamma \rightarrow \mathrm{K}$ within Figure 7. The irreducible labels allow us to determine the true degeneracy of each eigenmode as required by symmetry. Consequently, as the dielectric contrast is increased, we can predict how the photonic band structure will evolve, such as where photonic band gaps will appear. For example, at the K point, the irreducible labels are the nondegenerate A_2 and the doubly degenerate E. Increasing the dielectric contrast will cause a photonic band gap to open between the nondegenerate A_2 eigenmode, and the two doubly degenerate E eigenmodes. The irreducible labels of the second and third bands from $\Gamma \rightarrow \mathrm{K}$ are A and B, which are

both nondegenerate. As a result, bands 2 and 3 will split (i.e., become nondegenerate) as the dielectric contrast is increased. We can verify the symmetry predictions by examining the photonic band structure of a high dielectric contrast hexagonal photonic crystal slab, determined using the Finite element method (see Figure 16(c)). Figure 16(c) reveals the second and third bands are no longer degenerate and a photonic band gap appears where expected. Note that this symmetry assignment only applies to the electric field. The irreducible representations associated with magnetic field modes are part of the same point group, but their assignment differs as those associated with the electric field modes (see Section 3.3.3). Although, the choice of examining the electric or magnetic field of a given photonic crystal eigenmode does not change its symmetry degeneracy.

3.4.4 Projection operators and symmetry-adapted sums of basis modes

In Section 3.4.1, we determined that A_2 and E were the only allowed irreducible representations, when $\mathbf{T}_m^{(red)}$ are the partner functions of the reducible representation. Now, we use projection operators to determine the actual analytic forms of the partner functions of the irreducible representations A_2 and E. We will show using group theory that the partner functions of the irreducible representations are linear combinations of the basis modes $\mathbf{T}_m^{(red)}$. This will allow us to generate the analytic forms of the photonic crystal eigenmodes, because they are the partner functions of the irreducible representations.

We have illustrated, using Eq. (2.51), that the partner functions $\mathbf{E}_{\mathbf{k}ni}^{(\nu)}(\mathbf{r})$ of the irreducible representation can be expanded as a linear combination of the partner functions of a reducible representation $\mathbf{T}_m^{(red)}$. The reverse of this is also true; that is, the partner functions of the reducible representation $\mathbf{T}_m^{(red)}$ can be expanded as a linear combination of the partner functions of the irreducible representations $\mathbf{E}_{\mathbf{k}ni}^{(\nu)}(\mathbf{r})$ given by

$$\mathbf{T}_m^{(red)} = \sum_n \sum_v \sum_i b_{vni}^m \mathbf{E}_{\mathbf{k}ni}^{(v)}(\mathbf{r}), \tag{3.62}$$

where v denotes the irreducible representation, i is the degeneracy index ([116] pp. 125-128). The relevant band index n for Eq. (3.62) is determined by the eigenmodes, $\mathbf{E}_{\mathbf{k}ni}^{(v)}(\mathbf{r})$, that have the basis modes $\mathbf{T}_m^{(red)}$. In the example photonic crystal slab system, with Bloch wave vector $\mathbf{k} = \hat{\mathbf{x}} 4\pi/(3a)$ the band index is limited to $n = 1,2,3$. In order to extract the partner functions of the irreducible representation $\mathbf{E}_{\mathbf{k}ni}^{(v)}(\mathbf{r})$ from $\mathbf{T}_n^{(red)}$, we use a projection operator for a particular irreducible representation p defined as

$$P^{(p)} = \frac{l_p}{h} \sum_R \chi_R^{(p)} R, \tag{3.63}$$

where $R \in C_{nv}$, l_p is the dimension of the irreducible representation, and h is the number of elements in the group C_{nv}. The projection operator $P^{(p)}$ eliminates any part of Eq. (3.62) in which $v \neq p$ (i.e., does not belong to the irreducible representation p) ([116] p.138). For example, the application of the projection operator, Eq. (3.63), to Eq. (3.62) produces

$$P^{(p)}\mathbf{T}_m^{(red)} = P^{(p)}\left[\sum_n \sum_v \sum_i b_{vni}^m \mathbf{E}_{\mathbf{k}ni}^{(v)}(\mathbf{r})\right] = \sum_n \sum_i b_{pni}^m \mathbf{E}_{\mathbf{k}ni}^{(p)}(\mathbf{r}), \tag{3.64}$$

where the result is just the elements of Eq. (3.62) associated with the irreducible representation p. However, Eq. (3.64) reveals that if there are multiple bands n associated with the same irreducible representation p that are not degenerate (i.e., associated with the index i) these eigenmodes will not be separated, but appear as a linear combinations. This is a limitation of the projection operator method. The example photonic crystal slab system will not be affected by this limitation. Although, if we

choose to study a photonic crystal slab mode above the single mode cutoff frequency, there are possiblily multiple TE and TM dielectric slab modes with the same symmetry that will mix to form the photonic crystal slab mode, the index i in Eq. (3.64) indicates the summation over these multiple modes. Each $\mathbf{E}_{\mathbf{k}ni}^{(v)}(\mathbf{r})$ is associated with a unique irreducible representation or it is degenerate with another $\mathbf{E}_{\mathbf{k}ni}^{(v)}(\mathbf{r})$ with the same irreducible label. This is established based on the results of Section 3.4.1, where we determined that each of the allowed irreducible representations A_2 and E only appear once in the reducible representation (see Eq. (3.60)).

Returning to our example photonic crystal slab system, we now determine the partner functions of the nondegenerate A_2 irreducible representation and the double degenerate E irreducible representation using the projection operator Eq. (3.63). For A_2, the projection operator is

$$P^{(A_2)} = \frac{l_{A_2}}{h}\sum_R \chi_R^{(A_2)} R = \frac{1}{6}\left(E + C_3 + C_3^{-1} - \sigma_y - \sigma_y' - \sigma_y''\right) \tag{3.65}$$

where the characters $\chi^{(A_2)}(R)$ of the C_{3v} symmetry group are obtain from Table 1. Next we apply the projection operator Eq. (3.65) to $\mathbf{T}_1^{(red)}$:

$$P^{(A_2)}\mathbf{T}_1^{(red)} = \frac{1}{6}\left(E\mathbf{T}_1^{(red)} + C_3\mathbf{T}_1^{(red)} + C_3^{-1}\mathbf{T}_1^{(red)} - \sigma_y\mathbf{T}_1^{(red)} - \sigma_y'\mathbf{T}_1^{(red)} - \sigma_y''\mathbf{T}_1^{(red)}\right). \tag{3.66}$$

In Section 3.4.2, we determined $R\mathbf{T}_n^{(red)}(\mathbf{r})$ for each of the C_{3v} transformation operators (see Table 3). These results can be substituted into Eq. (3.66) and we obtain

$$P^{(A_2)}\mathbf{T}_1^{(red)} = \frac{1}{6}\left(\mathbf{T}_1^{(red)} + \tfrac{1}{2}\mathbf{T}_3^{(red)} - \tfrac{1}{2}\mathbf{T}_2^{(red)} + \mathbf{T}_1^{(red)} - \tfrac{1}{2}\mathbf{T}_2^{(red)} + \tfrac{1}{2}\mathbf{T}_3^{(red)}\right)$$
$$P^{(A_2)}\mathbf{T}_1^{(red)} = \frac{1}{6}\left(2\mathbf{T}_1^{(red)} - \mathbf{T}_2^{(red)} + \mathbf{T}_3^{(red)}\right). \tag{3.67}$$

This same process can be repeated for $\mathbf{T}_2^{(red)}$ and $\mathbf{T}_3^{(red)}$, and we obtain

$$P^{(A_2)}\mathbf{T}_2^{(red)} = \frac{1}{6}\left(-4\mathbf{T}_1^{(red)} + 2\mathbf{T}_2^{(red)} - 2\mathbf{T}_3^{(red)}\right), \tag{3.68}$$

$$P^{(A_2)}\mathbf{T}_3^{(red)} = \frac{1}{6}\left(4\mathbf{T}_1^{(red)} - 2\mathbf{T}_2^{(red)} + 2\mathbf{T}_3^{(red)}\right). \tag{3.69}$$

The results of Eqs. (3.67) -(3.69) are three sets of linear combinations of $\mathbf{T}_n^{(red)}$, which are linearly dependent. In general, we obtain l_{red} linear combinations of $\mathbf{T}_n^{(red)}$ from which we find l_v (degeneracy of the irreducible representation) that are linearly independent, orthonormal, and are the partner functions of the irreducible representations v. The A_2 representation is nondegenerate $l_{A_2} = 1$. Hence, we simply choose one linear combination, because the others are linearly dependent. Selecting Eq. (3.67) and substituting the reducible partner functions $\mathbf{T}_n^{(red)}$ from Eq. (3.52) into Eq. (3.67) we obtain the partner function of the A_2 irreducible representation:

$$\mathbf{E}_{\mathbf{k}}^{(A_2)}(\mathbf{r}) = \frac{1}{12}\left(\begin{pmatrix}0\\2\\0\end{pmatrix}e^{i4\pi x/3a} + \begin{pmatrix}-\sqrt{3}\\-1\\0\end{pmatrix}e^{-i2\pi\left(x/3a - y/\left(\sqrt{3}a\right)\right)} + \begin{pmatrix}\sqrt{3}\\-1\\0\end{pmatrix}e^{-i2\pi\left(x/3a + y/\left(\sqrt{3}a\right)\right)}\right)\cos\left(k_z z\right), \tag{3.70}$$

where Eq. (3.70) has been normalized to unity (using $\sqrt{\mathbf{E}_{\mathbf{k}}^{(A_2)}(\mathbf{r})\bullet\left(\mathbf{E}_{\mathbf{k}}^{(A_2)}(\mathbf{r})\right)^*} = 1$ and we have suppressed the band index n.

As a second example, we derive the partner functions of the double degenerate E irreducible representation. Again, we apply the projection operator $P^{(E)}$ to $\mathbf{T}_1^{(red)}$

$$P^{(E)}\mathbf{T}_1^{(red)} = \frac{2}{6}\left(2E - C_3 - C_3^{-1}\right)\mathbf{T}_1^{(red)}. \tag{3.71}$$

Substituting the results of Table 3 into Eq. (3.71), we obtain

$$P^{(E)}\mathbf{T}_1^{(red)} = \frac{1}{6}\left(4\mathbf{T}_1^{(red)} + \mathbf{T}_2^{(red)} - \mathbf{T}_3^{(red)}\right). \tag{3.72}$$

This same process can be repeated for $\mathbf{T}_2^{(red)}$ and $\mathbf{T}_3^{(red)}$, and we obtain

$$P^{(E)}\mathbf{T}_2^{(red)} = \frac{2}{6}\left(2\mathbf{T}_1^{(red)} + 2\mathbf{T}_2^{(red)} + \mathbf{T}_3^{(red)}\right) \tag{3.73}$$

$$P^{(E)}\mathbf{T}_3^{(red)} = \frac{2}{6}\left(-2\mathbf{T}_1^{(red)} + \mathbf{T}_2^{(red)} + 2\mathbf{T}_3^{(red)}\right). \tag{3.74}$$

The results are three equations Eqs. (3.72)-(3.74) that are linear combinations of $\mathbf{T}_n^{(red)}$. In contrast to the A_2 case, each equation is not linear dependent, and we require $l_E = 2$ partner functions of the E irreducible representation. To find the two partner function $\mathbf{E}_{\mathbf{k}1}^{(E)}(\mathbf{r})$ and $\mathbf{E}_{\mathbf{k}2}^{(E)}(\mathbf{r})$ (again suppressing the band index n, where 1 and 2 denote degeneracy) we use the orthogonality of the partner functions of from different irreducible representations (see Section 3.3.4). We assume the first partner function is given by Eq. (3.72),

$$\mathbf{E}_{\mathbf{k}1}^{(E)}(\mathbf{r}) = P^{(E)}\mathbf{T}_1^{(red)} = \frac{1}{6}\left(4\mathbf{T}_1^{(red)} + \mathbf{T}_2^{(red)} - \mathbf{T}_3^{(red)}\right). \tag{3.75}$$

This selection can be verified by checking it is orthogonal to the A_2 irreducible representation $\mathbf{E}_{\mathbf{k}}^{(A_2)}(\mathbf{r})$:

$$\int_V \left\{\mathbf{E}_{\mathbf{k}}^{(A_2)}(\mathbf{r})\right\}^* \cdot \mathbf{E}_{\mathbf{k}1}^{(E)}(\mathbf{r})\, d\mathbf{r} = 0, \tag{3.76}$$

substituting Eq. (3.72) and Eq. (3.67) into Eq. (3.76) we find

$$\int_V \frac{1}{6}\left(2\mathbf{T}_1^{(red)} - \mathbf{T}_2^{(red)} + \mathbf{T}_3^{(red)}\right)^* \cdot \frac{1}{6}\left(4\mathbf{T}_1^{(red)} + \mathbf{T}_2^{(red)} - \mathbf{T}_3^{(red)}\right) d\mathbf{r} = 0, \tag{3.77}$$

(see Appendix C for the full calculation). We can determine that

$$\mathbf{E}_{\mathbf{k}2}^{(E)}(\mathbf{r}) = P^{(E)}\mathbf{T}_2^{(red)} + P^{(E)}\mathbf{T}_3^{(red)} = \mathbf{T}_2^{(red)} + \mathbf{T}_3^{(red)} \tag{3.78}$$

is also orthogonal to $\mathbf{E}_{\mathbf{k}}^{(A_2)}(\mathbf{r})$

$$\int_V \left\{\mathbf{E}_{\mathbf{k}}^{(A_2)}(\mathbf{r})\right\}^* \cdot \mathbf{E}_{\mathbf{k}2}^{(E)}(\mathbf{r})\, d\mathbf{r} = 0, \tag{3.79}$$

(see Appendix C). Therefore Eq. (3.78) is also a possible partner function of E irreducible representation. To confirm that Eq. (3.75) and Eq. (3.78) are indeed the partner functions of E irreducible representation, we can determine the irreducible matrix representation, $\ddot{D}^{(E)}(R)$, using Eq. (3.75) and Eq. (3.78). From the irreducible matrix representations, $\ddot{D}^{(E)}(R)$, we can determine their characters $\chi_R^{(E)}$ and compare it to the expected results in the C_{3v} character table. In Appendix C, we derive an irreducible matrix representation from each of the conjugacy class: $\ddot{D}^{(E)}(E)$, $\ddot{D}^{(E)}(C_3)$, and $\ddot{D}^{(E)}(\sigma_y)$. Using Eq. (3.11), we find their characters

$$\chi_E^{(E)} = Tr\left\{\ddot{D}^{(E)}(E)\right\} = 1+1 = 2. \tag{3.80}$$

$$\chi_{C_3}^{(E)} = Tr\left\{\ddot{D}^{(E)}(C_3)\right\} = -1/2-1/2 = -1. \tag{3.81}$$

$$\chi_{\sigma_y}^{(E)} = Tr\left\{\ddot{D}^{(E)}(\sigma_y)\right\} = -1+1 = 0. \tag{3.82}$$

Checking the the C_{3v} character table (see Table 1), we discover that Eqs. (3.80)-(3.82) match the expected results, thus confirming Eq. (3.75) and Eq. (3.78) are the partner functions of E irreducible representation.

To obtain the final partner functions of the doubly degenerate E irreducible representation, we substitute the reducible partner function $\mathbf{T}_n^{(red)}$ from Eq. (3.52) into Eq. (3.75) and Eq. (3.78):

$$\mathbf{E}_{\mathbf{k}1}^{(E)}(\mathbf{r}) = \frac{1}{24}\left(\begin{pmatrix}0\\4\\0\end{pmatrix}e^{i4\pi x/3a} + \begin{pmatrix}\sqrt{3}\\1\\0\end{pmatrix}e^{-i2\pi\left(x/3a-y/(\sqrt{3}a)\right)} + \begin{pmatrix}-\sqrt{3}\\1\\0\end{pmatrix}e^{-i2\pi\left(x/3a+y/(\sqrt{3}a)\right)}\right)\cos(k_z z), \tag{3.83}$$

$$\mathbf{E}_{\mathbf{k}2}^{(E)}(\mathbf{r}) = \frac{\sqrt{3}}{24}\left(\begin{pmatrix}\sqrt{3}\\1\\0\end{pmatrix}e^{-i2\pi\left(x/3a-y/(\sqrt{3}a)\right)} + \begin{pmatrix}\sqrt{3}\\-1\\0\end{pmatrix}e^{-i2\pi\left(x/3a+y/(\sqrt{3}a)\right)}\right)\cos(k_z z), \tag{3.84}$$

where Eq. (3.83)-(3.84) have been normalized to unity and we have suppressed the band index n.

3.5 Site symmetry and point subgroups of the photonic crystal

3.5.1 Introduction

In Section 3.3, we examined the periodic symmetry subgroup and the photonic crystal point group. The transformation operators of the photonic crystal point group acted with respect to the principal axis of the photonic crystal. Here, we examine the irreducible representations of transformation operators that may act with respect to any axis in a photonic crystal, not just about the principal axis. These groups of transformation operators are known as site (local) symmetry groups. To explore the site symmetry, we must define new transformation operators that act with respect to an axis located a distance **d** away from the principal axis ([113], pp. 36-39). In three-dimensional space, the set of all possible transformation operators is called the Euclidean group E_3. The elements g of E_3 are the set of operators that leave the distance between any two points in space unchanged. Each element g can be mapped to a transformation operator in the Cartesian coordinate system (as defined in Section 3.3.1) that forms a group isomorphic to the group of Euclidean operations, which is also known as the Euclidean group E_3 ([113], p. 32). In Section 3.5.2, we review the properties of the Euclidean group, E_3 and how these transformation operators act upon spatially dependent functions. When we discuss the set of transformation operators from the Euclidean group that leave the dielectric profile of a photonic crystal invariant, this set of operators is known as the photonic crystal space group G and is discussed in Section 3.5.3. In Section 3.5.4, we examine the transformation properties of the Bloch modes when acted upon by the operators of the photonic crystal space group G and the associated irreducible representations.

3.5.2 Transformation operators of the site symmetry groups

The operators of E_3 in the Cartesian coordinate system take the form of the combined transformation operators,

$$\hat{g} = \left(R|\mathbf{a}\right) = t_{\mathbf{a}} R\,, \tag{3.85}$$

where this represents an operation R, such as a rotation or a mirror reflection followed by a translation over a vector **a** (note **a** can be any vector, not necessarily just a lattice vector **R**). If we apply the transformation operator $\left(R|\mathbf{a}\right)$ to a point in space we obtain

$$\mathbf{r}' = \left(R|\mathbf{a}\right)\mathbf{r} = R\mathbf{r} + \mathbf{a}\,; \tag{3.86}$$

in component form, this becomes

$$x_i' = \sum_j R_{ji} x_j + a_i\,, \tag{3.87}$$

where R_{ji} is an element of the matrix representation, $\tilde{R}$, of the Cartesian transformation operator defined in Section 3.3.1. The formal composition law of two successive transformation operations is given by

$$\left(R_2|\mathbf{a}_2\right)\left(R_1|\mathbf{a}_1\right) = \left(R_2R_1|R_2\mathbf{a}_1 + \mathbf{a}_2\right). \tag{3.88}$$

If we let the second element equal the inverse of the first element $\left(R_2|\mathbf{a}_2\right) = \left(R_1|\mathbf{a}_1\right)^{-1}$, the right-hand side of Eq. (3.88) is equal to the identity element $\left(E|0\right) = \left(R_2R_1|R_2\mathbf{a}_1 + \mathbf{a}_2\right)$. Then $R_2R_1 = E$ and $R_2\mathbf{a}_1 + \mathbf{a}_2 = 0$, and the inverse operator is given by

$$\left(R_1|\mathbf{a}_1\right)^{-1} = \left(R_1^{-1}|-R_1^{-1}\mathbf{a}_1\right). \tag{3.89}$$

In the same manner that we established conjugacy classes for the point groups we can also determine the conjugacy classes for the space group operators. Two operators $(R|\mathbf{a})$ and $(R|\mathbf{a})'$ are conjugate if there exists a third operator $(\tilde{R}|\mathbf{d})$, $(\tilde{R}|\mathbf{d}) \in E_3$, such that

$$(R|\mathbf{a})' = (\tilde{R}|\mathbf{d})(R|\mathbf{a})(\tilde{R}|\mathbf{d})^{-1} = (\tilde{R}R\tilde{R}^{-1}|\mathbf{d} + \tilde{R}\mathbf{a} - \tilde{R}R\tilde{R}^{-1}\mathbf{d}). \tag{3.90}$$

Operators which are conjugate to each other represent transformations which are essentially the same, but $(R|\mathbf{a})$ is shifted from the $(R|\mathbf{a})'$ by the spatial transformation $(\tilde{R}|\mathbf{d})$. If we examine Eq. (3.90) for the case $\mathbf{a} = 0$ and $\tilde{R} = E$ we find

$$(R|0)' = (E|\mathbf{d})(R|0)(E|\mathbf{d})^{-1} = (R|\mathbf{d} - R\mathbf{d}). \tag{3.91}$$

Now if we define $R = R_O$ as a rotation about an axis passing through the point O, then the operator $(R_O|0)'$ can be viewed as an identical rotation, but the axis of rotation is at a secondary point O' located a distance $\mathbf{d}$ from the point O:

$$(R_O|0)' = (R_{O'}|0) = (R_O|\mathbf{d} - R_O\mathbf{d}), \tag{3.92}$$

(see Figure 11) ([113], pp. 36-39). As stated in Section 3.3, the photonic crystal point group transformation operators of interest are confined to the *x-y* plane. Here also, the composite operators are restricted to the *x-y* plane and thus the vector $\mathbf{d}$ will be restricted to translations in the *x-y* plane.

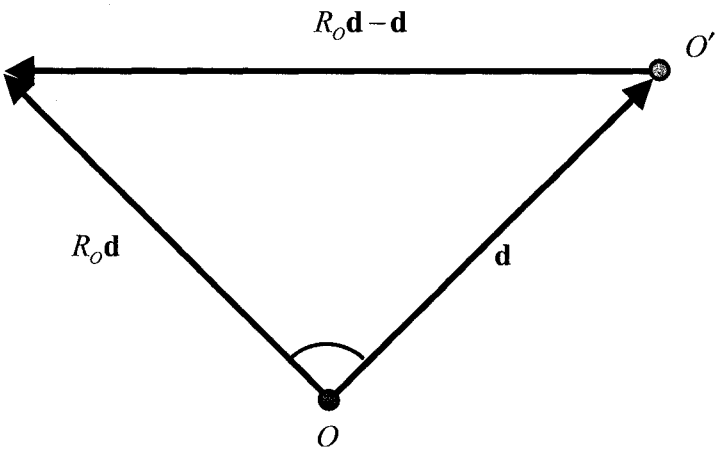

Figure 11. The displacement of a point transformation operation R from the principle axis O to a secondary axis O' a distance $\mathbf{d}$ away, with the accompanying supplementary translation $\mathbf{d}-R_O\mathbf{d}$.

Application of the composite transformation operator Eq. (3.91) to a scalar function $f(\mathbf{r})$ proceeds in the same manner as the application of a single operator R to a function (see Eq. (3.19)), whence

$$\begin{aligned}\left(R|\mathbf{d}-R\mathbf{d}\right)f(\mathbf{r}) &= f\left(\left(R|\mathbf{d}-R\mathbf{d}\right)^{-1}\mathbf{r}\right)\\ &= f\left(\left(R^{-1}|\mathbf{d}-R^{-1}\mathbf{d}\right)\mathbf{r}\right)=f\left(\ddot{R}^{-1}\mathbf{r}+\mathbf{d}-\ddot{R}^{-1}\mathbf{d}\right).\end{aligned} \tag{3.93}$$

Likewise, the composite transformation operator of Eq. (3.91) when transforming a vector field $\mathbf{F}(\mathbf{r})$, has the same form as the application of a single operator R to a vector function, cf. Eq. (3.20). The scalar part transforms as Eq. (3.93), and the vector portion transforms as Eq. (3.86), so that

$$\left(R\,|\mathbf{d}-R\,\mathbf{d}\right)\mathbf{F}(\mathbf{r})=\left(R\,|\mathbf{d}-R\,\mathbf{d}\right)\mathbf{F}\left(\ddot{R}^{-1}\mathbf{r}+\mathbf{d}-\ddot{R}^{-1}\mathbf{d}\right)=\mathbf{F}'\left(\ddot{R}^{-1}\mathbf{r}+\mathbf{d}-\ddot{R}^{-1}\mathbf{d}\right), \tag{3.94}$$

see Section 6.4.3 for the component form of Eq. (3.94) analogous to Eq. (3.21).

3.5.3 Photonic crystal space group: Crystallographic orbits, Wyckoff positions and fundamental domains

We now expand our symmetry considerations of the photonic crystal to its space group G, now including all symmetry elements, defined as

$$\left(R|\mathbf{a}\right)\varepsilon(\mathbf{r})=\varepsilon(\mathbf{r}), \tag{3.95}$$

where $\left(R|\mathbf{a}\right)\in G$. Every point $\mathbf{r}_i$ in a photonic crystal's dielectric profile $\varepsilon(\mathbf{r})$ may be classified into sets of symmetrically equivalent points known as crystallographic orbits. Beginning with any point $\mathbf{r}_1$ in a particular crystallographic orbit for $\varepsilon(\mathbf{r})$, the entire

crystallographic orbit can be obtained by applying all the transformation operators of the photonic crystal space group G to this point $\mathbf{r}_1$ (the generating point):

$$\left(R|\mathbf{a}\right)^{-1}\mathbf{r}_1 = \mathbf{r}_i, \tag{3.96}$$

where $\left(R|\mathbf{a}\right)^{-1} \in G$ (remembering that the inverse of every operator is also part of a group, see Eq. (3.4), where use of the inverse operator will be clear below) and $\mathbf{r}_i \in Q$ (Q is the set of all points part of the crystallographic orbit). From Eq. (3.95), we can define the complementary local transformation property of the dielectric profile as

$$\left(R|\mathbf{a}\right)\varepsilon(\mathbf{r}_1) = \varepsilon\left(\left(R|\mathbf{a}\right)^{-1}\mathbf{r}_1\right) = \varepsilon(\mathbf{r}_1), \tag{3.97}$$

then substituting Eq. (3.96) into Eq. (3.97) we find

$$\varepsilon(\mathbf{r}_i) = \varepsilon(\mathbf{r}_1), \tag{3.98}$$

where $\mathbf{r}_i \in Q$. Therefore, the significance of the crystallographic orbit is that it determines the set of points $\mathbf{r}_i \in Q$ which have identical dielectric constant values, $\varepsilon(\mathbf{r}_i)$, when transformed in space by $\left(R|\mathbf{a}\right) \in G$. Since the photonic crystal space group contains an infinite number of lattice translations, there will be an infinite number of points in every orbit. Not all the transformation operators $\left(R|\mathbf{a}\right)$ of the photonic crystal space group G will produce another point $\mathbf{r}_2$ in the crystallographic orbit, but some will instead transform $\mathbf{r}_1$ into itself:

$$\left(R|\mathbf{a}\right)\mathbf{r}_1 = \mathbf{r}_1, \tag{3.99}$$

which gives

$$\left(R|\mathbf{a}\right)\varepsilon\left(\mathbf{r}_1\right)=\varepsilon\left(\mathbf{r}_1\right). \tag{3.100}$$

The set of transformation operators that satisfy Eq. (3.99) form the site symmetry group $G_{\mathbf{r}_1}$ of $\varepsilon\left(\mathbf{r}_1\right)$ with respect to G. The site symmetry group $G_{\mathbf{r}_1}$ is isomorphic to one of the 32 crystallographic point groups, where the isomorphic point group of $G_{\mathbf{r}_1}$ will be a subgroup of the photonic crystal point group established in Section 3.3 (see Eq. (3.27)). Thus, elements of the photonic crystal point group are simply determined from

$$\left(R|0\right)\varepsilon\left(\mathbf{r}_1\right)=\varepsilon\left(\mathbf{r}_1\right) \tag{3.101}$$

where $\mathbf{r}_1$ is located at the principal axis of the photonic crystal and $R\in C_{nv}$. The site symmetry groups $G_{\mathbf{r}_i}$ of other points $\mathbf{r}_i\in Q$, part of the same crystallographic orbit, are conjugate subgroups of $G_{\mathbf{r}_1}$ such that $\left(R|\mathbf{a}\right)G_{\mathbf{r}_1}\left(R|\mathbf{a}\right)^{-1}=G_{\mathbf{r}_i}$ where $\left(R|\mathbf{a}\right)\in G$ and the operator $\left(R|\mathbf{a}\right)$ is not part of either site group, $\left(R|\mathbf{a}\right)\notin G_{\mathbf{r}_1}$, $\left(R|\mathbf{a}\right)\notin G_{\mathbf{r}_i}$. Consequently, every point $\mathbf{r}_i\in Q$, of a given crystallographic orbit has a site symmetry group $G_{\mathbf{r}_i}$ with essentially the same symmetry operators as the other points; that is the same number of operators, but operators of each site symmetry group $G_{\mathbf{r}_i}$ are applied with respect to the point $\mathbf{r}_i$ in space (we will consider an example at the end of the section). The points $\mathbf{r}_i\in Q$, of a crystallographic orbit are termed special points if the site symmetry groups $G_{\mathbf{r}_i}$ contain at least one transformation operator $\left(R|\mathbf{a}\right)$ in addition to the identity element $\left(E|0\right)$; otherwise they are known as general points.

A photonic crystal contains an infinite number of crystallographic orbits, which can be sub-divided into a finite number of so-called Wyckoff positions. The points associated with the same Wyckoff position have essentially the same site symmetry; that is the same number of elements, but the operators are applied with respect to different points in space. In other words, all points $\mathbf{r}_i \in W_D$ (W_D is all the points associated with the D Wyckoff position), that have conjugate site symmetry groups are associated with the same Wyckoff position; the conjugacy is given by $(R|\mathbf{a})G_{\mathbf{r}_i}(R|\mathbf{a})^{-1} = G_{\mathbf{r}_i}$, where $(R|\mathbf{a}) \in E_3$, $(R|\mathbf{a}) \notin G_{\mathbf{r}_i}$, $(R|\mathbf{a}) \notin G_{\mathbf{r}_j}$ ([117] p. 724). This statement is more general than the previous statement regarding conjugate site symmetry groups of points within a crystallographic orbit, because for Wyckoff positions, $(R|\mathbf{a})$ may be any Cartesian operator (i.e., $(R|\mathbf{a}) \in E_3$), not just an operator of the photonic crystal space group G. Consequently, for the two points $\mathbf{r}_1$ and $\mathbf{r}_2$, in which each point is part of a different crystallographic orbit, but associated with the same Wyckoff position, $\varepsilon(\mathbf{r}_1) = \varepsilon(\mathbf{r}_2)$ is not a requirement (i.e., $\mathbf{r}_1$ and $\mathbf{r}_2$ are not necessarily symmetry equivalent points in $\varepsilon(\mathbf{r})$). The international tables for crystallography list the Wyckoff positions and their site symmetry groups within the crystal primitive unit cell for every possible crystal space group [117]. Since there are an infinite number of site symmetry groups associated with a Wyckoff position only the conjugate point group C_{nv} is listed for simplicity, where C_{nv} will be a subgroup of the photonic crystal point group established in Section 3.3. The number of points for a given crystallographic orbit that appear in the primitive unit cell is equal to the order of the photonic crystal point group divided by the order of a site symmetry group associated with the Wyckoff position (choice does not matter because they all have the same order):

$$t = h_{C_{nv}} / h_{G_{\mathbf{r}}} \tag{3.102}$$

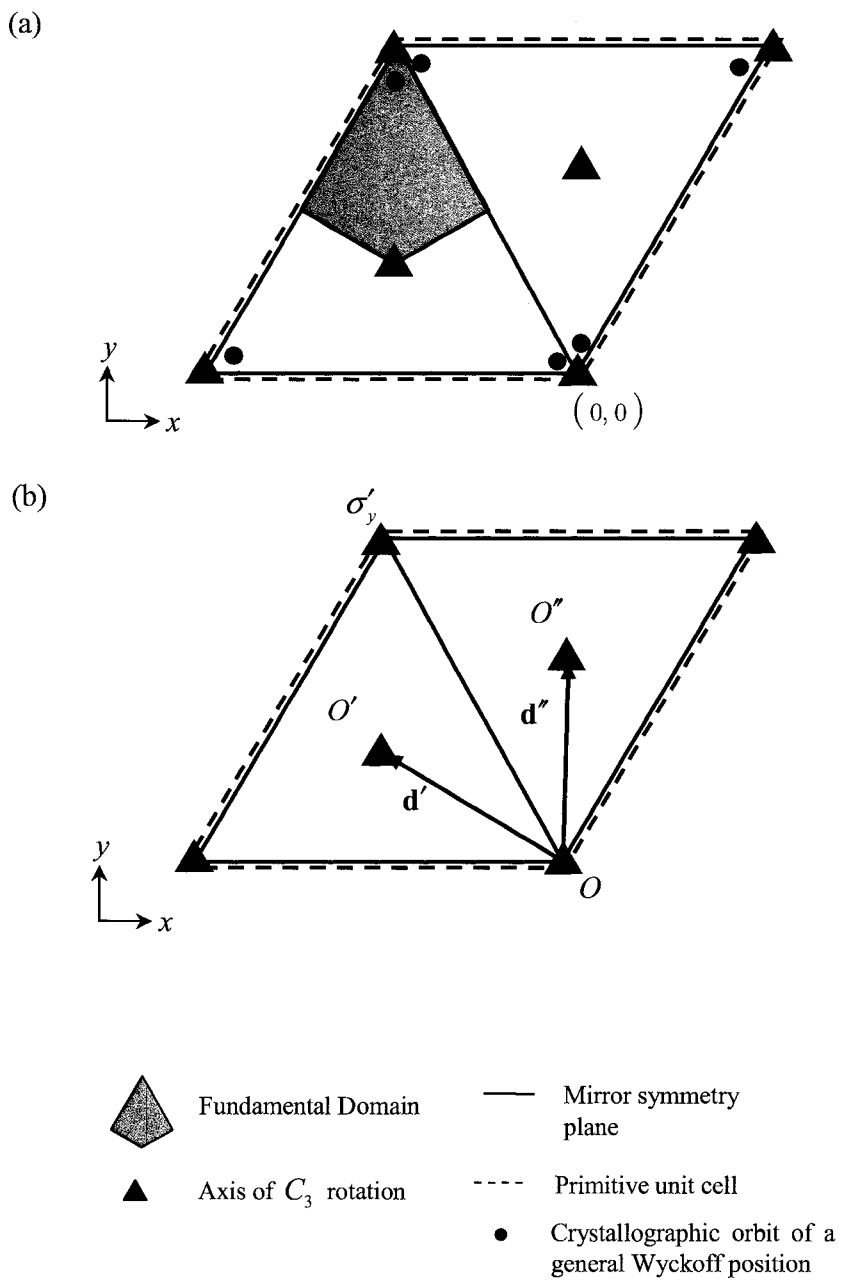

Figure 12. Primitive unit cell of a C_{3v} hexagonal lattice: (a) with the symmetry axes mark, fundamental domain and the positions the crystallographic orbit for a general Wyckoff position illustrated; (b) the same primitive unit cell, but now the fractional lattice vectors $\mathbf{d}'$ and $\mathbf{d}''$ are indicated for the two different points O' and O'', which are part of the same crystallographic orbit.

where $h_{C_{nv}}$ is the number of elements in the photonic crystal point group C_{nv}, and h_{G_r} is the number of elements of the chosen site symmetry group, G_{r_i} ([113], p. 50). Since all the crystallographic orbits associated with a Wyckoff position have conjugate subgroups, the value of Eq. (3.102) will be the same for all the crystallographic orbits associated with a particular Wyckoff position.

As an example, we examine a triangular lattice crystalline structure with C_{3v} point symmetry (see Figure 12(a)), where the first three main Wyckoff position are listed in Table 5. The primitive unit cell of the hexagonal lattice is a rhombus (composed of two equilateral triangles). Note in the next section, this same space group will be applied to a hexagonal photonic crystral eigenmode with C_{3v} point symmetry. A general point in this unit cell has a site symmetry containing just the identity operator, thus the number of times a point appears in the crystallographic orbit is $t = 6/1 = 6$ (see the black dots in Figure 12(a)). At the vertices of the equilateral triangles, the site symmetries are $C_{3v} = \{E, C_3, C_3^{-1}, \sigma_y, \sigma_y', \sigma_y''\}$. The vertices are part of the crystallographic orbit where the principal axis at $(0,0)$ is the generating point (associated with the W_a Wyckoff position and $t = 6/6 = 1$). At the middle of the equilateral triangles, $\left(-a/2, a/\left(2\sqrt{3}\right)\right)$ and $\left(0, a/\sqrt{3}\right)$, the site symmetry is $C_3 = \{E, C_3, C_3^{-1}\}$. These two points are part of the same crystallographic orbit (associated with the W_b Wyckoff position where $t = 6/3 = 2$). The mirror reflection planes coincide with the equilateral triangle line segments, on which the site symmetry is $C_{1h} = \{E, \sigma_v\}$. There are an infinite number of points on each line segment, whereby each point is a generating point of a separate crystallographic orbit associated with the
W_c Wyckoff position, $t = 6/2 = 3$. Figure 12(a) and the Wyckoff positions provide all the relevant information about the space group of the C_{3v} photonic crystal.

Table 5. Special Wyckoff positions in the C_{3v} hexagonal primitive unit cell

Wyckoff position	Site Symmetry	Multiplicity (t)	Location (Cartesian basis)
W_a	C_{3v}	1	$(0,0)$
W_b	C_3	2	$\left(-a/2, a/\left(2\sqrt{3}\right)\right)$, $\left(0, a/\sqrt{3}\right)$
W_c	C_{1h}	3	triangle line segments

To give an illustration of two conjugate site symmetry groups, we examine the points $\left(-a/2, a/\left(2\sqrt{3}\right)\right)$ and $\left(0, a/\sqrt{3}\right)$ (see Figure 12(b)) which are associated with W_b Wyckoff position. These two points are part of the same crystallographic orbit, and according to Table 5, their site symmetry groups are conjugate with the C_3 point group, where $C_3 = \{E, C_3, C_3^{-1}\}$. First, we start with Eq. (3.99) for the position O, the origin $(0,0)$, and apply the transformation operator $(E|\mathbf{d}')$ to shift to the secondary axis O' at $\left(-a/2, a/\left(2\sqrt{3}\right)\right)$:

$$\begin{aligned} (E|\mathbf{d}')(R|\mathbf{a})\varepsilon(\mathbf{r}_O) &= (E|\mathbf{d}')\varepsilon(\mathbf{r}_O) \\ (E|\mathbf{d}')(R|\mathbf{a})(E|\mathbf{d}')^{-1}(E|\mathbf{d}')\varepsilon(\mathbf{r}_O) &= (E|\mathbf{d}')\varepsilon(\mathbf{r}_O) \\ (R|\mathbf{d}' - R\mathbf{d}')\varepsilon(\mathbf{r}_{O'}) &= \varepsilon(\mathbf{r}_{O'}), \end{aligned} \tag{3.103}$$

where we have used Eq. (3.91) , $(E|\mathbf{d}')\varepsilon(\mathbf{r}_O) = \varepsilon(\mathbf{r}_{O'})$ and $R \in C_3$. Note that the point $\mathbf{r}_O$ is just the starting position of the derivation, because it is the location of the principal axis (i.e. the origin). $\mathbf{r}_O$ is not part of the same crystallographic orbit or associated with the same Wyckoff position as $\left(-a/2, a/\left(2\sqrt{3}\right)\right)$ and $\left(0, a/\sqrt{3}\right)$, because $(E|\mathbf{d}') \notin G$ and G_O is conjugate with C_{3v} respectively. The site symmetry group of the point O' will

contain all the elements $(R|\mathbf{d}'-R\mathbf{d}')\subset G$, where $R\in C_3$. To determine the conjugate subgroup at the second crystallographic orbit location O'', we apply the mirror reflection operator about the principal axis $(\sigma_y'|0)$ to Eq. (3.103):

$$\begin{aligned}
&(\sigma_y'|0)(R|\mathbf{d}'-R\mathbf{d}')\varepsilon(\mathbf{r}_{O'})=(\sigma_y'|0)\varepsilon(\mathbf{r}_{O'})\\
&(\sigma_y'|0)(R|\mathbf{d}'-R\mathbf{d}')(\sigma_y'|0)^{-1}(\sigma_y'|0)\varepsilon(\mathbf{r}_{O'})=(\sigma_y'|0)\varepsilon(\mathbf{r}_{O'})\\
&(\sigma_y' R\sigma_y'^{-1}|(\sigma_y'\mathbf{d}'-\sigma_y' R\sigma_y'^{-1}\sigma_y'\mathbf{d}'))\varepsilon(\mathbf{r}_{O''})=\varepsilon(\mathbf{r}_{O''}),
\end{aligned}\qquad (3.104)$$

where we have used Eq. (3.91) , $(\sigma_y'|0)\varepsilon(\mathbf{r}_{O'})=\varepsilon(\mathbf{r}_{O''})$ and $R\in C_3$. The site symmetry group of the point O'' will contain all elements $(\sigma_y' R\sigma_y'^{-1}|(\sigma_y'\mathbf{d}'-\sigma_y' R\sigma_y'^{-1}\sigma_y'\mathbf{d}'))\subset G$, where $R\in C_3$. Therefore, the second point O'' of the crystallographic orbit has a site symmetry group $G_{O''}$ that is conjugate to site symmetry group of the first point $G_{O'}$ by the operator $(\sigma_y'|0)$, hence they are conjugate site symmetry groups.

Finally, now that we have established the Wyckoff positions and their associated crystallographic orbits, we can define the fundamental domain. The fundamental domain is the volume of space that covers all space when acted upon by all the transformation operators $(R|\mathbf{a})$ of the photonic crystal space group *G*. The primitive unit cell defined in section 2.2.2 is the fundamental domain for the subgroup of periodic symmetry operators. In Figure 12(a), we can see that the fundamental domain reduces to 1/6 of the primitive unit cell when all of the transformation operators $(R|\mathbf{a})$ of the photonic crystal space group *G* are considered. The fundamental domain represents the smallest amount of information we need in order to reproduce the photonic crystal's dielectric profile. In Chapter 6, we will see that the description of the electromagnetic field can be reduced to fundamental domain.

3.5.4 Photonic crystal eigenmode symmetry transformations at a secondary axis

In the previous section, we considered the photonic crystal space group, focusing on the dielectric profile; the concepts introduced, however, apply equally to the photonic crystal eigenmodes. In Section 3.3.2, we established the transformation properties of photonic crystal eigenmodes and classified them by the irreducible matrix representations $\vec{D}^{(\nu)}(R)$ (see Eq. (3.38)) of the **k**-group (transformation operators acting about the principal axis, which is the location of highest site symmetry, see Section 3.3.2). In this section, we establish the irreducible matrix representations $\vec{D}^{(\nu)}(R|\mathbf{d}-R\mathbf{d})$ for the transformation operators acting with respect to any symmetry axis given by the space group G, where again the photonic crystal eigenmodes are the partner functions. For special cases, we will show that $\vec{D}^{(\nu)}(R|\mathbf{d}-R\mathbf{d})$ will be related by a phase factor to the irreducible matrix representations $\vec{D}^{(\nu)}(R)$ of the **k**-group. This will allow us to easily calculate $\vec{D}^{(\nu)}(R|\mathbf{d}-R\mathbf{d})$ when $\vec{D}^{(\nu)}(R)$ is already known. Here we focus on the global transformation properties of the photonic crystal eigenmodes and leave the analysis of points in the electromagnetic field to Chapter 6.

If we apply a general operator $(R|\mathbf{d}-R\mathbf{d})\in G$ of the photonic crystal space group G to the scalar Bloch mode Eq. (2.29), we obtain an equation similar to Eq. (3.33) (the application of the point group transformation operators $R\in C_{nv}$ to the Bloch mode):

$$\begin{aligned}(R|\mathbf{d}-R\mathbf{d})u_{\mathbf{k}n}(\mathbf{r})e^{i\mathbf{k}\cdot(\mathbf{r})} &= u_{\mathbf{k}n}\left(R^{-1}\mathbf{r}+\mathbf{d}-R^{-1}\mathbf{d}\right)e^{i\mathbf{k}\cdot\left(\mathbf{d}-R^{-1}\mathbf{d}\right)}e^{i\left(R\,\mathbf{k}\cdot\mathbf{r}\right)} \\ &= u'_{\mathbf{k}n}(\mathbf{r})e^{i\left(R\,\mathbf{k}\cdot\mathbf{r}\right)}.\end{aligned} \tag{3.105}$$

Note that we have suppressed the $\hat{\mathbf{z}}$ polarization due to its invariance to the transformation operators $(R|\mathbf{d}-R\mathbf{d})$. We focus on the TM case, but these results are equally applicable to the TE case. In general, application of any transformation operator

of the photonic crystal space group G will create a new Bloch mode $u'_{\mathbf{k}n}(\mathbf{r})e^{i(R\,\mathbf{k}\cdot\mathbf{r})}$ with a Bloch wave vector of $R\mathbf{k}$. Next, we apply the periodic symmetry transformation operator $T(\mathbf{R})=(E|\mathbf{R})$ to Eq. (3.105), we obtain

$$\begin{aligned}(E|\mathbf{R})u'_{\mathbf{k}n}(\mathbf{r})e^{i(R\,\mathbf{k}\cdot\mathbf{r})} &= u_{\mathbf{k}n}\left(R^{-1}\mathbf{r}+R^{-1}\mathbf{R}+\mathbf{d}-R^{-1}\mathbf{d}\right)e^{i\mathbf{k}\cdot\left(\mathbf{d}-R^{-1}\mathbf{d}\right)}e^{i(R\,\mathbf{k}\cdot(\mathbf{r}+\mathbf{R}))} \\ &= e^{i(R\,\mathbf{k}\cdot\mathbf{R})}u'_{\mathbf{k}n}(\mathbf{r})e^{i(R\,\mathbf{k}\cdot\mathbf{r})},\end{aligned} \tag{3.106}$$

where we use the fact that $u'_{\mathbf{k}n}(\mathbf{r})=u_{\mathbf{k}n}\left(R^{-1}\mathbf{r}+\mathbf{d}-R^{-1}\mathbf{d}\right)$ is periodic if $u_{\mathbf{k}n}(\mathbf{r})$ is (see Eq. (2.20)), because $\tilde{R}^{-1}\mathbf{R}$ is also a lattice vector ([113], p. 74). Equation (3.106) defines $e^{i\tilde{R}\mathbf{k}\cdot\mathbf{R}}$ as the irreducible matrix representation (matrix with a dimension of one) of $(E|\mathbf{R})$, in the new basis $u'_{\mathbf{k}n}(\mathbf{r})e^{i(R\,\mathbf{k}\cdot\mathbf{r})}$. Any wave vector that satisfies

$$R\mathbf{k}=\mathbf{k}'=\mathbf{k}+\mathbf{G} \tag{3.107}$$

is an equivalent wave vector due to Eq. (2.22). When Eq. (3.107) is satisfied, then $u_{\mathbf{k}n}(\mathbf{r})e^{i\mathbf{k}\cdot\mathbf{r}}$ and $u'_{\mathbf{k}n}(\mathbf{r})e^{i(R\,\mathbf{k}\cdot\mathbf{r})}$ are associated with the same irreducible matrix representation of $(E|\mathbf{R})$, because $e^{i\tilde{R}\mathbf{k}\cdot\mathbf{R}}=e^{i(\mathbf{k}+\mathbf{G})\cdot\mathbf{R}}=e^{i\mathbf{k}\cdot\mathbf{R}}$ (see Eq.(3.34) for the $u_{\mathbf{k}n}(\mathbf{r})e^{i\mathbf{k}\cdot\mathbf{r}}$ basis case). The irreducible matrix representation $e^{i\mathbf{k}\cdot\mathbf{R}}$ and the frequency identify the eigenmode, i.e. $\mathbf{k}$ and n. When $\mathbf{k}$ and n are the same, then $u_{\mathbf{k}n}(\mathbf{r})e^{i\mathbf{k}\cdot\mathbf{r}}$ and $u'_{\mathbf{k}n}(\mathbf{r})e^{i(R\,\mathbf{k}\cdot\mathbf{r})}$ must be either an equivalent eigenmode of the Maxwell operator, or a linear combination of the degenerate eigenmodes also associated with the same irreducible matrix representation $e^{i\mathbf{k}\cdot\mathbf{R}}$. Therefore, similar to the definition of the $\mathbf{k}$-group, the operators $(R|\mathbf{d}-R\mathbf{d})\in G$ of the photonic crystal space group G that satisfies Eq. (3.107) form the space $\mathbf{k}$-group $G_{\mathbf{k}}$ of the photonic crystal eigenmode. In other

words, the non-principal symmetry axes of the photonic crystal space group are also part of the photonic crystal eigenmode space **k**-group.

If we take a closer look at Eq. (3.105) and assume that $\mathbf{d}-R^{-1}\mathbf{d}=\mathbf{R}'$, where $\mathbf{R}'$ is a lattice vector, then

$$u_{\mathbf{k}n}\left(R^{-1}\mathbf{r}+\mathbf{d}-R^{-1}\mathbf{d}\right)=u_{\mathbf{k}n}\left(R^{-1}\mathbf{r}+\mathbf{R}'\right)=u_{\mathbf{k}n}\left(R^{-1}\mathbf{r}\right), \tag{3.108}$$

based on the periodicity of $u_{\mathbf{k}n}\left(R^{-1}\mathbf{r}\right)$ given by Eq. (3.35). Substituting Eq. (3.108) back into Eq. (3.105) we obtain

$$\left(R\middle|\mathbf{d}-R\mathbf{d}\right)u_{\mathbf{k}n}\left(\mathbf{r}\right)e^{i\mathbf{k}\cdot(\mathbf{r})}=e^{i\mathbf{k}\cdot\left(\mathbf{d}-R^{-1}\mathbf{d}\right)}u_{\mathbf{k}n}\left(R^{-1}\mathbf{r}\right)e^{i\left(R\,\mathbf{k}\cdot\mathbf{r}\right)}. \tag{3.109}$$

If the transformation operator R is part of the photonic crystal eigenmode's **k**-group, we find

$$Ru^{(\nu)}_{\mathbf{k}nj}\left(\mathbf{r}\right)e^{i\mathbf{k}\cdot(\mathbf{r})}=u^{(\nu)}_{\mathbf{k}nj}\left(R^{-1}\mathbf{r}\right)e^{i\left(R\,\mathbf{k}\cdot\mathbf{r}\right)}=\sum\nolimits_j^l D^{(\nu)}_{ji}\left(R\right)u^{(\nu)}_{\mathbf{k}nj}\left(\mathbf{r}\right)e^{i(\mathbf{k}\cdot\mathbf{r})}, \tag{3.110}$$

where we have substituted the scalar Bloch mode of Eq. (2.29) into Eq. (3.38) which defines the irreducible representations of the **k**-group (ν identifies the irreducible representation and j denotes the degeneracy). Finally we can substitute the results of Eq. (3.110) into Eq. (3.109) and we obtain

$$\begin{aligned}\left(R\middle|\mathbf{d}-R\mathbf{d}\right)u^{(\nu)}_{\mathbf{k}ni}\left(\mathbf{r}\right)e^{i\mathbf{k}\cdot(\mathbf{r})}&=e^{i\mathbf{k}\cdot\left(\mathbf{d}-R^{-1}\mathbf{d}\right)}\sum\nolimits_j^l D^{(\nu)}_{ji}\left(R\right)u^{(\nu)}_{\mathbf{k}nj}\left(\mathbf{r}\right)e^{i(\mathbf{k}\cdot\mathbf{r})}\\&=\sum\nolimits_j^l D^{(\nu)}_{ji}\left(R\middle|\mathbf{d}-R\mathbf{d}\right)u^{(\nu)}_{\mathbf{k}nj}\left(\mathbf{r}\right)e^{i(\mathbf{k}\cdot\mathbf{r})}\end{aligned}. \tag{3.111}$$

Equation (3.111) defines the elements of the irreducible matrix representation $\vec{D}^{(\nu)}\left(R|\mathbf{d}-R\mathbf{d}\right)$ of the transformation operator $\left(R|\mathbf{d}-R\mathbf{d}\right)$, where $u_{\mathbf{k}ni}^{(\nu)}(\mathbf{r})e^{i\mathbf{k}\cdot(\mathbf{r})}$ is the basis. Therefore, if $\mathbf{d}-R^{-1}\mathbf{d}=\mathbf{R}'$, then the irreducible matrix representations $\vec{D}^{(\nu)}\left(R|\mathbf{d}-R\mathbf{d}\right)$ of the photonic crystal eigenmode space **k**-group are equivalent to the irreducible matrix representation $\vec{D}^{(\nu)}\left(R\right)$ of the photonic crystal eigenmode **k**-group to within a phase factor:

$$\vec{D}^{(\nu)}\left(R|\mathbf{d}-R\mathbf{d}\right)=e^{i\mathbf{k}\cdot\left(\mathbf{d}-R^{-1}\mathbf{d}\right)}\vec{D}^{(\nu)}\left(R\right). \tag{3.112}$$

As an illustration, we now examine the irreducible matrix representations associated with site symmetry groups at non-principal axes for a non-degenerate photonic crystal eigenmode with C_{3v} point group symmetry associated with the A_2 irreducible representation, where $\mathbf{k}=\hat{\mathbf{x}}\,4\pi/(3a)$ (see Figure 12 for the space group). The irreducible matrix representations associated with non-degenerate eigenmodes are one-dimensional ($\vec{D}^{(\nu)}\left(R\right)=\chi_R^{(\nu)}$). As a result, we can obtain the A_2 irreducible matrix representations from the C_{3v} character table (see Table 1). For this example we choose the special Wyckoff position W_b, located within the unit cell at $\left(-a/2,a/\left(2\sqrt{3}\right)\right)$ and $\left(0,a/\sqrt{3}\right)$, with site symmetries of C_3 (see Table 6), where $C_3=\left\{E,C_3,C_3^{-1}\right\}$. We start by determining if $\mathbf{d}-R^{-1}\mathbf{d}=\mathbf{R}'$ for the transformation operators $\left(R|\mathbf{d}-R\mathbf{d}\right)$, $R\in C_3$ because if this is true we may use Eq. (3.112) to determine the irreducible matrix representations. First, we look at $\mathbf{d}-R^{-1}\mathbf{d}$ when $\mathbf{d}=\left(-a/2,a/\left(2\sqrt{3}\right)\right)$, for $R\in C_3$:

$$\begin{pmatrix}-\frac{a}{2}\\ \frac{a}{2\sqrt{3}}\\ 0\end{pmatrix}-E\begin{pmatrix}-\frac{a}{2}\\ \frac{a}{2\sqrt{3}}\\ 0\end{pmatrix}=a\begin{pmatrix}-\frac{1}{2}\\ \frac{1}{2\sqrt{3}}\\ 0\end{pmatrix}-a\begin{pmatrix}1&0&0\\0&1&0\\0&0&1\end{pmatrix}\begin{pmatrix}-\frac{1}{2}\\ \frac{1}{2\sqrt{3}}\\ 0\end{pmatrix}=\begin{pmatrix}0\\0\\0\end{pmatrix}, \tag{3.113}$$

$$\begin{pmatrix} -\frac{a}{2} \\ \frac{a}{2\sqrt{3}} \\ 0 \end{pmatrix} - C_3 \begin{pmatrix} -\frac{a}{2} \\ \frac{a}{2\sqrt{3}} \\ 0 \end{pmatrix} = a \begin{pmatrix} -\frac{1}{2} \\ \frac{1}{2\sqrt{3}} \\ 0 \end{pmatrix} - a \begin{pmatrix} -\frac{1}{2} & \frac{\sqrt{3}}{2} & 0 \\ -\frac{\sqrt{3}}{2} & -\frac{1}{2} & 0 \\ 0 & 0 & 1 \end{pmatrix} \begin{pmatrix} -\frac{1}{2} \\ \frac{1}{2\sqrt{3}} \\ 0 \end{pmatrix} = a \begin{pmatrix} -1 \\ 0 \\ 0 \end{pmatrix}, \tag{3.114}$$

$$\begin{pmatrix} -\frac{a}{2} \\ \frac{a}{2\sqrt{3}} \\ 0 \end{pmatrix} - C_3^{-1} \begin{pmatrix} -\frac{a}{2} \\ \frac{a}{2\sqrt{3}} \\ 0 \end{pmatrix} = a \begin{pmatrix} -\frac{1}{2} \\ \frac{1}{2\sqrt{3}} \\ 0 \end{pmatrix} - a \begin{pmatrix} -\frac{1}{2} & -\frac{\sqrt{3}}{2} & 0 \\ \frac{\sqrt{3}}{2} & -\frac{1}{2} & 0 \\ 0 & 0 & 1 \end{pmatrix} \begin{pmatrix} -\frac{1}{2} \\ \frac{1}{2\sqrt{3}} \\ 0 \end{pmatrix} = a \begin{pmatrix} -\frac{1}{2} \\ \frac{\sqrt{3}}{2} \\ 0 \end{pmatrix}. \tag{3.115}$$

For $R \in C_3$ and $\mathbf{d} = \left(0, a/\sqrt{3}\right)\mathbf{d} - R^{-1}\mathbf{d}$ is:

$$\begin{pmatrix} 0 \\ \frac{a}{\sqrt{3}} \\ 0 \end{pmatrix} - E \begin{pmatrix} 0 \\ \frac{a}{\sqrt{3}} \\ 0 \end{pmatrix} = a \begin{pmatrix} 0 \\ \frac{1}{\sqrt{3}} \\ 0 \end{pmatrix} - a \begin{pmatrix} 1 & 0 & 0 \\ 0 & 1 & 0 \\ 0 & 0 & 1 \end{pmatrix} \begin{pmatrix} 0 \\ \frac{1}{\sqrt{3}} \\ 0 \end{pmatrix} = \begin{pmatrix} 0 \\ 0 \\ 0 \end{pmatrix}, \tag{3.116}$$

$$\begin{pmatrix} 0 \\ \frac{a}{\sqrt{3}} \\ 0 \end{pmatrix} - C_3 \begin{pmatrix} 0 \\ \frac{a}{\sqrt{3}} \\ 0 \end{pmatrix} = a \begin{pmatrix} 0 \\ \frac{1}{\sqrt{3}} \\ 0 \end{pmatrix} - a \begin{pmatrix} -\frac{1}{2} & \frac{\sqrt{3}}{2} & 0 \\ -\frac{\sqrt{3}}{2} & -\frac{1}{2} & 0 \\ 0 & 0 & 1 \end{pmatrix} \begin{pmatrix} 0 \\ \frac{1}{\sqrt{3}} \\ 0 \end{pmatrix} = a \begin{pmatrix} -\frac{1}{2} \\ \frac{\sqrt{3}}{2} \\ 0 \end{pmatrix}. \tag{3.117}$$

$$\begin{pmatrix} 0 \\ \frac{a}{\sqrt{3}} \\ 0 \end{pmatrix} - C_3^{-1} \begin{pmatrix} 0 \\ \frac{a}{\sqrt{3}} \\ 0 \end{pmatrix} = a \begin{pmatrix} 0 \\ \frac{1}{\sqrt{3}} \\ 0 \end{pmatrix} - a \begin{pmatrix} -\frac{1}{2} & -\frac{\sqrt{3}}{2} & 0 \\ \frac{\sqrt{3}}{2} & -\frac{1}{2} & 0 \\ 0 & 0 & 1 \end{pmatrix} \begin{pmatrix} 0 \\ \frac{1}{\sqrt{3}} \\ 0 \end{pmatrix} = a \begin{pmatrix} \frac{1}{2} \\ \frac{\sqrt{3}}{2} \\ 0 \end{pmatrix}. \tag{3.118}$$

We can see from Eq. (3.113)-(3.118) that they are all linear combinations of the hexagonal lattice vectors $\mathbf{a}_1 = a\hat{x}$ and $\mathbf{a}_2 = \hat{\mathbf{x}}\, a/2 + \hat{\mathbf{y}}\sqrt{3}a/2$. Therefore we may use Eq. (3.112) to determine the irreducible matrix representations (in this case the character) for the non-principal axis operators $\left(R|\mathbf{d} - R\mathbf{d}\right)$, $R \in C_3$. Substituting the results of Eqs. (3.113)-(3.115) into Eq. (3.112) the characters at the point $\mathbf{d} = \left(-a/2, a/\left(2\sqrt{3}\right)\right)$ are:

$$\chi_{(E|\mathbf{d}-E\mathbf{d})}^{\left(-a/2,a/\left(2\sqrt{3}\right)\right)} = e^{-i0}\chi_E^{(A_2)} = 1, \tag{3.119}$$

Table 6. The C_3 Character Table

Γ	Conjugacy classes		
	E	C_3	C_3^{-1}
A	1	1	1
E	1	$-1/2+i\sqrt{3}/2$	$-1/2-i\sqrt{3}/2$
E^*	1	$-1/2-i\sqrt{3}/2$	$-1/2+i\sqrt{3}/2$

$$\chi^{\left(-a/2,a/\left(2\sqrt{3}\right)\right)}_{\left(C_3|\mathbf{d}-C_3\mathbf{d}\right)} = e^{-i4\pi/3}\chi^{(A_2)}_{C_3} = -1/2+i\sqrt{3}/2, \tag{3.120}$$

$$\chi^{\left(-a/2,a/\left(2\sqrt{3}\right)\right)}_{\left(C_3^{-1}|\mathbf{d}-C_3^{-1}\mathbf{d}\right)} = e^{-i2\pi/3}\chi^{(A_2)}_{C_3^{-1}} = -1/2-i\sqrt{3}/2. \tag{3.121}$$

Substituting Eq. (3.116)-(3.118) into into Eq. (3.112) the character at the point $\mathbf{d}=\left(0,a/\sqrt{3}\right)$ are:

$$\chi^{\left(-a/2,a/\left(2\sqrt{3}\right)\right)}_{\left(E|\mathbf{d}-E\mathbf{d}\right)} = e^{-i0}\chi^{(A_2)}_{E} = 1, \tag{3.122}$$

$$\chi^{\left(0,a/\sqrt{3}\right)}_{\left(C_3|\mathbf{d}-C_3\mathbf{d}\right)} = e^{-i2\pi/3}\chi^{(A_2)}_{C_3} = -1/2-i\sqrt{3}/2, \tag{3.123}$$

$$\chi^{\left(0,a/\sqrt{3}\right)}_{\left(C_3^{-1}|\mathbf{d}-C_3^{-1}\mathbf{d}\right)} = e^{i2\pi/3}\chi^{(A_2)}_{C_3^{-1}} = -1/2+i\sqrt{3}/2, \tag{3.124}$$

We can see that the characters given by Eqs. (3.119)-(3.121) match the characters of the E irreducible representation of the point symmetry group C_3 (see Table 6). In like manner, the characters given by Eqs. (3.122)-(3.124) match the characters of the E^* irreducible representation of the point symmetry group C_3 (see Table 6). All points in this crystallographic orbit have one of these two values. In Chapter 6, knowledge of the irreducible matrix representations of the photonic crystal space **k**-group will enable us to determine the location and type of polarization singularities in the electromagnetic field.

CHAPTER 4 – NUMERICAL METHODS: THE FINITE ELEMENT METHOD APPLIED TO TWO-DIMENSIONAL PHOTONIC CRYTSALS AND PHOTONIC CRYSTAL SLABS

4.1 Introduction

Up to this point, we have focused on establishing group theoretic approaches to treat photonic crystals, in which we have developed the analytical elements of our tool set. In this study, group theoretic predictions are verified by numerical simulations of photonic crystals in high dielectric contrast systems. This chapter focuses on this second complementary element in our tool set, numerical experimentation via computational physics. The numerical methods of computational physics play an important role in the extensive body of research devoted to photonic crystals. Our present analytical approximations are suited to develop a broad understanding, but they lack detail in the high dielectric contrast systems needed for experimental realization. In contrast to the quantum mechanical problems of solid state physics, Maxwell's equations can be solved for exactly within linear media [4]. As a result, using numerical methods, we obtain in-depth knowledge of the properties of the electromagnetic field in any dielectric configuration we can imagine, anywhere inside or outside the structure. Therefore, this allows us to study the sub-wavelength properties of the optical Bloch modes directly, which can lead to amazing discoveries when one is able view the actual electromagnetic field patterns. These patterns reveal subtleties that are not obvious when one is staring at a set of differential equations and group theory character tables. In fact, it was an unusual electromagnetic field pattern obtained from a computer simulation that sparked my curiosity, and led to the discovery of optical singularities in photonic crystals. Finally, the development of the simulation software will inform future experimental investigations of optical singularities within photonic crystals and photonic crystal applications. For example, in Appendix D, using the numerical models developed in this

study, we examine the optical forces on a sub-wavelength dielectric particle within a Bloch mode which contain optical singularities.

In the following sections, we first discuss the finite element method (FEM), our chosen numerical treatment for the solutions of Maxwell's equations for photonic crystals. We examine in detail the application of the FEM to two specific cases: the two-dimensional photonic crystal eigenvalue problem, and the photonic crystal slab eigenvalue problem. In the case of the two-dimensional photonic crystal eigenvalue problem, the scalar Maxwell operator is redefined as a function of the dielectric profile and the Bloch wave vector **k**. The solution space is reduced to a two-dimensional primitive unit cell with periodic boundary conditions. In the case of the photonic crystal slab eigenvalue problem, we take two distinct approaches to the application of the FEM: a generalized effective index method, and the full vector solution method. This novel self-consistent effective index method is able to actively match the frequency dependence of the effective dielectric permittivity to a particular photonic crystal eigenmode. The approach demonstrates a dramatic improvement in the application of the effective index method to high dielectric contrast photonic crystals. Finally, we outline the application of the full vector FEM to the photonic crystal slab eigenvalue problem. In this case, the full vector Maxwell's equations are solved, whereby we obtain the solutions to the full vector photonic crystal eigenmodes. Similar to the two-dimensional photonic crystal eigenvalue problem, the solution space of the photonic crystal slab is reduced to a primitive unit, with periodic boundary conditions in the *x*-*y* plane.

4.2 The Finite Element Method

From a numerical point of view, simulating linear photonic crystals requires solving a set of differential equations within a finite solution space (which defines the dielectric profile) for a particular set of boundary conditions. This can be further subdivided into two elementary problems: the eigenvalue problem and the driven problem. The eigenvalue problem, which is the focus of this body of research, defines a linear problem, and seeks to find a set of basis solutions, known as eigenmodes, that are the elementary

forms of the electromagnetic field (see Chapter 2). By contrast, the driven problem includes a source term in Maxwell's equations, and the solution space encompasses dynamic evolution of the electromagnetic radiation within the dielectric profile. There have been many numerical techniques applied to the study of photonic crystals, such as: the finite-difference time-domain method (FDTD); the plane wave expansion method (PWM); the scattering-matrix techniques; the multiple-multipole method; the Wannier-function approach; the Green's function technique; and the finite-element method (FEM). There is no one dominant numerical technique in the field of photonic crystals; each has strengths and weaknesses (see [93] for a full comparison of numerical techniques applied to photonic crystals). For this research, the FEM is the numerical technique chosen to determine the eigenmodes of two-dimensional photonic crystals and photonic crystal slabs.

The FEM uses a variational approach to fit a series of interconnected trial functions to the subdomains of the solution space, which minimizes the residual of an integral form of the differential equation while satisfying the boundary conditions [41]. The subdomains are defined by a series of interconnected tetrahedral elements that form a non-uniform mesh, and the electromagnetic field is defined at the apexes of the triangles. The FEM can be used to solve an eigenvalue problem directly or a source term can be included to solve a driven problem. The FEM is not as numerically efficient as the PWM in solving simple photonic crystal eigenvalue problems. In addition, the FEM is more complex to implement than the FDTD method when applied to driven problems, where one wants to observe time-dependent phenomena [42]. If, however, the source is time-harmonic (i.e., continuous wave phenomena), similar to the FDTD method, transmission and reflection characteristics can easily be obtained with the FEM. The strength of the FEM lies in its ability to easily handle both eigenvalue problems and driven problems with complex dielectric profiles, as well as unit cells with complex boundaries [42]. The FEM uses a non-uniform mesh that easily follows curved profiles, and the mesh density is permitted to vary dramatically within a problem's solution space. This allows dense mesh patterns in regions where the electromagnetic field changes rapidly, and sparse mesh patterns in

regions where the field is almost constant, resulting in a numerically efficient mesh pattern. The application of the FEM to determine the eigenmodes of a two-dimensional photonic crystal or a photonic crystal slab can be subdivided into solving a scalar eigenvalue problem or solving a full vector eigenvalue problem. In Section 2.4.1, it was shown that the two-dimensional photonic crystal eigenvalue problem may be reduced to a scalar problem with the eigenmodes uniformly polarized along the $\hat{\mathbf{z}}$ axis. Due to the scalar form of the problem, scalar finite elements may be used to model the electromagnetic field. The scalar form of the eigenvalue problem is also applicable to the photonic crystal slab problem, when the effective index method is used to determine the eigenvalues (see Section 4.4.2). By contrast, we cannot reduce the photonic crystal slab eigenvalue problem to a scalar equation, but instead must seek a full vector solution. The full vector solutions require vector finite elements. The essential feature of vector elements is that the vector components of the electromagnetic field are projected on to a basis set (within the element) that is polarized tangential to all the surfaces of the tetrahedral shape element [41]. This ensures that tangential components of the electric and magnetic fields are continuous across the dielectric boundaries (i.e., enforcement of the constitutive relationships Eq. (2.9) and Eq. (2.10)). Due to the vector nature of the elements, the implementation of the FEM code is significantly more complex, and requires much more computational resources compared to the scalar elements. The FEM is implemented through a powerful FEM solver called COMSOL Multiphysics. COMSOL Multiphysics was chosen for its capability to easily determine the eigenmodes of a photonic crystal, but more importantly, it can solve coupled physics problems. This ability to solve coupled physics problems has been applied to steady state nonlinear applications of photonic crystals [45]-[46] in our group's previous research and it will be important for future research projects based on this research.

4.3 Two-dimensional photonic crystal eigenvalue problem

A two-dimensional photonic crystal is an optical system that has a dielectric profile periodic in the *x-y* plane and infinite along the $\hat{\mathbf{z}}$ axis (that is, uniform in the $\hat{\mathbf{z}}$ direction),

as discussed in Chapter 2. If the Bloch wave vector **k** of the eigenmode is restricted to the *x-y* plane, then the eigenvalue problem is subdivided into a TM case, defined by Eq. (2.27), and a TE case, defined by Eq. (2.28). The eigenmodes of the two cases are uniformly polarized along the $\hat{\mathbf{z}}$ axis. As a result, the vector eigenvalue problem is reduced to a scalar problem. The scalar eigenvalue problem can be further reduced by substituting the scalar Bloch modes of Eq. (2.33) and Eq. (2.30) into the eigenvalue problems of Eq. (2.27) and Eq. (2.28):

$$\Theta_{TM}\left[\varepsilon(\mathbf{r}),\mathbf{k}\right]u_{\mathbf{k}n}(\mathbf{r}) = -\frac{1}{\varepsilon(\mathbf{r})}\left(\frac{\partial^2}{\partial^2 x}+ik_x\frac{\partial}{\partial x}+ik_x\frac{\partial}{\partial x}-k_x^2+\frac{\partial^2}{\partial^2 y}+ik_x\frac{\partial}{\partial y}+ik_x\frac{\partial}{\partial y}-k_y^2\right)u_{\mathbf{k}n}(\mathbf{r}) = \frac{\omega^2}{c^2}u_{\mathbf{k}n}(\mathbf{r}); \tag{4.1}$$

$$\Theta_{TE}\left[\varepsilon(\mathbf{r}),\mathbf{k}\right]v_{\mathbf{k}n}(\mathbf{r}) = -\left(\left(\frac{\partial}{\partial x}+ik_x\right)\frac{1}{\varepsilon(\mathbf{r})}\left(\frac{\partial}{\partial x}+ik_x\right)+\left(\frac{\partial}{\partial y}+ik_y\right)\frac{1}{\varepsilon(\mathbf{r})}\left(\frac{\partial}{\partial y}+ik_y\right)\right)v_{\mathbf{k}n}(\mathbf{r}) = \frac{\omega^2}{c^2}v_{\mathbf{k}n}(\mathbf{r}). \tag{4.2}$$

Equation (4.1) and Eq. (4.2) define two new operators: $\Theta_{TM}\left[\varepsilon(\mathbf{r}),\mathbf{k}\right]$ and $\Theta_{TE}\left[\varepsilon(\mathbf{r}),\mathbf{k}\right]$. These new operators are functions of the dielectric profile and the Bloch mode wave vector **k**. As a result, they are associated directly with the same symmetry group as the Bloch mode (see Section 3.3.2). The eigenmodes of the new operators $\Theta_{TM}\left[\varepsilon(\mathbf{r}),\mathbf{k}\right]$, and $\Theta_{TE}\left[\varepsilon(\mathbf{r}),\mathbf{k}\right]$ are $u_{\mathbf{k}n}(\mathbf{r})$ and $v_{\mathbf{k}n}(\mathbf{r})$, where

$$u_{\mathbf{k}n}(\mathbf{r}+\mathbf{R}) = u_{\mathbf{k}n}(\mathbf{r}), \tag{4.3}$$

$$v_{\mathbf{k}n}(\mathbf{r}+\mathbf{R}) = v_{\mathbf{k}n}(\mathbf{r}), \tag{4.4}$$

but the eigenvalue still remains ω^2/c^2. Since the new eigenmodes have the same periodicity as the Bravais lattice, the numerical solution space is reduced to a unit cell of

the photonic crystal (as defined in Section 2.2.2), and the boundary conditions given by Eq. (4.3) and Eq. (4.4), are periodic boundary conditions. COMSOL Multiphysics can be interfaced with Matlab (a script based programming language), to parametrically study the eigenmodes. Using the parametric approach, the photonic band structure is found by solving the eigenvalue problem at discrete points on the boundary of the irreducible Brillouin zone (for various Bloch wave vectors **k**). As an example, the photonic band structure is determined for a square lattice of dielectric columns. The lattice constant is $a = 3.75\times10^{-7}\,\mathrm{m}$ and the radii of the columns are $r = 0.2a$. The dielectric permittivity of the columns are $\varepsilon_2(\mathbf{r}) = 8.9$ in an air background of $\varepsilon_1(\mathbf{r}) = 1$. The unit cell chosen arbitrarily as a square that has a quarter of a column in each corner (see Figure 13(a)) with elementary lattice vectors $\mathbf{a}_1 = a\hat{x}$ and $\mathbf{a}_2 = a\hat{y}$. In reciprocal space, the Brillouin is also a square with elementary reciprocal lattice vectors $\mathbf{b}_1 = \pi/a\,\hat{x}$ and $\mathbf{b}_2 = \pi/a\,\hat{y}$. The irreducible Brillouin zone is an equilateral triangle, where, at the vertices of the triangle, the major symmetry points in reciprocal space are identified as M, X and Γ (see Figure 13(b)).

When numerically solving the eigenvalue problem, the dielectric profile and Bloch wave vector **k** are the input parameters and a stated number eigenvalues is the output. Theoretically, there is an infinite number of eigenvalues associated with Eq. (4.1) and (4.2), but as with all aspects of numerical modeling, the eigenvalues must be limited to a finite value. To remain computationally efficient, only the first ten eigenvalues are determined. The output of the solver is the first ten eigenvalues, where each value is labeled by a band index *n*. The eigenvalues may be nondegenerate or degenerate; this is determined by the symmetry as described in Chapter 3. In Figure 13(c), the photonic band structure is plotted in normalized units of $\omega a/2\pi c$ versus $ka/2\pi$, where it is clear the eigenvalues change continuously around the irreducible Brillouin zone. For the TM case, there is a band gap between bands 1 and 2 for the range $\omega a/2\pi c = 0.325 - 0.42$. The TE case does

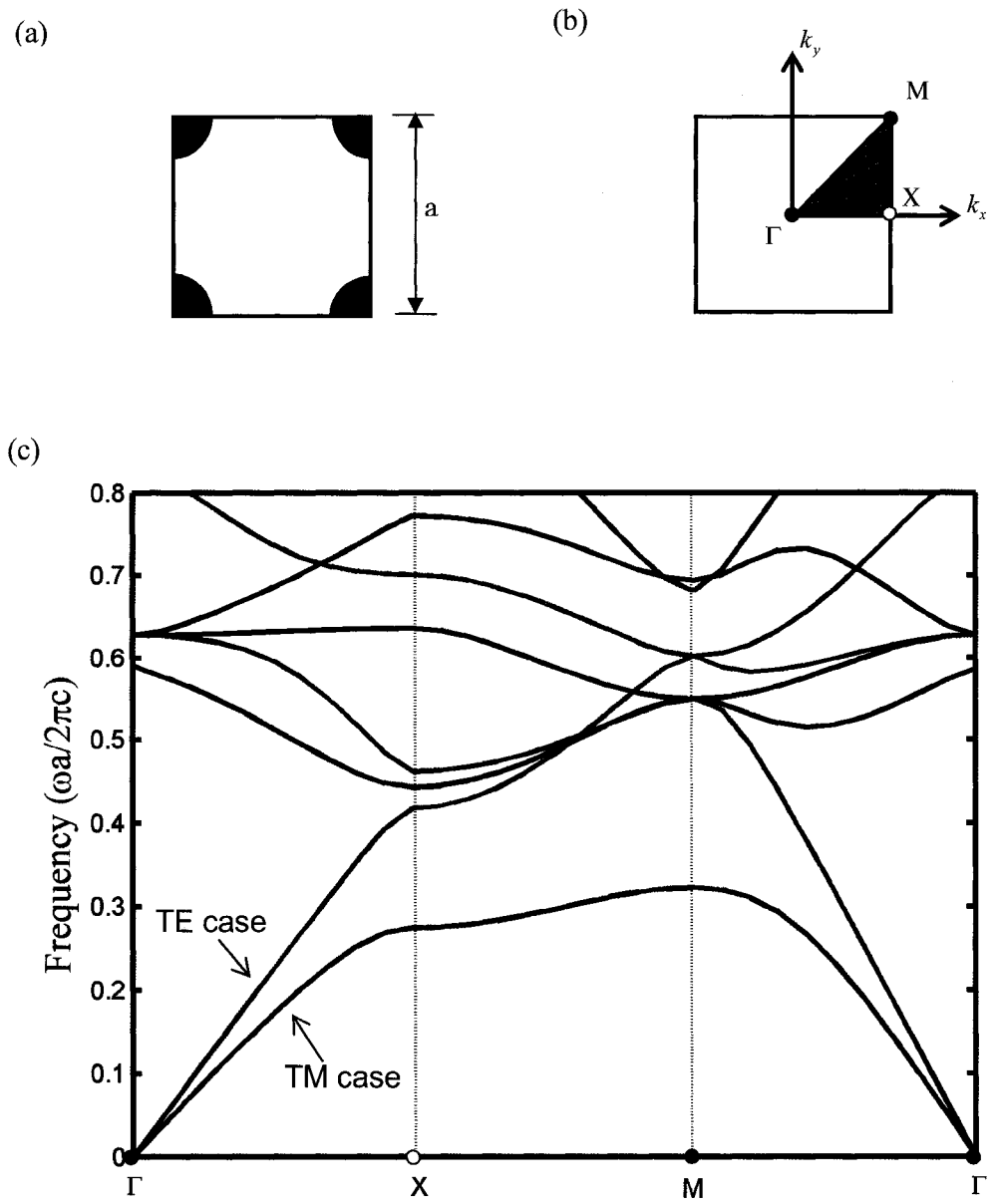

Figure 13. Dielectric columns in a square lattice: (a) unit cell, (b) first Brillouin zone, (c) photonic band structure TE bands (red) and TM bands (blue).

not have any band gaps, hence the square lattice is not considered a full band gap photonic crystal.

An alternate way to view the photonic band structure is to determine the eigenvalues for wave vectors not only on the boundary of the irreducible Brillouin zone but also inside, subsequently mapping the irreducible Brillouin zone over the full Brillouin zone. This is the dispersion surface. In Figure 14(a), we see the normalized frequency values $\omega a/2\pi c$ (vertical axis) for all the normalized Bloch wave vectors $ka/2\pi$ (horizontal plane) in first Brillouin zone for the band one TM eigenmodes. The shape is roughly a cone that is repeated in reciprocal space with the same symmetry as the dielectric profile, as predicted by the photonic crystal point group (see Section 3.3.2). In Figure 14(b), we see a similar situation of repeated frequency values within the first Brillouin zone, but for the second band TM eigenmodes.

The Bloch modes of the photonic crystal are determined by multiplying the eigenmodes of Eq. (4.3) and (4.4) by the phase factor $e^{i\mathbf{k}\cdot\mathbf{r}}$. In Figure 15(a), we see an example of an electric field TM Bloch mode in normalized units, for band 1, where $\mathbf{k} = (\hat{\mathbf{x}} + \hat{\mathbf{y}})4\pi/(5a)$; the symmetry group is $C_{1h} = \{E, \sigma_h\}$. From the electric field TM Bloch mode, the associated magnetic field can be determined using Maxwell's equations. The spatially dependent Poynting vector field is found using Eq. (2.32), and we can see in Figure 15(b) that the Poynting vector field does not necessarily flow parallel to the Bloch wave vector, as noted in Section 2.4.2.

Typical solution times, for a single Bloch wave vector simulation, are between 2.3 seconds for 970 mesh points, to 55.3 s for 15520 mesh points, where the calculations were performed on a Pentium 4 CPU 2.4 GHz computer with 2 GB of RAM. The number of mesh points chosen was 3880 because it was found that the first five eigenvalues changed 0.001% or less when the number of mesh points was increased to 15520.

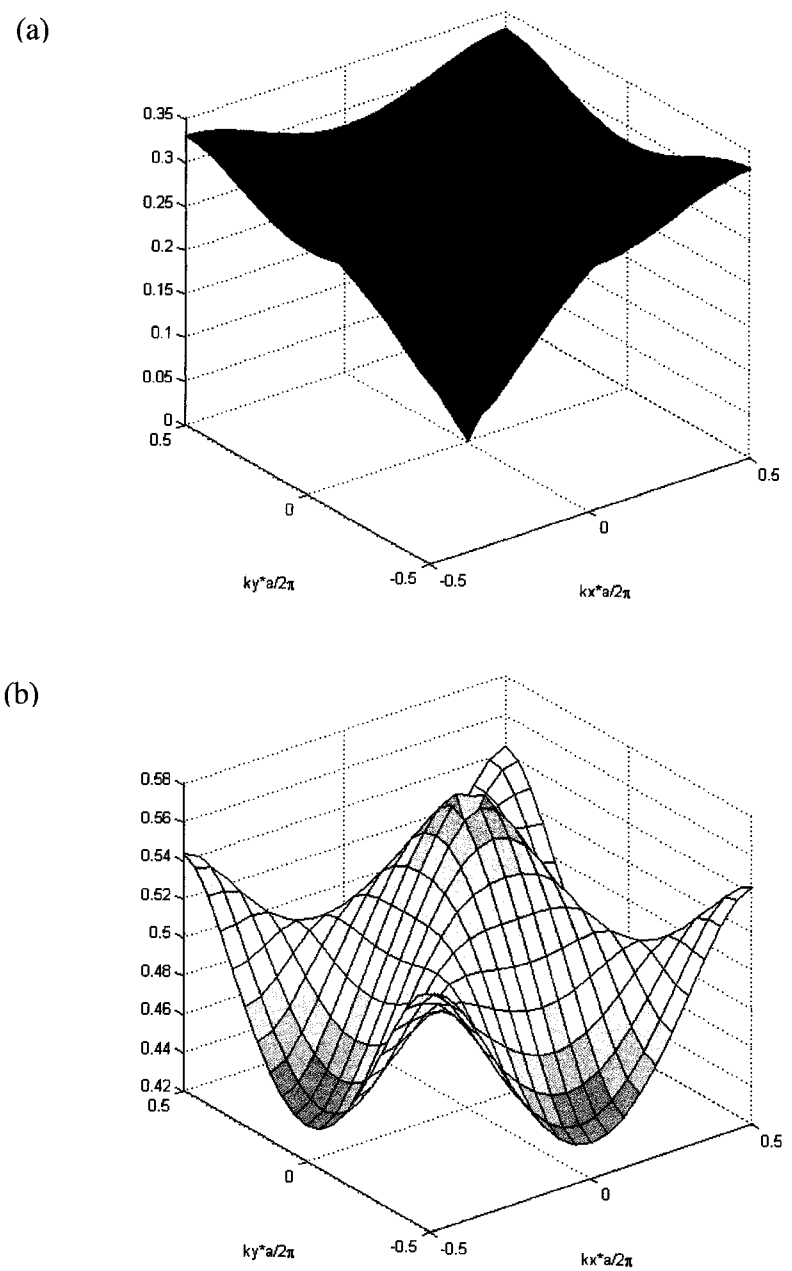

Figure 14. TM photonic band structure of dielectric columns in a square lattice plotted over the entire Brillouin zone structure, normalized frequency $\omega a/2\pi c$ (vertical axis) and Bloch wave vector $ka/2\pi$ (horizontal plane): (a) band 1, (b) band 2.

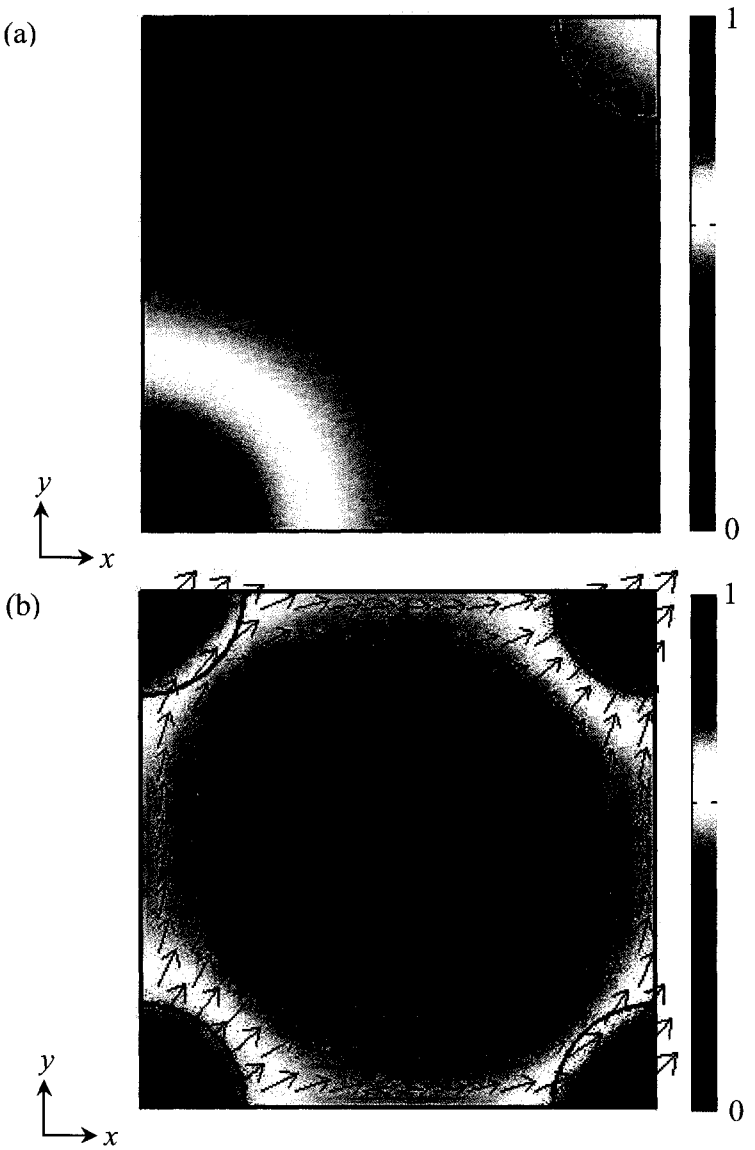

Figure 15. TM eigenmode band $n=1$, $k=0.8\pi/a(\hat{x}+\hat{y})$ (a) electric field, where $\mathbf{E}_{kn}(\mathbf{r})=E_z(\mathbf{r})\hat{z}$ and (b) Poynting vector magnitude and direction, both in normalized units. Bold lines represent the edges of the unit cell and the dielectric columns.

4.4 Photonic crystal slab eigenvalue problem

4.4.1 Introduction

In Chapter 2, the photonic crystal slab was described as an optical system that has a dielectric profile which is periodic in the *x-y* plane, but is no longer infinite along the $\hat{\mathbf{z}}$ axis (see Figure 4(b)). In the $\hat{\mathbf{z}}$ direction, light is confined to a region that is on the order of the wavelength of the light, because the slab thickness is chosen for single mode response. This region has a dielectric permittivity that is larger than the surrounding medium, where the light is index guided (see Section 2.4). If the Bloch wave vector **k** of the eigenmode is restricted to the *x-y* plane, then the eigenvalue problem is defined by Eq. (2.12) or Eq. (2.11). The eigenmodes of the photonic crystal slab are polarized in many directions; hence a full vector solution is required. In contrast to the two-dimensional photonic crystal eigenvalue problem, there is no rigorous method to reduce the full vector problem to a scalar one. Nevertheless, we can use an approximate scalar technique to determine the photonic band structure of a photonic crystal slab. This technique is called the effective index method, which has been used by many authors [34], [43], [92], [94], [95] and [108]. In the following sections, we examine the implementation of the full vector eigenvalue problem, but first we present an improved, self-consistent, effective index method. This self-consistent effective index method dramatically increases the accuracy of the traditional effective index method for high dielectric contrast photonic crystals, as noted by full vector solutions.

4.4.2 Self-consistent effective index method

All effective index methods approximate the photonic band structure of a photonic crystal slab by solving the two-dimensional photonic crystal eigenvalue problem, with the dielectric permittivity (index) of the background medium being replaced by an effective dielectric permittivity of the guided modes of an unperturbed dielectric slab. The frequency dependent effective dielectric permittivity of the dielectric slab eigenmode is given by

$$\varepsilon_{eff}(\omega) = (n_{eff})^2 = (k_x(\omega)c/\omega)^2, \tag{4.5}$$

where ω is the frequency and $k_x(\omega)$ is the wave vector of Eq. (2.42), explicitly as a function of frequency. The validity of the effective index method rests on two criteria: First, that the dielectric slab eigenmodes are a suitable basis functions to expand photonic crystal slab eigenmodes (see Section 2.5). Second, that the photonic crystal slab eigenmodes in the *x*-*y* plane bisecting the photonic crystal slab $(x, y, 0)$ are identical to the electric and the magnetic fields of the two-dimensional photonic crystal eigenmodes:

$$\mathbf{E}_{\mathbf{k}n}^{(PCslab)}(x, y, 0) = \mathbf{E}_{\mathbf{k}n}^{(2DPC)}(\mathbf{r}), \tag{4.6}$$

$$\mathbf{H}_{\mathbf{k}n}^{(PCslab)}(x, y, 0) = \mathbf{H}_{\mathbf{k}n}^{(2DPC)}(\mathbf{r}), \tag{4.7}$$

where the eigenmodes compared have the same Bloch wave vector **k** [34] (see example in Section 5.4). As a consequence of its basic premise, the effective index method is only valid in the single mode region of the dielectric slab eigenmodes [34]. Outside of the single mode region of the dielectric slab eigenmodes, the effective dielectric permittivity of the photonic crystal slab eigenmodes would need to be approximated by dielectric slab eigenmodes with multiple effective dielectric permittivities (similar to the vanishing dielectric contrast eigenmodes discussed in Section 2.5.3). The basic premise of substituting an effective dielectric permittivity into the two-dimensional photonic crystal eigenvalue problem clearly cannot treat multiple effective dielectric permittivities.

To implement the effective index method, the dispersion relationship ($\varepsilon_{eff}(\omega)$ vs. ω) of the unperturbed dielectric slab (i.e., of a solid slab formed from the same base material) is calculated using a simple numerical root-finding technique (see [97] pp. 19-22), where the frequency ω of the dielectric slab eigenmode is the input parameter and the frequency dependent effective index $\varepsilon_{eff}(\omega)$ is the output as defined by Eq. (4.5). This is different from the vanishing dielectric contrast approximation, where we found the

dispersion relationship for a dielectric slab with the average dielectric permittivity of the photonic crystal slab, and then folded the bands into the first Brillouin zone. In general, the effective dielectric permittivity determined by the dispersion relationship will be a range of values bounded at the upper limit by the dielectric permittivity of the dielectric slab and at the lower limit by the dielectric permittivity of the surrounding medium (i.e. $\varepsilon_{sur} \leq \varepsilon_{eff}(\omega) \leq \varepsilon_{slab}$) ([97], pp. 16-19).

The challenge when applying an effective index method is that $\varepsilon_{eff}(\omega)$ must be chosen before one can solve the two-dimensional photonic crystal eigenvalue problem, but we do not know the correct ω until afterwards. Previous research solved this issue by assigning an average value to the dielectric permittivity of the base two-dimensional photonic crystal medium. We will refer to this method as the average effective index method. For low dielectric contrast photonic crystals, the two-dimensional photonic crystal eigenvalues calculated with an average effective dielectric permittivity are very good approximations to the eigenvalues of a full vector solution, even over extended frequency ranges encompassing many frequency bands [34]. For the effective index method, low dielectric contrast refers to the surrounding medium (i.e. substrate and superstrate). Low dielectric contrast does not refer to the two materials comprising the two-dimensional photonic crystal (as is the case for the vanishing dielectric contrast approximation). A large dielectric permittivity difference between the base medium (effective medium) of the photonic crystal and the second material, such as air holes, is perfectly acceptable when using the effective index method. This means characteristic features of the photonic crystals such as photonic band gaps can be studied. It is for this reason that the effective index method is far superior approximation to the vanishing dielectric contrast approximation (see Section 2.5.3) when accurate photonic band structures are sought. However, as the dielectric contrast is increased, the range of effective index values also is increased. Therefore, an average effective dielectric permittivity does not suffice. The difference between the two-dimensional eigenvalues calculated with the average effective index method and the eigenvalues of the full vector solution becomes much greater. In

this case, the average effective index method is only a good approximation over a very small frequency range [34]. To increase the accuracy of the effective index method, we are proposing a self-consistent effective index method. The self-consistent effective index method is able to match the frequency dependent effective dielectric permittivity $\varepsilon_{eff}(\omega)$ to the proper photonic crystal eigenmode frequency ω.

The self-consistent effective index method is implemented as follows: To start, the two-dimensional photonic crystal eigenvalue problem is solved using an average effective dielectric permittivity, where we obtain the eigenmode frequency ω_1. This frequency value then is used to determine a frequency dependent effective dielectric permittivity $\varepsilon_{eff}(\omega_1)$; $\varepsilon_{eff}(\omega_1)$ is used to solve the two-dimensional photonic crystal eigenvalue problem again; a new frequency value ω_2 is obtained and again used to determine a new frequency dependent effective dielectric permittivity $\varepsilon_{eff}(\omega_2)$; this loop continues until $\varepsilon_{eff}(\omega_{i+1}) - \varepsilon_{eff}(\omega_i) \le error$ ($error$ is an input parameter), where the algorithm is performed for each value of Bloch wave vector **k** and separately for each frequency band n.

To demonstrate the improved performance of the self-consistent effective index method over that of the average effective index method, we compare the eigenvalues (frequencies) of both methods to the eigenvalues (frequencies) of the full vector solution. The system we choose to simulate is a hexagonal photonic crystal slab from the Γ point to the K point in reciprocal space (see Figure 16). The photonic crystal slab has a lattice constant of $a = 3.75\times10^{-7}\,\mathrm{m}$, where there are air holes of radii $r = 0.25a$ in a dielectric slab with a thickness of $d = 0.5a$ and a base dielectric permittivity of $\varepsilon_2 = 11.56$ (GaAs). The photonic crystal slab is surrounded by air on all sides. The normalized single mode TE cutoff frequency of the dielectric slab is $\omega_{TEcutoff} = \omega a/2\pi c = 0.384$. The frequency dependent effective dielectric permittivity is equal to $1 \le \varepsilon_{eff}(\omega) \le 7.84$ in the frequency

range $0 \leq \omega \leq \omega_{TEcutoff}$. In Figure 16(c), we see the photonic band structure calculated using the three different methods: the average effective index method (red lines), the self-consistent effective index method (blue line with an $error = 0.0001$), and the full vector solution (black circles, where the full vector solution will be described in the next section). Over the entire range of Bloch wave vectors, from Γ to K, and for all three frequency bands, the self-consistent effective index method shows a much better agreement with the vector solution than the average effective index method, where the most pronounced improvement is in the higher frequency second and third bands. We found that, in the case of the photonic band structure determined using the average effective index method, the narrow frequency region, where the accuracy of the eigenvalue determination is good, varies in location depending on the average effective dielectric permittivity chosen. Although, without comparing to the full vector solutions, there is no way to determine which frequency range is a good approximation to the full vector solutions. This is one of the main issues of implementing the average effective index method that we address with the self-consistent effective index method. For this example, we chose an average effective dielectric permittivity of $\varepsilon_{eff} = 6.00$, which matches the frequency of a photonic crystal eigenmode close to the band edge (see the crossing point of the red and blue first bands in Figure 16(c)). The self-consistent effective index method provides the best possible fit to the vector solution achievable by an effective index method, because the dispersion of the base material is accounted for within the calculation, which is applicable for every point in the photonic band structure simultaneously (below the single mode cutoff frequency). Another deficiency in the photonic band structure determined using an average effective index method is that it is just a scaled version of the two-dimensional photonic crystal photonic band structure. Many authors have shown that the actual photonic band structures of photonic crystal slabs significantly differ from their analogous two-photonic crystal photonic band structures [101]. By contrast, the self-consistent effective index method is able to overcome the two-dimensional photonic crystal bias in the average effective index treatment more faithfully describing the true photonic band structure.

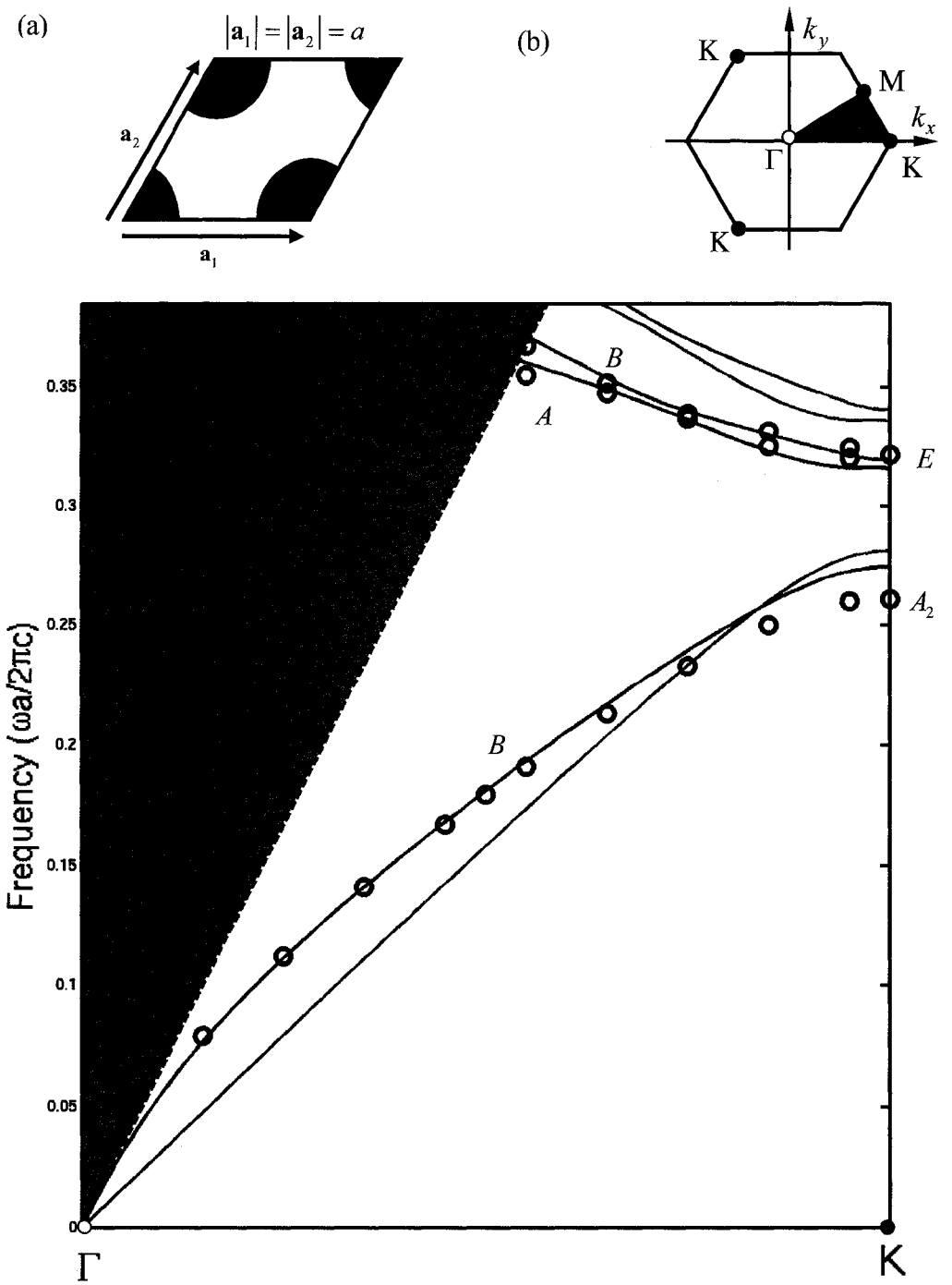

Figure 16. Hexagonal slab photonic crystal (a) unit cell, and elementary lattice vectors, in Cartesian space; (b) Brillouin zone (black) in reciprocal space; (c) photonic band structure for first three bands between Γ and K point in the irreducible Brillouin zone, the average effective index method (red), the self-consistent effective index method (blue) and the full vector solution (black circles). The axes are in normalized frequency $\omega a/2\pi c$ and normalized wave vector $ka/2\pi$. Irreducible labels are for the electric field.

Photonic band structures determined using effective index methods have the largest relative errors, as compared to the full vector solution, close to the edge of the Brillouin zone (K point), because they are based on an averaging approximation. Close to the edge of the Brillouin zone, the wavelength of the light is on the order of the lattice vectors and thus interference effects play a dominant role. When the error parameter of the self-consistent effective index method was reduced to $error = 0.0001$, the calculated eigenvalues have the greatest relative error as compared to full vector eigenvalues at the K point, where it is 5% for band 1, 2% for band 2, and 0.7% for band 3. These relative error values remained consistent to within one significant digit as the error parameter was varied between $0.0001 \le error \le 0.1$. What does change as the error parameter varies is the accuracy of the self-consistent effective index method at known degenerate eigenvalues, such as the doubly degenerate bands 2 and 3 at the edge of the Brillouin zone (K point). The two photonic crystal slab eigenmodes at the K point are associated with the two-dimensional E irreducible representation of the C_{3v} point group (see Figure 6(b)). As the self-consistent error parameter is reduced, the two different eigenvalues of band 2 and 3 converge to the degenerate full vector eigenvalue. The photonic band structure determined with an average effective index method can be made to match these relative error values for band 1 or for band 2, 3 depending on the average effective dielectric permittivity chosen. Independent of the type of effective index method, the light cone of the dielectric slab accurately predicts the region in reciprocal space where the full vector photonic crystal slab eigenmodes become unbounded (i.e., the eigenmode is not guided by the photonic crystal slab). The light cone is determined by dispersion relationship of the surrounding medium, in this case air (i.e., $\omega_{LC}(\mathbf{k}) = c\sqrt{\mathbf{k}\cdot\mathbf{k}}$)

Although we can obtain significantly better accuracy with the self-consistent effective index method, the downside is much longer computational times, because we are calculating each photonic crystal eigenvalue multiple times. The self-consistent effective index method must be calculated for each frequency band separately, whereas the average effective index method and the full vector method determine all the eigenvalues

at once for each Bloch wave vector **k**. The number of iterations before the self-consistent effective index method converges depends on the error parameter. In the case of the hexagonal photonic crystal slab, the smallest error parameter tested was $error = 0.0001$, where the self-consistent method converged on average in 9 iterations, with a maximum of 11 iterations. For the largest error parameter tested $error = 0.1$, the self-consistent method converged on average in 3 iterations, with a maximum of 4 iterations. For our given example, these values will be multiplied by three, one for each of the three bands. Regardless, these increased computational times are still much less than the full vector calculations, and they can be performed on an ordinary desktop computer (the full vector solutions require a much more powerful system; see Section 4.4.3). To obtain eigenvalues for the first three frequency bands, a typical full vector calculation takes about 330 seconds and the average effective index method take about 2 seconds. Obtaining the same frequency bands using the self-consistent effective index method on the same computer takes 55 seconds on average, when $error = 0.0001$ and 19 seconds on average, when $error = 0.1$ (where the computational time of the FEM dominates the run time of each iteration). This result is approximately 5.9 to 17.4 times faster using the self-consistent effective index method over the full vector solution, depending on the error parameter chosen.

In conclusion, the presented self-consistent effective index method is a significant improvement over the average effective index method. The self-consistent effective index method demonstrates the best possible accuracy for any solutions based on an effective dielectric permittivity, regardless of the dielectric contrast of the photonic crystal slab. Furthermore, the self-consistent effective index method is able to capture the differences in the photonic band structure when one is comparing two-dimensional photonic crystals and photonic crystal slabs. The average effective index method is unable to model these differences between the two-dimensional photonic crystals and photonic crystal slabs. Finally, these improvements to the effective index method are obtained with a moderate increase in computational complexity as compared to the solutions of the average effective index method.

4.4.3 Full vector eigenvalue problem

The most accurate method to determine the eigenvalues and eigenmodes of a photonic crystal slab is to solve the full vector eigenvalue problem given by Eq. (2.11) or Eq. (2.12), where both equations give the same electric and magnetic fields. In the case of a full vector solution to the photonic crystal slab eigenvalue problem, it is not possible to reduce the vector problem to a scalar problem, as in the case of the two-dimensional photonic crystal eigenvalue problem. However, the photonic crystal slab is periodic in the *x-y* plane and has the form of a Bloch mode in these directions (see Section 2.5). Due to the periodicity of the Bloch mode, we can reduce the solution space in the *x-y* plane to a two-dimensional primitive unit cell, similar to the two-dimensional photonic crystal eigenvalue problem (see Section 4.3). The boundary conditions applied to the edges of the primitive unit cell due to the periodicity are:

$$\mathbf{E}_{kn}(\mathbf{r}+\mathbf{R}) = e^{i\mathbf{k}\cdot\mathbf{R}}\mathbf{E}_{kn}(\mathbf{r}), \tag{4.8}$$

$$\mathbf{H}_{kn}(\mathbf{r}+\mathbf{R}) = e^{i\mathbf{k}\cdot\mathbf{R}}\mathbf{H}_{kn}(\mathbf{r}). \tag{4.9}$$

The walls of the two-dimensional primitive unit cell are the boundaries of the solution space parallel to the $\hat{\mathbf{z}}$ axis. Equation (4.8) and Eq. (4.9) are Floquet-periodic boundary conditions and they are a direct result of the periodicity of the Bloch modes, given in Eq. (2.20). Along the $\hat{\mathbf{z}}$ axis, the photonic crystal slab eigenfunctions are mostly confined within the photonic crystal slab and decay exponentially outside of this region (see Section 2.5.3). Theoretically, to model the exponential decay, the solution space should extend to infinity along the positive and negative the $\hat{\mathbf{z}}$ axis. However, the magnitude of the photonic crystal slab eigenmode becomes very small a short distance outside of the photonic crystal slab, which allows us to truncate the solution space without any significant loss of accuracy. The boundary conditions on the planes perpendicular to the $\hat{\mathbf{z}}$ axis are set to perfect electrical conductors $\mathbf{n}\times\mathbf{E}(\mathbf{r})=0$, where $\mathbf{n}$ is a unit vector normal to the plane. The truncation of the solution space is done by inspection, where the height is varied until the photonic crystal eigenvalues no longer change significantly.

Since this is a three-dimensional problem, it is computationally intensive, so a non-uniform mesh is used to reduce the run times. The mesh is densest inside the photonic crystal slab, where the electromagnetic field varies the most, and decreases moving away from this region. Furthermore, on the boundaries of the solution space, the mesh pattern is copied from one surface and an image of the mesh pattern is placed on the opposite surface. This helps the program enforce the Floquet-periodic boundary conditions, which reduces the eigenmode error. As mentioned in the Section 4.2, vector finite elements are used to model the photonic crystal slab eigenvalue problem. As a consequence of the vector finite elements, false eigenmodes may be obtained. Reduction in the number of false eigenmodes is achieved by presenting a good guess to the FEM solver. This guess value is typically the eigenvalue obtained from the photonic band structure calculated using the vanishing dielectric contrast limit approximation (see Section 2.5.3), or for more accuracy, the eigenmode obtained from the effective index method (see Section 4.4.2). Moreover, to identify the real eigenmodes, we must determine that its spatial symmetry is correct, and that the eigenvalue is reasonable when compared to the approximate methods. The identification of physical photonic crystal slab eigenmodes is one of the important reasons for studying their approximate solutions and their symmetry transformation properties. As an example, we calculate the magnetic field, electric field and the Poynting vector for a hexagonal photonic crystal slab eigenmode with the same parameters as described in the previous section, for the first band, and with a Bloch wave vector $\mathbf{k} = \hat{\mathbf{x}} 4\pi/(5a)$. In Figure 17 to Figure 19, we see the three-dimensional view of the magnetic field, electric field and Poynting vector respectively, where the arrows represent the field vectors and the magnitude is proportional to length. The magnitudes of the fields are also given by the background colour in normalized units. The field vectors are shown in the *x*-*y* planes at the middle of the slab $z = 0$, and at the bottom of the photonic crystal slab $z = -a/4$. There is a third plane (*y*-*z* plane at $z = 0$) that shows the vertical dependence of the magnitude along the $\hat{\mathbf{z}}$ axis. The bold black lines represent the edges of the photonic crystal slab primitive unit cell and the location of the air hole. The magnetic field vectors are parallel to the *x*-*y* plane at $z = 0$ and the electric field

vectors are parallel to the $\hat{\mathbf{z}}$ axis at $z = 0$, which means the photonic crystal eigenmode is a quasi-TM mode. This eigenmode is only a quasi-TM mode because the electric field vectors are no longer parallel to the $\hat{\mathbf{z}}$ axis away from the $z = 0$ plane (see $z = -a/4$ plane in Figure 18). The Poynting vector is always parallel to the x-y plane within the photonic crystal slab (see $z = 0$ plane and $z = -a/4$ plane in Figure 19). In Figure 20(a), we can see the top view of the Poynting vector in the $z = 0$ plane, where it is clear the direction of energy transport is spatially dependent. Moreover, the Poynting vector field is only average parallel to its Bloch wave vector $\mathbf{k} = \hat{\mathbf{x}} 4\pi/(5a)$, similar to the two-dimensional photonic crystal eigenmodes. In Figure 20(b), we can see a cross section of the Poynting vector magnitude along a plane that cuts the air hole, where it is clear the Poynting vector is at a maximum inside the air hole and disappears very quickly outside of the photonic crystal slab (the edge of the photonic crystal slab is the bold black line). The fact that the Poynting vector is mostly confined within the photonic crystal slab is one of the primary indicators that it is a physical photonic crystal slab eigenmode in addition to the identification of the quasi-TM characteristics of the electric fields and the magnetic fields.

The full vector calculations were performed on an IBM server with 24 GB of RAM and two Xeon quad 2.6 GHz processors, because memory requirements are significant, beyond conventional desktop systems. To determine six physical eigenvalues at a particular Bloch wave vector **k**, the solution time was on average 5.5 minutes (328.2 seconds) when the mesh contained 11067 elements (89148 degrees of freedom). In comparison, the two-dimensional photonic crystal eigenvalue problem on the same computer system would take about 2 seconds. There were several mesh densities tried and it was found that 11067 elements provided the right balance between accuracy and computation time.

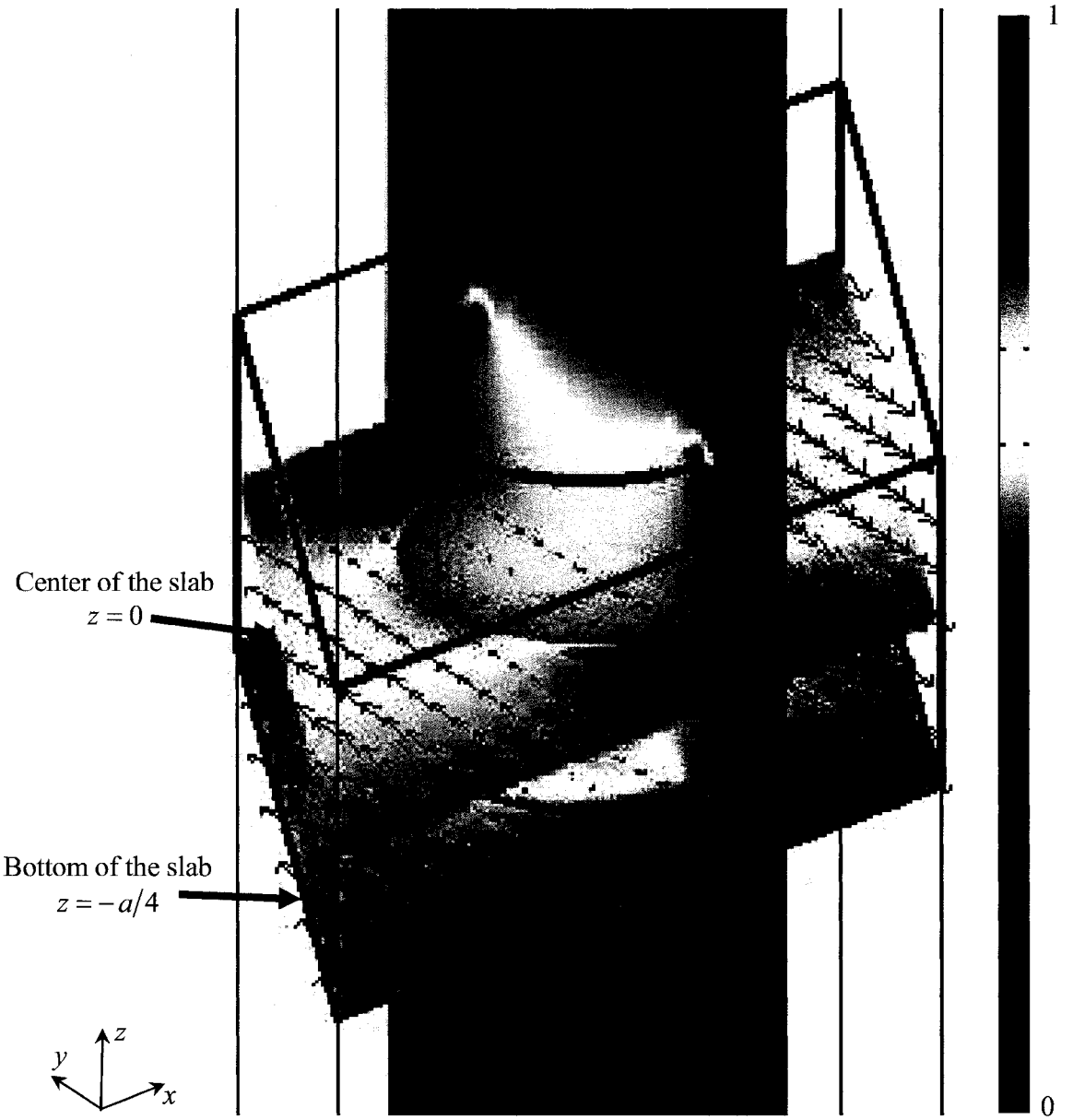

Figure 17. Hexagonal photonic crystal slab lattice air holes in dielectric background Bloch mode, band 1, $\mathbf{k} = \hat{\mathbf{x}}\,4\pi/(5a)$ magnetic field magnitude and direction (arrows) three-dimensional view. Bold lines represent the edges of the photonic crystal slab unit cell.

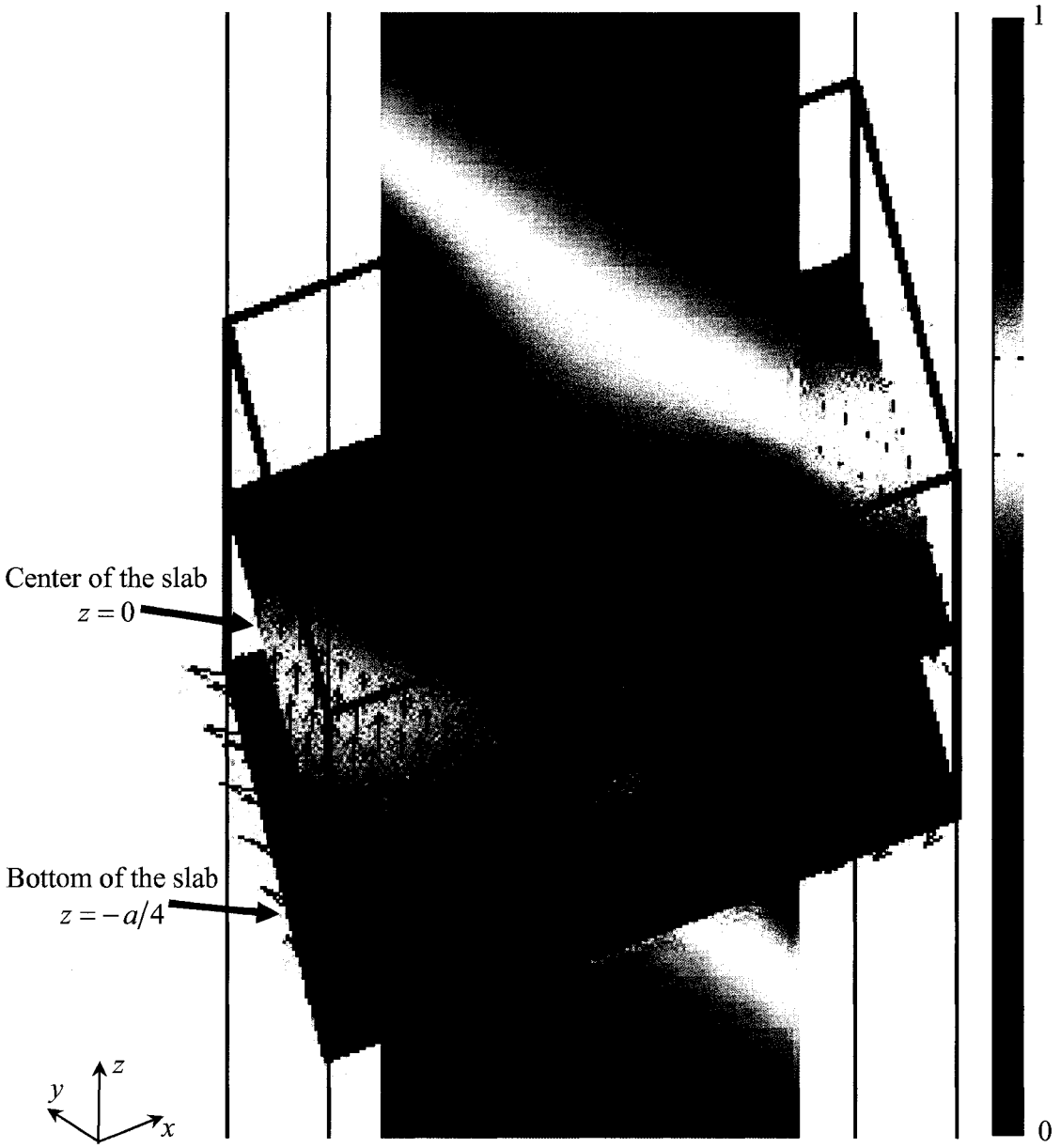

Figure 18. Hexagonal photonic crystal slab lattice air holes in dielectric background Bloch mode, band 1, $\mathbf{k} = \hat{\mathbf{x}}\, 4\pi/(5a)$ electric field magnitude and direction (arrows) three-dimensional view. Bold lines represent the edges of the photonic crystal slab unit cell.

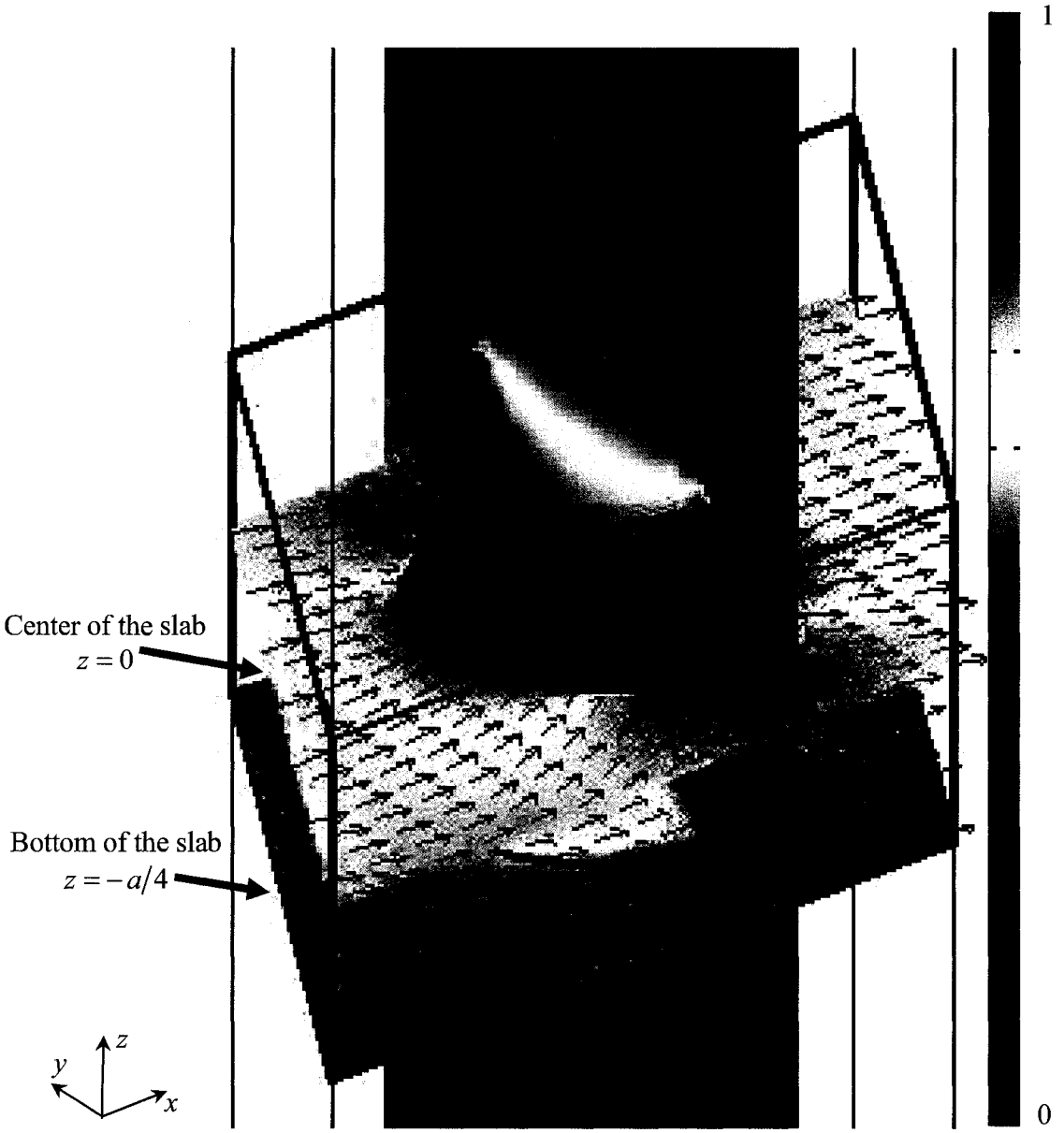

Figure 19. Hexagonal photonic crystal slab lattice air holes in dielectric background Bloch mode, band 1, $\mathbf{k} = \hat{\mathbf{x}}\, 4\pi/(5a)$ Poynting vector magnitude and direction (arrows) three-dimensional view. Bold lines represent the edges of the photonic crystal slab unit cell.

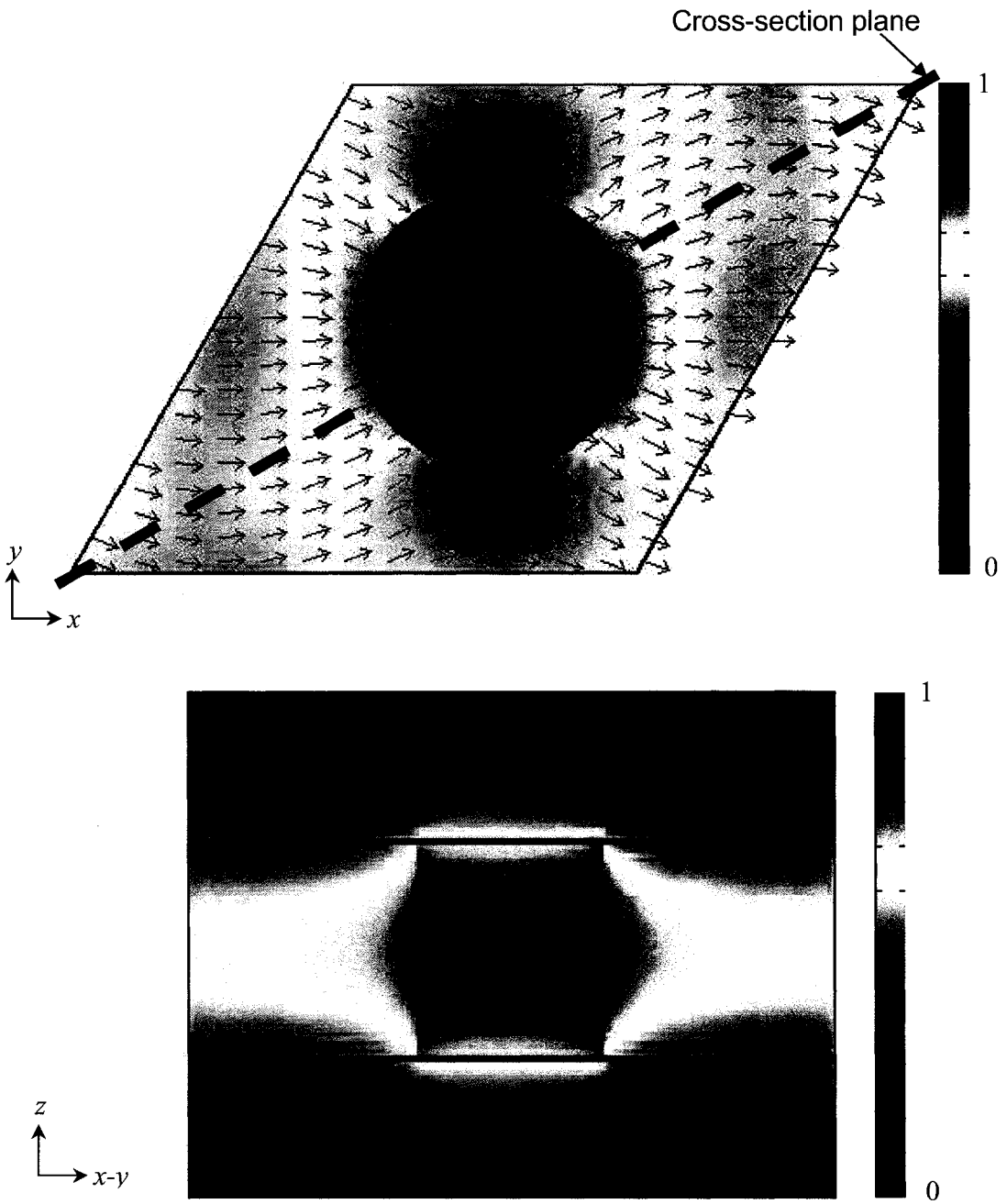

Figure 20. Hexagonal photonic crystal slab lattice air holes in dielectric background Bloch mode, band 1, $\mathbf{k} = \hat{\mathbf{x}}\, 4\pi/(5a)$ Poynting vector magnitude and direction (arrows) (a) top view x-y plane at $z = 0$, (b) cross section view (along dashed line in part (a)). Bold lines represent the edges of the photonic crystal slab unit cell.

CHAPTER 5 – SYMMETRY CONSTRAINTS AND THE EXISTENCE OF BLOCH MODE VORTICES IN LINEAR PHOTONIC CRYSTALS

5.1 Introduction

Akin to flow vortices in the more familiar mass transport systems, the defining feature of an optical vortex is the circulation of the flux about a singular point. This singular point, while a zero in the optical intensity, is also the terminus of a dislocation in the phase of the optical field [77]. Unambiguous definition of the local phase is achieved through the relation between real and imaginary parts of a complex field description. The phase behavior in the vicinity of the singularity quantifies the system vorticity, which is necessarily related to the angular momentum of the optical mode [56], and thus a primary motivator for research into such states [78]-[79]. The vorticity υ is an integer quantity arising from a contour integration for the change in phase $d\vartheta$ around the singularity [77], as

$$\oint d\vartheta = 2\pi\upsilon . \tag{5.1}$$

In this chapter, we report the existence of modal phase singularities within photonic crystals, whereby we present a general analytic methodology of predictive power based on group theoretic principles and plane wave interference in the limit of vanishing dielectric contrast. We have validated this approach by numerical simulation at higher dielectric contrasts, exploiting the finite element method to generate the Bloch mode and phase distributions for photonic crystals of various symmetries. Both approaches agree, showing modal phase singularities associated with the classical flux vortices revealed by Poynting's vector maps of optical intensity within the photonic crystal's unit cell.

To our knowledge, this is the first report describing phase singularities within the Bloch modes of linear photonic crystals [55]. Flux vortices were earlier noted in photonic crystal defect state (waveguiding) systems [47]-[48], but were neither identified as phase singularities nor further studied. Photonic crystals have been mentioned as a potential source of vortex arrays, but the discussion focused only on the angular momentum for a system of rectangular symmetry [56]. Phase singularities have recently been identified in other systems of discrete rotational symmetry, such as finite optical lattices and photonic crystal fibers [80]-[83]. These are all systems where the net flow of optical energy parallels the nodal line, as originally noted in the now-familiar Laguerre-Gaussian beam illustration [84], and they are known as pure screw phase dislocations ([85] p.98). By contrast, phase singularities in linear photonic crystals need not, in general, form nodal lines, nor are the energy circulation and phase variation constrained to planes normal to the mean transport direction. In particular, for purely two-dimensional (2D) photonic crystals, where the spatial dependence of the optical mode is invariant along the direction of continuous translational symmetry, the resulting nodal lines are purely orthogonal (not parallel) to the mean energy flow direction. This is known as a pure edge type phase dislocation ([85] p.99).

Here, we examine optical vortices within two-dimensional photonic crystals, because the symmetry classes of two-dimensional photonic crystals and photonic crystal slabs are easy to visualize, and the analytic and numerical treatments comprehensive. We establish the basic principles of vortex formation by exploring several cases of pure two-dimensional photonic crystals, and then finally conclude by examining a particular case of the photonic crystal slab to determine the effect of light confinement in the $\hat{\mathbf{z}}$ axis. The extension to three dimensional photonic crystals, while tedious, is straightforward. The existence of phase singularities in photonic crystals is predicated on general symmetry principles involving specifically the photonic crystal eigenmode point group (**k**-group see Section 3.3.2). By merging group theory with a phasor representation of interfering plane waves, in the limit of vanishing dielectric contrast (see Chapters 2 and 3), we find that their locations in real and reciprocal space may be determined. By

examining the geometry and symmetry of the summation of degenerate plane waves, we can determine which modes fundamentally contain phase singularities. Since our phase singularities are associated with a complex field, the geometry of this sum is most easily examined in phasor notation. Two distinct singularity classes are identified: *(i)* symmetry singularities, which appear at locations in reciprocal space of high symmetry, and *(ii)* accidental singularities, which appear at locations in the band diagram where there is accidental mixing of modes from adjacent bands. The former may be predicted solely via group theoretic principles; by contrast, the latter can only be determined by an eigenmode decomposition technique such as the phasor representation of interfering plane waves.

5.2 Analytic description of phase singularities

We represent the relevant optical modes as complex quantities, for example, the magnetic component of the TE eigenmode of a two-dimensional photonic crystal can be separated in real and imaginary parts given by

$$\mathbf{H}_{kn}(\mathbf{r}) = \hat{\mathbf{z}} H_z(\mathbf{r}) = \hat{\mathbf{z}}\left(P_z(\mathbf{r}) + iQ_z(\mathbf{r})\right), \tag{5.2}$$

where $P_z(\mathbf{r})$ is the spatial dependent real part and $Q_z(\mathbf{r})$ is the spatial dependent imaginary part of the magnetic field. In phasor notation, Eq. (5.2) can be rewritten as

$$\mathbf{H}_{kn}(\mathbf{r}) = \hat{\mathbf{z}}\left(P_z(\mathbf{r}) + iQ_z(\mathbf{r})\right) = \hat{\mathbf{z}} F(\mathbf{r}) e^{i\vartheta(\mathbf{r})}, \tag{5.3}$$

where $F(\mathbf{r}) = \sqrt{P_z^2(\mathbf{r}) + Q_z^2(\mathbf{r})}$ the field magnitude and the modal phase $\vartheta(\mathbf{r})$ is defined as

$$\vartheta(\mathbf{r}) = \arctan\left[Q_z(\mathbf{r})/P_z(\mathbf{r})\right]. \tag{5.4}$$

The modal phase $\vartheta(\mathbf{r})$ becomes undefined, and hence singular at points in the field when $P_z(\mathbf{r}_0)=Q_z(\mathbf{r}_0)=0$. In Figure 21, we see an example of the modal phase $\vartheta(\mathbf{r})$ of the magnetic field, given by

$$\mathbf{H}_{kn}(\mathbf{r})=\hat{\mathbf{z}}(x+iy), \tag{5.5}$$

where the phase goes from π to $-\pi$ (note this field is not of a particular system, but chosen as a simple example). There is a phase dislocation as noted in Figure 21, which terminates on the singularity at the origin, $(x,y)=(0,0)$. The vorticity of this singular point is $\upsilon=1$ as defined by the contour integral Eq. (5.1).

In this chapter, we employ modal decomposition into the dominant components of a plane wave basis set in the vanishing dielectric contrast limit to determine an analytic form for the eigenmodes, where the focus is on the TE eigenmodes of a two-dimensional photonic crystal and the TE eigenmodes of a photonic crystal slab (see Section 2.4.2 and Section 2.5.3). The base form of the two-dimensional photonic crystal eigenmodes is given by Eq. (2.30), and for the photonic crystal slab, by Eq. (2.51). The coefficients of the base forms are determined using the projection operator method outlined in Section 3.4.4. The analytic forms of the eigenmodes are analyzed using phasor geometry to illustrate how two distinct types of singularities arise for various symmetry classes of 2D photonic crystals.

Our analytic approach is indebted to earlier contributions [81]-[82]. These groups studied optical vortices analytically by examining interfering plane waves in free space systems, in which they established the required plane wave geometry for the formation of optical vortices. It is these same criteria we use for this study of optical vortices within photonic crystals, where the criteria are described in the following. Vortex locations may be determined by finding the spatial locations where the complex field vanishes.

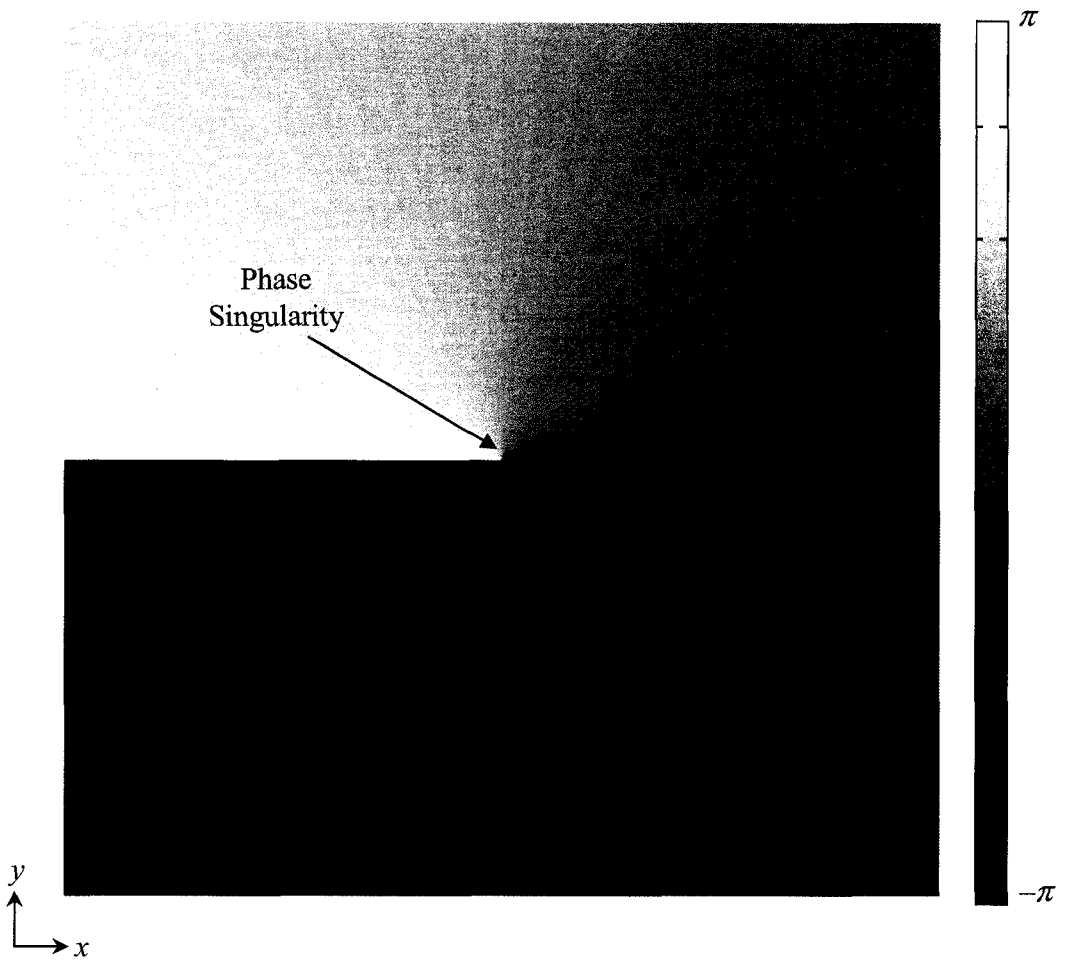

Figure 21. Modal phase $\vartheta(\mathbf{r})$ of a magnetic field, given by $\mathbf{H}_{kn}(\mathbf{r}) = \hat{\mathbf{z}}(x+iy)$, with a phase singularity at the origin, $(x, y) = (0,0)$.

We express the TE eigenmode of a two-dimensional photonic crystal (Eq. (2.34)) as a linear combination of plane waves in phasor form as

$$\mathbf{H}_{kn}(\mathbf{r}) = \hat{\mathbf{z}} \sum_{\mathbf{G}} H_{kn}(\mathbf{G}) e^{i(\mathbf{k}+\mathbf{G})\cdot\mathbf{r}} = \hat{\mathbf{z}} \sum_{s}^{S} F_s e^{i\theta_s(\mathbf{r})}, \tag{5.6}$$

where $H_{kn}(\mathbf{G})$ is a complex coefficient for the plane wave; F_s is the magnitude of the s^{th} plane wave, and $\theta_s(\mathbf{r})$ is its spatially dependent phase in complex notation. Note that a plane wave in complex notation has a magnitude F_s that is not spatial dependent. Adding the phasors vectorially, if they form a closed path at any point, the complex field vanishes. The existence of phase vortices thus requires

$$F_S \leq F_1 + F_2 + \ldots + F_{S-1}. \tag{5.7}$$

Consequently, there must be three or more plane waves to form a phase singularity. If there are less than three, it can be shown that the overall phase is constant along contours that are infinitely long; therefore dislocations in a phase contour cannot be formed, which is characteristic of a phase singularity [81]. Closed-form determination of the existence and location of phase singularities requires mapping system symmetries to the band structure using group theory, where phasor analysis of the Bloch mode generated by a tractable plane wave expansion spatially locates the singularity. In Section 5.3, we show this for the vanishing contrast case of the two-dimensional photonic crystal, which limits the plane waves to only those apparently required by the system symmetries. Numerical treatment, and a discussion of higher contrast systems, is found in Section 5.3.2. Finally, in Section 5.4, we examine the phase singularities in the eigenmodes of photonic crystal slabs.

5.3 Two-dimensional photonic crystals

5.3.1 Symmetry and the vortex state

We describe below an investigation of all permissible C_{nv} point groups of the TE eigenmodes of two-dimensional photonic crystals, specifically the odd and even rotational symmetries, focusing simply on how one determines vortex location. In Section 5.3.2, we demonstrate explicitly that the singularities thus identified are indeed optical vortices via the behavior of phase and local Poynting vector flux distributions. Since the choice of **k** sets the point group (see Section 3.3.2), we consider the various symmetries for both the hexagonal and square lattices. Consider the hexagonal lattice, whose unit cell is a rhombus composed of two equilateral triangles with sides of length a, shown in Figure 22(a); its Brillouin zone is shown in Figure 22(b). Consider the K point, $\mathbf{k} = \hat{\mathbf{x}}\, 4\pi/(3a)$: this point is associated with the C_{3v} point group. At the K point, bands 1, 2 and 3 mix; this is shown in the vanishing dielectric contrast limit in Figure 22(c), the bands having been determined by unique choice of reciprocal lattice vectors. To determine the photonic crystal eigenmodes, we consult the C_{3v} character table (see Table 1) and employing the decomposition technique of Section 3.4. These eigenmodes will individually be associated with either the A_1 or E representation; the former is one dimensional and the latter is two dimensional. The analytic forms for the Bloch modes (in the vanishing dielectric contrast limit) that correspond to these representations are

$$\{A_1\}: \qquad \mathbf{H}_{\mathbf{k}1}(\mathbf{r}) = \hat{\mathbf{z}} H_{\mathbf{k}1}(0)\left(1 + e^{-i2\pi\left(x/a - y/\left(\sqrt{3}a\right)\right)} + e^{-i2\pi\left(x/a + y/\left(\sqrt{3}a\right)\right)}\right) e^{ix(4\pi/3a)}, \tag{5.8}$$

$$\{E\}: \qquad \mathbf{H}_{\mathbf{k}2}(\mathbf{r}) = \hat{\mathbf{z}} H_{\mathbf{k}1}(0)\left(2 - e^{-i2\pi\left(x/a - y/\left(\sqrt{3}a\right)\right)} - e^{-i2\pi\left(x/a + y/\left(\sqrt{3}a\right)\right)}\right) e^{ix(4\pi/3a)}, \tag{5.9}$$

$$\{E\}: \qquad \mathbf{H}_{\mathbf{k}3}(\mathbf{r}) = \hat{\mathbf{z}} H_{\mathbf{k}1}(0)\sqrt{3}\left(-e^{-i2\pi\left(x/a - y/\left(\sqrt{3}a\right)\right)} + e^{-i2\pi\left(x/a + y/\left(\sqrt{3}a\right)\right)}\right) e^{ix(4\pi/3a)}. \tag{5.10}$$

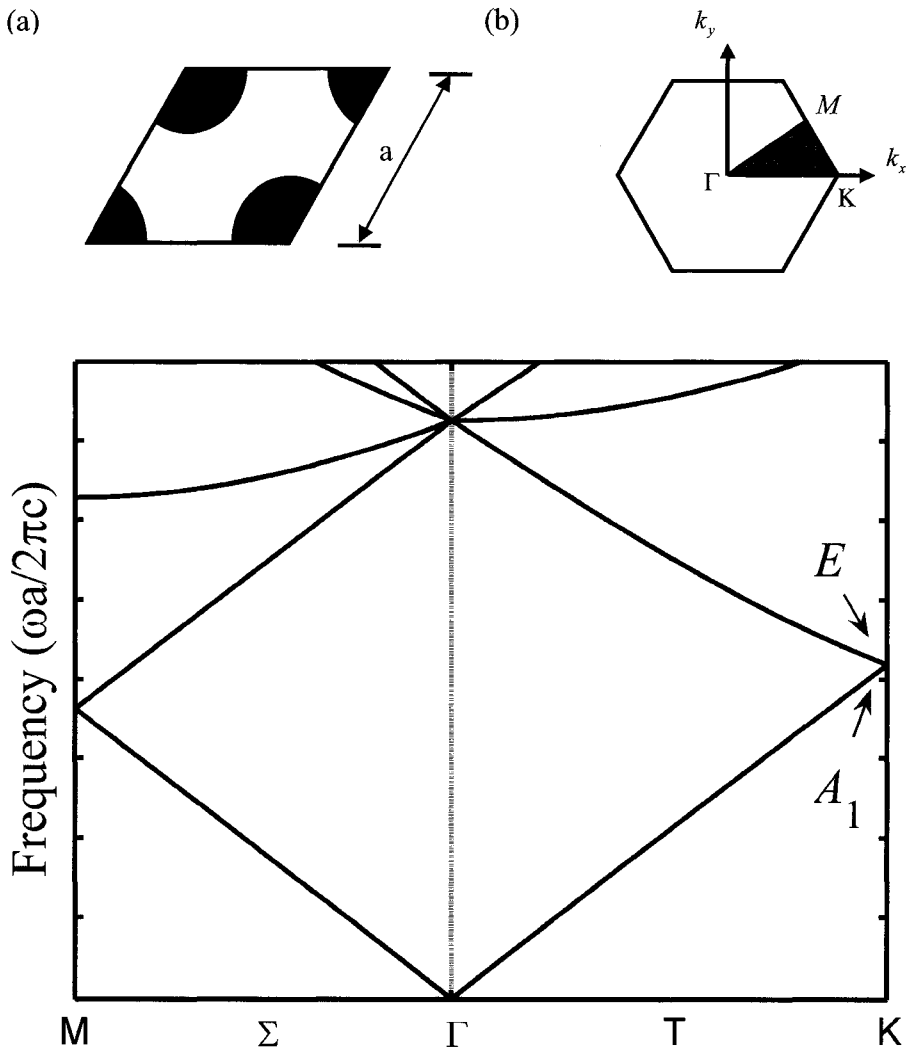

Figure 22. The hexagonal lattice: (a) real-space unit cell, (b) the Brillouin zone, and (c) the band structure in the vanishing dielectric contrast limit with the locations of the modes associated with the A_1 and E irreducible representations of the C_{3v} point group.

The origin of Eq. (5.8) to Eq. (5.10) is located at the **k**-group principal axis of the hexagonal lattice unit cell (see Figure 9), and the magnitude of each plane wave component is normalized to same arbitrary coefficient $H_{\mathrm{k},1}(0)$. Inspection of Eq. (5.8) and (5.9) reveals that each mode is simply a superposition of three unique plane waves, thus each may form a closed geometry with attendant phase singularities. Equation (5.10), however, contains only two plane waves and therefore cannot contain any singularities. Let us consider Eq. (5.8) and Eq. (5.9) individually, and then the E representations collectively. We rely on the fact that, for the Bloch mode associated with the A_1 representation, all the phasors have the same magnitude, $F_1 = F_2 = F_3$, thus satisfying $F_3 \leq F_1 + F_2$ (see Eq. (5.7)). Phase singularities will occur thus at the spatial locations where the phasors form equilateral triangles, resulting in the complex field vanishing. Since there are two unique vector forms for an equilateral triangle, the A_1 representation gives rise to two distinct vortices: one with $\upsilon = 1$, where the phase increases in a counterclockwise direction around the singularity, and one with $\upsilon = -1$, where the opposite occurs; these are shown in Figure 23(a) and Figure 23(b), respectively. Examining Figure 23, we find $(\theta_b, \theta_c) = (2\pi/3, 4\pi/3)$ for $\upsilon = 1$, and $(\theta_b, \theta_c) = (4\pi/3, 2\pi/3)$ for $\upsilon = -1$. By direct comparison with the phase angles of Eq. (5.8), these yield the respective sets of linear equations

$$\begin{bmatrix} -2\pi/a & 2\pi/\sqrt{3}a \\ 2\pi/a & 2\pi/\sqrt{3}a \end{bmatrix} \begin{bmatrix} x \\ y \end{bmatrix} = \begin{bmatrix} 4\pi/3 \\ 2\pi/3 \end{bmatrix} \text{ and } \begin{bmatrix} -2\pi/a & 2\pi/\sqrt{3}a \\ 2\pi/a & 2\pi/\sqrt{3}a \end{bmatrix} \begin{bmatrix} x \\ y \end{bmatrix} = \begin{bmatrix} 2\pi/3 \\ 4\pi/3 \end{bmatrix}. \quad (5.11)$$

These band-edge vortices are thus located, for $\upsilon = 1$, and $\upsilon = -1$, at $(x, y) = \left(-a/2, a/2\sqrt{3}\right)$ and $(x, y) = \left(-a/2, -a/2\sqrt{3}\right)$, respectively; these are the centers of the equilateral triangles which comprise our real-space unit cell (crystallographic orbit associated with the special Wyckoff position W_b, see Table 5). A

(a)

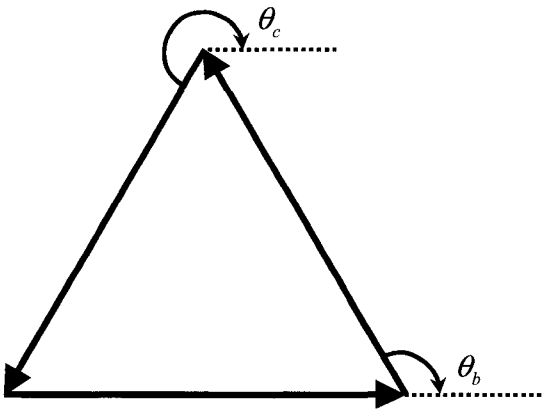

(b)

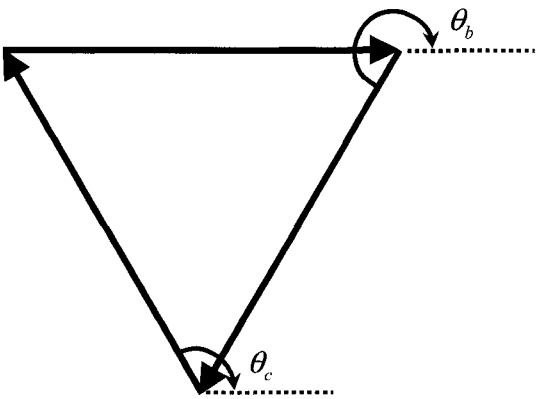

Figure 23. Phasor geometries for the Bloch mode of the A_1 representation, where (a) is $\upsilon = 1$ and (b) is $\upsilon = -1$.

more comprehensive discussion of the phase and optical flux distribution within the unit cell, including the impact of increasing dielectric contrast, is deferred to Section 5.4.

We now consider the Bloch mode of the first E representation, as given in Eq. (5.9). This mode contains three plane waves whose magnitudes satisfy $F_3 = F_1 + F_2$. Figure 24 demonstrates the two permissible phasor arrangements that yield vanishing complex fields. Clearly, the phase angles $\theta_b = \theta_c = \pi$ do not depend on the order in which the phasors are added together. Thus, the same set of linear equations

$$\begin{bmatrix} -2\pi/a & 2\pi/\sqrt{3}a \\ 2\pi/a & 2\pi/\sqrt{3}a \end{bmatrix} \begin{bmatrix} x \\ y \end{bmatrix} = \begin{bmatrix} \pi \\ \pi \end{bmatrix}, \tag{5.12}$$

characterizes the locations of both the $v=1$ and $v=-1$ vortices. Hence, $(x,y)=(-a/2,0)$ is the point where the two vortices of opposite spin annihilate each other; no phase singularities manifest under this circumstance. The E representation, being doubly-degenerate, may be written as a linear combination of Eq. (5.9) and Eq. (5.10). The general form may thus be expressed, for arbitrary normalization, as

$$\mathbf{H}_{\mathrm{k}}(\mathbf{r}) = \mathbf{H}_{\mathrm{k}2}(\mathbf{r}) + (A+iB)\mathbf{H}_{\mathrm{k}3}(\mathbf{r}), \tag{5.13}$$

where $(A+iB)$ is a complex coefficient, and thus

$$\mathbf{H}_{\mathrm{k}}(\mathbf{r}) = \left(2 - (A+1+iB)e^{-i2\pi\left(x/a - y/\left(\sqrt{3}a\right)\right)} + (A-1+iB)e^{-i2\pi\left(x/a + y/\left(\sqrt{3}a\right)\right)}\right)e^{ix(4\pi/3a)}. \tag{5.14}$$

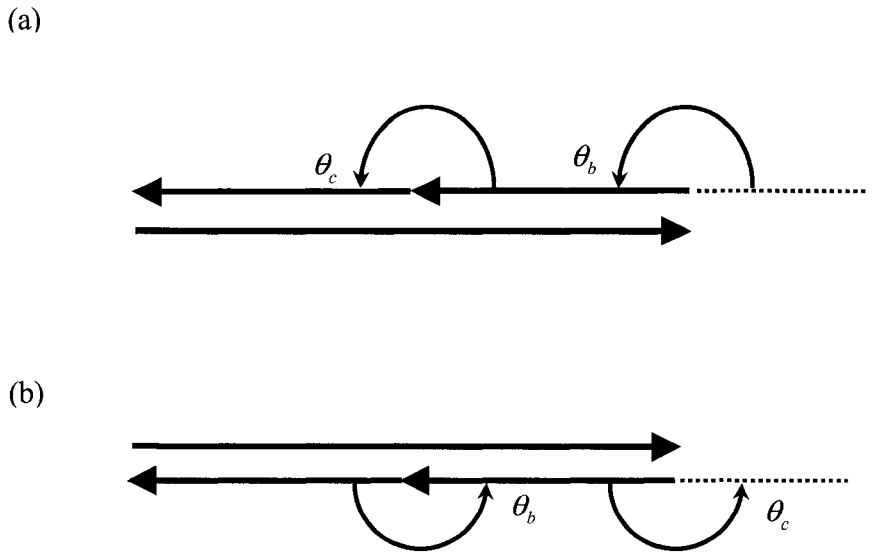

Figure 24. Phasor geometries for the Bloch mode of the first E representation, where (a) is $\upsilon = 1$ and (b) is $\upsilon = -1$.

Equation (5.14) has the required minimum of three plane waves; if their coefficient magnitudes F are such that $F_3 \leq F_1 + F_2$, as required by Eq. (5.7), then the doubly-degenerate case may manifest vortices. In general, this may occur when

$$2 \leq \sqrt{(A+1)^2 + B^2} + \sqrt{(A-1)^2 + B^2} \tag{5.15}$$

is satisfied. As earlier illustrated for the first E representation alone, the case of $F_3 = F_1 + F_2$ will once again result in two vortices of opposite spin occupying the same location in real space. For relative source amplitudes governed by Eq. (5.15), vortices will arise in those locations with closed phasor geometry. This suggests that the location of such vortices may be tuned by varying the phase or intensity of the $\mathbf{H}_{\mathbf{k}3}(\mathbf{r})$ sources relative to that of the $\mathbf{H}_{\mathbf{k}2}(\mathbf{r})$ source.

The odd rotational symmetries here permissible are n = 1 and 3: Having demonstrated that vortices exist for the C_{3v} group, we now consider the former, that is, the C_{1h} group. In the case of vanishing contrast, only a single plane wave is required by symmetry to describe a C_{1h} Bloch mode. In comparison with the case described above, the reduction in symmetry means that vortices are, *ipso facto*, impossible. However, the understanding of a vortex state as a plane wave mixing effect suggests that a vortex may arise where three or more adjacent bands mix. For the photonic crystal eigenmodes associated with the C_{1h} point group, determined in the vanishing dielectric contrast limit, the only way multiple plane waves may mix is at a **k** vector which locates a three-fold accidental degeneracy. Consistent with this nomenclature, we refer to such vortices as accidental phase singularities. As illustration of such, let us consider the square lattice in vanishing-contrast, whose band structure diagram appears in Figure 25(c). The Σ direction is associated with the C_{1h} point group (see Table 2), hence an n = 1 rotational symmetry.

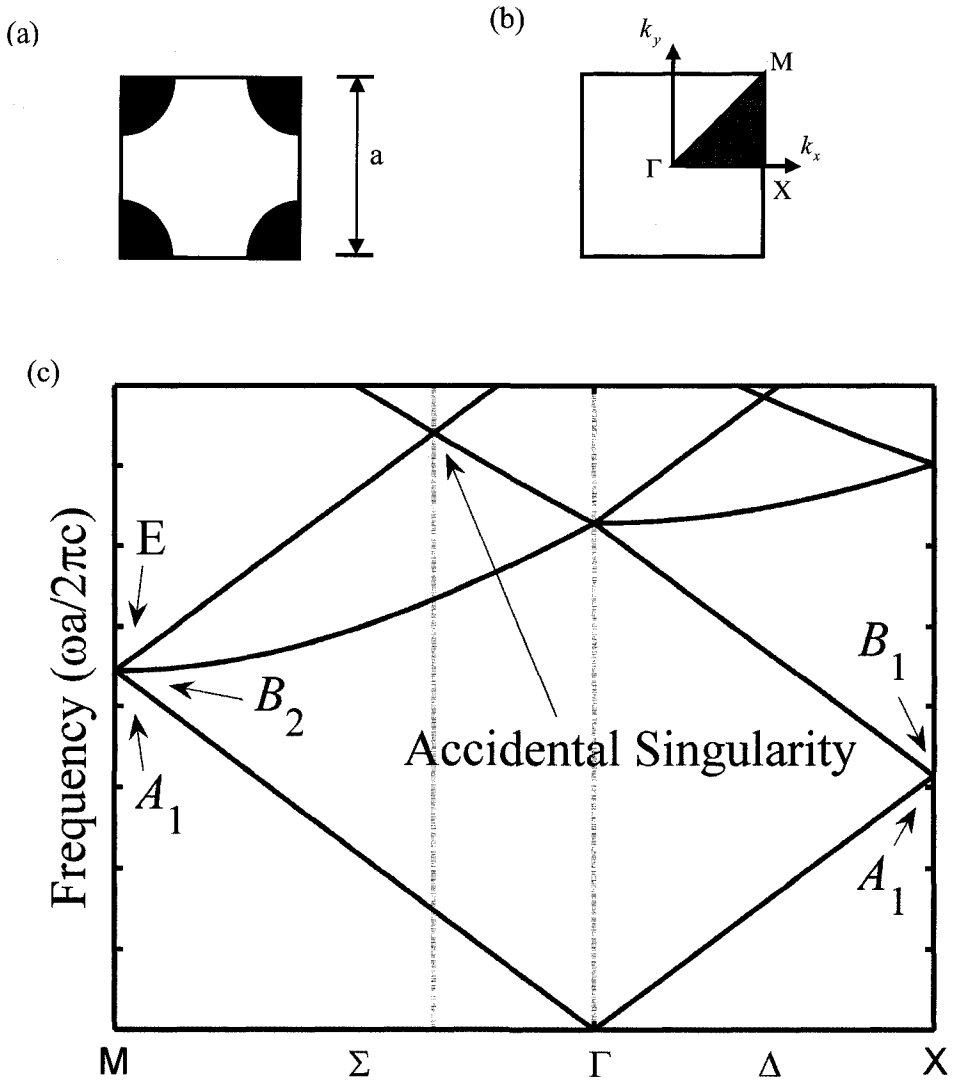

Figure 25. Square lattice (a) the unit cell in real space (b) the irreducible Brillouin zone and (c) the band structure (in the vanishing dielectric contrast limit) with the locations of the accidental singularity and the modes which are associated with the A_1, B_2 and E irreducible representations of the C_{4v} point group.

Inspection of the band structure diagram reveals that bands 4, 5 and 6 are all degenerate at $\mathbf{k} = \hat{\mathbf{x}}\pi/(3a) + \hat{\mathbf{y}}\pi/(3a)$; the sum mode of the three individual plane waves is

$$\mathbf{H}_{ksum}(\mathbf{r}) = \hat{\mathbf{z}} H_{\mathbf{k},4}(\hat{\mathbf{x}} 2\pi/a)\left(e^{i2\pi x/a} + e^{i2\pi y/a} + e^{-i2\pi(x/a+y/a)}\right) e^{i2\pi(x/3a+y/3a)}. \qquad (5.16)$$

Equation (5.16) clearly satisfies the necessary condition (specifically, $F_1 = F_2 = F_3$, see Eq. (5.7)), and one may determine six spatial locations (x, y) where closed phasor geometries exist via the manner described above. However, on symmetry grounds, in the vanishing dielectric contrast limit, there is no justification for stating that all odd rotational symmetries must have vortices. What is the situation when n is even? Let us return to the square lattice of Figure 25 and consider the M point, where $\mathbf{k} = \hat{\mathbf{x}}\pi/a + \hat{\mathbf{y}}\pi/a$, thus an eigenmode associated with the C_{4v} point group. At M, four bands are frequency-degenerate: bands 1, 2, 3 and 6. These correspond to the two one-dimensional representations A_1 and B_2, and to the two-dimensional representation E. By examining the character table for C_{4v} (see Table 7 and Section 3.4), the Bloch modes for the individual representations may be found as

$$\{A_1\}: \quad \mathbf{H}_{\mathbf{k},1}(\mathbf{r}) = \hat{\mathbf{z}} H_{\mathbf{k},1}(0)\left(e^{i\pi(x/a+y/a)} + e^{i\pi(-x/a+y/a)} + e^{i\pi(x/a-y/a)} + e^{i\pi(-x/a-y/a)}\right), \qquad (5.17)$$

$$\{B_2\}: \quad \mathbf{H}_{\mathbf{k},2}(\mathbf{r}) = \hat{\mathbf{z}} H_{\mathbf{k},1}(0)\left(e^{i\pi(x/a+y/a)} - e^{i\pi(-x/a+y/a)} - e^{i\pi(x/a-y/a)} + e^{i\pi(-x/a-y/a)}\right), \qquad (5.18)$$

$$\{E\}: \quad \mathbf{H}_{\mathbf{k},3}(\mathbf{r}) = \hat{\mathbf{z}} H_{\mathbf{k},1}(0)\left(e^{i\pi(-x/a+y/a)} - e^{i\pi(x/a-y/a)}\right), \text{ and} \qquad (5.19)$$

$$\{E\}: \quad \mathbf{H}_{\mathbf{k},4}(\mathbf{r}) = \hat{\mathbf{z}} H_{\mathbf{k},1}(0)\left(e^{i\pi(x/a+y/a)} - e^{i\pi(-x/a-y/a)}\right). \qquad (5.20)$$

Table 7. C_{4v} character table

Γ	Conjugacy classes				
	E	$2C_4$	C_2	$2\sigma_v$	$2\sigma_d$
A_1	1	1	1	1	1
A_2	1	1	1	-1	-1
B_1	1	-1	1	1	-1
B_2	1	-1	1	-1	1
E	2	0	-2	0	0

The E representations contain only two plane waves, and thus individually do not meet the necessary condition for the formation of phase singularities. Unlike the C_{3v} case for the degenerate E representation, there are no linear combinations of the E representations in the C_{4v} case that are not wholly real. The necessary phase dislocations required by Eq. (5.1) for vortex formation are symmetry-forbidden in states of even rotational symmetry, since all plane waves occur as conjugate pairs. Moreover, plane wave pairs from each Bloch mode remain conjugate under any transformation operator of the symmetry group. Since the conjugate relationship between the plane waves comprising the modes is maintained under group transformations, any linear combination of degenerate Bloch modes belonging to an even rotational symmetry group forms a standing wave pattern (i.e., no energy transport at the global or local level), precluding the existence of vortices.

5.3.2 Phase and local flux distributions

Using analytic descriptions of the photonic crystal eigenmodes in the vanishing dielectric contrast limit, we have determined the spatial location of the phase singularities. Now, we identify them by revealing the modal phase $\vartheta(\mathbf{r})$ and local flux distributions (Poynting vector field) for the symmetries of the hexagonal and square unit cells. We

explicitly demonstrate for each phase singularity that the modal phase $\vartheta(\mathbf{r})$ does indeed satisfy Eq. (5.1), and that the local energy flux does circulate about the singular point. Also, we touch upon their scaling with increasing dielectric contrast (*i.e.,* vortex stability). This was achieved by numerically solving the eigenvalue problem, described by the Maxwell's equation for the magnetic field (TE Bloch mode), using our proprietary code based on COMSOL's Multiphysics finite element analysis software 8 (see Section 4.3).

We have extracted the local phase from the relation between real and imaginary parts of the numerically determined field, and have found the local flux from the time-averaged Poynting's vector (see Eq. (2.31)). Figure 26 to Figure 33 detail the results of the field simulations in hexagonal and square-lattice unit cells for both weak and strong dielectric contrast, the half approximating the vanishing contrast case at a ratio of 1.2, and the others ten times greater. The phase is denoted by grey scale mapping from $-\pi$ (black) to π (white). The direction of optical power flow is shown separately by the black arrows, flux magnitudes being proportional to arrow length, and the magnitude as the colour backdrop, given in arbitrary units. Dislocatons in phase occur as contours with 2π discontinuities that terminate in phase singularities.

Figure 26 and Figure 27 present our simulation results for the n = 3 odd rotational symmetry case introduced in Section 5.3; the band 1 TE mode for the hexagonal lattice at $\mathbf{k} = \hat{\mathbf{x}}\, 4\pi/(3a)$ (the A_1 representation of the C_{3v} point group). The simulation is of an array of periodic air holes $\varepsilon_{air} = 1$, with radii of $r = 0.25a$, in a dielectric background ε_{BG}, where the lattice constant is $a = 3.75\times10^{-7}\,\mathrm{m}$. In Figure 26, the low contrast images are displayed, where $\varepsilon_{BG} = 1.2$, while in Figure 27, the high contrast images are displayed, where $\varepsilon_{BG} = 12$. As predicted by our group theoretic and phasor geometric approach, there are two phase singularities located at either end of a phase dislocation line, where the phase changes by 2π, and thus must have opposite vorticity

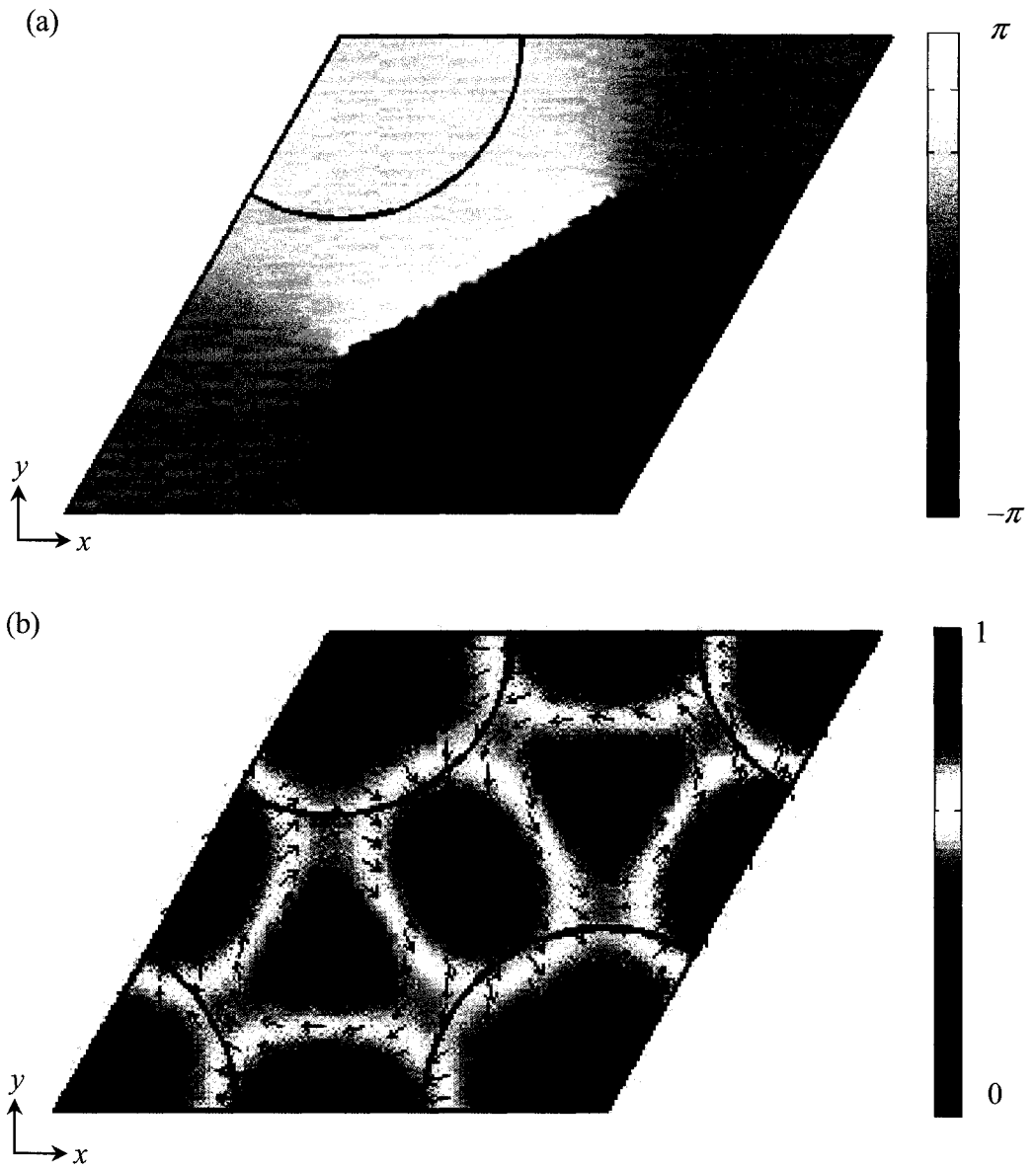

Figure 26. Hexagonal lattice Bloch mode, band 1, $\mathbf{k} = \hat{\mathbf{x}}\,4\pi/(3a)$, and low dielectric contrast of 1.2. (a) Modal phase with two symmetry singular points (grey scale from $-\pi$ to π), and (b) Poynting vector magnitude and direction. Bold black lines represent edges of the air holes and unit cell.

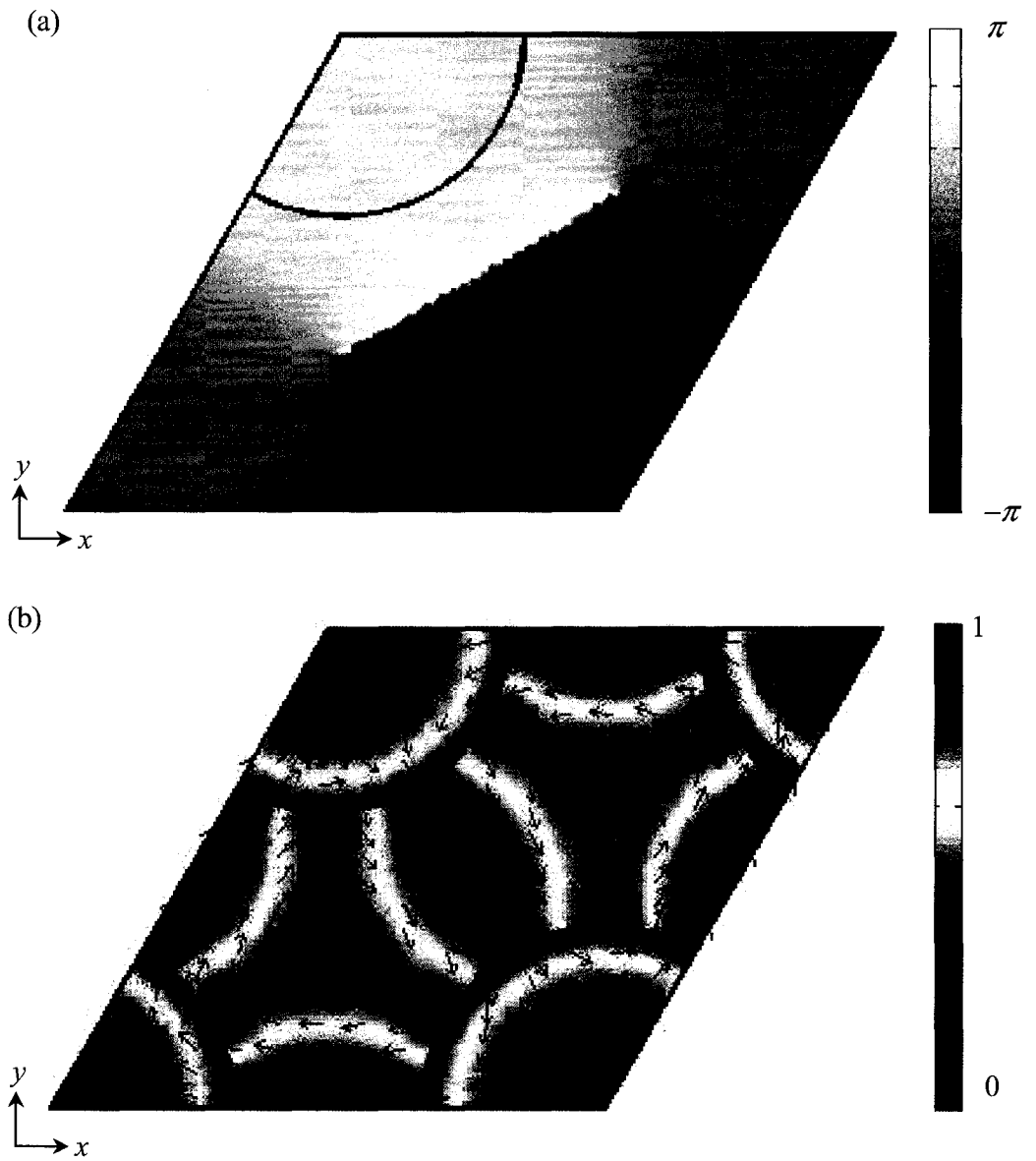

Figure 27. Hexagonal lattice Bloch mode, band 1, $\mathbf{k} = \hat{\mathbf{x}}\,4\pi/(3a)$, and high dielectric contrast of 12. (a) Modal phase with two symmetry singular points (grey scale from $-\pi$ to π), and (b) Poynting vector magnitude and direction. Bold black lines represent edges of the air holes and unit cell.

(see Figure 26(a) and Figure 27(a)). Further confirmation is noted in the circulation of energy flux about these same points, the flux magnitude vanishing at the ends of the phase dislocation line (see Figure 26(b) and Figure 27(b)). Comparison of Figure 26 and Figure 27 with the analytic results reveals the locational stability of the vortex pair with increasing dielectric contrast. This demonstrates that sufficient information is retained in the vanishing dielectric contrast limit to fully quantify vortex properties for the general n = 3 odd symmetry case.

Figure 28 and Figure 29 give the numerical results for the even rotational symmetry case discussed in Section 5.3; the Band 1 TE mode for the square lattice at $\mathbf{k} = \hat{\mathbf{x}}\pi/a + \hat{\mathbf{y}}\pi/a$ (the A_1 representation of the C_{4v} point group). The simulation is of an array of dielectric columns (with $\varepsilon_{col} = 1.2$ low dielectric contrast case and $\varepsilon_{col} = 12$ high dielectric contrast case), with radii of $r = 0.25a$, in a dielectric background $\varepsilon_{air} = 1$, where the lattice constant is $a = 3.75\times10^{-7}\,\mathrm{m}$. The phase profiles shown in Figure 28(a) and Figure 29(a) are constant in each of their four quadrants, changing discontinuously from $-\pi$ to zero along orthogonal nodal lines. This reflects the underlying nature of the mode as a set of conjugate plane waves, that is, either wholly real or wholly imaginary. The nodal lines express the symmetry of the system. Since the mode is a standing wave, the flux is essentially zero; the randomly oriented arrows in Figure 28(b) and Figure 29(b) are due to numerical noise, the arrow length arbitrarily scaled to the peak noise magnitude. Again, comparison of these two plots with the analytic results demonstrates that the vanishing contrast approach fully quantifies system response for the general even symmetry case.

Figure 30 to Figure 33 give the low and high contrast simulation results for the n = 1 odd rotational symmetry case introduced in section 5.3; the band 4 TE mode for the square lattice at $\mathbf{k} = \hat{\mathbf{x}}\pi/(3a) + \hat{\mathbf{y}}\pi/(3a)$ (the A representation of the C_{1h} point group). In Figure 30 and Figure 31, the simulation is an array of dielectric columns (with $\varepsilon_{col} = 1.2$, the low dielectric contrast case and $\varepsilon_{col} = 12$, the high dielectric contrast case), with

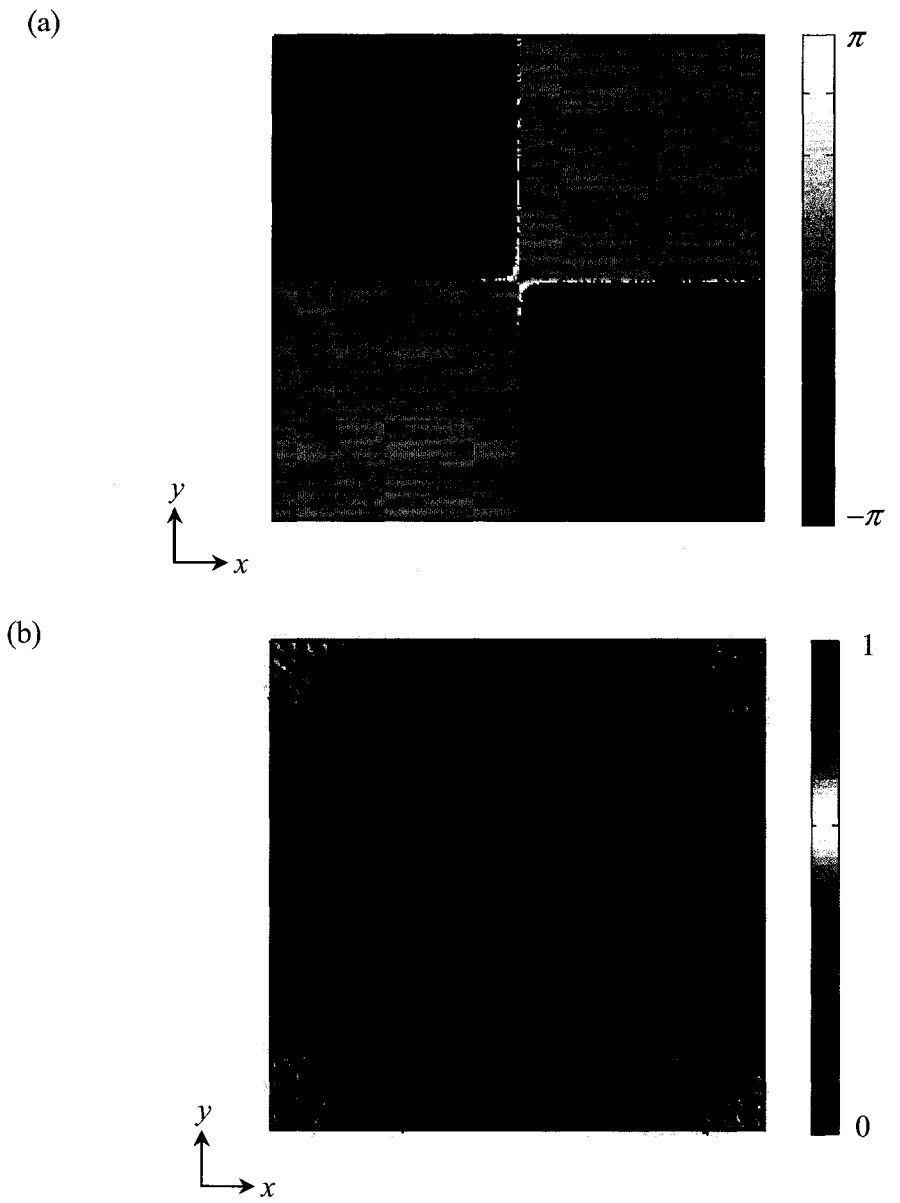

Figure 28. Square lattice Bloch mode, band 1, $\mathbf{k} = \hat{\mathbf{x}}\pi/a + \hat{\mathbf{y}}\pi/a$, and low dielectric contrast of 1.2. (a) Modal phase with no singular points (grey scale from $-\pi$ to π), and (b) Poynting vector magnitude and direction that is zero everywhere (standing wave). Bold black lines represent edges of the air holes and unit cell.

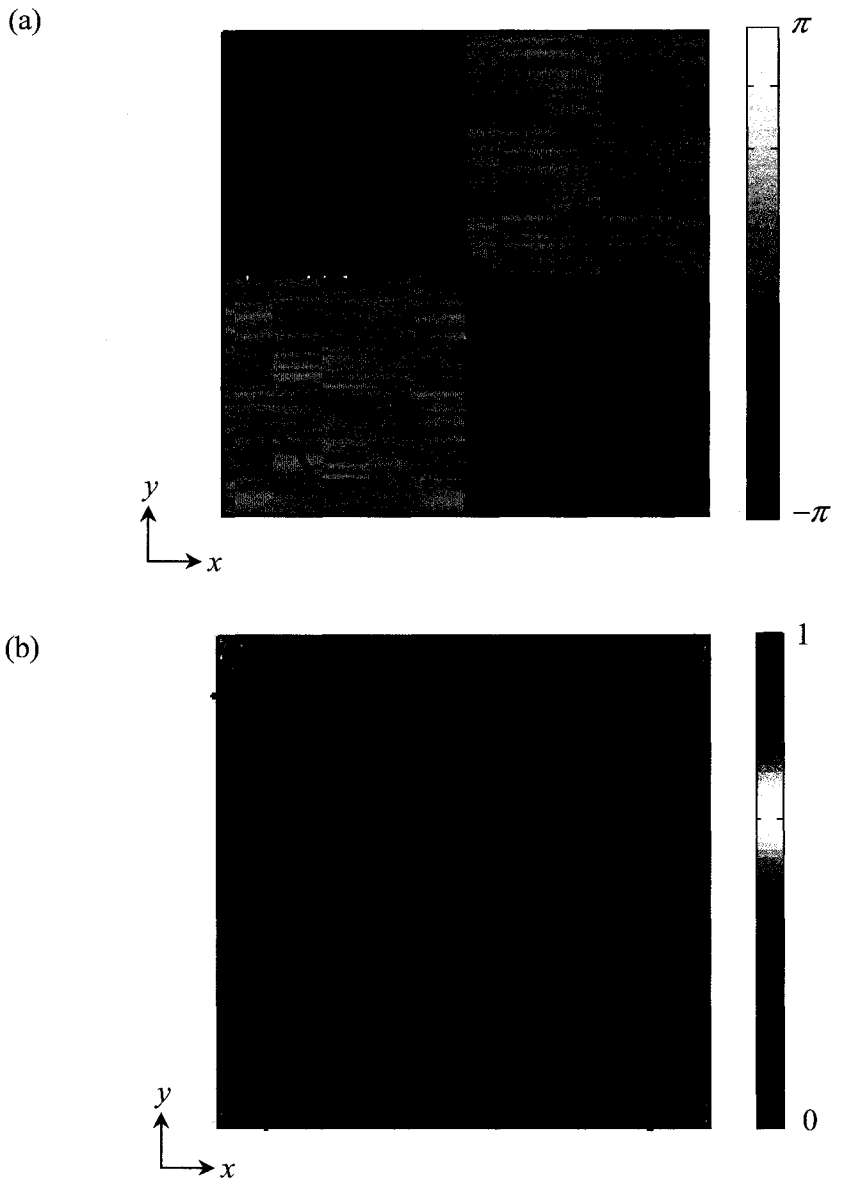

Figure 29. Square lattice Bloch mode, band 1, $\mathbf{k} = \hat{\mathbf{x}}\pi/a + \hat{\mathbf{y}}\pi/a$, and high dielectric contrast of 12. (a) Modal phase with no singular points (grey scale from $-\pi$ to π), and (b) Poynting vector magnitude and direction that is zero everywhere (standing wave). Bold black lines represent edges of the air holes and unit cell.

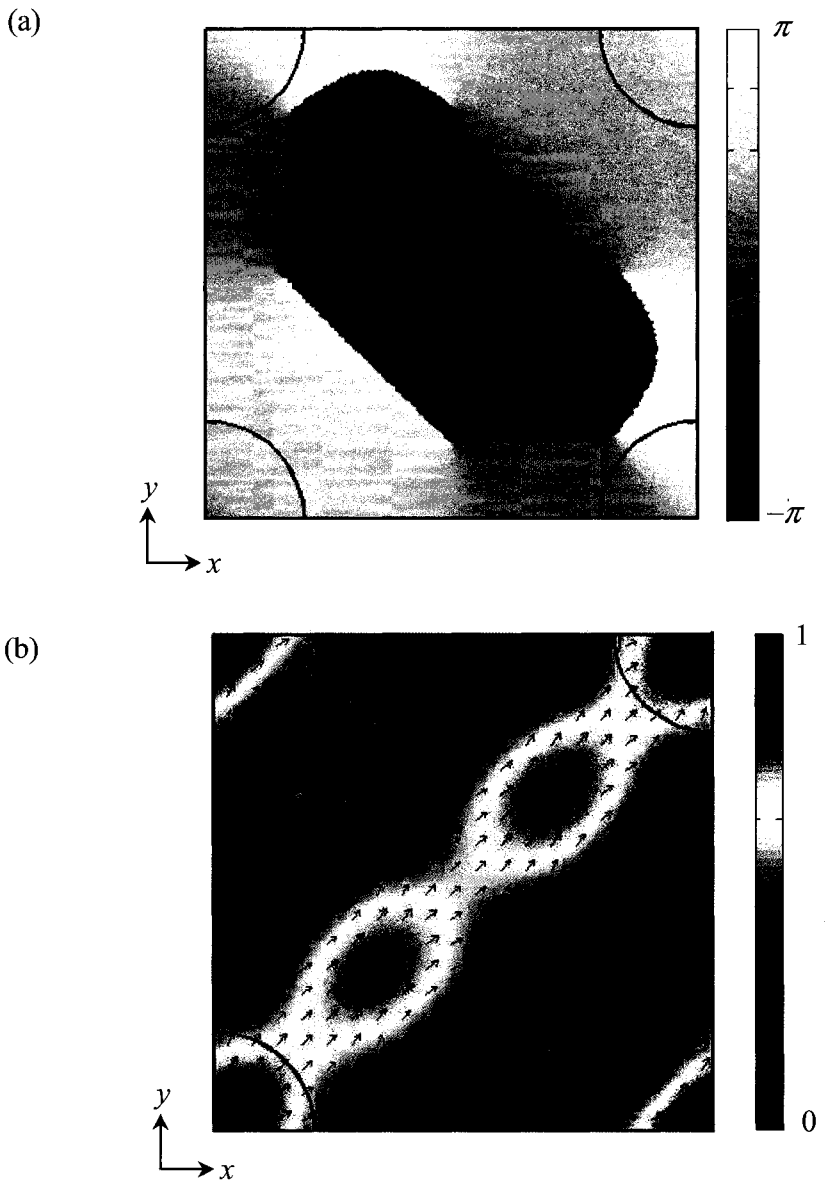

Figure 30. Square lattice dielectric columns in air background Bloch mode, band 4, $\mathbf{k} = \hat{\mathbf{x}}\pi/(3a) + \hat{\mathbf{y}}\pi/(3a)$, and low dielectric contrast of 1.2. (a) Modal phase with six accidental singular points (grey scale from $-\pi$ to π), and (b) Poynting vector magnitude and direction. Bold black lines represent edges of the air holes and unit cell.

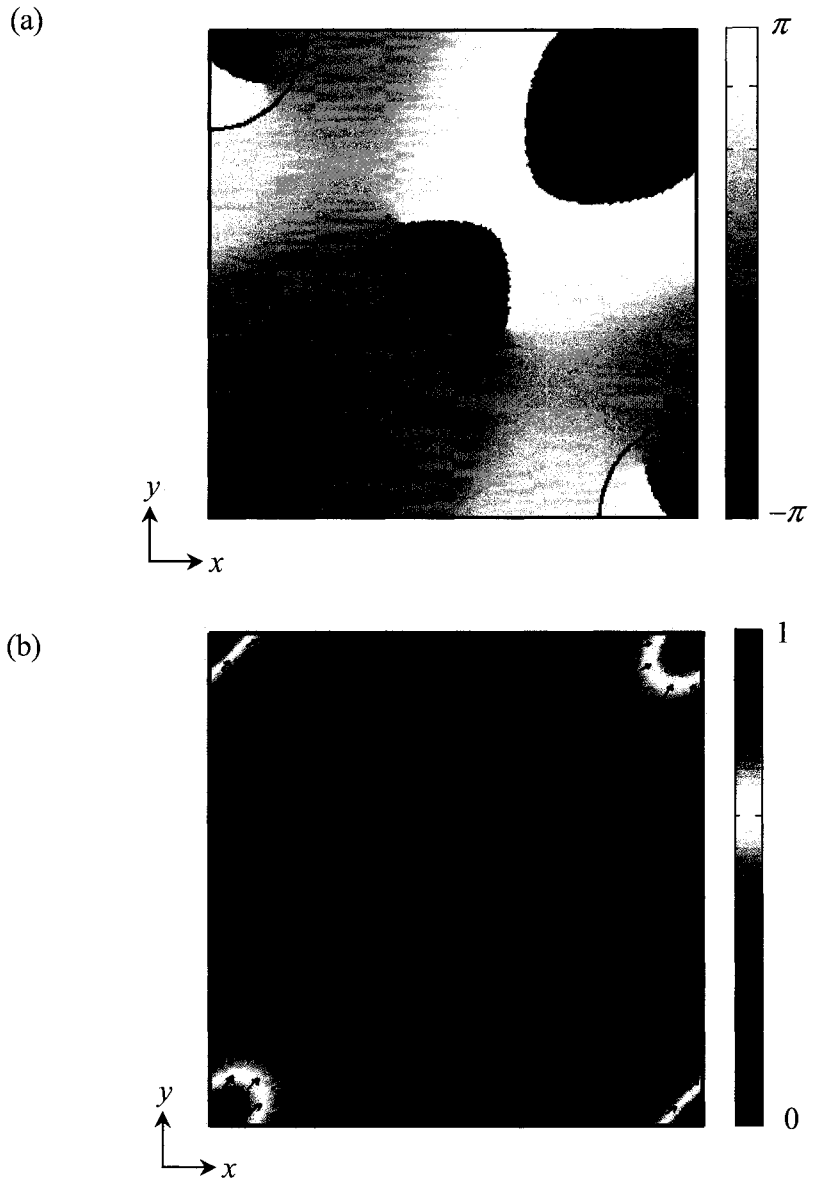

Figure 31. Square lattice dielectric columns in air background Bloch mode, band 4, $\mathbf{k} = \hat{\mathbf{x}}\pi/(3a) + \hat{\mathbf{y}}\pi/(3a)$, and high dielectric contrast of 12. (a) Modal phase with four accidental singular points (grey scale from $-\pi$ to π), and (b) Poynting vector magnitude and direction.

radii of $r = 0.28a$ (or 0.25 volume fraction of the columns versus the square unit cell), in a dielectric background $\varepsilon_{air} = 1$, where the lattice constant is $a = 3.75 \times 10^{-7}\,\mathrm{m}$. Recall, in the vanishing dielectric contrast limit (see Section 5.3.1), we asserted the appearance of six phase singularities. In Figure 30(a), we reveal their locations explicitly; a dielectric contrast of 1.2 is sufficiently close to the vanishing contrast limit that no significant shift in vortex location is anticipated. We see again that all vortices occur in counter-rotating pairs, a consequence of finite dislocation line lengths and angular momentum conservation, as illustrated by the flux circulation (see Figure 30(b)). In contrast to the C_{3v} case, we found in the vanishing contrast limit C_{1h} case, that vortices may only arise when there is an accidental crossing of three or more bands, and we classified them as "accidental singularities". Thus, we expect a marked change in the vortex state with increasing contrast, as is revealed in Figure 31. These singularities experience a large change in form and number when plane waves from higher-order Brillouin zones are coupled into the description of the Bloch mode. Their analytic description and classification require a treatment beyond the vanishing contrast limit.

In Figure 32 and Figure 33, we see the same eigenmode, but now the simulation is for the opposite case of an array of periodic air holes $\varepsilon_{air} = 1$, with radii of $r = 0.28a$ (or 0.25 volume fraction of the columns versus the square unit cell), in a dielectric background ε_{BG} (with $\varepsilon_{BG} = 1.2$ low dielectric contrast case and $\varepsilon_{BG} = 12$ high dielectric contrast case), where the lattice constant is $a = 3.75 \times 10^{-7}\,\mathrm{m}$. If we compare the low dielectric contrast case for the two opposite dielectric configurations (see Figure 30 and Figure 32), it is clear that both have the same number and form of phase dislocations, and similar vortex structures. By contrast, in the high dielectric contrast cases, the two dielectric configurations (see Figure 31 and Figure 33) are not only different from their low dielectric contrast counterparts, but also from each other. This again emphasizes the change in the form and structure of the accidental vortices when the dielectric profile is changed.

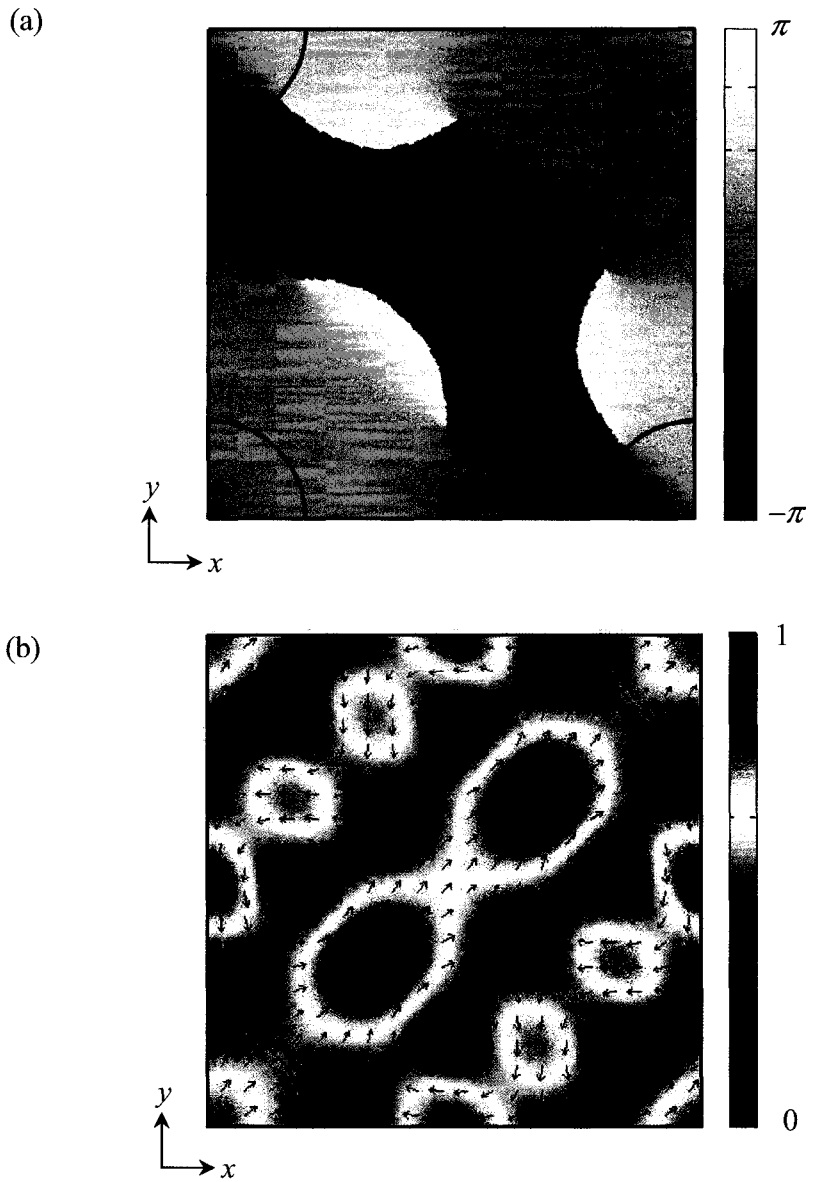

Figure 32. Square lattice air holes in dielectric background Bloch mode, band 6, $\mathbf{k} = \hat{\mathbf{x}}\pi/(3a) + \hat{\mathbf{y}}\pi/(3a)$, and low dielectric contrast of 1.2. (a) Modal phase with four accidental singular points (grey scale from $-\pi$ to π), and (b) Poynting vector magnitude and direction.

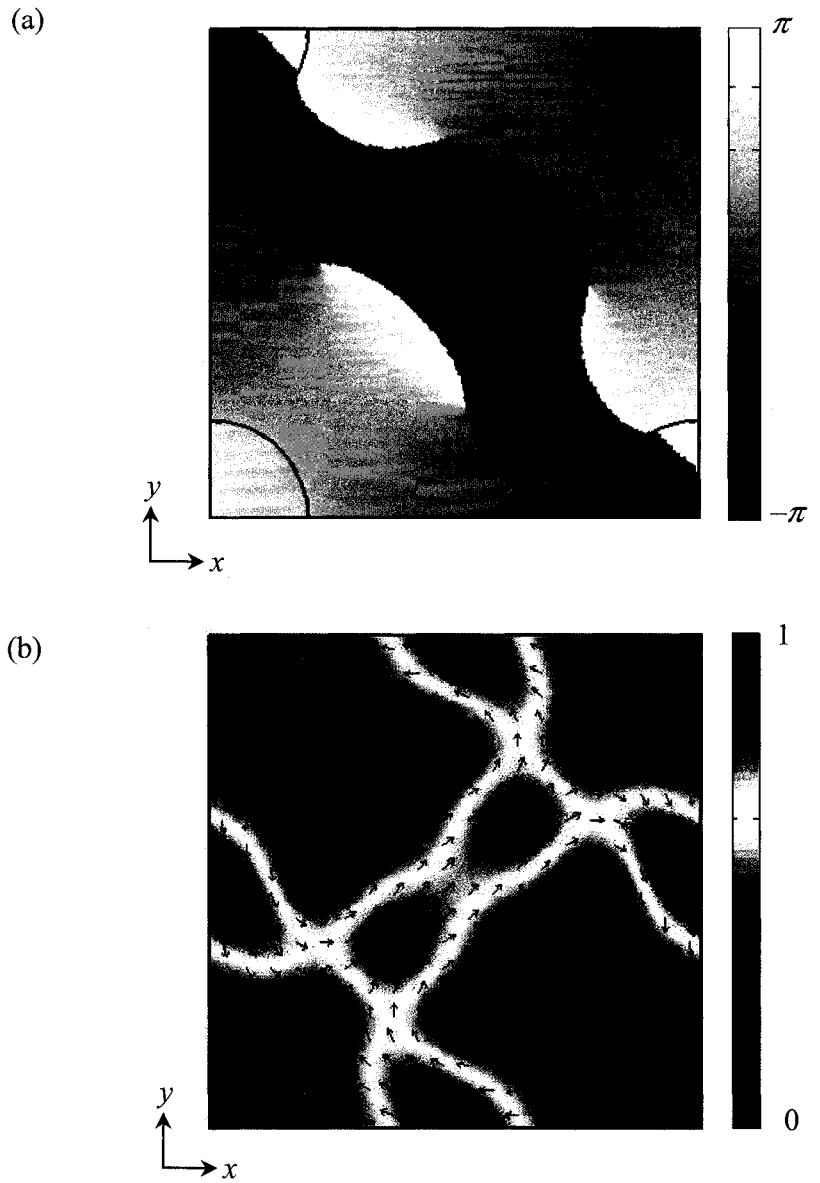

Figure 33. Square lattice air holes in dielectric background Bloch mode, band 6, $\mathbf{k} = \hat{\mathbf{x}}\pi/(3a) + \hat{\mathbf{y}}\pi/(3a)$, and high dielectric contrast of 12. (a) Modal phase with four accidental singular points (grey scale from $-\pi$ to π), and (b) Poynting vector magnitude and direction.

5.4 Photonic crystal slabs

The basic principles used to determine vortex location have been established by examining the eigenmodes of two-dimensional photonic crystals, and the methods have been confirmed by comparing the results to numerical simulations. This final section will apply the same approach to the eigenmodes of photonic crystal slabs to determine if vortices appear when there is vertical confinement of the light. As described in Section 4.4.2, the electric and magnetic field profiles of the two-dimensional photonic crystal eigenmodes and photonic crystal slabs eigenmodes are identical in the *x*-*y* plane that bisects the photonic crystal slab when the Bloch wave vector **k** and band index *n* of the two eigenmodes are the same (with the same *x*-*y* plane dielectric profiles). As a result, we choose to examine the hexagonal photonic crystal slab eigenmode for band 1 and Bloch wave vector $\mathbf{k} = \hat{\mathbf{x}} 4\pi/(3a)$; this is the same location in reciprocal space where the symmetry vortices appear in the two-dimensional photonic crystal. Therefore, we predict symmetry vortices will also appear in the photonic crystal slab eigenmode with the same parameters. In Section 3.4.4, we derive the photonic crystal slab eigenmode for band 1 and Bloch wave vector $\mathbf{k} = \hat{\mathbf{x}} 4\pi/(3a)$; we restate Eq. (3.70) for the reader:

$$\mathbf{E}_{\mathbf{k}1}(\mathbf{r}) = \left(\begin{pmatrix} 0 \\ 2 \\ 0 \end{pmatrix} e^{i4\pi x/3a} + \begin{pmatrix} -\sqrt{3} \\ -1 \\ 0 \end{pmatrix} e^{-i2\pi\left(x/3a - y/\left(\sqrt{3}a\right)\right)} + \begin{pmatrix} \sqrt{3} \\ -1 \\ 0 \end{pmatrix} e^{-i2\pi\left(x/3a + y/\left(\sqrt{3}a\right)\right)} \right) \cos\left(k_z z\right). \quad (5.21)$$

Using Maxwell's equations (Eq. (2.7)), we can find the associated magnetic field:

$$\mathbf{H}_{\mathbf{k}1}(\mathbf{r}) = \frac{1}{\mu_0 \omega}\left(\begin{pmatrix} -2ik_z \sin(k_z z) \\ 0 \\ \frac{8\pi}{3a}\cos(k_z z) \end{pmatrix} e^{i4\pi x/3a} + \begin{pmatrix} ik_z \sin(k_z z) \\ -i\sqrt{3}k_z \sin(k_z z) \\ \frac{8\pi}{3a}\cos(k_z z) \end{pmatrix} e^{-i2\pi\left(x/3a - y/(\sqrt{3}a)\right)} + \begin{pmatrix} ik_z \sin(k_z z) \\ i\sqrt{3}k_z \sin(k_z z) \\ \frac{8\pi}{3a}\cos(k_z z) \end{pmatrix} e^{-i2\pi\left(x/3a + y/(\sqrt{3}a)\right)}\right). \tag{5.22}$$

At $z = 0$ the x-y plane bisects the photonic crystal slab; substituting $z = 0$ into Eq. (5.22), we find the magnetic field as

$$\mathbf{H}_{\mathbf{k}1}(\mathbf{r}) = \frac{8\pi}{\mu_0 \omega 3a}\left(\begin{pmatrix} 0 \\ 0 \\ 1 \end{pmatrix} e^{i4\pi x/3a} + \begin{pmatrix} 0 \\ 0 \\ 1 \end{pmatrix} e^{-i2\pi\left(x/3a - y/(\sqrt{3}a)\right)} + \begin{pmatrix} 0 \\ 0 \\ 1 \end{pmatrix} e^{-i2\pi\left(x/3a + y/(\sqrt{3}a)\right)}\right). \tag{5.23}$$

Comparing Eq. (5.8) (the two-dimensional photonic crystal eigenmode) and Eq. (5.23) (the photonic crystal slab eigenmode), we can confirm that the magnetic fields are the same to within a scalar constant. It is clear from Eq. (5.22) that the phasor geometry is more complex because now the magnetic field is polarized in many different directions, but we can break it down by examining each polarization component separately. True vector analysis of singularities is the subject of the following chapter on polarization singularities. The $\hat{\mathbf{x}}$ axis polarization of Eq. (5.22) contains three plane wave components, but their magnitudes are $F_1 = F_2 + F_3$. This situation yields the same phasor geometry as Figure 24; hence there will be two vortices of opposite sign that annihilate each other. The $\hat{\mathbf{y}}$ axis polarization of Eq. (5.22) only contains two elements and thus manifests no vortices. Finally the $\hat{\mathbf{z}}$ axis polarization of Eq. (5.22) matches the two-dimensional eigenmode (5.8) in the x-y plane at $z = 0$. As a result, there will be two symmetry vortices that match the phasor geometry of Figure 23, which appear at the same locations within the unit cell $(x, y, z) = \left(-a/2, a/2\sqrt{3}, 0\right)$ and $(x, y, z) = \left(-a/2, -a/2\sqrt{3}, 0\right)$. Beyond the $z = 0$ x-y plane, the $\hat{\mathbf{z}}$ axis polarization

maintains the same form, but is modified by a cosine z dependence. Therefore, we expect the phase singularities to continue infinitely along the positive and negative directions of the $\hat{\mathbf{z}}$ axis, maintaining the same locations in the x-y plane.

Once again, we confirm the analytical predictions by revealing the phase and local flux distributions of the photonic crystal slab eigenmode for band 1 and Bloch wave vector $\mathbf{k} = \hat{\mathbf{x}} 4\pi/(3a)$. This is achieved by numerically solving the photonic crystal slab eigenvalue problem, using COMSOL Multiphysics (see Section 4.4.3). Since it was shown in Section 5.3.2 that symmetry vortices are locationally stable over a wide range of dielectric contrasts, we focus on the high dielectric case of the photonic crystal slab. In Figure 34 to Figure 36, the simulations are of an array of periodic air holes $\varepsilon_{air} = 1$, with radii of $r = 0.25a$, in a dielectric slab $\varepsilon_{slab} = 12$ with a thickness of $d = a/2$, where the lattice constant is $a = 3.75 \times 10^{-7}\,\mathrm{m}$. The simulation space is the hexagonal lattice unit cell in the x-y plane with periodic boundary conditions, where the unit cell is slightly shifted so that the air hole is located at the center. In Figure 34, two cross-sections of the flux distribution photonic crystal slab are shown (the x-y plane at $z = 0$, and the y-z plane through the middle of the unit cell), where the edges of the photonic crystal slab are highlighted with bold lines. As expected, we can see two locations where there is circulation of energy flux in the x-y plane, and the y-z plane cross-section reveals that the majority of the energy flow takes place within the photonic crystal slab. This is further reinforced in Figure 35(a), where we view the $z = 0$ plane from the top. In Figure 35(b), we observe a cross-section of the local flux distributions perpendicular to the x-y plane that passes through the centers of the two vortices. This figure clearly shows that the vortices (where the flux is zero) are lines which extent through the photonic crystal slab. This is similar to the lines of zero energy flux in the two-dimensional photonic crystal. In Figure 36, we display the modal phase of $H_z(\mathbf{r})$ and we confirm that the flux magnitude vanishes at the ends of the phase dislocation lines, as predicted (see Figure 36(a)). In addition, these phase dislocations extend infinitely in the $\hat{\mathbf{z}}$ axis, as also predicted (see Figure 36(b)). Therefore, we have demonstrated that the essential forms and locations of

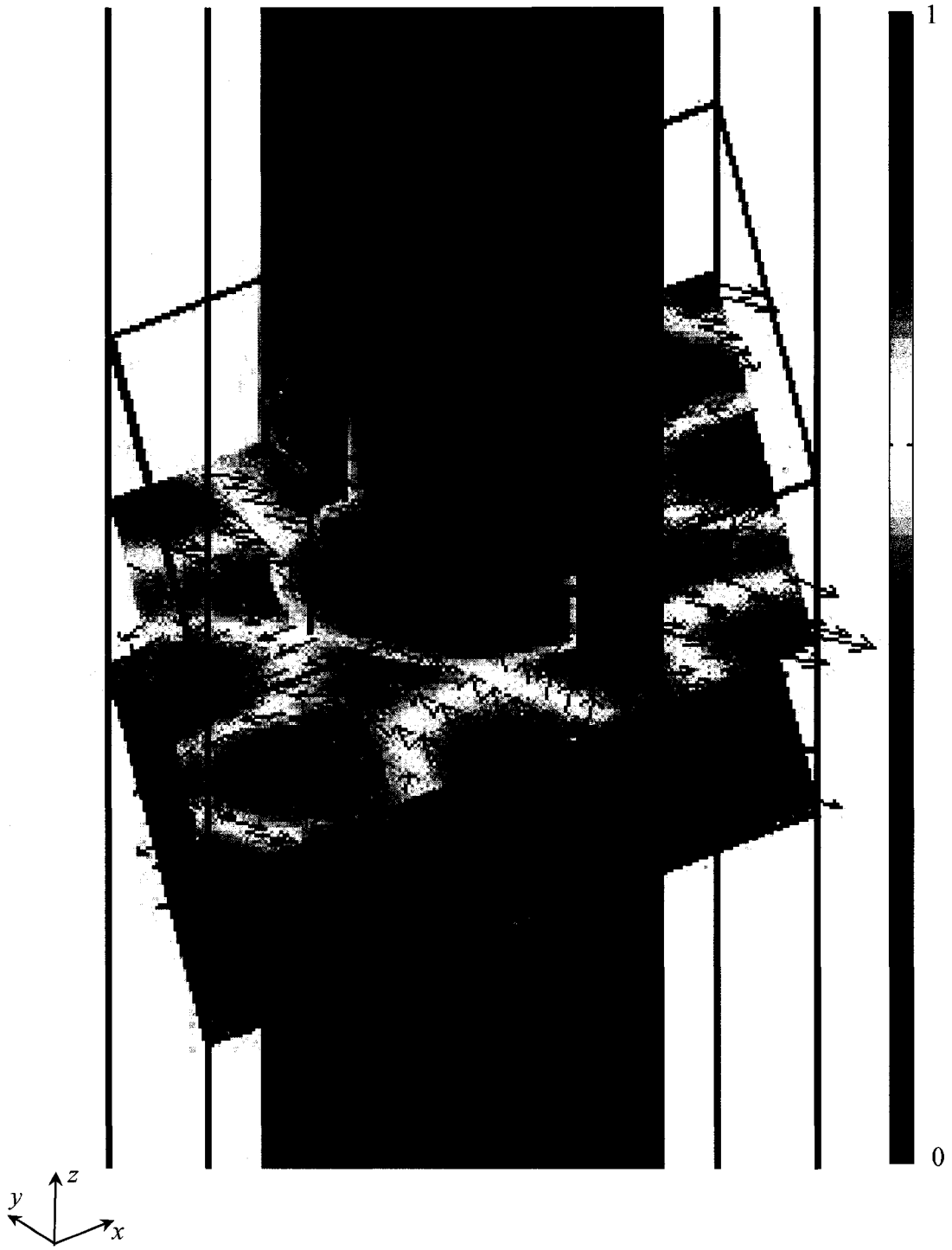

Figure 34. Hexagonal photonic crystal slab lattice air holes in dielectric background Bloch mode, band 1, $\mathbf{k} = \hat{\mathbf{x}}\,4\pi/(3a)$ Poynting vector magnitude and direction (arrows) three-dimensional view. Bold lines represent the edges of the photonic crystal slab unit cell.

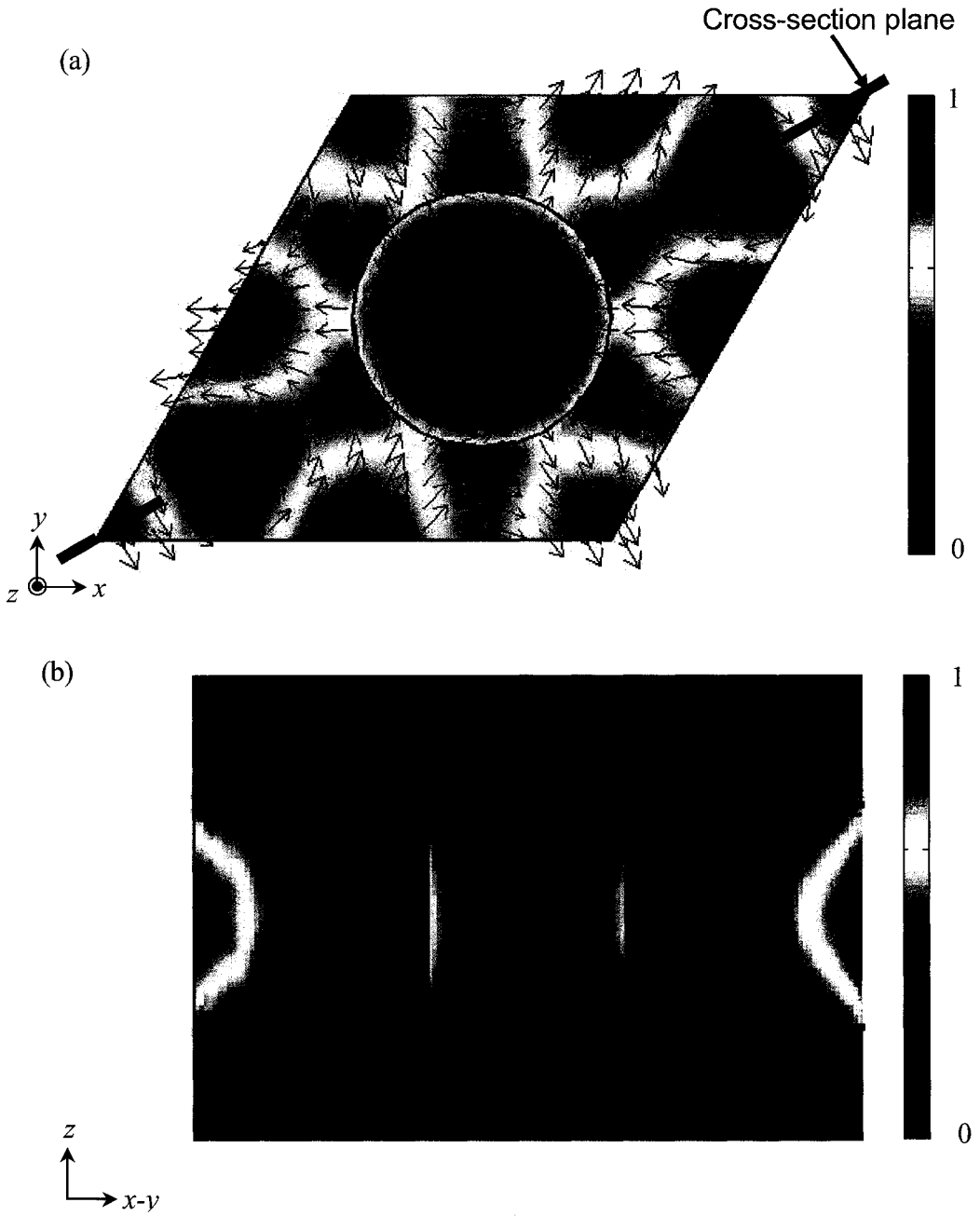

Figure 35. Hexagonal photonic crystal slab lattice air holes in dielectric background Bloch mode, band 1, $\mathbf{k} = \hat{\mathbf{x}}\,4\pi/(3a)$ Poynting vector magnitude and direction (arrows) (a) top view x-y plane at $z = 0$, (b) cross section view (along dashed line in part (a)). Bold lines represent the edges of the photonic crystal slab unit cell.

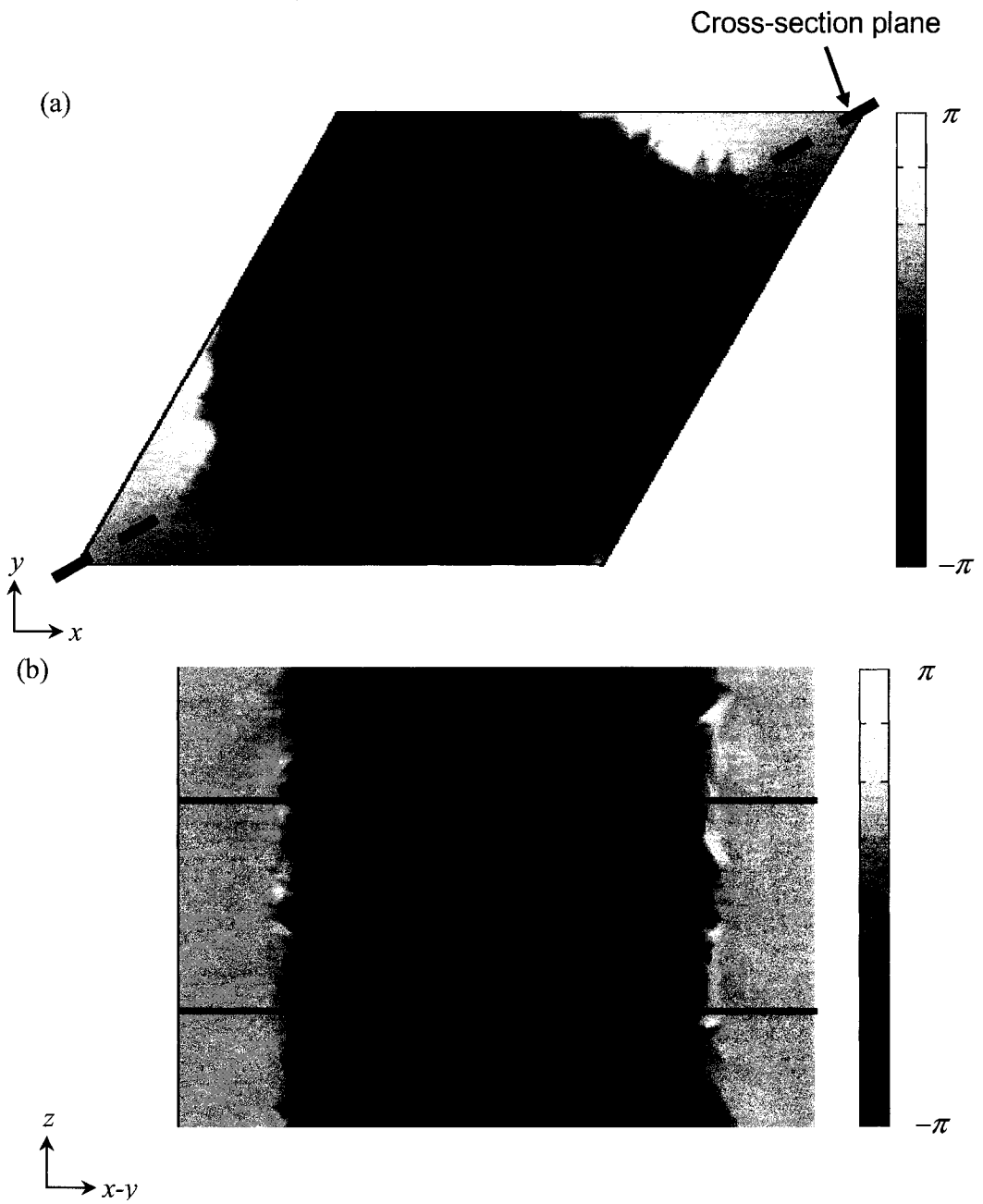

Figure 36. Hexagonal photonic crystal slab lattice air holes in dielectric background Bloch mode, band 1, $\mathbf{k} = \hat{\mathbf{x}}\,4\pi/(3a)$ modal phase of H_z with two symmetry singular points (grey scale from $-\pi$ to π) (a) top view x-y plane at $z = 0$, (b) cross section view (along dashed line in part (a)). Bold lines represent the edges of the photonic crystal slab unit cell.

symmetry vortices are maintained in a photonic crystal slab structure, and that index confinement of the light does not alter the vortices.

5.5 Conclusions

In this chapter, we have reported fundamental symmetry rules for the existence of phase singularities within the modes of linear photonic crystals. Initial insights were extracted by applying phasor geometry and group theoretic principles to analytically describe Bloch modes in the vanishing contrast limit. This permitted the number, type, and location of optical phase vortices to be determined, and revealed the existence of two distinct types of vortex state: the symmetry and the accidental. The former are a transparent expression of the contrast-insensitive $n = 3$ symmetry, while the origin of the latter arise from a more subtle expression of the $n = 1$ symmetry. That is, the modes associated with the irreducible representations of the C_{3v} symmetry group fundamentally have the required number of plane waves to form a phase singularity (and thus demonstrate form and locational stability with varying dielectric contrast), whereas the modes associated with the C_{1h} symmetry group do not, unless adjacent bands contribute to form the appropriate accidental degeneracy. These accidental singularities do evolve with increasing dielectric contrast and swiftly vanish, implying a *prima facie* limitation to our analytic approach, as is otherwise implied by the existence of different phase singularities at high dielectric contrast. We also saw that modes of even rotational symmetry cannot have phase singularities, since they are composed exclusively of conjugate plane waves. Such observations were all validated through numerical simulation of the various 2D photonic crystal symmetry classes at low and high contrast, where the vortex states were more clearly presented. Furthermore, it was demonstrated that vortices also exist in photonic crystal slab structures. The significance of the vortex state in photonic crystals may also have implications for the robust generation of optical vortex arrays. Moreover, a 2D planar photonic crystal that contains quantum-confined structures at predicted vortex locations may permit interesting experimental

investigations, in addition to the novel expression and control of vortex arrays. One such experiment may be the measurement of the quantum cores of optical phase singularities [86].

CHAPTER 6 – SYMMETRY TRANSFORMATION PROPERTIES EXPRESS POLARIZATION SINGULARITIES IN BLOCH MODE SYSTEMS

6.1 Introduction

The state of polarization of the electromagnetic field is one of its most fundamental properties, quantifying the vectorial character of the optical response of systems ranging from the simple to the complex. In general, it is a spatially-dependent quantity, represented by an ellipse extracted at every point by mapping the modulation of the field vector over a temporal period. The polarization state is circumscribed by three distinct types of singularities: pure circular polarization (indeterminate ellipse rotation angle); pure linear polarization (indeterminate polarization handedness); and disclinations (indeterminate polarization direction with a concomitant vanishing field). Polarization singularities in transverse electromagnetic fields were first discussed in depth by Hajnal [87]. A generalization to random vector fields was performed by Berry and Dennis [88]. However, it appears that no formal treatment of polarization singularities in optical systems of high symmetry has yet been reported. We demonstrate, based on an analytic approach derived from group theory, that symmetry transformation properties allow us to map the general states of local polarization. Furthermore, we reveal how polarization singularities are expressed, noting that a system's symmetry will constrain local states of polarization to subsets of the system's polarization response. A linear two-dimensional photonic crystal is used to demonstrate the theoretical method, since it has complex symmetry properties and tractable analytic solutions in the vanishing dielectric contrast limit. Because the results are inherent to system symmetry, they are invariant to dielectric contrast and the mode order of the same irreducible representation. This invariance to dielectric contrast will be demonstrated by comparing the group theoretic predictions to numerical simulations of high dielectric contrast two-dimensional photonic

crystals and photonic crystal slabs. Our approach provides an important tool for understanding the polarization response of structured complex optical systems. To the best of our knowledge, ours is the first report quantifying the predictive power of group theory in describing the local states of polarization in optical systems with discrete symmetry 4-5. Previous reports have noted polarization singularities in such periodic systems as optical lattices [89], including polarization gradients in photonic crystals [53], but without formal reference to symmetry and its field impact.

In Chapter 3, we introduced the formal language of group theory in the context of the Bloch mode, whereby we classified the optical Bloch modes according to the irreducible representations of the point groups; this quantified the global transformation properties (see Section 3.3). In addition, we established that group-theoretic concepts of site (local) symmetry may be applied to the study of photonic crystals and their eigenmodes (see Section 3.5). These concepts are commonly applied to conventional solid state physics and molecular chemistry problems, but they had yet to be applied to the field of photonic crystals. In this chapter, we further develop in three stages, the application of site symmetry to the local state of polarization of photonic crystal eigenmodes. First, we examine the global transformation properties of the local state of polarization, whereby it is shown that when a photonic crystal eigenmode is transformed by the operators of its **k**-group, the sense of rotation of the local state of polarization (i.e., left-handed or right-handed polarization) remains invariant. Second, we reveal how a specific point within the electromagnetic field, with a given local polarization state, transforms under the operators of the photonic crystal's eigenmode space **k**-group, whereby we are able to define the crystallographic orbits of the local field vectors. Furthermore, we express the eigenmode's fundamental domain from which the entire mode can be constructed. Third, we demonstrate that particular polarization singularities must appear at those positions associated with special Wyckoff positions, where the site symmetry (the sets of all symmetry operators that leave the local field vector spatially invariant) contains at least one element in addition to the identity operation.

6.2 Group theory and the symmetry transformation properties of Bloch modes and its associated electric field

To establish the general transformation properties of the local state of polarization, we restrict ourselves to the purely two-dimensional TE photonic crystal eigenmodes of Eq. (2.28). The eigenfunctions of the operator Eq. (2.28) are the magnetic fields, $\mathbf{H}_{\mathbf{k}n}(\mathbf{r})$ given by Eq. (2.30) (see Section 2.4.1), whose polarization is always parallel to the *z*-axis. The corresponding electric field, $\mathbf{E}_{\mathbf{k}n}(\mathbf{r})$, may be determined directly from the curl of the magnetic field (see Eq. (3.41)), and its polarization must thus lie within the *x*-*y* plane. In Section 3.3.2, we defined the irreducible matrix representations $\vec{D}^{(\nu)}(R)$ of the photonic crystal transformation operators *R*, in which the photonic crystal eigenmodes are the partner functions, where ν denotes the irreducible representation. For simplicity, we have restricted ourselves to nondegenerate modes, $l=1$, whereby we may obtain $\chi_R^{(\nu)}$ directly from known character tables, obviating matrix determination, since now $\chi_R^{(\nu)} = \vec{D}^{(\nu)}(R)$ (see Section 3.3.2). If $\mathbf{F}^{(\nu)}(\mathbf{r})$ is a partner function to one of the irreducible matrix representations, $\vec{D}^{(\nu)}(R) = \chi_R^{(\nu)}$, of the photonic crystal eigenmode **k**-group, then Eq. (3.38) provides the symmetry transformation relation,

$$R\mathbf{F}^{(\nu)}(\mathbf{r}) = \chi_R^{(\nu)}\mathbf{F}^{(\nu)}(\mathbf{r}). \tag{6.1}$$

where $R \in C_{n\nu}$. Equation (6.1) holds for $\mathbf{H}_{\mathbf{k},n}(\mathbf{r})$ and its assoicated $\mathbf{E}_{\mathbf{k},n}(\mathbf{r})$, with their k-group, $C_{n\nu}$, fixed by the choice of $[\varepsilon(\mathbf{r}),\mathbf{k}]$. Their characters are related by

$$\chi_R^{(\nu\to\mathbf{E})} = \left(\det \vec{R}\right)\chi_R^{(w\to\mathbf{H})}, \tag{6.2}$$

where v and w denote the irreducible representations for the electric and magnetic fields respectively (see Section 3.3.3). Note that $\det \ddot{R} = 1$ for proper transformations (rotation operators, C_n), and $\det \ddot{R} = -1$ for improper transformations (reflection operators, σ_y).

As in the case of phase singularities in Chapter 5, we again consider a two-dimensional photonic crystal and we examine eigenmodes of a hexagonal lattice (see Figure 9(a)) and of a square lattice (see Figure 9(b)). For the hexagonal lattice, we chose to examine the fundamental mode ($n=1$) at the K point, $\mathbf{k} = \hat{\mathbf{x}}(4\pi/3a)$ (see Figure 10(a)). The **k**-group associated with this eigenmode is $C_{3v} = \{E, 2C_3, 3\sigma_y\}$, where the magnetic field is associated with the A_1 irreducible representation and the electric field is associated with the A_2 irreducible representation (see Section 3.3.3). We exploit the vanishing dielectric contrast approximation to access a simple analytic form (see Section 2.4.2):

$$\{A_1\}: \qquad \mathbf{H}_{\mathbf{k}1}(\mathbf{r}) = \begin{pmatrix} 0 \\ 0 \\ 1 \end{pmatrix} H_{\mathbf{k}1}(0)\left(1 + e^{-i2\pi\left(x/a - y/\left(\sqrt{3}a\right)\right)} + e^{-i2\pi\left(x/a + y/\left(\sqrt{3}a\right)\right)}\right) e^{ix(4\pi/3a)}, \tag{6.3}$$

where $H_{\mathbf{k}1}(0)$ is an arbitrary scaling coefficient and the vector components are in column matrix form. From Eqs. (6.3) and (3.41), we obtain the associated electric field:

$$\{A_2\}: \quad \mathbf{E}(\mathbf{r}) = \frac{-4\pi H_{\mathbf{k}1}(0)}{3a\omega\varepsilon_0\varepsilon}\left[\begin{pmatrix} 0 \\ 2 \\ 0 \end{pmatrix} e^{i4\pi x/3a} + \begin{pmatrix} -\sqrt{3} \\ -1 \\ 0 \end{pmatrix} e^{-i2\pi\left(x/3a - y/\left(\sqrt{3}a\right)\right)} + \begin{pmatrix} \sqrt{3} \\ -1 \\ 0 \end{pmatrix} e^{-i2\pi\left(x/3a + y/\left(\sqrt{3}a\right)\right)}\right]. \tag{6.4}$$

For the square lattice, we chose to examine the fundamental mode ($n=1$) at the M point, $\mathbf{k} = \hat{\mathbf{x}}(\pi/a) + \hat{\mathbf{y}}(\pi/a)$ (see Figure 10(b)). The **k**-group associated with this eigenmode is $C_{4v} = \{E, C_4, C_4^{-1}, C_2, \sigma_x, \sigma_y, \sigma_d', \sigma_d''\}$, where the magnetic field is associated

with the A_1 irreducible representation and the electric field is associated with the A_2 irreducible representation. Again, we use the vanishing dielectric contrast approximation, to access the simple analytic form (see Section 2.4.2):

$$\{A_1\}: \qquad \mathbf{H}_{\mathbf{k},1}(\mathbf{r}) = \begin{pmatrix} 0 \\ 0 \\ 1 \end{pmatrix} H_{\mathbf{k}1}(0)\left(e^{i\pi(x/a+y/a)} + e^{i\pi(-x/a+y/a)} + e^{i\pi(x/a-y/a)} + e^{i\pi(-x/a-y/a)}\right), \tag{6.5}$$

and from Eqs. (6.5) and (3.41), we obtain the associated electric field:

$$\{A_2\} \qquad \mathbf{E}_{\mathbf{k}1}(\mathbf{r}) = \frac{-\pi H_{\mathbf{k}1}(0)}{a\omega\varepsilon_0\varepsilon}\left[\begin{pmatrix} 1 \\ -1 \\ 0 \end{pmatrix} e^{i(\pi x/a+\pi y/a)} + \begin{pmatrix} 1 \\ 1 \\ 0 \end{pmatrix} e^{i(-\pi x/a+\pi y/a)} + \begin{pmatrix} -1 \\ -1 \\ 0 \end{pmatrix} e^{i(\pi x/a-\pi y/a)} + \begin{pmatrix} -1 \\ 1 \\ 0 \end{pmatrix} e^{-i\pi(x/a+y/a)}\right]. \tag{6.6}$$

In this chapter, we focus on the electric field, because it has a nontrivial polarization state when transformed in the *x*-*y* plane.

In Section 3.5, the concepts of site symmetry groups, crystallographic orbits, and the fundamental domain were applied to the dielectric profile of a photonic crystal. The application of these concepts to photonic crystal eigenmodes is more complex because they are full vector functions, this is the focus of Sections 6.4.3 and 6.4.4. The global symmetry transformation properties of a Bloch mode about the principal axis are given by Eq. (6.1), where the character $\chi_R^{(\nu)}$ of the irreducible matrix representation associated with the Bloch mode quantifies the transformation. These symmetry transformation properties remain invariant to lateral shifts of the principal axis when it is shifted by a lattice vector **R** (i.e., all points of the crystallographic orbit where the origin is the

generating point). If a symmetry transformation R acts with respect to an axis located a distance $\mathbf{d}$ away from the principal axis, we can define transformation of $\mathbf{F}^{(\nu)}(\mathbf{r})$ by

$$\left(R|\mathbf{d}-R\mathbf{d}\right)\mathbf{F}^{(\nu)}(\mathbf{r})=e^{i\mathbf{k}\cdot\left(\mathbf{d}-R^{-1}\mathbf{d}\right)}\chi_R^{(\nu)}\mathbf{F}^{(\nu)}(\mathbf{r}), \tag{6.7}$$

where $\left(R|\mathbf{d}-R\mathbf{d}\right)\in G_{\mathbf{k}}$, $\mathbf{d}$ is any distance such that $\mathbf{R}'=\mathbf{d}-R^{-1}\mathbf{d}$ is a lattice vector and $\chi_R^{(\nu)}$ is the same character from Eq. (6.1) (see Section 3.5.4, Eq. (3.112)). Equation (6.7) holds for $\mathbf{H}_{\mathbf{k},n}(\mathbf{r})$ and its assoicated $\mathbf{E}_{\mathbf{k},n}(\mathbf{r})$, with their space **k**-group, $G_{\mathbf{k}}$, fixed by the choice of $\left[\varepsilon(\mathbf{r}),\mathbf{k}\right]$. In Section 6.4.3, we will find that the global transformation properties of the electric field are closely related to the transformation properties of individual points in the electric field. This is the primary motivation for determining the global transformation properties at points other than the principal axis.

6.3 Expressing polarization: local variation and the existence of singularities

6.3.1 The local polarization state

To quantify the local state of polarization, we note that the electric field is complex, whence

$$\mathbf{E}(\mathbf{r})=\mathbf{P}(\mathbf{r})+i\mathbf{Q}(\mathbf{r}), \tag{6.8}$$

where $\mathbf{P}(\mathbf{r})$ is the spatially dependent real part of the field and $\mathbf{Q}(\mathbf{r})$ is the spatially dependent imaginary part of the field. The two parts $\mathbf{P}(\mathbf{r})$ and $\mathbf{Q}(\mathbf{r})$ are not necessarily orthogonal, but if we define $\mathbf{a}(\mathbf{r})$ and $\mathbf{b}(\mathbf{r})$ such that

$$\left[\mathbf{P}(\mathbf{r})+i\mathbf{Q}(\mathbf{r})\right]=\left[\mathbf{a}(\mathbf{r})+i\mathbf{b}(\mathbf{r})\right]e^{i\tau(\mathbf{r})}, \tag{6.9}$$

a judicious choice of the phase angle,

$$\tau(\mathbf{r})=\tfrac{1}{2}\tan^{-1}\left[2\mathbf{P}(\mathbf{r})\cdot\mathbf{Q}(\mathbf{r})/\left(\mathbf{P}^2(\mathbf{r})-\mathbf{Q}^2(\mathbf{r})\right)\right]+n_{\mathbf{r}}\pi \tag{6.10}$$

will ensure $\mathbf{a}(\mathbf{r})\perp\mathbf{b}(\mathbf{r})$, where $n_{\mathbf{r}}$ is a spatially dependent integer ([102], p. 35; [85], p. 272). This spatially dependent integer, $n_{\mathbf{r}}$, is chosen to make certain $|\mathbf{a}|\geq|\mathbf{b}|$ at each point in the field. Note that $\tau(\mathbf{r})$ is not necessarily continuously cyclical within an electric field because it is just an orthogonality constant. Given in terms of $\mathbf{P}(\mathbf{r})$, $\mathbf{Q}(\mathbf{r})$ and $\tau(\mathbf{r})$, $\mathbf{a}(\mathbf{r})$ and $\mathbf{b}(\mathbf{r})$ are

$$\mathbf{a}(\mathbf{r})=\mathbf{P}(\mathbf{r})\cos\left[\tau(\mathbf{r})\right]+\mathbf{Q}(\mathbf{r})\sin\left[\tau(\mathbf{r})\right], \tag{6.11}$$

$$\mathbf{b}(\mathbf{r})=-\mathbf{P}(\mathbf{r})\sin\left[\tau(\mathbf{r})\right]+\mathbf{Q}(\mathbf{r})\cos\left[\tau(\mathbf{r})\right]. \tag{6.12}$$

Finally, the spatially varying, time-dependent electric field is determined by substituting Eq. (6.9) into Eq. (2.13):

$$\begin{aligned}\mathbf{E}(\mathbf{r},t)&=\mathrm{Re}\left[\left[\mathbf{a}(\mathbf{r})+i\mathbf{b}(\mathbf{r})\right]e^{i\tau(\mathbf{r})}e^{-i\omega t}\right]\\ \mathbf{E}(\mathbf{r},t)&=\mathbf{a}(\mathbf{r})\cos\left[\tau(\mathbf{r})-\omega t\right]+\mathbf{b}(\mathbf{r})\sin\left[\tau(\mathbf{r})-\omega t\right]\end{aligned} \tag{6.13}$$

These vectors $\mathbf{a}(\mathbf{r})$ and $\mathbf{b}(\mathbf{r})$ are the semi-major and semi-minor axes, respectively, of polarization ellipses in the time domain, given by Eq. (6.13), and uniquely defined at every field location (or undefined at a polarization singularity, further discussed below). The tilt of the polarization ellipse, $\gamma(\mathbf{r})$ (with respect to the x-axis), is quantified by

$$\gamma(\mathbf{r}) = \tan^{-1}\left[a_y(\mathbf{r})/a_x(\mathbf{r})\right], \tag{6.14}$$

where $a_x(\mathbf{r})$ and $a_y(\mathbf{r})$ are the $\hat{\mathbf{x}}$ and $\hat{\mathbf{y}}$ components of $\mathbf{a}(\mathbf{r})$ respectively. To demonstrate that the polarization state may indeed exhibit an intrinsically rich and spatially varying character, intimately connected with the underlying symmetry of the structure within which the optical mode propagates, we have generated the polarization ellipses for the fundamental mode of a two-dimensional hexagonal photonic crystal. At the K point, the optical mode is described by Eq. (6.4) in the vanishing contrast limit, and is placed into the form given by Eq. (6.13) before plotting. The result is shown in Figure 37(a) by the blue ellipses, which were generated for an equally-spaced array of points by mapping the tip of the electric field vectors over one temporal period, where a common major axis length has been imposed for clarity. The large grey circles are the putative locations of the hexagonally arrayed cylinders. The direction of polarization is determined from

$$\mathbf{P}(\mathbf{r})\times\mathbf{Q}(\mathbf{r}), \tag{6.15}$$

which is perpendicular to the plane defined by the polarization ellipse (Eq. (6.13)). Since the state of polarization of the electric field is restricted to the *x*-*y* plane for this discussion, Eq. (6.15) is restricted to the $\hat{\mathbf{z}}$ direction. The $\hat{\mathbf{z}}$ component of Eq. (6.15) is positive for the left-hand polarization (i.e., the state of polarization rotates counterclockwise in the time domain, for an observer, whose eye the light is entering), and negative for the right-hand polarization (i.e., the state of polarization rotates clockwise in the time domain, for an observer, whose eye the light is entering), as shown in Figure 37(b). Figure 38(a) reveals the actual magnitude of the electric field, for comparison. Similarly, we have generated the polarization ellipses for the fundamental mode of a two-dimensional square photonic crystal at the M point, as described by Eq. (6.6) in the vanishing contrast limit. Figure 39(a) and Figure 39(b) display the local state of polarization, which is linear everywhere, and the resulting $\mathbf{P}(\mathbf{r})\times\mathbf{Q}(\mathbf{r}) = 0$

$(\mathbf{P}(\mathbf{r})\times\mathbf{Q}(\mathbf{r})=0$ is explained in the context of L lines, see Section 6.4.3). Figure 40(a) reveals the magnitude of the electric field. Further discussion follows below.

6.3.2 Singularities in the local state of polarization

The local state of polarization may be undefined with respect to its mathematical descriptors at distinct locations, $\mathbf{r}_0$. These points are known as polarization singularities and three types have been noted: C points, L lines and disclinations ([85], pp. 271-291). We now illustrate their existence explicitly from the modal response of our optical systems, deferring discussion of system symmetries to the following section.

C points are generally individual points in space, $\mathbf{r}_0$, (inclusively, lines at higher dimension) where the local state of polarization is circular, whence $\tau(\mathbf{r}_0)$ is undefined and from Eqs. (6.11)-(6.12) $\mathbf{a}(\mathbf{r}_0)$, $\mathbf{b}(\mathbf{r}_0)$ are also undefined. From Eq. (6.10), $\mathbf{P}(\mathbf{r}_0)\cdot\mathbf{Q}(\mathbf{r}_0)=\mathbf{P}(\mathbf{r}_0)^2-\mathbf{Q}(\mathbf{r}_0)^2=0$ in consequence. For the hexagonal lattice, in Figure 37(a), the C points of the electric field are marked as red circles. These locations correspond, in Figure 37(b), to extrema in $\mathbf{P}(\mathbf{r})\times\mathbf{Q}(\mathbf{r})$. Alternatively, we can plot the phase term $\tau(\mathbf{r})$, which ranged in value from ± 0.785 and $n_r=0$ for the entire field. The C points occur at a dislocation in $\tau(\mathbf{r})$ (see Figure 38(b)) (i.e. where $\tau(\mathbf{r})$ is discontinuous), but we note that this discontinunity does not go from π to $-\pi$, such as the phase singularities of Chapter 5, because $\tau(\mathbf{r})$ is not required to be continuously cyclical in the field. There are no C points in the square lattice.

L lines are continuous arrays of points in space (inclusively, planes at higher dimension) where the local state of polarization is linear. On an L line, $\mathbf{b}(\mathbf{r}_0)=0$ and the direction of the vector normal to the ellipse must vanish, $\mathbf{P}(\mathbf{r}_0)\times\mathbf{Q}(\mathbf{r}_0)=0$. This may occur when

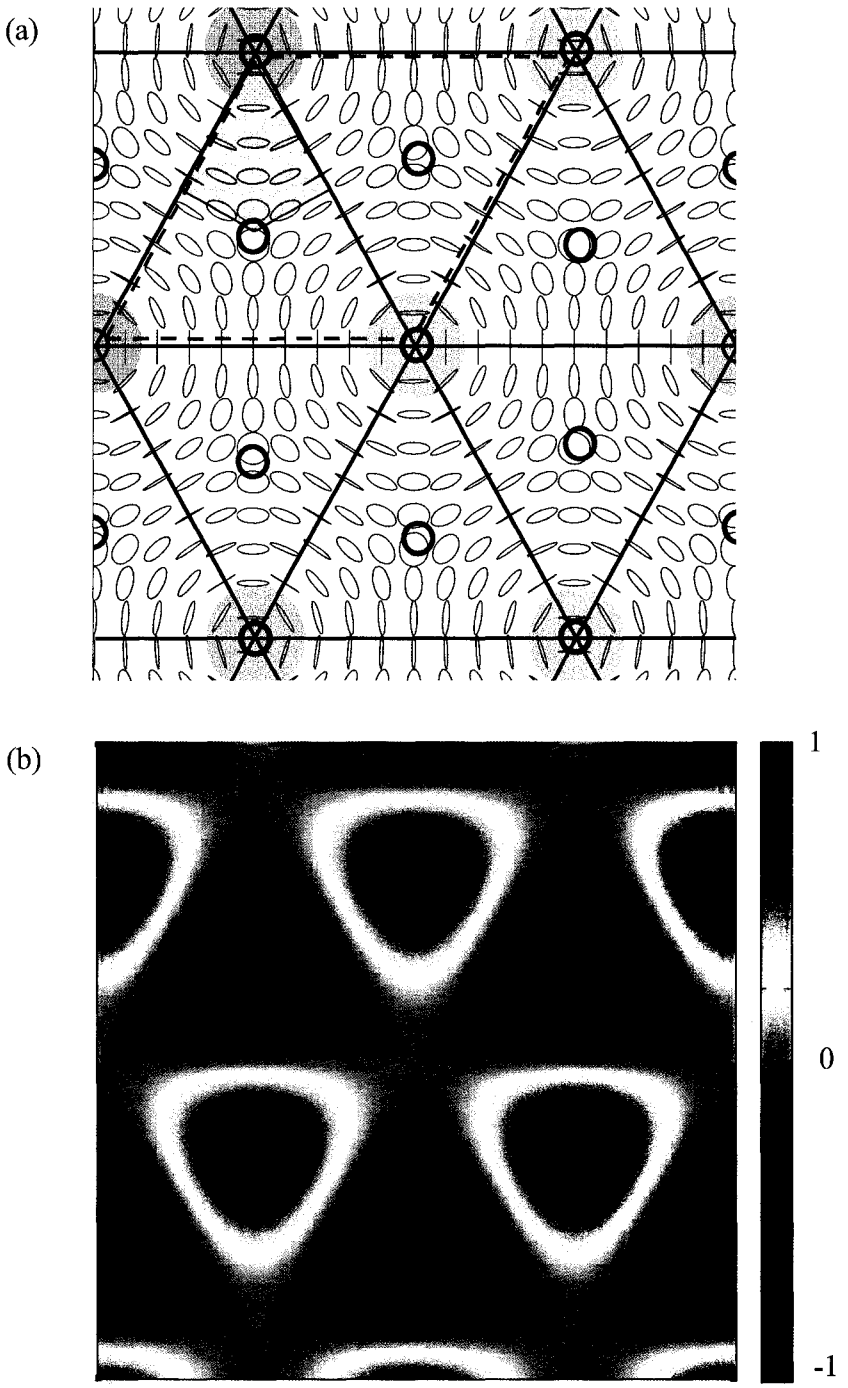

Figure 37. Polarization response for the electric field associated with the A_2 irreducible representation of C_{3v}. (a) Calculated local polarization states: polarization ellipses (blue), dielectric columns (closed grey circles), linear polarization (black lines), circular polarization (red circles) disclinations (green circles); the primitive unit cell is delineated by the dashed red lines and the fundamental domain is shown in gold; (b) $\mathbf{P}(\mathbf{r})\times\mathbf{Q}(\mathbf{r})$.

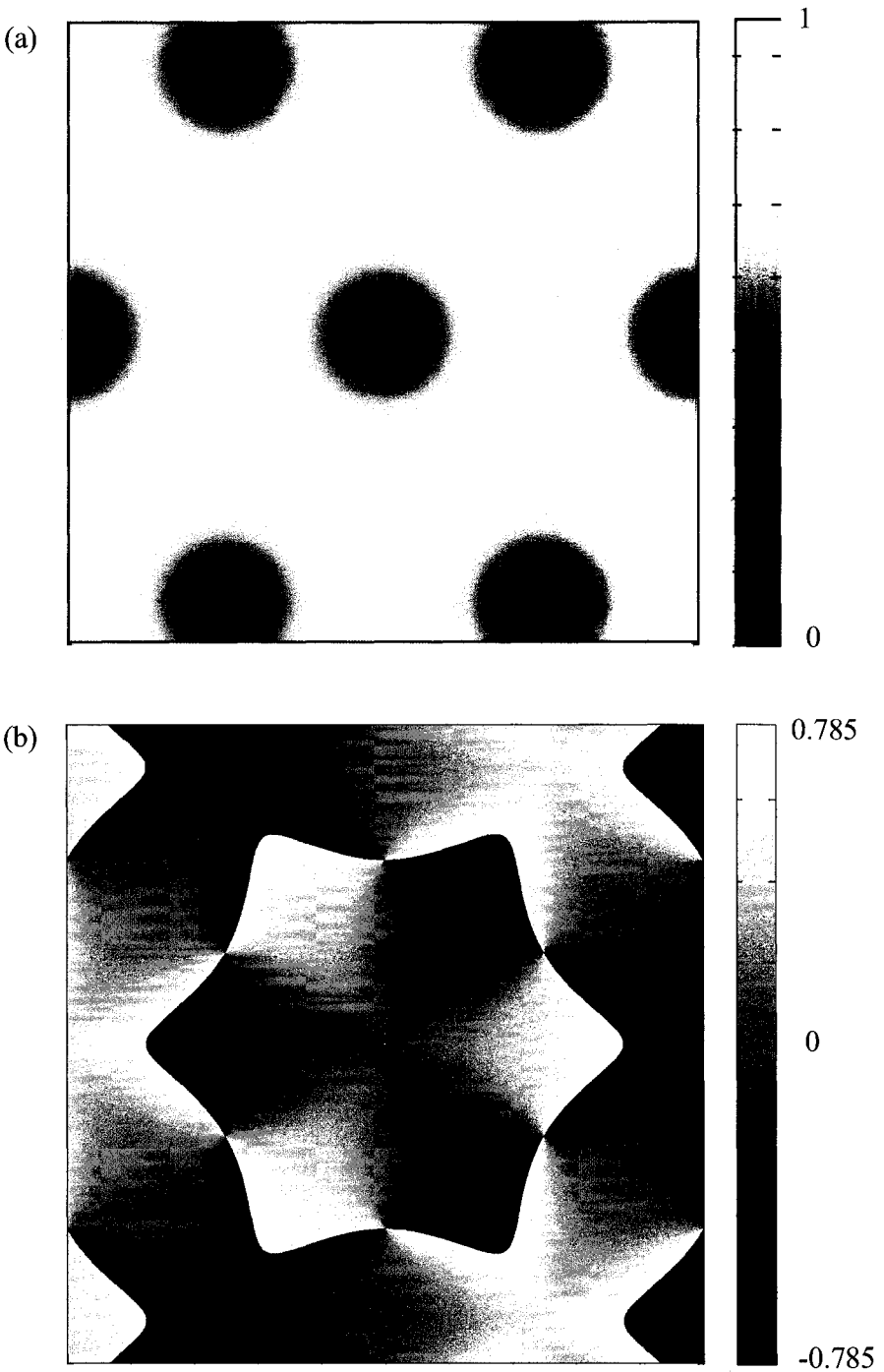

Figure 38. Polarization response for the electric field associated with the A_2 irreducible representation of C_{3v}. (a) Magnitude of the electric field $\sqrt{\mathbf{E}\bullet\mathbf{E}}$, arbitrary units; (b) Phase angle $\tau(\mathbf{r})$ that ensures $\mathbf{a}(\mathbf{r}) \perp \mathbf{b}(\mathbf{r})$ in units of radians, which is discontinuous at C points and disclinations.

either $\mathbf{P}(\mathbf{r}_0)$ or $\mathbf{Q}(\mathbf{r}_0)$ vanish, or are (anti)parallel. For the hexagonal lattice, in Figure 37(a), the L lines are denoted by the straight line segments in black. These lines correspond, in Figure 37(b), to the demarcation between regions of right-handed (negative) and left-handed (positive) polarization. For the square lattice, the entire field is linearly polarized, whereby there is an L plane parallel to the *x-y* plane (see Figure 39(a)).

Disclinations are locations where the field magnitude vanishes and the local state of polarization is completely undefined. This arises because $\mathbf{P}(\mathbf{r}_0)=\mathbf{Q}(\mathbf{r}_0)=0$, and Eq. (6.10) shows $\tau(\mathbf{r}_0)$, $\mathbf{a}(\mathbf{r}_0)$, and $\mathbf{b}(\mathbf{r}_0)$ are consequently undefined, similar to C points. In the hexagonal lattice, we note that the field magnitudes vanish at the column centers (see Figure 38(a)). In the square lattice, we note that the field magnitude vanishes at the column centers and the centers of the unit cells (see Figure 40(a)). In Figure 37(a) and Figure 39(a), these locations are indicated by the green circles. Figure 38(b) reveals the disclinations are also located at dislocations in $\tau(\mathbf{r})$. In Figure 40(b), the square lattice, the dislocations are much harder to locate because $\tau(\mathbf{r})=\pi$, everywhere except at the points mentioned, where it is undefined. $\tau(\mathbf{r})=\pi$ because it is linearly polarized which means $\mathbf{b}(\mathbf{r})=0$ and in this case $n_r=1$ over the entrie electric field. In Sections 6.5, the dislocations in $\tau(\mathbf{r})$ will allow us to identify the locations of the C points and disclinations in high dielectric contrast photonic crystals.

Similar to $\tau(\mathbf{r})$, for the C points and the disclinations, the tilt of the polarization ellipse, $\gamma(\mathbf{r})$, is undefined (see Eq. (6.14)). Figure 37(a) and Figure 39(a) reveal that if we make a complete circuit about these singular points, the tilt, $\gamma(\mathbf{r})$, of the local state of polarization rotates, similar to the Poynting vector around a phase singularity (see Chapter 5). This can be made more apparent when we plot $\gamma(\mathbf{r})$ directly.

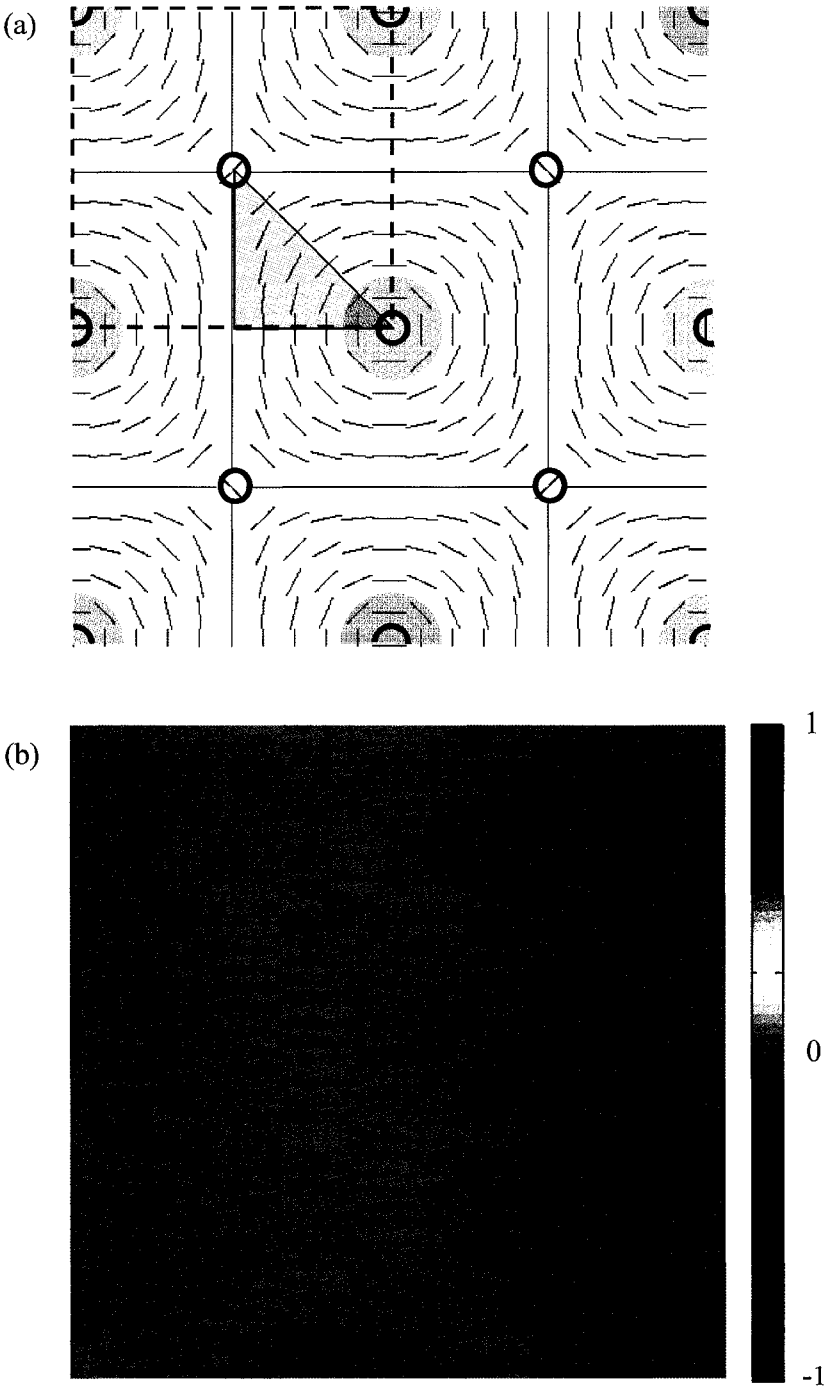

Figure 39. Polarization response for the electric field associated with the A_2 irreducible representation of C_{4v}. (a) Calculated local polarization states: polarization ellipses (blue lines), dielectric columns (closed grey circles), disclinations (green circles); the primitive unit cell is delineated by the dashed red lines and the fundamental domain is shown in gold; (b) $\mathbf{P}(\mathbf{r})\times\mathbf{Q}(\mathbf{r})=0$ everywhere.

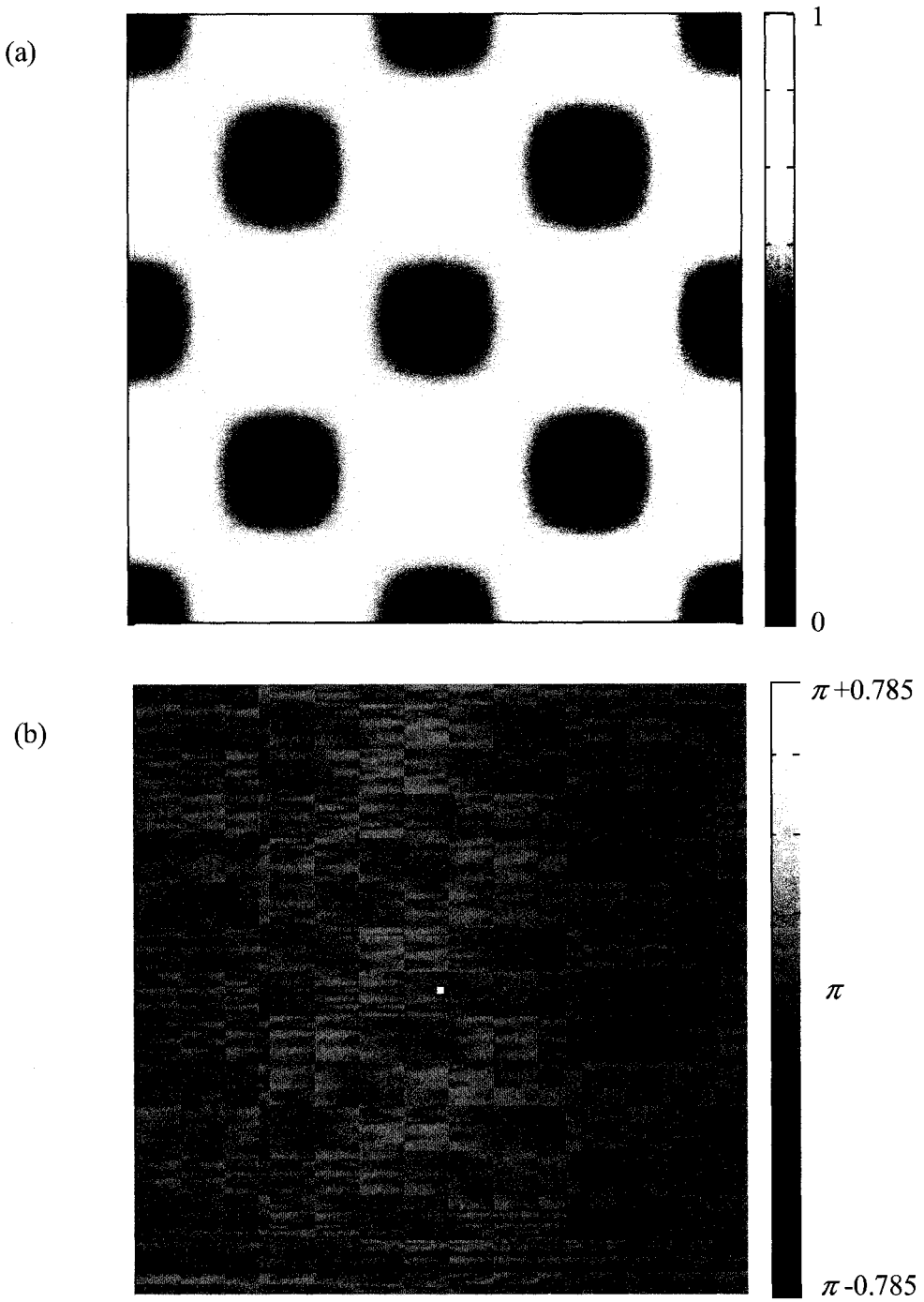

Figure 40. Polarization response for the A_2 irreducible representation of C_{4v}. (a) Magnitude of the electric field $\sqrt{\mathbf{E}\bullet\mathbf{E}}$, arbitrary units; (b) Phase angle $\tau(\mathbf{r})$ which ensures $\mathbf{a}(\mathbf{r}) \perp \mathbf{b}(\mathbf{r})$ in units of radians.

A complete circuit about these singular points reveals that $\gamma(\mathbf{r})$ goes from $\pi/2$ to $-\pi/2$ (see Figure 41(a) and Figure 41(b)), similar to the contour integral definition of vorticity (see Eq. (5.1)). Since polarization ellipses are distinguished only by a major and minor axis, the tilt, $\gamma(\mathbf{r})$, has a modulus of π. In contrast, the phase singularities of Chapter 5 were of modulus of $v2\pi$ (see Eq. (5.1)) depending on the vorticity v.

6.4 Symmetry transformation of the local state of polarization

6.4.1 Symmetry and the local state of polarization

Singularities provide a framework for establishing the spatial variation of the local polarization state from the underlying group structure. In the previous section, we employed an earlier developed group theoretic technique for deriving analytic expressions of photonic crystal modes (see Section 2.4.2), from which the local polarization states were extracted, noting singularities in particular locations. Using the photonic crystal eigenmode space **k**-group symmetry transformation properties, we now more specifically establish the following: first, the invariance of the global polarization state under point group symmetry mode transformation; second, the mapping of local polarization states via their symmetry transformations, where we establish the behaviour of the local field vectors within a crystallographic orbit; third, the specific site symmetry of distinct locations, the special Wyckoff positions, will by necessity constrain the local state of polarization to one of three types of polarization singularities.

Before we examine the properties of polarization singularities, we review the space **k**-groups for our example systems, the hexagonal lattice and the square lattice. Each space **k**-group transformation operator $(R|\mathbf{d}-R\mathbf{d})\in G_{\mathbf{k}}$ acts with respect to an axis located a distance **d** from the principal axis. In the following, we display the space **k**-group in the graphical format of the international crystallographic tables, which indicates the location, **d**, of each

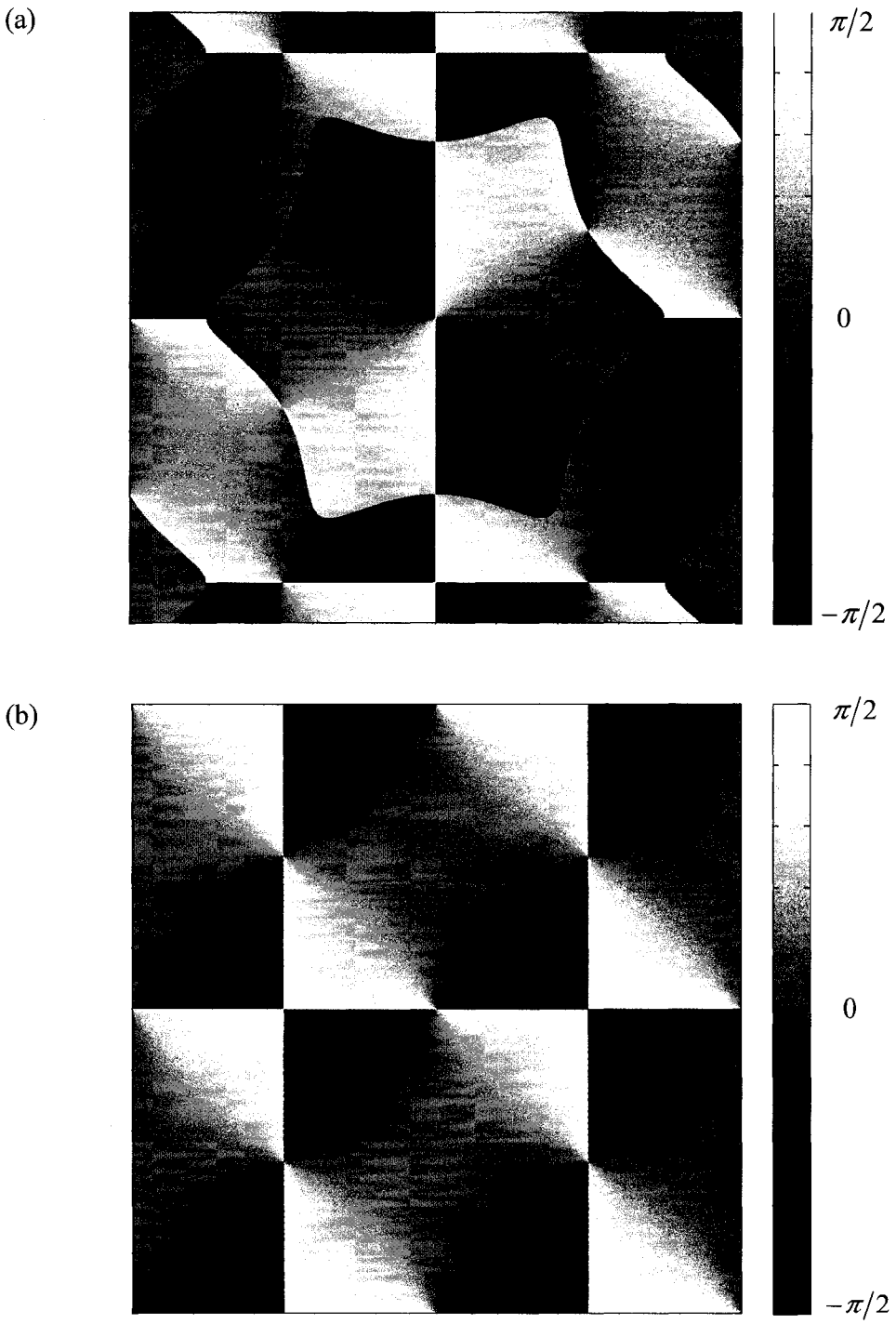

Figure 41. $\gamma(\mathbf{r})$ the tilt with respect to the $\hat{\mathbf{x}}$ axis of the polarization ellipses for (a) the electric field associated with the A_2 irreducible representation of C_{3v} and (b) the electric field associated with the A_2 irreducible representation of C_{4v}.

symmetry axis, and the set of operators $\{(R|\mathbf{d}-R\mathbf{d})\}$ that acts with respect to this axis. In Figure 42(a), the space **k**-group, $G_{\mathbf{k}}$, of the C_{3v} Bloch mode is displayed ([117], p.74). It shows the following features: the edge of the primitive unit cell (dashed line); the fundamental domain (a third of an equilateral triangle in orange); the mirror reflection segments (black lines) that form two equilateral triangles; and the axes of C_3 rotational symmetry (red triangles) which lie at the vertices of the triangles and the center. The principal axis of the unit cell is located at the point of highest site symmetry, namely the origin $(0,0)$, where the center of C_3 rotational symmetry and three mirror reflection planes intersect. There are three other symmetry equivalent points to the principal axis which lie at the vertices of the mirror reflection segments equilateral triangles. The transformation properties of the eigenmodes with respect to principal axis and its three symmetry equivalent points is given by Eq. (6.1) or the more general Eq. (6.7). The two other axes located at the centers of the equilateral triangles are not symmetry equivalent to the principal axis. As result, the transformation properties of the eigenmodes with respect to these axes are given by the more general form Eq. (6.7). Similarly in Figure 42(b), the space **k**-group, $G_{\mathbf{k}}$, of the C_{4v} Bloch mode is displayed ([117], p. 70). It shows the following features: the edge of the primitive unit cell (dashed line); the fundamental domain (an eighth of a square in orange); the mirror reflection segments (black lines) that form four smaller squares within the unit cell; the centers of C_4 rotational symmetry (red squares) at the vertices of the mirror reflection plane squares; and the centers of C_2 rotational symmetry (red ellipses) between the vertices of the mirror reflection plane squares. The principal axis is located at the edge of the unit cell, the origin $(0,0)$, where the center of C_4 rotational symmetry and three mirror reflection planes intersect. There are three other symmetry equivalent points to the principal axis located at the other edges of the unit cell. Note, at the center of the unit cell, there is an addition point with the same site symmetry as the principal axis C_{4v}.

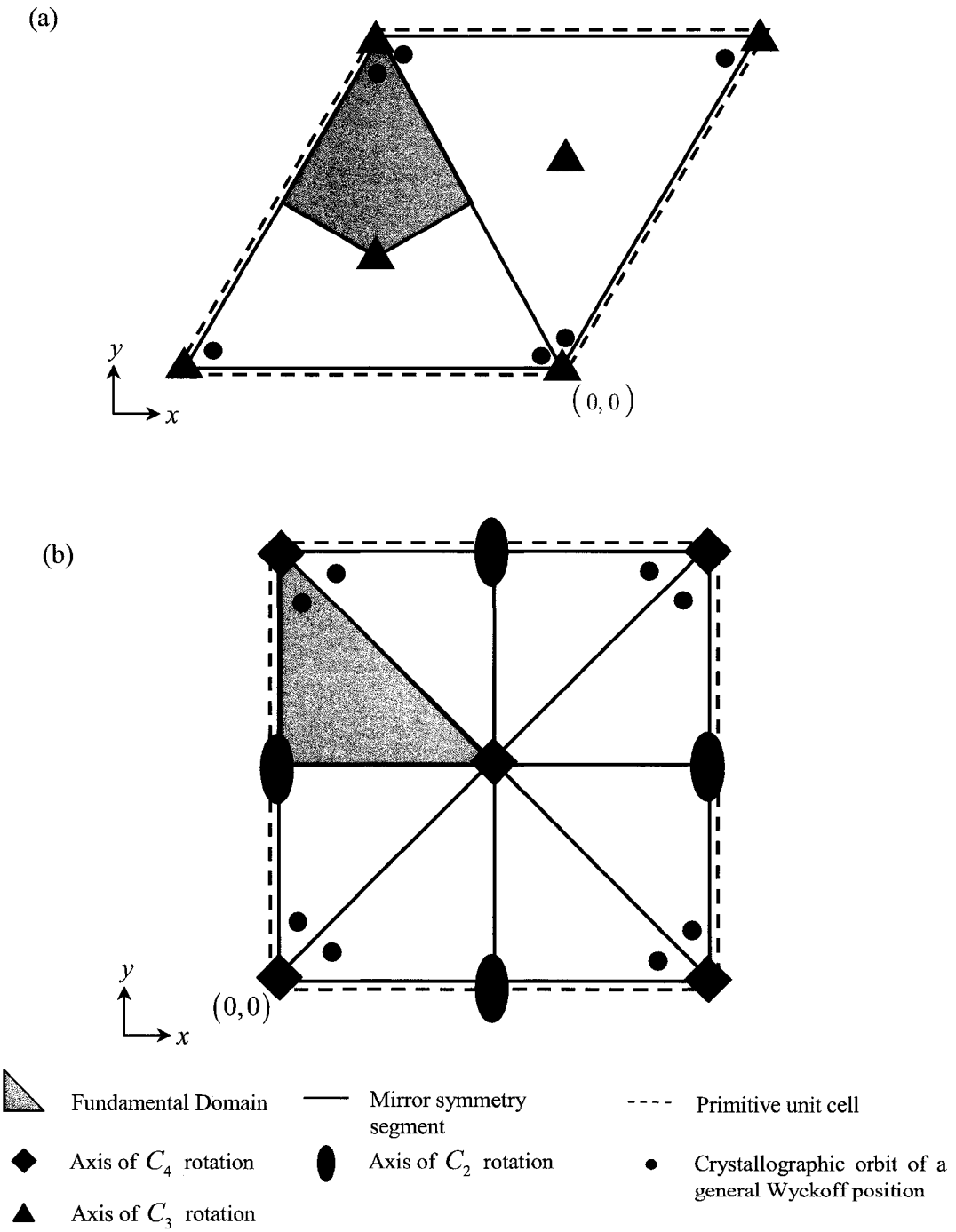

Figure 42. Primitive unit cell: with the symmetry axes mark, fundamental domain and the positions the crystallographic orbit for a general Wyckoff position (a) of a C_{3v} hexagonal lattice, and (b) of a C_{4v} square lattice.

This point is not symmetry-equivalent to the principal axis, and in Section 6.4.4, it will be demonstrated that the character of the transformations about this point are different from the principal axis (see Eq. (6.7)).

6.4.2 The global transformation of $\mathbf{P}(\mathbf{r})\times\mathbf{Q}(\mathbf{r})$

In Figure 37(b), we presented the polarization response of the hexagonal system as a map of $\mathbf{P}(\mathbf{r})\times\mathbf{Q}(\mathbf{r})$. Inspection reveals that it clearly possesses the full space group symmetry of the mode at the K point. What are the transformation properties of this polarization metric when the photonic crystal eigenmode is transformed by operators of its space **k**-group? Consider the application of $(R|\mathbf{d}-R\mathbf{d})$ to a nondegenerate electric field mode, $\mathbf{E}(\mathbf{r})$, where $(R|\mathbf{d}-R\mathbf{d})\in G_{\mathbf{k}}$. From Eq. (6.7), and Eq. (6.8), we note that

$$\begin{aligned}(R|\mathbf{d}-R\mathbf{d})\mathbf{E}^{(\nu)}(\mathbf{r}) &= (R|\mathbf{d}-R\mathbf{d})\mathbf{P}(\mathbf{r})+i(R|\mathbf{d}-R\mathbf{d})\mathbf{Q}(\mathbf{r}) \\ &= e^{i\mathbf{k}\cdot(\mathbf{d}-R^{-1}\mathbf{d})}\chi_R^{(\nu)}(\mathbf{P}(\mathbf{r})+i\mathbf{Q}(\mathbf{r})).\end{aligned} \tag{6.16}$$

Linearity asserts that $\mathbf{P}(\mathbf{r})$ and $\mathbf{Q}(\mathbf{r})$ must have the same character, $e^{i\mathbf{k}\cdot(\mathbf{d}-R^{-1}\mathbf{d})}\chi_R^{(\nu)}$, and so they must have identical symmetry transformation properties. Thus, on mode transformation, the operator drives a corresponding transformation in the polarization response

$$(R|\mathbf{d}-R\mathbf{d})\mathbf{P}(\mathbf{r})\times(R|\mathbf{d}-R\mathbf{d})\mathbf{Q}(\mathbf{r}) = e^{i2\mathbf{k}\cdot(\mathbf{d}-R^{-1}\mathbf{d})}(\chi_R^{(\nu)})^2\,\mathbf{P}(\mathbf{r})\times\mathbf{Q}(\mathbf{r}). \tag{6.17}$$

Since $\chi_R^{(\nu)}=\pm 1$ for nondegenerate modes and $e^{i\mathbf{k}\cdot(\mathbf{d}-R^{-1}\mathbf{d})}=1$ when $\mathbf{d}=0$, $\mathbf{P}(\mathbf{r})\times\mathbf{Q}(\mathbf{r})$ will remain completely invariant to any point group transformation $(R|0)$ applied to the electric field mode, when $R\in C_{3v}$. Hence, any modal excitation that is symmetry

equivalent, *i.e.*, $(R|0)\mathbf{E}(\mathbf{r}) = \mathbf{E}'(\mathbf{r}) = \chi_R^{(\nu)}\mathbf{E}(\mathbf{r})$, has identical polarization response, $\mathbf{P}(\mathbf{r})\times\mathbf{Q}(\mathbf{r}) = \mathbf{P}'(\mathbf{r})\times\mathbf{Q}'(\mathbf{r})$.

6.4.3 Local transformation, crystallographic orbits and fundamental domains

In Section 3.5.3, we established sets of symmetry equivalent points that defined the crystallographic orbits within the dielectric profile, $\varepsilon(\mathbf{r})$, where the value of the dielectric profile was shown to be the same at each symmetry equivalent point. Similarly, we can define crystallographic orbits within the electric field, $\mathbf{E}(\mathbf{r})$. A crystallographic orbit is generated by applying all the symmetry operators $(R|\mathbf{d}-R\mathbf{d})^{-1} \in G_{\mathbf{k}}$ of the space **k**-group, $G_{\mathbf{k}}$ (see Section 3.5.4), to a point in space $\mathbf{r}_1$ (the generating point), which defines the set of symmetry equivalent points

$$(R|\mathbf{d}-R\mathbf{d})^{-1}\mathbf{r}_1 = \mathbf{r}_i, \tag{6.18}$$

where $\mathbf{r}_1, \mathbf{r}_i \in Q_{\mathbf{k}}$ ($Q_{\mathbf{k}}$ being the set of all points that comprise the crystallographic orbit). Since Eq. (6.7) must be valid at every point $\mathbf{r}_1$ within the electric field, we can define the complementary local electric field relation

$$(R|\mathbf{d}-R\mathbf{d})\mathbf{E}^{(\nu)}(\mathbf{r}_1) = e^{i\mathbf{k}\cdot(\mathbf{d}-R^{-1}\mathbf{d})}\chi_R^{(\nu)}\mathbf{E}^{(\nu)}(\mathbf{r}_1). \tag{6.19}$$

Applying the operator $(R|\mathbf{d}-R\mathbf{d})$ to the vector and scalar parts of $\mathbf{E}^{(\nu)}(\mathbf{r}_1)$ we find

$$\left((R|\mathbf{d}-R\mathbf{d})\mathbf{E}^{(\nu)}\right)\left((R|\mathbf{d}-R\mathbf{d})^{-1}\mathbf{r}_1\right) = e^{i\mathbf{k}\cdot(\mathbf{d}-R^{-1}\mathbf{d})}\chi_R^{(\nu)}\mathbf{E}^{(\nu)}(\mathbf{r}_1), \tag{6.20}$$

and upon substituting Eq. (6.18) into Eq. (6.20) we find

$$\left(\left(R\middle|\mathbf{d}-R\mathbf{d}\right)\mathbf{E}\right)^{(\nu)}(\mathbf{r}_i)=e^{i\mathbf{k}\cdot\left(\mathbf{d}-R^{-1}\mathbf{d}\right)}\chi_R^{(\nu)}\,\mathbf{E}^{(\nu)}(\mathbf{r}_1). \tag{6.21}$$

Therefore, Eq. (6.21) defines the relationship between the local electric field vector $\mathbf{E}^{(\nu)}(\mathbf{r}_1)$ at $\mathbf{r}_1$ and the local electric field vector, $\mathbf{E}^{(\nu)}(\mathbf{r}_i)$, at its symmetry equivalent points $\mathbf{r}_i \in Q_{\mathbf{k}}$. Since every point in the electric field can be associated with a crystallographic orbit, this allows us to quantify the local transformation properties of the entire electric field.

To examine Eq. (6.21) explicitly, we expand the local electric field at $\mathbf{r}_1$ into its components

$$\mathbf{E}^{(\nu)}(\mathbf{r}_1)=E_x(\mathbf{r}_1)\,\hat{\mathbf{x}}+E_y(\mathbf{r}_1)\,\hat{\mathbf{y}}+E_z(\mathbf{r}_1)\,\hat{\mathbf{z}}. \tag{6.22}$$

The application of $\left(R\middle|\mathbf{d}-R\mathbf{d}\right)$ to Eq. (6.22) allows us to examine the transformation of the local electric field (the left-hand side of Eq. (6.21)) in more detail:

$$\begin{aligned}\left(R\middle|\mathbf{d}-R\mathbf{d}\right)\mathbf{E}^{(\nu)}(\mathbf{r}_1)=E_x\Big(\left(R\middle|\mathbf{d}-R\mathbf{d}\right)^{-1}\mathbf{r}_1\Big)\left(R\middle|\mathbf{d}-R\mathbf{d}\right)\hat{\mathbf{x}}+E_y\Big(\left(R\middle|\mathbf{d}-R\mathbf{d}\right)^{-1}\mathbf{r}_1\Big)\left(R\middle|\mathbf{d}-R\mathbf{d}\right)\hat{\mathbf{y}}\\ +E_z\Big(\left(R\middle|\mathbf{d}-R\mathbf{d}\right)^{-1}\mathbf{r}_1\Big)\left(R\middle|\mathbf{d}-R\mathbf{d}\right)\hat{\mathbf{z}}.\end{aligned} \tag{6.23}$$

Equation (6.23) is the analog to Eq. (3.21), for the space **k**-group. Substituting Eq. (6.18) into Eq. (6.23), we can transform the scalar components:

$$\begin{aligned}\left(R\middle|\mathbf{d}-R\mathbf{d}\right)\mathbf{E}^{(\nu)}(\mathbf{r}_1)=E_x(\mathbf{r}_i)\left(R\middle|\mathbf{d}-R\mathbf{d}\right)\hat{\mathbf{x}}+E_y(\mathbf{r}_i)\left(R\middle|\mathbf{d}-R\mathbf{d}\right)\hat{\mathbf{y}}\\ +E_z(\mathbf{r}_i)\left(R\middle|\mathbf{d}-R\mathbf{d}\right)\hat{\mathbf{z}}.\end{aligned} \tag{6.24}$$

The application of $\left(R|\mathbf{d}-R\mathbf{d}\right)$ to the unit vectors of $\mathbf{E}^{(\nu)}(\mathbf{r}_i)$ can be expanded as

$$\left(R|\mathbf{d}-R\mathbf{d}\right)\hat{\mathbf{x}}_i=\hat{\mathbf{x}}_i'=\sum_j R_{ji}\hat{\mathbf{x}}_j+\mathbf{R}', \tag{6.25}$$

where $\hat{\mathbf{x}}_1=\hat{\mathbf{x}}$, $\hat{\mathbf{x}}_2=\hat{\mathbf{y}}$, $\hat{\mathbf{x}}_3=\hat{\mathbf{z}}$ and $\mathbf{R}'=\mathbf{d}-R\mathbf{d}$ ($\mathbf{R}'$ is a lattice vector) (see Section 3.5.2). The point operators $\vec{R}$ (where R_{ji} is an element) are similarity transformations (see Section 3.3.1), which means the length of the unit vector $\hat{\mathbf{x}}_i$ remains unchanged (this will be shown explicitly for the local electric field below). Additionally, any lateral shift of a unit vector, $\hat{\mathbf{x}}_i$, by a lattice vector, such as $\mathbf{R}'$, creates an equivalent unit vector, because the origin (principal axis) of the second unit vector is renormalized by a lattice vector; in a periodic system, axes separated by lattice vectors are equivalent (see Section 3.5.3). As a result, when we examine transformations of the vector part of the local electric field, $\mathbf{E}^{(\nu)}(\mathbf{r}_1)$, we may focus on the effects of the point operator $\vec{R}$.

The left-hand side and right-hand side of Eq. (6.21) are both complex vectors, where the components from both sides must be equivalent and the magnitude of both sides must be equal. The magnitude of the left-hand side of Eq. (6.21) is

$$\left|\left(\left(R|\mathbf{d}-R\mathbf{d}\right)\mathbf{E}\right)^{(\nu)}(\mathbf{r}_i)\right|=\sqrt{\left\{\left(\left(R|\mathbf{d}-R\mathbf{d}\right)\mathbf{E}\right)^{(\nu)}(\mathbf{r}_i)\right\}^*\cdot\left\{\left(\left(R|\mathbf{d}-R\mathbf{d}\right)\mathbf{E}\right)^{(\nu)}(\mathbf{r}_i)\right\}}. \tag{6.26}$$

Substituting Eq. (6.24) into Eq. (6.26) we find

$$\left|\left(\left(R\middle|\mathbf{d}-R\mathbf{d}\right)\mathbf{E}\right)^{(\nu)}(\mathbf{r}_i)\right| = \sqrt{E_x^*(\mathbf{r}_i)E_x(\mathbf{r}_i)+E_y^*(\mathbf{r}_i)E_y(\mathbf{r}_i)+E_z^*(\mathbf{r}_i)E_z(\mathbf{r}_i)} = \left|\mathbf{E}^{(\nu)}(\mathbf{r}_i)\right|, \tag{6.27}$$

which demonstrates that the magnitude of a vector when transformed by $\left(R\middle|\mathbf{d}-R\mathbf{d}\right)$, a similarity transformation is invariant. Similarly, we can find the magnitude of the right-hand side of Eq. (6.21)

$$\left|e^{i\mathbf{k}\cdot\left(\mathbf{d}-R^{-1}\mathbf{d}\right)}\chi_R^{(\nu)}\mathbf{E}^{(\nu)}(\mathbf{r}_1)\right| = \sqrt{\left\{e^{i\mathbf{k}\cdot\left(\mathbf{d}-R^{-1}\mathbf{d}\right)}\chi_R^{(\nu)}\mathbf{E}^{(\nu)}(\mathbf{r}_1)\right\}^* \cdot \left\{e^{i\mathbf{k}\cdot\left(\mathbf{d}-R^{-1}\mathbf{d}\right)}\chi_R^{(\nu)}\mathbf{E}^{(\nu)}(\mathbf{r}_1)\right\}} = \left|\mathbf{E}^{(\nu)}(\mathbf{r}_1)\right| \tag{6.28}$$

where we have used $\chi_R^{(\nu)} = \pm 1$ (from Section 6.4.2). We can equate the magnitudes of the left-hand side, Eq. (6.27), and right-hand side, Eq. (6.28), of Eq. (6.21), where we find

$$\left|\mathbf{E}^{(\nu)}(\mathbf{r}_i)\right| = \left|\mathbf{E}^{(\nu)}(\mathbf{r}_1)\right|. \tag{6.29}$$

Therefore, the magnitude of the local electric field, $\left|\mathbf{E}^{(\nu)}(\mathbf{r}_i)\right|$, is invariant at each point $\mathbf{r}_i$ in a crystallographic orbit.

The transformation of the mode at any point, $\left(R\middle|\mathbf{d}-R\mathbf{d}\right)\mathbf{E}(\mathbf{r}_1)$, drives a corresponding transformation in the local state of polarization,

$$\left(R\middle|\mathbf{d}-R\mathbf{d}\right)\mathbf{P}(\mathbf{r}_1)\times\left(R\middle|\mathbf{d}-R\mathbf{d}\right)\mathbf{Q}(\mathbf{r}_1), \tag{6.30}$$

where $\left(R|\mathbf{d}-R\mathbf{d}\right)\in G_{\mathrm{k}}$. Applying the transformation operators to the scalar components (substitution of Eq. (6.18)) and to the vector components of Eq. (6.30) we find

$$\left(R|\mathbf{d}-R\mathbf{d}\right)\mathbf{P}(\mathbf{r}_1)\times\left(R|\mathbf{d}-R\mathbf{d}\right)\mathbf{Q}(\mathbf{r}_1)=\left(\left(R|\mathbf{d}-R\mathbf{d}\right)\mathbf{P}\right)(\mathbf{r}_i)\times\left(\left(R|\mathbf{d}-R\mathbf{d}\right)\mathbf{Q}\right)(\mathbf{r}_i), \tag{6.31}$$

where $\mathbf{r}_1,\mathbf{r}_i\in Q_{\mathrm{k}}$. From Eq. (6.17), the complementary local relation for the states of polarization is obtained

$$\begin{aligned}&\left(\left(R|\mathbf{d}-R\mathbf{d}\right)\mathbf{P}\right)\left(\left(R|\mathbf{d}-R\mathbf{d}\right)^{-1}\mathbf{r}_1\right)\times\left(\left(R|\mathbf{d}-R\mathbf{d}\right)\mathbf{Q}\right)\left(\left(R|\mathbf{d}-R\mathbf{d}\right)^{-1}\mathbf{r}_1\right)\\&\qquad=e^{i2\mathbf{k}\cdot\left(\mathbf{d}-R^{-1}\mathbf{d}\right)}\left(\chi_R^{(v)}\right)^2\mathbf{P}(\mathbf{r}_1)\times\mathbf{Q}(\mathbf{r}_1).\end{aligned} \tag{6.32}$$

Substituting Eq. (6.31) into Eq. (6.32) and noting that $\chi_R^{(v)}=\pm1$, we can express the relationship between states of local polarization, at the points $\mathbf{r}_i$ of a crystallographic orbit as

$$\left(\left(R|\mathbf{d}-R\mathbf{d}\right)\mathbf{P}\right)(\mathbf{r}_i)\times\left(\left(R|\mathbf{d}-R\mathbf{d}\right)\mathbf{Q}\right)(\mathbf{r}_i)=e^{i2\mathbf{k}\cdot\left(\mathbf{d}-R^{-1}\mathbf{d}\right)}\mathbf{P}(\mathbf{r}_1)\times\mathbf{Q}(\mathbf{r}_1). \tag{6.33}$$

where $\mathbf{r}_i\in Q_{\mathrm{k}}$. We may make this more explicit by first considering the point operator $\ddot{R}$. The cross product of any two vectors, **F** and **G**, forms a third vector $\mathbf{J}=\mathbf{F}\times\mathbf{G}$. If the two vectors **F** and **G** are transformed in space by the operator $\ddot{R}$, the cross product of the vectors $\ddot{R}\mathbf{F}$ and $\ddot{R}\mathbf{G}$ creates another vector $\mathbf{J}'=\ddot{R}\mathbf{F}\times\ddot{R}\mathbf{G}$. The vectors **J** and **J**′ are related by the transformation law for the cross product as

$$\mathbf{J}'=\left(\det\ddot{R}\right)\ddot{R}\mathbf{J}, \tag{6.34}$$

where $\ddot{R}\mathbf{J}$ is a direct transformation of the vector $\mathbf{J}$ ([103] p. 269). In this case, the electric field polarization is restricted to the *x-y* plane, and the vector $\mathbf{P}(\mathbf{r}_1)\times\mathbf{Q}(\mathbf{r}_1)$ only contains a $\hat{\mathbf{z}}$ component at any point in the field. Transformations $\ddot{R}$ within the *x-y* plane leave the vector $\mathbf{P}(\mathbf{r}_1)\times\mathbf{Q}(\mathbf{r}_1)$ (parallel to the $\hat{\mathbf{z}}$ axis) unchanged. The invariance of $\mathbf{P}(\mathbf{r}_1)\times\mathbf{Q}(\mathbf{r}_1)$ allows us to simplify Eq. (6.34), in which $\ddot{R}\mathbf{J}=\mathbf{J}$, and the cross product transformation law reduces to

$$\ddot{R}\mathbf{F}\times\ddot{R}\mathbf{G}=\left(\det\ddot{R}\right)(\mathbf{F}\times\mathbf{G}). \tag{6.35}$$

When discussing Eq. (6.25), we noted that we could focus on the point operator R, because the lateral shift $\mathbf{R}'=\mathbf{d}-R\mathbf{d}$ created equivalent unit vectors. If we now apply this to vector $\mathbf{P}(\mathbf{r}_1)\times\mathbf{Q}(\mathbf{r}_1)$, and apply the transformation law for the cross product, Eq. (6.35), Eq. (6.33) becomes

$$\left(\det\ddot{R}\right)\left(\mathbf{P}(\mathbf{r}_i)\times\mathbf{Q}(\mathbf{r}_i)\right)=e^{i2\mathbf{k}\cdot\left(\mathbf{d}-R^{-1}\mathbf{d}\right)}\mathbf{P}(\mathbf{r}_1)\times\mathbf{Q}(\mathbf{r}_1). \tag{6.36}$$

where $\det\ddot{R}=1$ for proper transformations (rotation operators, C_n), and $\det\ddot{R}=-1$ for improper transformations (reflection operators, σ_y). Using the same steps that led to Eq. (6.29), we find that polarization response magnitudes (*i.e.,* ellipticity),

$$\left|\mathbf{P}(\mathbf{r}_i)\times\mathbf{Q}(\mathbf{r}_i)\right|=\left|\mathbf{P}(\mathbf{r}_2)\times\mathbf{Q}(\mathbf{r}_2)\right|, \tag{6.37}$$

are the same for all members of the crystallographic orbit. The polarization direction, however, depends directly on the nature of the symmetry operation and the value of $e^{i2\mathbf{k}\cdot\left(\mathbf{d}-R^{-1}\mathbf{d}\right)}$. In general, for any transformation $\left(R\middle|\mathbf{d}-R\mathbf{d}\right)$ applied with respect to the principal axis ($\mathbf{d}=0$), or one of its symmetry equivalent points, where $e^{i2\mathbf{k}\cdot\left(\mathbf{d}-R^{-1}\mathbf{d}\right)}=1$. In

this case rotations will preserve the handedness ($\det\left(\vec{\vec{R}}\right)=1$), while reflections will reverse it ($\det\left(\vec{\vec{R}}\right)=-1$).

The polarization response of the field, Eq. (6.4), is shown in Figure 37(a) for the extended hexagonal lattice to more clearly reveal the symmetry. In Section 3.5.3, we determined the characters of the transformation operators of the hexagonal lattice for the C_3 site symmetry group acting with respect to the axes located at the centers of the equilateral triangles (see Figure 42(a)). These two axes are the only ones within the unit cell not equivalent to the principal axis. From Eqs. (3.119) through (3.124), we can determine that $e^{i2\mathbf{k}\cdot\left(\mathbf{d}-R^{-1}\mathbf{d}\right)}=1$ for each symmetry operator acting with respect to these two non-principal axes. Therefore, the transformations of the local state of polarization, given by Eq. (6.36), will change in the same manner regardless of the symmetry axes (i.e., rotations will preserve the handedness, $\det\left(\vec{\vec{R}}\right)=1$, while reflections will reverse it, $\det\left(\vec{\vec{R}}\right)=-1$). The parallelogram inscribed by the dashed red lines (comprising two equilateral triangles) denotes a primitive unit cell, and the optical response clearly possesses its full translational invariance. Selecting an arbitrary position $\mathbf{r}_1$, close to the origin, as a general Wyckoff position, we see that there are six elements comprising the crystallographic orbit ($t=n_{C_{3v}}/n_{G_{r1}}=6/1=6$) in the primitive unit cell (see Figure 42(d)). The crystallographic orbit with generating point $\mathbf{r}_1$ within the primitive unit cell has two elements deriving from the subgroup of rotation operators $2C_3$, where ellipticity is again preserved, and polarization handedness is maintained (*e.g.*, $\mathbf{P}(\mathbf{r}_i)\times\mathbf{Q}(\mathbf{r}_i)=\mathbf{P}(\mathbf{r}_1)\times\mathbf{Q}(\mathbf{r}_1)$ where $i=2,3$) (see Figure 37(b)). The orientation of the polarization ellipse is advanced by the rotation angle $2\pi/3$ (see Figure 37(a)), which can be understood by the local transformation properties of the electric field given by Eq. (6.21). Likewise, it has three elements, deriving from the reflection operator σ_y' applied to the first three elements, where the orientation and ellipticity of the polarization ellipses

are mirror-symmetric, with Figure 37(b) demonstrating their opposite polarization directions (*e.g.*, $\mathbf{P}(\mathbf{r}_i)\times\mathbf{Q}(\mathbf{r}_i)=-\mathbf{P}(\mathbf{r}_1)\times\mathbf{Q}(\mathbf{r}_1)$, where $i=4,5,6$). The full optical response of the entire extended system can thus be expressed by the fundamental domain, where one element from each crystallographic orbit of all local field vectors exists, denoted by the shaded one-third of an equilateral triangle. Note that this region is one-sixth the primitive unit cell. In contrast, the transformations of the polarization response $\mathbf{P}(\mathbf{r}_1)\times\mathbf{Q}(\mathbf{r}_1)$ within the square lattice are trivial, due to $\mathbf{P}(\mathbf{r})\times\mathbf{Q}(\mathbf{r})=0$ (see Figure 39(b)). Figure 39(a) reveals, however, that the orientation of the local linear polarization states transforms as expected when points $\mathbf{E}^{(\nu)}(\mathbf{r}_1)$ are transformed in space within their crystallographic orbits as given by Eq. (6.21). Therefore, based on the examples presented, it is clear that we may associate every point in the electric field with a crystallographic orbit, where the local state of polarization of the symmetry equivalent points will change, according to Eqs. (6.21) and (6.36).

6.4.4 Symmetry transformation properties of fields at special Wyckoff positions

We have thus far established only the transformation properties of the local polarization state at general Wyckoff positions. However, for local fields at special Wyckoff positions, we may show that the site symmetry reveals the local state of polarization to be a polarization singularity. The local field symmetry transformation at a special Wyckoff position, from Eq. (6.21), proceeds as

$$\left(R\middle|\mathbf{d}-R\mathbf{d}\right)\mathbf{E}^{(\nu)}(\mathbf{r}_1)=e^{i\mathbf{k}\cdot\left(\mathbf{d}-R^{-1}\mathbf{d}\right)}\chi_R^{(\nu)}\,\mathbf{E}^{(\nu)}(\mathbf{r}_1), \tag{6.38}$$

which is an eigenvalue equation, where $e^{i\mathbf{k}\cdot\left(\mathbf{d}-R^{-1}\mathbf{d}\right)}\chi_R^{(\nu)}$ is the eigenvalue and $\mathbf{E}^{(\nu)}(\mathbf{r}_1)$ the eigenvector. To relate the singular nature of a local state of polarization to a particular site symmetry, we will express the local field, via Eq. (6.8), as

$$\mathbf{E}^{(\nu)}(\mathbf{r}_1)=\left[\mathbf{P}(\mathbf{r}_1)+i\mathbf{Q}(\mathbf{r}_1)\right]=\begin{pmatrix} P_x(\mathbf{r}_1)+iQ_x(\mathbf{r}_1) \\ P_y(\mathbf{r}_1)+iQ_y(\mathbf{r}_1) \\ 0 \end{pmatrix}=\Omega(\mathbf{r}_1)\begin{pmatrix} D(\mathbf{r}_1)+iB(\mathbf{r}_1) \\ C(\mathbf{r}_1) \\ 0 \end{pmatrix}; \quad (6.39)$$

components

$$D(\mathbf{r}_1)=P_x(\mathbf{r}_1)P_y(\mathbf{r}_1)+Q_x(\mathbf{r}_1)Q_y(\mathbf{r}_1), \quad (6.40)$$

$$B(\mathbf{r}_1)=-P_x(\mathbf{r}_1)Q_y(\mathbf{r}_1)+Q_x(\mathbf{r}_1)P_y(\mathbf{r}_1), \quad (6.41)$$

and

$$C(\mathbf{r}_1)=P_y^2(\mathbf{r}_1)+Q_y^2(\mathbf{r}_1) \quad (6.42)$$

are purely real, while

$$\Omega(\mathbf{r}_1)=1/\left(P_y(\mathbf{r}_1)-iQ_y(\mathbf{r}_1)\right) \quad (6.43)$$

is a complex phase factor. For any $\mathbf{r}_1$, substitution of Eq. (6.39) into Eq. (6.38) will yield a self-consistency condition contingent on the local symmetry. We now consider, in general, local fields with either reflection or rotation symmetry (or both), with the goal of identifying the site symmetry subgroups of C_{3v} and C_{4v}, and the respective natures of their local polarization states.

In Section 6.4.3, we established that elements of the crystallographic orbit related by reflections, $\left(\sigma_v\middle|\mathbf{d}-R\mathbf{d}\right)\mathbf{E}^{(\nu)}(\mathbf{r}_2)=e^{i\mathbf{k}\cdot\left(\mathbf{d}-R^{-1}\mathbf{d}\right)}\chi_R^{(\nu)}\mathbf{E}^{(\nu)}(\mathbf{r}_1)$, have an equal but opposite polarization handedness, $\mathbf{P}(\mathbf{r}_2)\times\mathbf{Q}(\mathbf{r}_2)=-\mathbf{P}(\mathbf{r}_1)\times\mathbf{Q}(\mathbf{r}_1)$, when $e^{i2\mathbf{k}\cdot\left(\mathbf{d}-R^{-1}\mathbf{d}\right)}=1$. Hence, for $\left(\sigma_v\middle|\mathbf{d}-R\mathbf{d}\right)\mathbf{E}^{(\nu)}(\mathbf{r}_1)=e^{i\mathbf{k}\cdot\left(\mathbf{d}-R^{-1}\mathbf{d}\right)}\chi_R^{(\nu)}\mathbf{E}^{(\nu)}(\mathbf{r}_1)$, we require $\mathbf{P}(\mathbf{r}_1)\times\mathbf{Q}(\mathbf{r}_1)=0$, whence the sense of rotation is undefined, and thus mirror planes must constitute L lines. It now remains to determine the linear polarization rotation angle, vis-à-vis the respective mirror planes. Let us investigate the self-consistency condition, employing $\left(\sigma_y\middle|0\right)$ for illustration, where $\sigma_y\in C_{3v}$ or $\sigma_y\in C_{4v}$ depending on which system is being considered. The argument is general and proceeds identically for all the other mirror reflection planes

passing through the principal axis. The site symmetry of the general case of a field vector located on this mirror plane is clearly $C_{1h}=\{E,\sigma_y\}$, where the symmetry axis is located at the principal axis. Suppressing $\mathbf{r}_1$, for convenience, we obtain

$$\begin{bmatrix}1 & 0 & 0\\ 0 & -1 & 0\\ 0 & 0 & 1\end{bmatrix}\begin{pmatrix}D+iB\\ C\\ 0\end{pmatrix}=\begin{pmatrix}D+iB\\ -C\\ 0\end{pmatrix}=e^{i\mathbf{k}\cdot\left(\mathbf{d}-R^{-1}\mathbf{d}\right)}\chi^{(\nu)}_{\sigma_y}\begin{pmatrix}D+iB\\ C\\ 0\end{pmatrix}, \tag{6.44}$$

As it stands, Eq. (6.44) does not provide any insight into the required form of the eigenvector, $\mathbf{E}^{(\nu)}(\mathbf{r}_1)$ (i.e., local field) upon a mirror symmetry plane. However, we can turn to the global transformation properties of the mode given by Eq. (6.7) to provide additional information. Field vectors located on this mirror plane have a character given Eq. (6.7) as $e^{i\mathbf{k}\cdot\left(\mathbf{d}-R^{-1}\mathbf{d}\right)}\chi^{(\nu)}_{\sigma_y}=(1)\chi^{(A_2)}_{\sigma_y}=-1$ (remembering $e^{i\mathbf{k}\cdot\left(\mathbf{d}-R^{-1}\mathbf{d}\right)}=1$ on the principal axis), this is the character of the A_2 irreducible representation about the principal axis. Substituting this value into Eq. (6.44) then generates the constraint $D=B=0$, where C is given by Eq. (6.42), whence $\mathbf{E}(\mathbf{r}_1)=\Omega(\mathbf{r}_1)(0,C(\mathbf{r}_1),0)$, either in the +$y$-direction or in the –$y$-direction, depending on phase. The polarization direction is thus orthogonal to the mirror plane. Similar expressions may be found for any other mirror plane that passes through the principal axis or any points in the crystallographic orbit where the principal axis is the generating point. This is in accord with the singular states determined for the C_{3v} eigenmode by direct calculation of Eq. (6.4), where Figure 37(a) reveals the L lines and Figure 37(b) their polarization directions (from $\mathbf{P}\times\mathbf{Q}=0$). Similarly, Figure 39(a) reveals the L lines of the C_{4v} eigenmode by direct calculation of Eq. (6.6), where the local state of polarization is orthogonal to any of the mirror planes that pass through the principal axis or any point part of its crystallographic orbit; although, this is not the case for all the points on mirror reflection planes. In the C_{4v} unit cell, there are four mirror reflection planes that intersect at $(a/2,a/2)$, where two of the mirror reflection planes do

not pass through the principal axis or any of its symmetry equivalent points (see Figure 42(b)). Upon these mirror reflection planes the local state of polarization is parallel to the plane (see Figure 39(a)). To explain the change in orientation of the local state of polarization along these secondary mirror reflection planes, we examine the global transformation properties of the photonic crystal eigenmode about the axis $(a/2,a/2)$ given by Eq. (6.7):

$$\left(\sigma_y\middle|\left(a/2\left(\hat{\mathbf{x}}+\hat{\mathbf{y}}\right)\right)-\sigma_y\left(a/2\left(\hat{\mathbf{x}}+\hat{\mathbf{y}}\right)\right)\right)\mathbf{E}^{(\nu)}(\mathbf{r})=\chi^{(a/2(\hat{\mathbf{x}}+\hat{\mathbf{y}}))}_{(\sigma_y|\mathbf{d}-\sigma_y\mathbf{d})}\,\mathbf{E}^{(\nu)}(\mathbf{r}). \tag{6.45}$$

From Section 6.2, if $\mathbf{R}'=\mathbf{d}-R^{-1}\mathbf{d}$ (where $\mathbf{R}'$ is a lattice vector), then Eq. (6.7) may be used to determined $\chi^{(a/2(\hat{\mathbf{x}}+\hat{\mathbf{y}}))}_{(\sigma_y|\mathbf{d}-\sigma_y\mathbf{d})}$. In this case,

$$\mathbf{d}-R^{-1}\mathbf{d}=\begin{pmatrix}a/2\\a/2\\0\end{pmatrix}-\begin{pmatrix}1&0&0\\0&-1&0\\0&0&1\end{pmatrix}\begin{pmatrix}a/2\\a/2\\0\end{pmatrix}=\begin{pmatrix}0\\a\\0\end{pmatrix}, \tag{6.46}$$

whereby $\mathbf{R}'=(0,a,0)$ is a C_{4v} lattice vector. Then from Eq. (6.7)

$$\chi^{(a/2(\hat{\mathbf{x}}+\hat{\mathbf{y}}))}_{(\sigma_y|\mathbf{d}-\sigma_y\mathbf{d})}=\exp\left(i\left[\left(\hat{\mathbf{x}}+\hat{\mathbf{y}}\right)\pi/a\right]\cdot\left[\hat{\mathbf{y}}a\right]\right)\chi^{(A_2)}_{\sigma_y}=(-1)(-1)=1. \tag{6.47}$$

To determine the orientation of the local state of polarization along the secondary mirror reflection planes, we substitute Eq. (6.47) into Eq. (6.44). Equation (6.44) then generates the constraint $C=0$, where $D+iB$ is determined by Eqs. (6.40) and (6.41), whence $\mathbf{E}^{(\nu)}(\mathbf{r}_1)=\Omega(\mathbf{r}_1)\left(D(\mathbf{r}_1)+iB(\mathbf{r}_1),0,0\right)$, either in the $+x$-direction or in the $-x$-direction, depending on phase. The polarization direction is thus parallel to the secondary mirror planes in the square lattice (see Figure 39(a)).

We next determine if there are any locations where Eq. (6.38) is valid for rotation operations. However, because polarization handedness is maintained upon rotation, no specific insight is gained from the general local transformation properties, established in Section 6.4.4 for rotation operators. Employing C_n in the self-consistency condition yields

$$\begin{bmatrix} \cos\left(\frac{2\pi}{n}\right) & -\sin\left(\frac{2\pi}{n}\right) & 0 \\ \sin\left(\frac{2\pi}{n}\right) & \cos\left(\frac{2\pi}{n}\right) & 0 \\ 0 & 0 & 1 \end{bmatrix} \begin{pmatrix} D+iB \\ C \\ 0 \end{pmatrix} = e^{i\mathbf{k}\cdot\left(\mathbf{d}-R^{-1}\mathbf{d}\right)} \chi_{C_n}^{(\nu)} \begin{pmatrix} D+iB \\ C \\ 0 \end{pmatrix}, \tag{6.48}$$

where we focus on the point translations R of $\left(R|\mathbf{d}-R\mathbf{d}\right)$ applied to the vector, Eq. (6.39), because the lateral translations simply create equivalent unit vectors (see Eq.(6.25)). Inspection reveals that there are no local field solutions where Eq. (6.48) identifies singularities for $n=1$ or $n=2$. However, for $n=3$, we find two distinct types of singularities, dependent on the site symmetry to which the C_3 operator belongs. The expected form of the state of local polarization can be determined for the rotation operator C_3; Eq. (6.48) becomes

$$\frac{1}{2}\begin{pmatrix} -(D+iB)-C\sqrt{3} \\ (D+iB)\sqrt{3}-C \\ 0 \end{pmatrix} = e^{i\mathbf{k}\cdot\left(\mathbf{d}-R^{-1}\mathbf{d}\right)} \chi_{C_3}^{(A_2)} \begin{pmatrix} D+iB \\ C \\ 0 \end{pmatrix}. \tag{6.49}$$

In contrast to Eq. (6.44), we can determine the form of the eigenvector $\mathbf{E}^{(\nu)}(\mathbf{r}_1)$ and its eigenvalue $e^{i\mathbf{k}\cdot\left(\mathbf{d}-R^{-1}\mathbf{d}\right)}\chi_{C_3}^{(A_2)}$ from Eq. (6.49). These eigenvalues $e^{i\mathbf{k}\cdot\left(\mathbf{d}-R^{-1}\mathbf{d}\right)}\chi_{C_3}^{(A_2)}$ will be compared to global transformation characters determined by Eq. (6.7). When the eigenvalues and the global transformation characters match then the local field we be in the same form as the eigenvector of Eq. (6.49). If they do not match the local field must vanish. Taking the ratio of the two vector component equations, to eliminate

$e^{i\mathbf{k}\cdot\left(\mathbf{d}-R^{-1}\mathbf{d}\right)}\chi_{C_3}^{(A_2)}$, cross-multiplying and equating the consequent real and imaginary parts yields $B^2 = C^2 + D^2$ and $BD = 0$, respectively. The only possible solutions to this constraint system, for non-zero fields, are $D = 0$, $B = \pm C$ or $B = 0$, $D = \pm iC$. From all possibilities, there are only two unique eigenvectors for Eq. (6.49): the eigenvector in the form of left-hand circularly polarized light given by

$$\mathbf{E}^{(v)}(\mathbf{r}_1) = C(\mathbf{r}_1)\Omega(\mathbf{r}_1)(i,1,0), \tag{6.50}$$

where the eigenvalue is $e^{i\mathbf{k}\cdot\left(\mathbf{d}-R^{-1}\mathbf{d}\right)}\chi_{C_3}^{(A_2)} = \left(-1+i\sqrt{3}\right)/2$; or the eigenvector in the form of right-hand circularly polarized light given by

$$\mathbf{E}^{(v)}(\mathbf{r}_1) = C(\mathbf{r}_1)\Omega(\mathbf{r}_1)(-i,1,0), \tag{6.51}$$

where the eigenvalue is $e^{i\mathbf{k}\cdot\left(\mathbf{d}-R^{-1}\mathbf{d}\right)}\chi_{C_3}^{(A_2)} = \left(-1-i\sqrt{3}\right)/2$.

Similarly for $n = 4$, the expected form of the state of local polarization (i.e. eigenvalue and eigenvector) can be determined for the rotation operator C_4, whence Eq. (6.48) becomes

$$\begin{pmatrix} -C \\ D+iB \\ 0 \end{pmatrix} = e^{i\mathbf{k}\cdot\left(\mathbf{d}-R^{-1}\mathbf{d}\right)}\chi_{C_4}^{(A_2)}\begin{pmatrix} D+iB \\ C \\ 0 \end{pmatrix}. \tag{6.52}$$

Again, taking the ratio of the two vector component equations, to eliminate $e^{i\mathbf{k}\cdot\left(\mathbf{d}-R^{-1}\mathbf{d}\right)}\chi_{C_4}^{(A_2)}$, cross-multiplying and equating the consequent real and imaginary parts yields $B^2 = C^2 + D^2$ and $BD = 0$, respectively. The only possible solution to this constraint system, for non-zero fields, is $D = 0$, $B = \pm C$ or $B = 0$, $D = \pm iC$. From all

four possibilities we only obtain two unique eigenvectors for Eq. (6.52): the eigenvector in the form of left-hand circularly polarized light given by

$$\mathbf{E}^{(\nu)}(\mathbf{r}_1) = C(\mathbf{r}_1)\Omega(\mathbf{r}_1)(i,1,0), \tag{6.53}$$

where the eigenvalue is $e^{i\mathbf{k}\cdot\left(\mathbf{d}-R^{-1}\mathbf{d}\right)}\chi_{C_4}^{(A_2)} = i$; and the eigenvector in the form of right-hand circularly polarized light given by

$$\mathbf{E}^{(\nu)}(\mathbf{r}_1) = C(\mathbf{r}_1)\Omega(\mathbf{r}_1)(-i,1,0), \tag{6.54}$$

where eigenvector is $e^{i\mathbf{k}\cdot\left(\mathbf{d}-R^{-1}\mathbf{d}\right)}\chi_{C_4}^{(A_2)} = -i$. Therefore, upon the centers of C_3 and C_4 rotational symmetry, the local states of polarization must be circularly polarized (i.e., C points).

Are there any locations within the unit cell of the hexagonal lattice which have global transformation characters (given by Eq. (6.7)) which match the eigenvalues derived from Eq. (6.49), when $n=3$? The cyclic group $C_3 = \{E, C_3, C_3^{-1}\}$ identifies points of pure three-fold rotational symmetry in the hexagonal lattice at the centers of equilateral triangles located at $\left(a/2, a/\left(2\sqrt{3}\right)\right)$ and $\left(a, a/\sqrt{3}\right)$ in the unit cell, as shown in Figure 42(a). These two points are part of the same crystallographic orbit. In Section 3.5.3, we determined that a general Bloch mode transformed by the C_3 symmetry operator about the points $\left(a/2, a/\left(2\sqrt{3}\right)\right)$, $\left(a, a/\sqrt{3}\right)$ in the unit cell, possessed characters of $\chi_{(C_3|\mathbf{d}-C_3\mathbf{d})}^{\left(-a/2, a/\left(2\sqrt{3}\right)\right)} = \left(-1+i\sqrt{3}\right)/2$ and $\chi_{(C_3|\mathbf{d}-C_3\mathbf{d})}^{\left(a, a/\sqrt{3}\right)} = \left(-1-i\sqrt{3}\right)/2$, respectively (see Eqs. (3.120) and (3.123). Matching the global characters $\chi_{(C_3|\mathbf{d}-C_3\mathbf{d})}^{\left(-a/2, a/\left(2\sqrt{3}\right)\right)}$ and $\chi_{(C_3|\mathbf{d}-C_3\mathbf{d})}^{\left(a, a/\sqrt{3}\right)}$ to the two different eigenvalues determined by Eq. (6.49), we can predict that, at the point

$\left(a/2, a/\left(2\sqrt{3}\right)\right)$, the state of local polarization will be left-hand circularly polarized, and that at $\left(a, a/\sqrt{3}\right)$ the state of local polarization will be right-hand circularly polarized. The remaining C_3 points within the hexagonal unit cell (associated with the special Wyckoff position of highest symmetry) are found at the intersections of the mirror planes, where they possess both C_3 and C_{1h} symmetries, *i.e.,* the point group symmetry of the mode, $C_{3v} = \{E, 2C_3, 3\sigma_y\}$. These positions are the points of the crystallographic orbit where the principal axis is the generating point and $\chi_{C_3}^{(A_2)} = 1$. $\chi_{C_3}^{(A_2)} = 1$ does not match the two possible eigenvalues as determined by Eq. (6.49); therefore the field must vanish and form a disclination. Analytic determination of the mode, via Eq. (6.4), reveals that C points (circular polarization states), denoted by the red open circles in Figure 37(a), do indeed exist at all points in the crystallographic orbit where $\left(a/2, a/\left(2\sqrt{3}\right)\right)$ is the generating point. Moreover, the observed polarization handedness, as noted in Figure 37(b), conforms to that anticipated by the symmetry arguments (i.e. left-handed $\mathbf{P}\times\mathbf{Q}$ positive, right-handed $\mathbf{P}\times\mathbf{Q}$ negative) and alternates when two points in a crystallographic orbit span a mirror reflection plane. Secondly, disclinations indicated by green circles in Figure 37(a), appear as expected at the principal axis and all of its symmetry equivalent points.

What of the square lattice – are there any locations in space that match the eigenvalues derived by Eq. (6.52), when $n = 4$? Each center of C_4 of rotational symmetry with the square lattice, also possesses mirror reflection symmetry for a total site symmetry of $C_{4v} = \{E, C_4, C_4^{-1}, C_2, \sigma_x, \sigma_y, \sigma_d', \sigma_d''\}$. At the principal axis and its symmetry-equivalent points, the global C_4 character is $\chi_{C_4}^{(A_2)} = 1$. At the secondary axis $(a/2, a/2)$ and its symmetry-equivalent points, the global C_4 character is $\chi_{(C_4|\mathbf{d}-C_4\mathbf{d})}^{(a/2(\hat{\mathbf{x}}+\hat{\mathbf{y}}))} = -1$ ($\chi_{(C_4|\mathbf{d}-C_4\mathbf{d})}^{(a/2(\hat{\mathbf{x}}+\hat{\mathbf{y}}))}$ is determined using the same process to obtain $\chi_{(\sigma_y|\mathbf{d}-\sigma_y\mathbf{d})}^{(a/2(\hat{\mathbf{x}}+\hat{\mathbf{y}}))}$, given by Eq. (6.47). Neither of

these results matches the expected eigenvalues from Eq. (6.52), when $n=4$, and therefore disclination must appear at these locations. Analytic determination of the mode, via Eq. (6.6), reveals that disclinations, denoted by the green open circles in Figure 39(a), do indeed exist at all the centers of C_4 rotational symmetry.

There is an alternate, more intuitive method to determine the locations of disclinations. In this section, we determined that the local state of polarization must be linear upon a mirror reflection plane. In contrast, upon the center of C_3 or C_4 rotation symmetry, the local state of polarization must be circular polarized. When a mirror reflection plane and a center of rotational symmetry coincide, the local state of polarization cannot be simultaneously linear and circular polarized. Therefore, the electric field must vanish at these locations (when its polarization is confined to the *x*-*y* plane) and thus it forms a disclination.

6.5 Polarization singularities in eigenmodes of high dielectric contrast photonic crystals

6.5.1 Purely two-dimensional photonic crystals

Using group theoretic arguments, we have determined the spatial locations of the polarization singularities. Furthermore, we have confirmed the existence of polarization singularities in the vanishing dielectric contrast limit, by plotting the spatially dependent polarization response, derived from the analytic descriptions Eq. (6.4) and Eq. (6.6). The group theoretic arguments are based solely upon the symmetry of the photonic crystal whence they are ubiquitous, regardless of the dielectric contrast of the photonic crystal. We now verify that the polarization singularities appear at locations so predicted by group theoretic arguments for high dielectric contrast, purely two-dimensional photonic crystals. This was achieved by numerically solving the scalar eigenvalue problem, described by the Maxwell's equation for the magnetic field (TE Bloch mode) Eq. (2.28),

using our proprietary code based on COMSOL's Multiphysics finite element analysis software (see Section 4.3), where we concentrate on the hexagonal lattice.

Figure 43 and Figure 44 present our simulation results of band 1 TE mode for the hexagonal lattice at $\mathbf{k} = \hat{\mathbf{x}} 4\pi/(3a)$ (the electric field associated with the A_2 representation of the C_{3v} point group). The simulation is of an array of periodic air holes $\varepsilon_{air} = 1$, with radii of $r = 0.25a$, in a dielectric background $\varepsilon_{BG} = 12$, where the lattice constant is $a = 3.75 \times 10^{-7}\,\mathrm{m}$. We have extracted the related full vector electric field from the numerically determined magnetic field using Eq. (3.41), where the direction is shown by blue arrows (length proportional to vector components), and the time-averaged magnitude, $|\mathbf{E}(\mathbf{r})| = \sqrt{\mathbf{E}^*(\mathbf{r}) \cdot \mathbf{E}(\mathbf{r})}$, as the background color (see Figure 43). Figure 43(a) and Figure 43(b) display the electric field at two different points in the time domain: $\omega t = 0$ and $\omega t = \pi/2$ respectively. In Figure 44(a), we have extracted the polarization response $\mathbf{P}(\mathbf{r}) \times \mathbf{Q}(\mathbf{r})$ for the electric field ($\hat{\mathbf{z}}$ direction), and in Figure 44(b), we plotted the phase angle $\tau(\mathbf{r})$ defined by Eq. (6.10). The principal axis of the C_{3v} point group is located at the center of the bottom right air hole, indicated in each figure (see Figure 42 for the full symmetry).

Initially, we can examine the transformation properties of $\mathbf{P}(\mathbf{r}) \times \mathbf{Q}(\mathbf{r})$, as discussed in Section 6.4.3. Figure 44(a) reveals $\mathbf{P}(\mathbf{r}) \times \mathbf{Q}(\mathbf{r})$ has the same characteristic C_{3v} symmetry as the vanishing dielectric contrast case displayed in Figure 37(b). These characteristics include the change in sign of $\mathbf{P}(\mathbf{r}_1) \times \mathbf{Q}(\mathbf{r}_1)$ across a mirror reflection plane and the invariance of $\mathbf{P}(\mathbf{r}_1) \times \mathbf{Q}(\mathbf{r}_1)$ when rotated by the operator C_3. This confirms that the transformation properties of $\mathbf{P}(\mathbf{r}_1) \times \mathbf{Q}(\mathbf{r}_1)$ (defined in Section 6.4.3) are maintained in a high dielectric contrast photonic crystal.

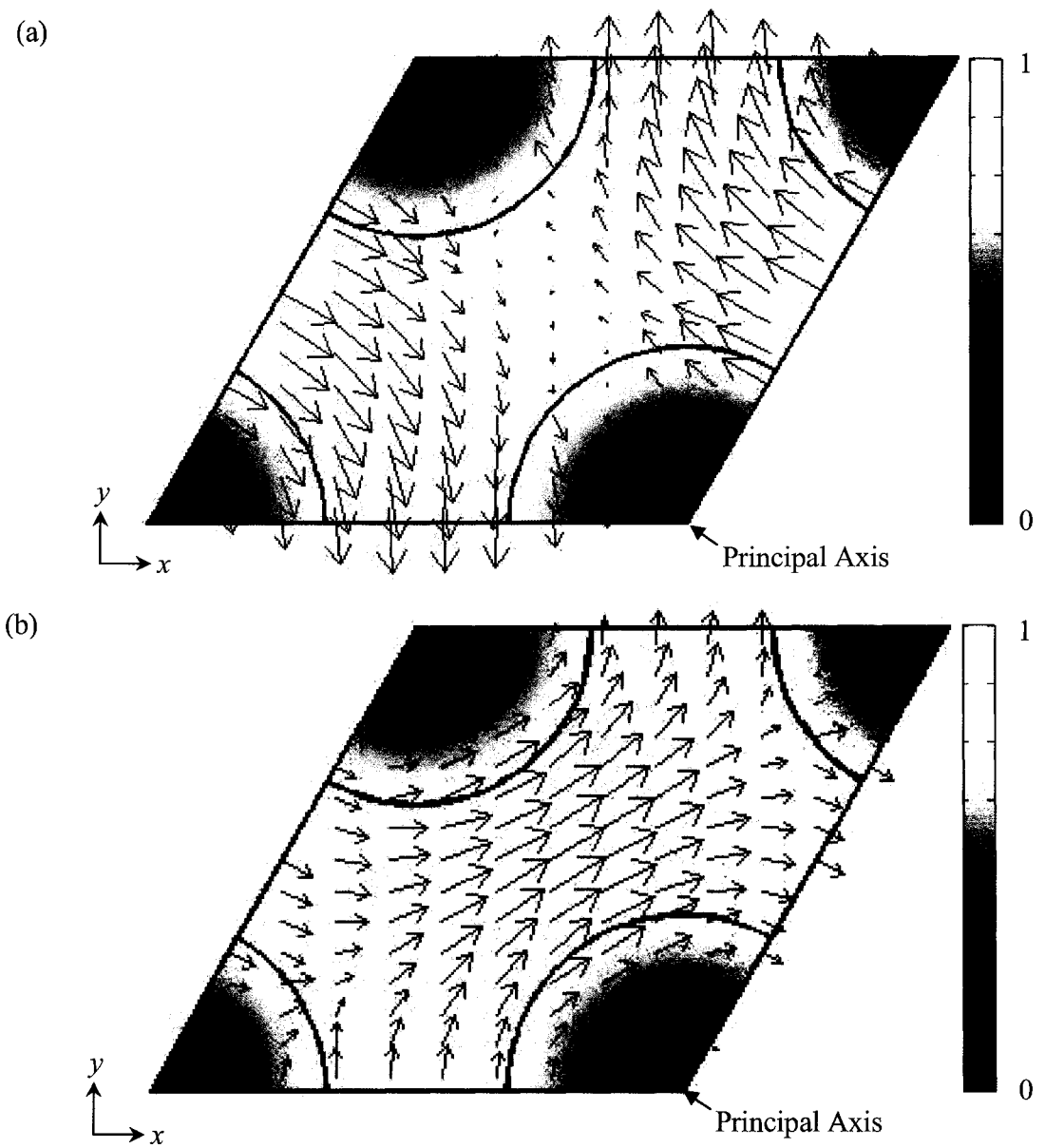

Figure 43. Hexagonal lattice Bloch mode, band 1, $\mathbf{k} = \hat{\mathbf{x}}\,4\pi/(3a)$, and high dielectric contrast of 12. The electric field is associated with the A_2 irreducible representation of C_{3v}. The electric field direction (blue arrows, length proportional to vector components) and $\sqrt{\mathbf{E}\cdot\mathbf{E}^*}$ magnitude time-averaged (background color), of the field (a) at time $\omega t = 0$, and (b) at time $\omega t = \pi/2$. Bold black lines are edges of the unit cell and holes.

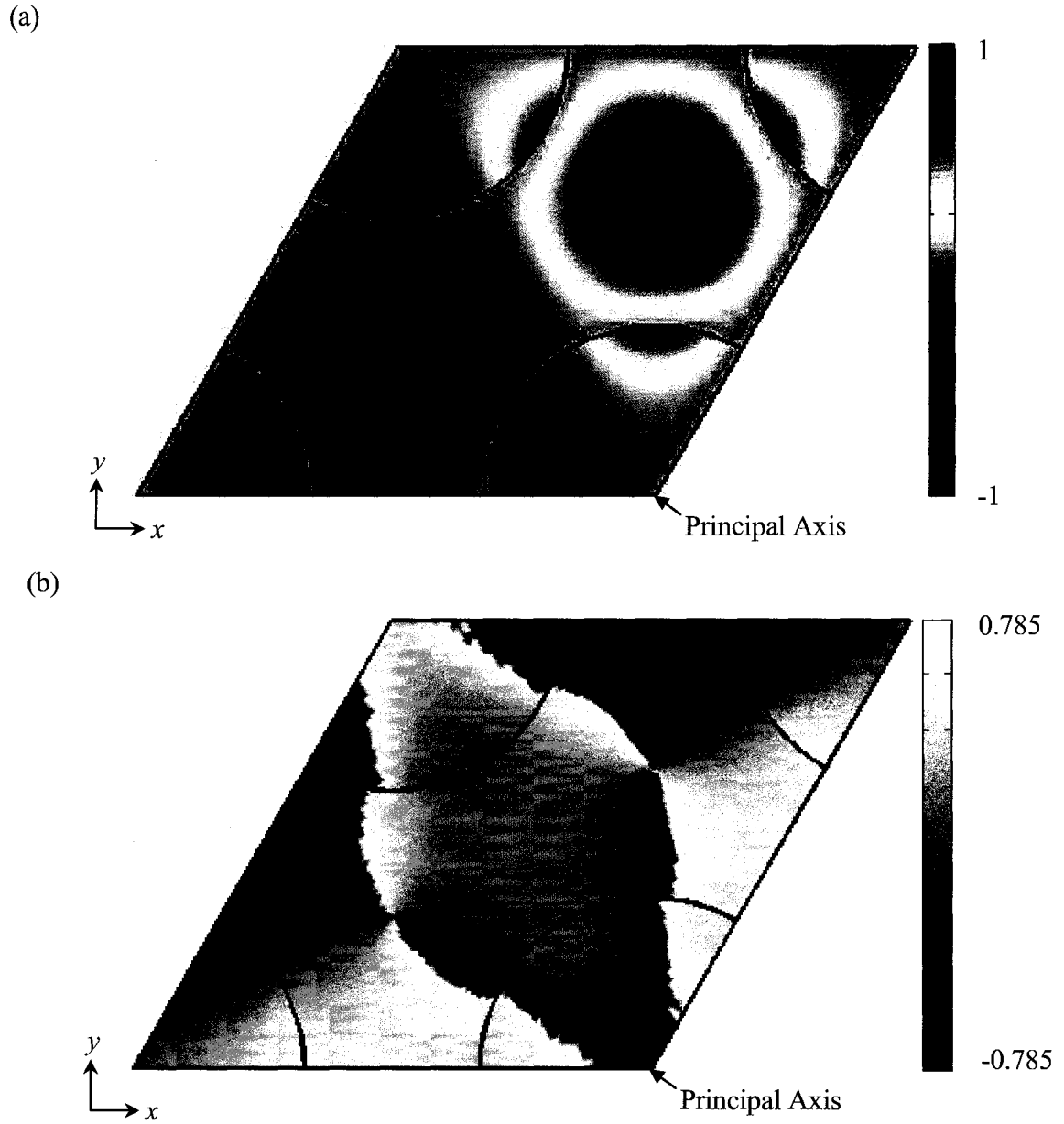

Figure 44. Hexagonal lattice Bloch mode, band 1, $\mathbf{k} = \hat{\mathbf{x}}\,4\pi/(3a)$, and high dielectric contrast of 12. The electric field is associated with the A_2 irreducible representation of C_{3v}. The (a) electric field polarization response, $\mathbf{P}(\mathbf{r})\times\mathbf{Q}(\mathbf{r})$ ($\hat{\mathbf{z}}$ direction), and (b) the phase $\tau(\mathbf{r})$, which ensures $\mathbf{a}(\mathbf{r}) \perp \mathbf{b}(\mathbf{r})$. Bold black lines are edges of the unit cell and holes.

Next, we examine the local state of polarization and confirm the existence of polarization singularities, as predicted by our group theoretic arguments. The group theoretic prediction are the existence of L lines along the mirror reflection planes, of C points at the centers of C_3 site symmetry, and of disclinations at the centers of C_{3v} site symmetry. Figure 44(a) reveals that $\mathbf{P}(\mathbf{r})\times\mathbf{Q}(\mathbf{r})=0$ along the mirror symmetry planes, which indicates the existence of L lines. This is further confirmed in Figure 43(a) and Figure 43(b), where the local state of polarization on the mirror reflection planes maintains its orientation in time and is perpendicular to the mirror symmetry planes (as predicted for electric fields associated with the A_2 irreducible representation, see Section 6.4.3). Figure 44(b) reveals $\tau(\mathbf{r})$ is discontinuous at the centers of C_3 site symmetry. The discontinuity of $\tau(\mathbf{r})$ is characteristic of a C point. Equally important, at these same locations, Figure 43(a) and Figure 43(b) indicate that the local state of polarization maintains a constant magnitude over time, but changes its orientation by π between the two slices in time, which are the characteristics of circular polarized light. Thus we can confirm the presence of C points at the centers of C_3 site symmetry. At the centers of C_{3v} site symmetry (the centers of the air holes) the electric field vanishes, indicating the presences of polarization disclinations (see Figure 43(a) and Figure 43(b)). As well, in Figure 43(a) and Figure 43(b), the orientation of the electric field vectors, $\gamma(\mathbf{r})$, rotates about the center of C_{3v} site symmetry, where the centers of orientation rotation alternate locations between the two slices in time. This is consistent with the location of disclinations presented in Figure 41(a), where disclinations were singular points in the field $\gamma(\mathbf{r})$. With this evidence, we can confirm the presence of disclinations at the centers of C_{3v} site symmetry. Note, in Figure 44(b), we expect the dislocations to appear at singular points in $\tau(\mathbf{r})$. In practice, the registration of the unit cell did not lend itself well to spotting the discontinuities in $\tau(\mathbf{r})$ at the edges of the solution space. Furthermore, there is evidence of poor numerical accuracy in calculating $\tau(\mathbf{r})$

approaching a disclination, when the calculations are compared to the photonic crystal slab case (see Figure 48(a); further discussion regarding why this is a valid comparison in the next section). As mentioned, the electric field was calculated from the numerically solved magnetic field, and from the electric field numerous calculations were performed to determine $\tau(\mathbf{r})$. At each calculation step, the numerical error increases; when coupled with the vanishing electric field as we approach a disclination, this introduces significant noise into $\tau(\mathbf{r})$. In the case of a photonic crystal slab, the full vector electric field is solved directly, which significantly reduces the error in $\tau(\mathbf{r})$. For future work, this issue could be addressed by solving the purely two-dimensional photonic crystal problem using the full vector FEM solver, but at a significant increase in numerical resources.

6.5.2 Two-dimensional photonic crystal slabs

To demonstrate that the group theoretic arguments used to locate the polarization singularities are applicable beyond purely two-dimensional photonic crystals, we now examine the two-dimensional photonic crystal slab case. All of the results derived for the purely two-dimensional photonic crystals were for the TE modes case, where the electric field vectors are restricted to the *x-y* plane. To simplify the analysis of the photonic crystal slab system, we examine a photonic crystal slab Bloch mode with a electric field profile similar to the purely two-dimensional photonic crystal eigenmodes. As described in Section 4.4.2, the electric and magnetic field profiles of the two-dimensional photonic crystal eigenmodes and photonic crystal slabs eigenmodes are identical in the *x-y* plane that bisects the photonic crystal slab when the Bloch wave vector **k** and band index *n* of the two eigenmodes are the same (with the same *x-y* plane dielectric profiles). Furthermore, in Section 2.5.3, we determined that even photonic crystal slab eigenmodes with frequencies below the single mode cutoff of a similar uniform dielectric slab were well approximated by a summation of even TE dielectric slab modes. The electric field vectors of the TE dielectric slab modes are restricted to the *x-y* plane, whereby we expect the even photonic crystal slab Bloch mode to have the same polarization restriction. As a result, we chose to examine the electric field of the photonic crystal slab eigenmode for

band 1 and Bloch wave vector $\mathbf{k} = \hat{\mathbf{x}} 4\pi/(3a)$; this is the same location in reciprocal space that was examined in the two-dimensional hexagonal lattice photonic crystal example. Therefore, we predict polarization singularities will also appear in the photonic crystal slab eigenmode with the same parameters in the electric field.

We confirm the analytical predictions by revealing the local state of polarization of the photonic crystal slab eigenmode for band 1 and Bloch wave vector $\mathbf{k} = \hat{\mathbf{x}} 4\pi/(3a)$. This is achieved by numerically solving the photonic crystal slab eigenvalue problem, using COMSOL Multiphysics (see Section 4.4.3). In Figure 45 to Figure 48, the simulations are of an array of periodic air holes $\varepsilon_{air} = 1$, with radii of $r = 0.25a$, in a dielectric slab $\varepsilon_{slab} = 12$ with a thickness of $d = a/2$, where the lattice constant is $a = 3.75 \times 10^{-7}\,\mathrm{m}$. The simulation space is the hexagonal lattice unit cell in the *x-y* plane with periodic boundary conditions, where the unit cell is shifted so that the air hole is located at the center. Similar to the two-dimensional photonic crystal, the electric field direction (blue arrows, length proportional to vector components), and the time-averaged magnitude, $|\mathbf{E}(\mathbf{r})| = \sqrt{\mathbf{E}^*(\mathbf{r}) \cdot \mathbf{E}(\mathbf{r})}$ (background color) are displayed for the two time steps $\omega t = 0$ and $\omega t = \pi/2$; there are *x-y* plane cross-sections at the center of the slab, $z = 0$, and the bottom surface of the slab, $z = -a/4$, and a *y-z* cross-section centered on the principal axis (see Figure 45 and Figure 46). The principal axis of *x-y* plane point symmetry, C_{3v}, is located at the center of the air hole, in the middle of the unit cell. The edges of the photonic crystal slab are highlighted with bold black lines. Figure 47 reveals the $\mathbf{P}(\mathbf{r}) \times \mathbf{Q}(\mathbf{r})$ field, where the arrows indicate the direction (length proportional to vector components) and the background color is the time averaged magnitude in $\hat{\mathbf{z}}$ direction. Finally, Figure 48 displays the spatially dependent phase factor $\tau(\mathbf{r})$ in the *x-y* plane at $z = 0$ and at $z = -a/4$.

Figure 45 and Figure 46 reveal the local state of polarization of the electric field is restricted to the *x-y* plane. This is reinforced by the plot of $\mathbf{P}(\mathbf{r})\times\mathbf{Q}(\mathbf{r})$, where the vector field only points along the $\hat{\mathbf{z}}$ axis (see Figure 47). The field $\mathbf{P}(\mathbf{r})\times\mathbf{Q}(\mathbf{r})$ displays full C_{3v} symmetry the same as the two-dimensional case, where a point in the $\mathbf{P}(\mathbf{r})\times\mathbf{Q}(\mathbf{r})$ distribution changes sign across mirror reflection planes, but maintains direction and magnitude when rotated by C_3. $\mathbf{P}(\mathbf{r}_1)\times\mathbf{Q}(\mathbf{r}_1)=0$ along the mirror reflection planes, which indicated the presence of L planes. This is confirmed by examining the local state of polarization at the two different time steps, where the electric field maintains the same direction and it is perpendicular to the mirror reflection plane (as expected for the electric associated with the A_2 irreducible representation) (see Figure 45 and Figure 46). The C points are located at the centers of C_3 site symmetry, indicated by the two singular points in $\tau(\mathbf{r})$ located on either side of the air hole (see Figure 48). Again, this can be confirmed by examining the electric field at the two time steps, where at the C point, the electric field maintains the same magnitude at each time step, but the electric field direction rotates by 90 degrees (see Figure 45 and Figure 46). This is the behaviour characteristic of circular polarized light, which confirms the presence of the C point. The third singularity in $\tau(\mathbf{r})$ is associated with a disclination and it is located at the center of C_{3v} site symmetry at the principal axis (see Figure 48). At the center of the air hole, the electric field vanishes and the orientation of the electric field vectors, $\gamma(\mathbf{r})$, rotates about the point, thus confirming the presence of a disclination at this point.

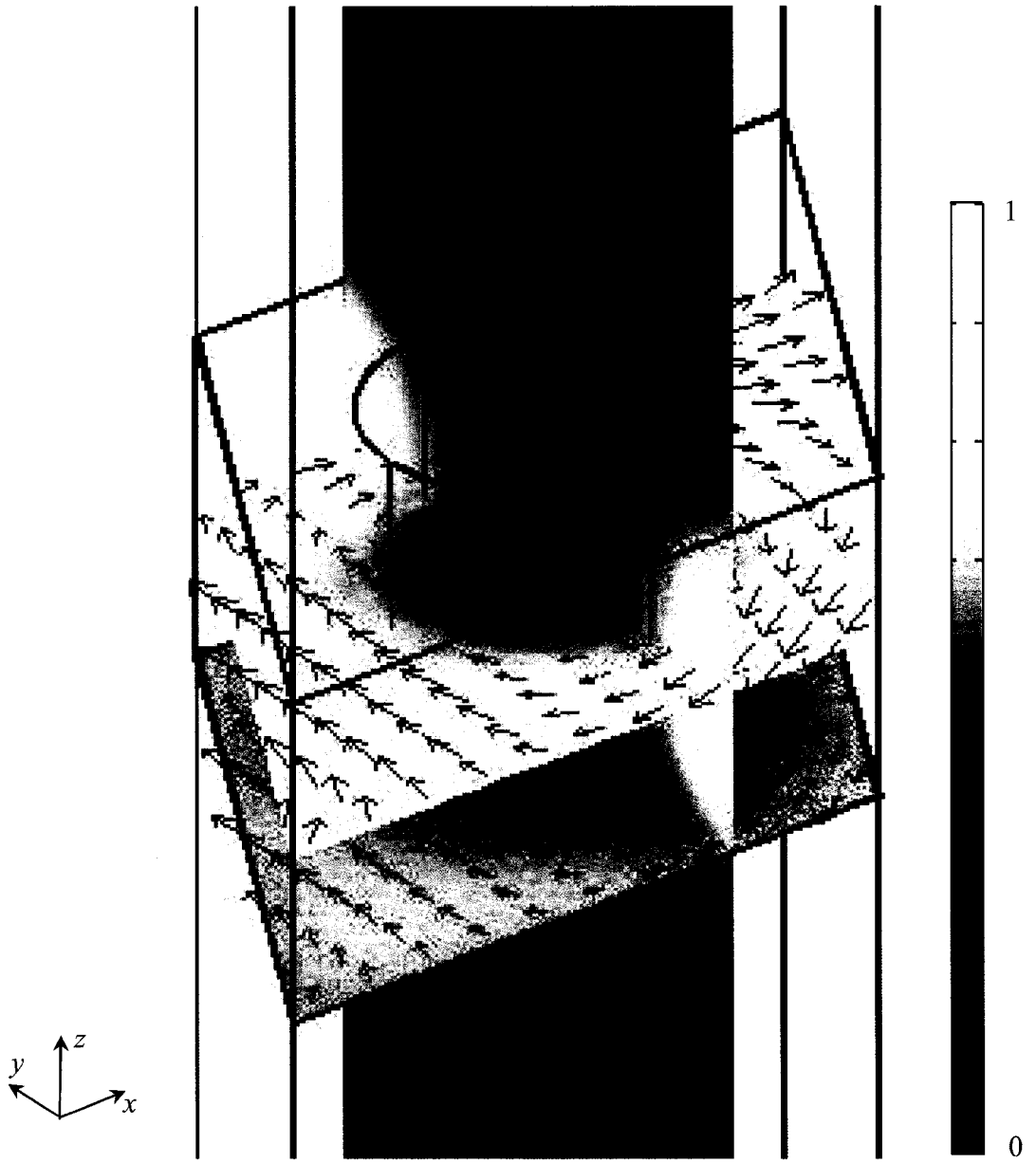

Figure 45. Hexagonal photonic crystal slab lattice air holes in a dielectric background, Bloch mode, band 1, $\mathbf{k} = \hat{\mathbf{x}}\, 4\pi/(3a)$. The electric field is associated with the A_2 irreducible representation of C_{3v}, where the direction (arrow length proportional to vector components) and $\sqrt{\mathbf{E}\cdot\mathbf{E}^*}$ magnitude time-averaged (background color) of the electric field at time $\omega t = 0$. Bold black lines are edges of the unit cell and holes.

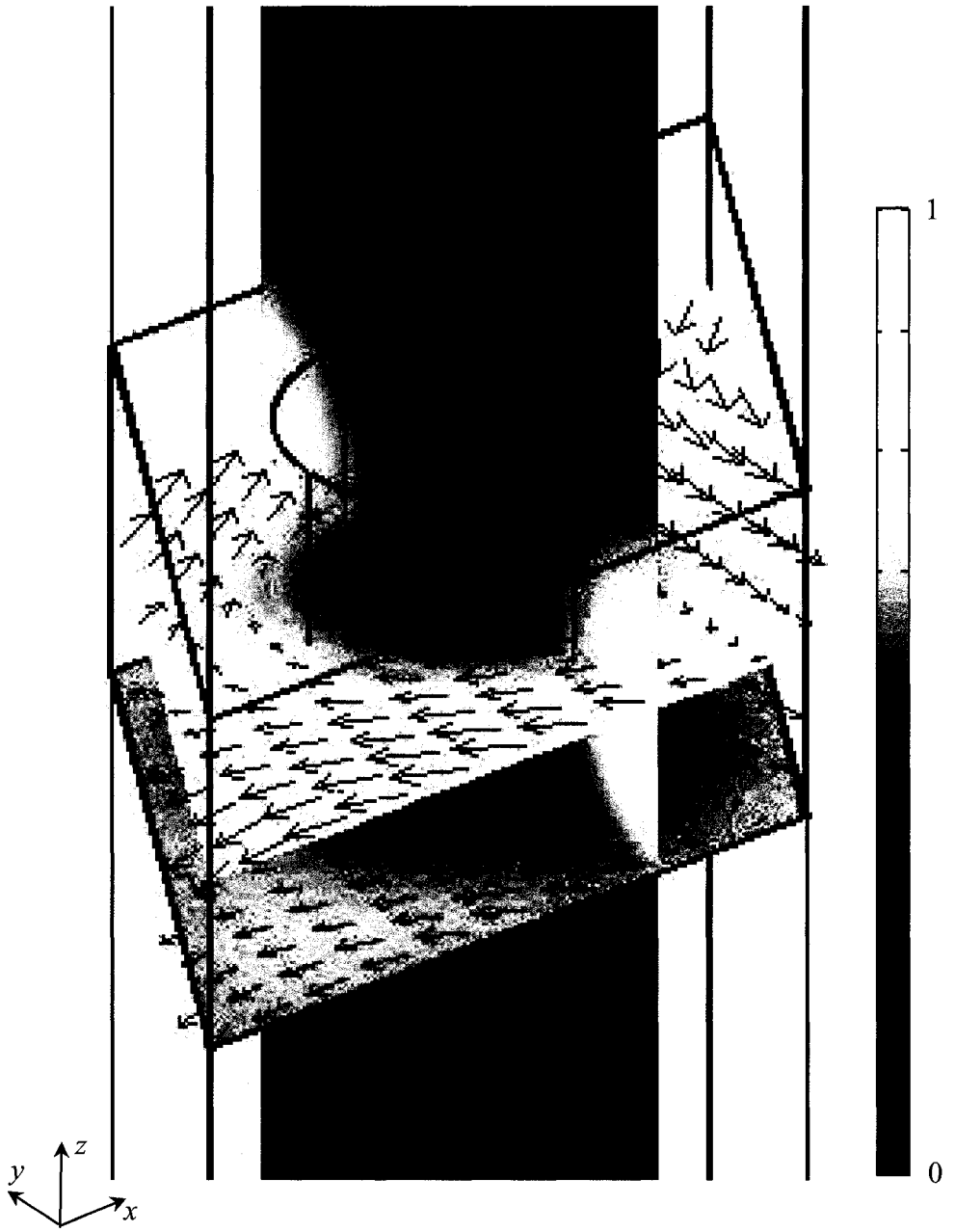

Figure 46. Hexagonal photonic crystal slab lattice air holes in a dielectric background, Bloch mode, band 1, $\mathbf{k} = \hat{\mathbf{x}}\, 4\pi/(3a)$. The electric field is associated with the A_2 irreducible representation of C_{3v}, where the direction (arrow length proportional to vector components) and $\sqrt{\mathbf{E}\cdot\mathbf{E}^*}$ magnitude time-averaged (background color) of the electric field at time $\omega t = \pi/2$. Bold black lines are edges of the unit cell and holes.

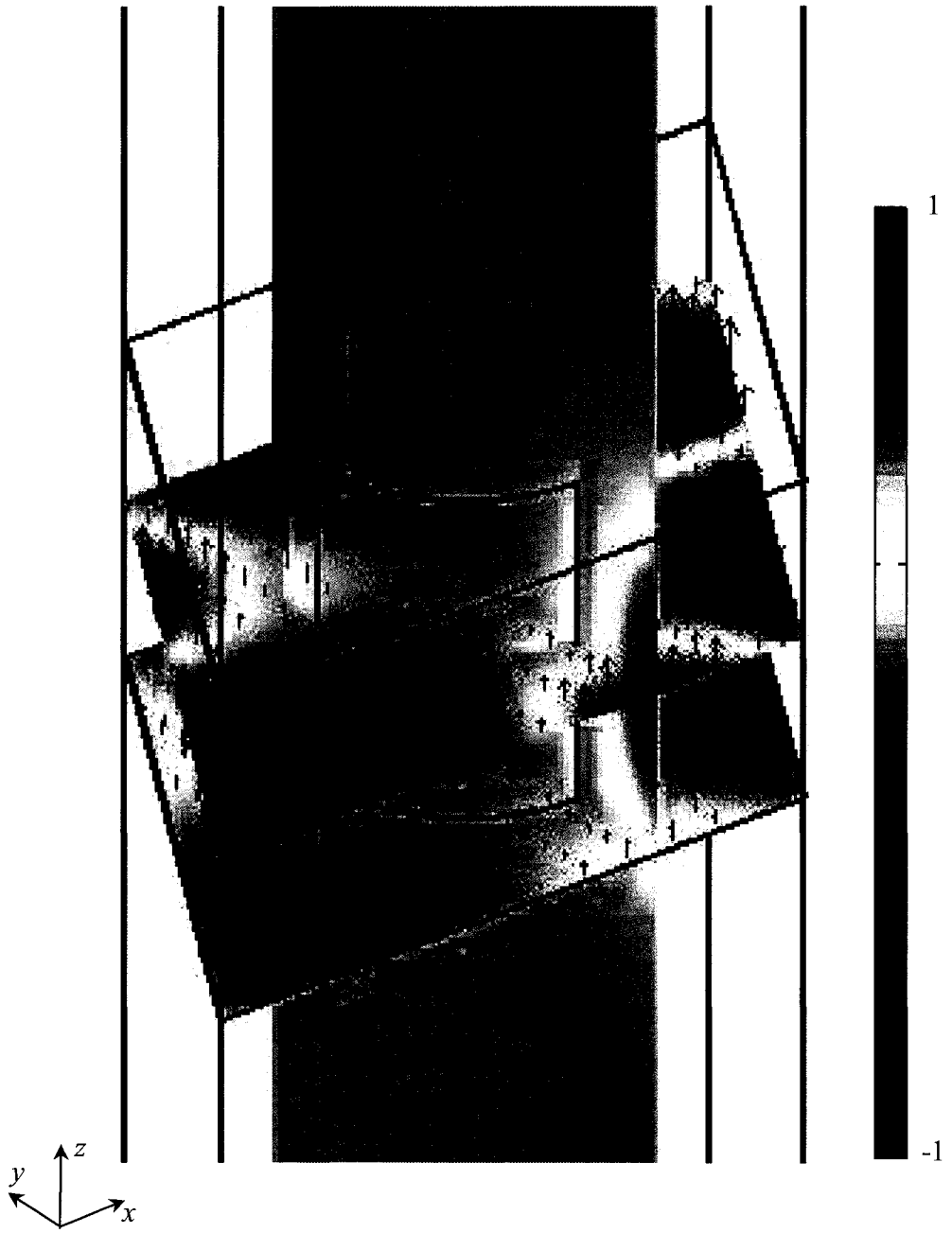

Figure 47. Hexagonal photonic crystal slab lattice air holes in a dielectric background, Bloch mode, band 1, $\mathbf{k} = \hat{\mathbf{x}} 4\pi/(3a)$. The electric field is associated with the A_2 irreducible representation of C_{3v}, where the polarization response $\mathbf{P}(\mathbf{r}) \times \mathbf{Q}(\mathbf{r})$ is displayed, arrows give the direction (which are proportional to length) and magnitude in the $\hat{\mathbf{z}}$ direction is the background color. Bold black lines are edges of the unit cell and holes.

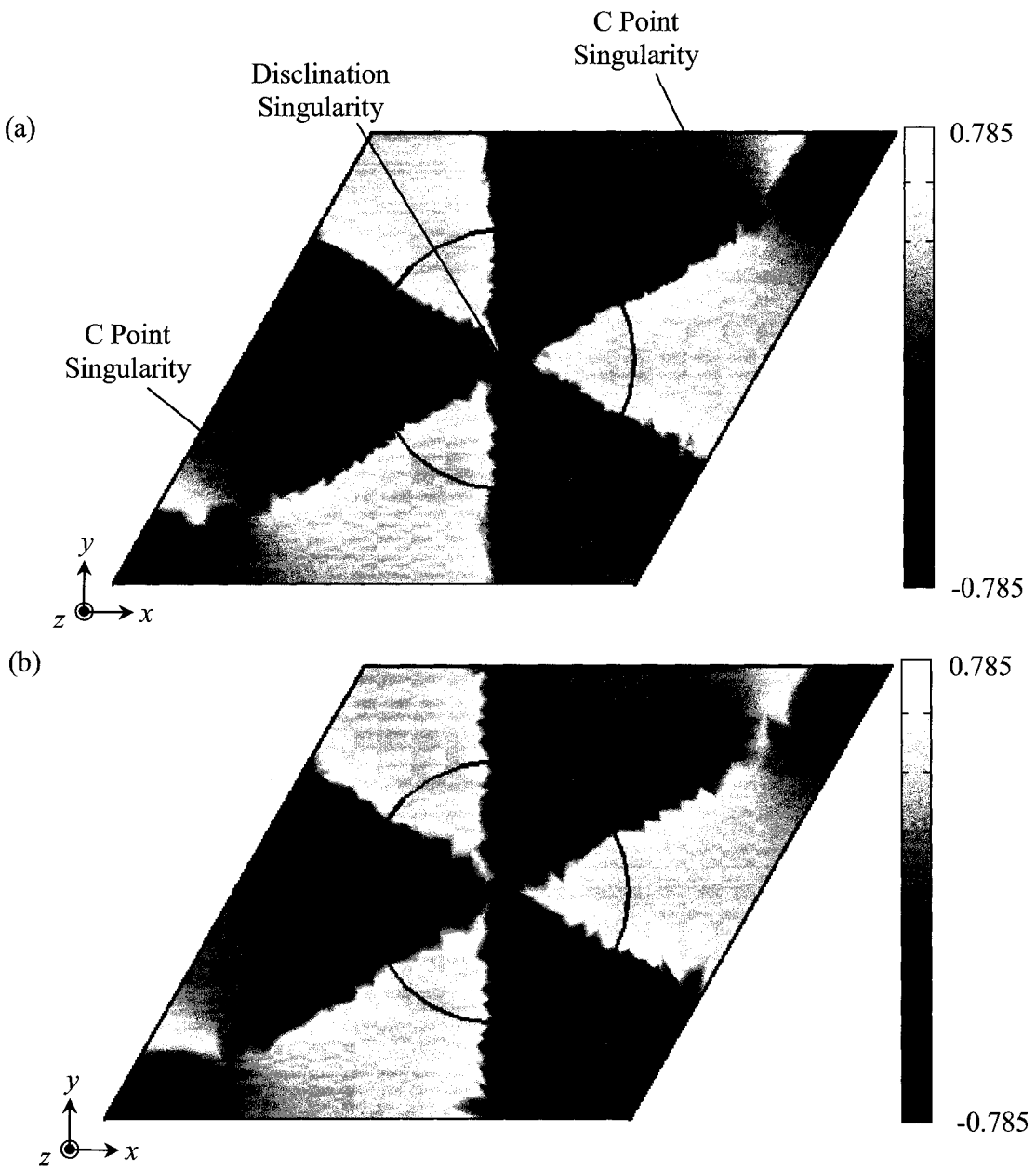

Figure 48. Hexagonal photonic crystal slab lattice air holes in a dielectric background, Bloch mode, band 1, $\mathbf{k} = \hat{\mathbf{x}} 4\pi/(3a)$. The electric field is associated with the A_2 irreducible representation of C_{3v}, displayed the phase angle $\tau(\mathbf{r})$ (a) x-y plane cross-section at the center of the slab and (b) x-y plane cross-section at the bottom of the slab. Bold black lines are edges of the unit cell and holes.

6.6 Conclusions

In this chapter, we developed a set of polarization symmetry insights based on the full space symmetry of the optical system. These polarization symmetry insights were as follows: From the global perspective of the electric field, $\mathbf{E}(\mathbf{r})$, we showed that the local state of polarization characterized by $\mathbf{P}(\mathbf{r})\times\mathbf{Q}(\mathbf{r})$ does not change when the electric field was transformed in space by a symmetry operator R of its point group; From the local perspective, we showed the transformation properties of the local electric field between its symmetry-equivalent locations (i.e., crystallographic orbit), where at locations called special Wyckoff positions, polarization singularity appeared in the local electric field. Since every point in the electric field was associated with a crystallographic orbit, we were able to define the fundamental domain of the photonic crystal eigenmode. Collectively, these polarization symmetry insights allow us to determine many of the defining features of the state of local polarization of our example optical system, the electric field of a hexagonal lattice photonic crystal. Finally, these symmetry insights were verified by comparing the theoretical predictions with simulations of high-dielectric contrast, purely two-dimensional photonic crystal, and for a two-dimensional photonic crystal slab.

The polarization insights were presented from the viewpoint of this particular optical system, but they can apply equally well in designing an optical system with specific polarization characteristics. Therefore, future work may be focused on using the polarization symmetry insights to design an optical system with a desired optical response. This research will be especially important to any area that requires precise control over the local state of polarization, such as the laser cooling of atoms, where large changes in the local state of polarization increase the efficiency of the laser cooling ([104] pp. 231-235).

CHAPTER 7 – CONCLUSIONS

7.1 Summary of the central findings

A definitive study on the sub-wavelength features of the optical modes of photonic crystals expressed through the optical singularities of the electromagnetic field was successfully accomplished. This work is the first comprehensive study to examine phase singularities and polarization singularities in purely two-dimensional photonic crystals and photonic crystal slabs using the fundamental principles of group theory, and supported by numerical simulations of physically realizable systems. It has consequently allowed fundamental design paradigms to be addressed regarding the sub-wavelength features of the electromagnetic field within optical systems of distinct symmetry. The central findings of the research are summarized below.

The first of the two types of optical singularities, the phase singularity, was reported in Chapter 5, where fundamental symmetry rules for the existence of phase singularities within the eigenmodes of photonic crystals were described. Initial insights were extracted by applying phasor geometry and group theoretic principles to analytical optical Bloch modes in the vanishing contrast limit. This permitted the determination of the spatial locations and the number of optical vortices within the photonic crystal eigenmodes. Furthermore, we were able to characterize the vortices into two distinct types: symmetry vortices and accidental vortices. In both cases, the optical vortices were found to exist within the photonic crystal eigenmodes associated with odd rotational symmetry **k**-groups, (i.e. C_{nv}, where $n=1$ or 3). We also determined that photonic crystal eigenmodes associated with even rotational symmetry **k**-groups, (i.e. C_{nv}, where $n=2,4$ or 6) cannot have phase singularities, since they are composed exclusively of conjugate plane waves. Such observations were validated through numerical simulation of the various two-dimensional photonic crystal **k**-groups, C_{nv}, at low and high dielectric

contrast. The optical vortex states were more clearly presented by examining the dislocations in the phase and the circulation of the Poynting vector about these dislocations. In simulations of the photonic crystal eigenmodes associated with odd rotation **k**-groups, we demonstrated that the spatial positions of the symmetry vortices remain invariant to changes in the dielectric contrast. In comparison, the accidental vortices experienced large changes in their spatial positions between the high and low dielectric contrast cases. The simulations of the photonic crystal eigenmodes associated with even rotation **k**-groups displayed no phase singularities. The symmetry vortices are associated with contrast-insensitive $n = 3$ symmetry, while the origin of the accidental vortices arise from a more subtle expression of the $n = 1$ symmetry. That is, the modes associated with the irreducible representations of the C_{3v} **k**-group fundamentally have the required number of plane waves to form a phase singularity (and thus demonstrate form and locational stability with varying dielectric contrast). In contrast, the modes associated with the C_{1h} **k**-group do not unless adjacent bands contribute to form the appropriate accidental degeneracy. These accidental singularities do evolve with increasing dielectric contrast and swiftly vanish, implying a *prima facie* limitation to our analytic approach, as is otherwise implied by the existence of different phase singularities at high dielectric contrast. Furthermore it was demonstrated that vortices also exist in photonic crystal slab structures. In these photonic crystal slab structures, we verified that optical vortices appeared at the same locations in the *x*-*y* plane as within the two-dimensional photonic crystals. It was also shown that the phase singularities extended infinitely along the $\hat{\mathbf{z}}$ axis beyond the confines of the photonic crystal slab structure. This is a direct result of the identical group theoretic description of the symmetry within the *x*-*y* plane between the purely two-dimensional photonic crystals and the photonic crystal slabs, which leads the way to the application of these techniques to more complex optical systems.

In Chapter 6, a second type of optical singularity was studied: the polarization singularity. Here the complex state of local polarization of the electromagnetic field was

systematically analyzed by locating the polarization singularities within the field and by deriving the symmetry transformation properties of the local state of polarization. The polarization symmetry insights were derived based on the site (local) symmetry of the optical system and ranged from the global perspective to individual points within the electromagnetic field. From the global perspective of the electric field, $\mathbf{E}(\mathbf{r})$, we showed that the state of polarization, characterized by the vector field $\mathbf{P}(\mathbf{r})\times\mathbf{Q}(\mathbf{r})$, does not change even when the electric field is transformed in space $(R|0)\mathbf{E}(\mathbf{r})$ by a symmetry operator R of its **k**-group. Next, the crystallographic orbits were defined, which are sets of symmetry-equivalent points in the electric field. In the crystallographic orbit, relative polarization relationships between points were established based on the symmetry transformation properties of $\mathbf{E}(\mathbf{r}_i)$. When all the points in the field were classified according to a crystallographic orbit, the fundamental domain of the photonic crystals eigenmode space **k**-group was defined. It was shown that, from the fundamental domain, the entire polarization response of the eigenmode is obtained. Finally, for points within the electromagnetic field congruent to positions of high symmetry, we demonstrated that the local state of polarization must be singular. These points in the field $\mathbf{E}(\mathbf{r}_i)$ appeared at locations known as special Wyckoff positions, where it was found: first, upon a mirror reflection planes, L lines must appear; second, upon a center of rotation symmetry (C_n, where $n \geq 3$), a C-point must appear; and third, at the crossing point between a mirror reflection plane and center of rotational symmetry (C_n, where $n \geq 3$), the field would vanish and a disclination must appear. Collectively, these polarization symmetry insights allow us to determine many of the defining features of the state of local polarization. These group theoretic insights where shown to be universal by examining the polarization singularities within high-dielectric contrast, purely two-dimensional photonic crystal, and two-dimensional photonic crystal slabs. In each case it was found that the polarization singularities were at locations predicted by their site symmetry maps.

This thesis reported on marked accomplishment in the novel application of the techniques of group theory to the optical response of photonic crystals. A notable result was the application of site (local) symmetry to photonic crystal eigenmodes. Previous work had focused on transformation operators R of the photonic crystal eigenmode **k**-group ($R \in C_{nv}$), with respect to the principal axis of the dielectric structure. By contrast, this work derived the irreducible matrix representations of the transformation operators $(R|\mathbf{a})$ of the photonic crystal eigenmode space **k**-group ($(R|\mathbf{a}) \in G$), which may be applied with respect to any symmetry axis. As a result, the symmetry transformation properties of the local state of polarization could be derived in Chapter 6. Furthermore, a general method to determine the analytical forms of the optical Bloch modes in the vanishing dielectric contrast limit was presented, which was previously absent from the literature.

The final objective of this research was achieved by developing FEM numerical models of purely two-dimensional photonic crystals and photonic crystal slabs including a fully developed FEM software package. These numerical models provided confirmation of all the group theoretic insights, and they will be the basis of future experimental investigations of optical singularities within photonic crystals. While developing the numerical models of the photonic crystal slabs, an original self-consistent effective index method was developed, which addressed the deficiencies of the standard effective index method when applied to high dielectric contrast photonic crystal slabs. For this body of research, the improved self-consistent effective index method provided a much needed verification of the full vector simulations of the photonic crystals slab modes in high dielectric contrast systems. This was accomplished with a modest increase in numerical resources as compared to the standard effective index method, but still much faster than full vector approaches.

7.2 Future Work

Due to the fundamental nature of this body of research, many different avenues for future work have been opened up. First and foremost is the experimental confirmation of optical singularities within photonic crystals. The challenge of this endeavor will be to fabricate a photonic crystal sample and then map the local energy flow and the local state of polarization within a photonic crystal where the optical singularities can be observed. The local characterization of the optical modes of the photonic crystal could be measured using near-field scanning optical microscopy (NSOM) [105]-[112], which allows resolution below the diffraction limit $\lambda/2$ (i.e. sub-wavelength resolution) of the electromagnetic field. This work would require a complementary numerical study to correlate the NSOM probe results with the expected behaviour of the electromagnetic field around an optical singularity, as continuation of the work by [105]-[106]. The concept of the fundamental domain would be critical to this study in order to obtain the maximum information about the optical mode within a minimum scanning area.

The significance of the vortex state in photonic crystals has implications for the robust generation of optical vortex arrays. Optical vortices have been shown to be innately related to the orbital angular momentum of the light [60], [73]. In other systems, such as Laguerre-Gaussian laser modes, it has been demonstrated that the light can transfer orbital angular momentum to dielectric particles, causing them to rotate around a vortex structure [78]-[79], and [84]. Very preliminary numerical investigations have revealed that the optical vortices within two-dimensional photonic crystals are not amenable to rotation of isotropic dielectric particles (see Appendices D-E). However, a full investigation needs to be conducted to explore the full potential of possibilities regarding the relationship between optical forces and optical singularities within photonic crystals. There are further possibilities regarding the manipulation of anisotropic particles, where it has been shown that different states of polarization can rotate such particles [118]-[119]. This study would include developing a group theoretic understanding of the

optical forces, in which desired behaviours would be mapped to system symmetries. In addition to nano-particle manipulation, planar photonic crystals that contain quantum-confined structures at predicted vortex locations may permit interesting experimental investigations. One such experiment may be the measurement of the quantum cores of optical phase singularities [86].

For the polarization symmetry insight developed in Chapter 6, future research would entail application to other systems with distinct symmetry, such as optical waveguides and optical cavities. This would be most interesting for applications that are sensitive to polarization, such as laser cooling of atoms, where large changes in the local state of polarization increase the efficiency of the laser cooling [53], ([104] pp. 231-235) or manipulation of anisotropic particles as mentioned previously.

APPENDICES

A. Derivation of the Poynting vector, scalar Bloch modes

In Section 2.4.1, we stated the form of the Poynting vector within a two-dimensional photonic crystal Bloch mode given by Eq. (2.31) and Eq. (2.32), they are restated here for the reader:

$$\mathbf{S}_{\mathbf{k}n}^{TE}(\mathbf{r}) = \frac{1}{2\omega\varepsilon_0\varepsilon(\mathbf{r})}\left[\mathbf{k}\left|v_{\mathbf{k}n}(\mathbf{r})\right|^2 - \mathrm{Im}\left[\left(v_{\mathbf{k}n}^*(\mathbf{r})\nabla v_{\mathbf{k}n}(\mathbf{r})\right)\right]\right], \tag{8.1}$$

$$\mathbf{S}_{\mathbf{k}n}^{TM}(\mathbf{r}) = \frac{1}{2\omega\mu_0}\left[\mathbf{k}\left|u_{\mathbf{k}n}(\mathbf{r})\right|^2 - \mathrm{Im}\left[\left(u_{\mathbf{k}n}^*(\mathbf{r})\nabla u_{\mathbf{k}n}(\mathbf{r})\right)\right]\right]. \tag{8.2}$$

In this appendix we explicitly derive TE case, Eq. (2.31), for the reader. By definition, the time average Poynting vector is

$$\mathbf{S}(\mathbf{r}) = \tfrac{1}{2}\mathrm{Re}\left(\mathbf{E}(\mathbf{r})\times\mathbf{H}^*(\mathbf{r})\right) \tag{8.3}$$

For the TE case, the magnetic field is linear polarized along the $\hat{\mathbf{z}}$ axis, and the related electric field is determined using Eq. (3.41):

$$\mathbf{E}(\mathbf{r}) = \left(\frac{i}{\omega\varepsilon_0\varepsilon(\mathbf{r})}\right)\left(\frac{\partial H(\mathbf{r})}{\partial y}\hat{\mathbf{x}} - \frac{\partial H(\mathbf{r})}{\partial x}\hat{\mathbf{y}}\right) \tag{8.4}$$

Taking the cross product of Eq. (8.4) with related magnetic field $H(\mathbf{r})$:

$$\mathbf{E}(\mathbf{r})\times\mathbf{H}^{*}(\mathbf{r})=\left(\frac{i}{\omega\varepsilon_{0}\varepsilon(\mathbf{r})}\right)\begin{vmatrix}\hat{\mathbf{x}} & \hat{\mathbf{y}} & \hat{\mathbf{z}}\\ \dfrac{\partial H(\mathbf{r})}{\partial y} & -\dfrac{\partial H(\mathbf{r})}{\partial x} & 0\\ 0 & 0 & H^{*}(\mathbf{r})\end{vmatrix}$$
$$=\left(\frac{i}{\omega\varepsilon_{0}\varepsilon(\mathbf{r})}\right)\left(-H^{*}(\mathbf{r})\frac{\partial H(\mathbf{r})}{\partial x}\hat{\mathbf{x}}-H^{*}(\mathbf{r})\frac{\partial H(\mathbf{r})}{\partial y}\hat{\mathbf{y}}\right) \tag{8.5}$$

Equation (8.5) is substituted into Eq. (8.3)

$$\mathbf{S}(\mathbf{r})=\tfrac{1}{2}\mathrm{Re}\left[\left(\frac{-i}{\omega\varepsilon_{0}\varepsilon(\mathbf{r})}\right)\left(H^{*}(\mathbf{r})\left(\frac{\partial H(\mathbf{r})}{\partial x}\right)\hat{\mathbf{x}}+H^{*}(\mathbf{r})\frac{\partial H(\mathbf{r})}{\partial y}\hat{\mathbf{y}}\right)\right] \tag{8.6}$$

where it can be rewritten as

$$\mathbf{S}(\mathbf{r})=\tfrac{1}{2}\mathrm{Re}\left[\left(\frac{-i}{\omega\varepsilon_{0}\varepsilon(\mathbf{r})}\right)\left(H^{*}(\mathbf{r})\nabla H(\mathbf{r})\right)\right] \tag{8.7}$$

We can eliminate i by using $\mathrm{Re}(a+ib)=a=\mathrm{Im}(i(a+ib))$ and then Eq. (8.7) becomes

$$\mathbf{S}(\mathbf{r})=\left(\frac{1}{2\omega\varepsilon_{0}\varepsilon(\mathbf{r})}\right)\mathrm{Im}\left[\left(H^{*}(\mathbf{r})\nabla H(\mathbf{r})\right)\right] \tag{8.8}$$

The periodic symmetry of the system allows us to state the magnetic field in the form of a Bloch mode $\mathbf{H}_{kn}(\mathbf{r})=\hat{\mathbf{z}}H_{kn}(\mathbf{r})=\hat{\mathbf{z}}v_{kn}(\mathbf{r})e^{i\mathbf{k}\cdot\mathbf{r}}$, (see Eq. (2.30)). The spatial derivative of Eq. (2.30) in the $\hat{\mathbf{x}}$ direction is

$$\frac{\partial H_{kn}(\mathbf{r})}{\partial x}=\frac{\partial}{\partial x}\left(v_{kn}(\mathbf{r})\exp(i\mathbf{k}\cdot\mathbf{r})\right)=\frac{\partial v_{kn}(\mathbf{r})}{\partial x}\exp(i\mathbf{k}\cdot\mathbf{r})+ik_{x}v_{kn}(\mathbf{r})\left(\exp(i\mathbf{k}\cdot\mathbf{r})\right)$$
$$=\left(\exp(i\mathbf{k}\cdot\mathbf{r})\right)\left(\frac{\partial v_{kn}(\mathbf{r})}{\partial x}+ik_{x}v_{kn}(\mathbf{r})\right), \tag{8.9}$$

and in the $\hat{\mathbf{y}}$ direction is

$$\frac{\partial H_{kn}(\mathbf{r})}{\partial y}=\frac{\partial}{\partial y}\left(v_{kn}(\mathbf{r})\exp(i\mathbf{k}\cdot\mathbf{r})\right)=\frac{\partial v_{kn}(\mathbf{r})}{\partial y}\exp(i\mathbf{k}\cdot\mathbf{r})+ik_y v_{kn}(\mathbf{r})\left(\exp(i\mathbf{k}\cdot\mathbf{r})\right)$$
$$=\left(\exp(i\mathbf{k}\cdot\mathbf{r})\right)\left(\frac{\partial v_{kn}(\mathbf{r})}{\partial y}+ik_y v_{kn}(\mathbf{r})\right). \tag{8.10}$$

Substitution of Eqs. (2.30), (8.9) and (8.10) into Eq. (8.6) and we obtain the Poynting vector in terms of the Bloch wave vector $\mathbf{k}$ and its periodic part $v_{kn}(\mathbf{r})$:

$$\mathbf{S}_{kn}^{TE}(\mathbf{r})=\tfrac{1}{2}\mathrm{Re}\left[\left(\frac{-i}{\omega\varepsilon_0\varepsilon(\mathbf{r})}\right)\left(v_{kn}^{*}(\mathbf{r})\left(\frac{\partial v_{kn}(\mathbf{r})}{\partial x}+ik_x v_{kn}(\mathbf{r})\right)\hat{\mathbf{x}}+v_{kn}^{*}(\mathbf{r})\left(\frac{\partial v_{kn}(\mathbf{r})}{\partial y}+ik_y v_{kn}(\mathbf{r})\right)\hat{\mathbf{y}}\right)\right] \tag{8.11}$$

Alternately we can express Eq. (8.11) in form similar to Eq. (8.7):

$$\mathbf{S}_{kn}^{TE}(\mathbf{r})=\tfrac{1}{2}\mathrm{Re}\left[\left(\frac{-i}{\omega\varepsilon_0\varepsilon(\mathbf{r})}\right)\left(i\mathbf{k}\left|v_{kn}(\mathbf{r})\right|^2+v_{kn}^{*}(\mathbf{r})\nabla v_{kn}(\mathbf{r})\right)\right]$$

$$\mathbf{S}_{kn}^{TE}(\mathbf{r})=\left(\frac{1}{2\omega\varepsilon_0\varepsilon(\mathbf{r})}\right)\mathbf{k}\left|v_{kn}(\mathbf{r})\right|^2+\mathrm{Re}\left[\left(\frac{-i}{\omega\varepsilon_0\varepsilon(\mathbf{r})}\right)\left(v_{kn}^{*}(\mathbf{r})\nabla v_{kn}(\mathbf{r})\right)\right] \tag{8.12}$$

Finally using $\mathrm{Re}(a+ib)=a=\mathrm{Im}(i(a+ib))$ again,

$$\mathrm{Re}\left[\left(\frac{1}{2\omega\varepsilon_0\varepsilon(\mathbf{r})}\right)\left(v_{kn}^{*}(\mathbf{r})\nabla v_{kn}(\mathbf{r})\right)\right]=\left(\frac{1}{2\omega\varepsilon_0\varepsilon(\mathbf{r})}\right)\mathrm{Im}\left[\left(v_{kn}^{*}(\mathbf{r})\nabla v_{kn}(\mathbf{r})\right)\right] \tag{8.13}$$

we can obtain a form similar to Eq. (8.8)

$$\mathbf{S}(\mathbf{r})=\left(\frac{1}{2\omega\varepsilon_0\varepsilon(\mathbf{r})}\right)\left\{\mathbf{k}\left|v_{kn}(\mathbf{r})\right|^2-\mathrm{Im}\left[\left(v_{kn}^{*}(\mathbf{r})\nabla v_{kn}(\mathbf{r})\right)\right]\right\}. \tag{8.14}$$

B. Two-dimensional photonic crystal eigenmodes plane wave expansion

This is an expanded derivation of the two-dimensional photonic crystal eigenmodes in the vanishing dielectric contrast limit, as discussed in Section 2.4.2. In the vanishing dielectric contrast limit, we show that photonic crystal eigenmodes are well approximated as linear combinations of a small number of degenerate plane waves. This will be acomplished using the plane wave expansion method applied to the TM eigenvalue problem and examining the general form of the Fourier coefficients.

The eigenvalue problems for the TE and TM modes are as follows as given in Section 2.4.1:

$$\mathsf{L}_E^{(TM)} E_z(\mathbf{r}) \equiv -\frac{1}{\varepsilon(\mathbf{r})}\left(\frac{\partial^2}{\partial x^2}+\frac{\partial^2}{\partial y^2}\right)E_z(\mathbf{r}) = \frac{\omega^2}{c^2}E_z(\mathbf{r}), \tag{8.15}$$

$$\mathsf{L}_E^{(TE)} H_z(\mathbf{r}) \equiv -\left(\frac{\partial}{\partial x}\frac{1}{\varepsilon(\mathbf{r})}\frac{\partial}{\partial x}+\frac{\partial}{\partial y}\frac{1}{\varepsilon(\mathbf{r})}\frac{\partial}{\partial y}\right)H_z(\mathbf{r}) = \frac{\omega^2}{c^2}H_z(\mathbf{r}). \tag{8.16}$$

From Eqs. (2.33) and (2.34), the Fourier expansion of the Bloch mode for the TE and TM cases is

$$E_{\mathbf{k}n}(\mathbf{r}) = \sum_{\mathbf{G}} E_{\mathbf{k}n}(\mathbf{G}) e^{i(\mathbf{k}+\mathbf{G})\cdot\mathbf{r}}, \tag{8.17}$$

$$H_{\mathbf{k}n}(\mathbf{r}) = \sum_{\mathbf{G}} H_{\mathbf{k}n}(\mathbf{G}) e^{i(\mathbf{k}+\mathbf{G})\cdot\mathbf{r}}, \tag{8.18}$$

where we suppress $\hat{\mathbf{z}}$ for convenience and place the term $e^{i\mathbf{k}\cdot\mathbf{r}}$ inside the summation. The dielectric profile is a periodic function with the periodicity of the Bravais lattice, as discussed in Section 2.2.2 given by Eq. (2.2). Therefore, $1/\varepsilon(\mathbf{r})$ can also be expanded in a Fourier series just as the Bloch modes:

$$1/\varepsilon(\mathbf{r}) = \sum_{\mathbf{G}} \kappa(\mathbf{G}) e^{i\mathbf{G}\cdot\mathbf{r}}, \tag{8.19}$$

where $\kappa(\mathbf{G})$ is the Fourier coefficient in reciprocal space and because the dielectric profile is a real function $\kappa(-\mathbf{G}) = \kappa^*(\mathbf{G})$ ([5], p. 14). Focusing on the TM case, we substitute Eqs. (8.17) and (8.19) into Eq. (8.15) and obtain

$$-1/\varepsilon(\mathbf{r}) = \sum_{\mathbf{G}'} \kappa(\mathbf{G}') e^{i\mathbf{G}'\cdot\mathbf{r}} \left(\frac{\partial^2}{\partial x^2} + \frac{\partial^2}{\partial y^2} \right) \sum_{\mathbf{G}} E_{kn}(\mathbf{G}) e^{i(\mathbf{k}+\mathbf{G})\cdot\mathbf{r}} = \frac{\omega^2}{c^2} \sum_{\mathbf{G}} E_{kn}(\mathbf{G}) e^{i(\mathbf{k}+\mathbf{G})\cdot\mathbf{r}}. \tag{8.20}$$

Using standard techniques ([5], pp. 19-21), from Eq.(8.20), we can obtain the following eigenvalue relationship for each Fourier coefficients $E_{kn}(\mathbf{G})$ of Eq. (8.17):

$$\sum_{\mathbf{G}'} \kappa(\mathbf{G}-\mathbf{G}') |\mathbf{k}+\mathbf{G}'|^2 E_{kn}(\mathbf{G}') = \frac{\omega_{kn}^2}{c^2} E_{kn}(\mathbf{G}) \tag{8.21}$$

where ω_{kn} is the frequency of the $(\mathbf{k}, n)$ photonic crystal eigenmode. Now, we can rearrange the lefthand side of Eq. (8.21), so that the Fourier coefficient $E_{kn}(\mathbf{G}')$, when $\mathbf{G}' = \mathbf{G}$, is placed outside the summation:

$$\kappa(\mathbf{G}-\mathbf{G}) |\mathbf{k}+\mathbf{G}|^2 E_{kn}(\mathbf{G}) + \sum_{\mathbf{G}' \neq \mathbf{G}} \kappa(\mathbf{G}-\mathbf{G}') |\mathbf{k}+\mathbf{G}'|^2 E_{kn}(\mathbf{G}') = \frac{\omega_{kn}^2}{c^2} E_{kn}(\mathbf{G}) \tag{8.22}$$

and then place all the coefficients $E_{kn}(\mathbf{G})$ on one side

$$\sum_{\mathbf{G}' \neq \mathbf{G}} \kappa(\mathbf{G}-\mathbf{G}') |\mathbf{k}+\mathbf{G}'|^2 E_{kn}(\mathbf{G}') = \left[\frac{\omega_{kn}^2}{c^2} - \kappa(0) |\mathbf{k}+\mathbf{G}|^2 \right] E_{kn}(\mathbf{G}). \tag{8.23}$$

Then the general relationship for a Fourier coefficient $E_{kn}(\mathbf{G})$ becomes

$$E_{kn}(\mathbf{G}) = \frac{c^2}{\left[\omega_{kn}^2 - \kappa(0)|\mathbf{k}+\mathbf{G}|^2 c^2\right]} \sum_{\mathbf{G}' \neq \mathbf{G}} \kappa(\mathbf{G}-\mathbf{G}')|\mathbf{k}+\mathbf{G}'|^2 E_{kn}(\mathbf{G}'). \tag{8.24}$$

The relative weighting coefficient of the general Fourier coefficient $E_{kn}(\mathbf{G})$ is determined by

$$\frac{1}{\left[\omega_{kn}^2 - \kappa(0)|\mathbf{k}+\mathbf{G}|^2 c^2\right]}, \tag{8.25}$$

from Eq. (8.24). In Eq. (8.25),

$$\kappa(0)|\mathbf{k}+\mathbf{G}|^2 c^2 = \omega^2 \tag{8.26}$$

where ω is equal to the frequency of a plane wave with a wave vector $\mathbf{k}+\mathbf{G}$ in a medium with the dielectric permittivity of $\varepsilon = 1/\kappa(0)$, in which the plane wave dispersion relationship is $\omega/|\mathbf{k}| = c/\sqrt{\varepsilon}$. In the Fourier expansion given by Eq. (8.19), the zero order term is $\kappa(0) = 1/\varepsilon(0)$, where $\varepsilon(0)$ is the average dielectric permittivity of the photonic crystal. Therefore, ω from Eq. (8.26) is the frequency of a plane wave with a wave vector $\mathbf{k}+\mathbf{G}$ in a medium that has a dielectric permittivity equal to the average of the photonic crystal. If

$$\omega_{kn}^2 \approx \kappa(0)|\mathbf{k}+\mathbf{G}|^2 c^2 \tag{8.27}$$

then Eq. (8.25) becomes very large, which means $E_{\mathbf{k}n}(\mathbf{G}) \gg E_{\mathbf{k}n}(\mathbf{G}')$, where $\mathbf{G}' \neq \mathbf{G}$. In this case, we can assume the Fourier coefficient $E_{\mathbf{k}n}(\mathbf{G})$ dominates and all other Fourier coefficient $E_{\mathbf{k}n}(\mathbf{G}') \approx 0$. Then Eq. (8.17) becomes

$$E_{\mathbf{k}n}(\mathbf{r}) \simeq E_{\mathbf{k}n}(\mathbf{G}) e^{i(\mathbf{k}+\mathbf{G})\cdot\mathbf{r}}. \tag{8.28}$$

If there are multiple wave vectors $\mathbf{k}+\mathbf{G}$ such that

$$\omega_{\mathbf{k}n}^2 \approx \kappa(0)|\mathbf{k}+\mathbf{G}|^2 c^2 = \kappa(0)|\mathbf{k}+\mathbf{G}'|^2 c^2 = \kappa(0)|\mathbf{k}+\mathbf{G}''|^2 c^2, \tag{8.29}$$

then the Fourier coefficients $E_{\mathbf{k}n}(\mathbf{G})$, $E_{\mathbf{k}n}(\mathbf{G}')$ and $E_{\mathbf{k}n}(\mathbf{G}'')$ dominate Eq. (8.17) and then the photonic crystal eigenmode is

$$E_{\mathbf{k}n}(\mathbf{r}) \approx E_{\mathbf{k}n}(\mathbf{G}) e^{i(\mathbf{k}+\mathbf{G})\cdot\mathbf{r}} + E_{\mathbf{k}n}(\mathbf{G}') e^{i(\mathbf{k}+\mathbf{G}')\cdot\mathbf{r}} + E_{\mathbf{k}n}(\mathbf{G}'') e^{i(\mathbf{k}+\mathbf{G}'')\cdot\mathbf{r}} + \ldots \tag{8.30}$$

From Section 2.4.2, in the vanishing dielectric contrast limit, the two different dielectric permittives of the photonic crystal are $\varepsilon_1 \approx \varepsilon_2$. The wave vector $\mathbf{q}$ can be mapped into the first Brillouin zone using Eq. (2.22) and the dispersion relationship becomes

$$\omega(\mathbf{k}) \approx v_{ph}|\mathbf{q}| = v_{ph}\sqrt{(\mathbf{k}+\mathbf{G})\cdot(\mathbf{k}+\mathbf{G})}. \tag{8.31}$$

which is equivalent to Eq. (8.27). Therefore, when Eq. (8.31) is true, Eq. (8.25) ensures that just a small number of Fourier coefficients $E_{\mathbf{k}n}(\mathbf{G})$ are needed to obtain a good approximation to the photonic crystal eigenmode $E_{\mathbf{k}n}(\mathbf{r})$ given by Eq. (8.30), where the plane waves are degenerate (see Eq. (8.29)).

C. Projection operators and irreducible representations: inner product of two partner functions and irreducible matrix representations

In Section 3.3.4, we reviewed that the partner functions from two different irreducible representations are orthogonal when their inner product is defined as

$$\int_V \left\{\mathbf{E}_{\mathbf{k}i}^{(v)}(\mathbf{r})\right\}^* \cdot \mathbf{E}_{\mathbf{k}'j}^{(w)}(\mathbf{r})\, d\mathbf{r} = V\delta_{\mathbf{k},\mathbf{k}'}\delta_{v,w}, \tag{8.32}$$

where the integral is over the entire photonic crystal with a volume of V and $\delta_{p,d} = 0$ when $p \neq d$.

From Section 3.4.4, we need to use the orthogonality of the partner functions to determine the partner functions of the E irreducible representation. The following is the explicit calculation of the inner product

$$\int_V \left\{\mathbf{E}_{\mathbf{k}}^{(A_2)}(\mathbf{r})\right\}^* \cdot \mathbf{E}_{\mathbf{k}1}^{(E)}(\mathbf{r})\, d\mathbf{r} = 0. \tag{8.33}$$

Substituting Eq. (3.72) and Eq. (3.67) into Eq. (8.33) we find

$$\int_V \frac{1}{6}\left(2\mathbf{T}_1^{(red)} - \mathbf{T}_2^{(red)} + \mathbf{T}_3^{(red)}\right)^* \cdot \frac{1}{6}\left(4\mathbf{T}_1^{(red)} + \mathbf{T}_2^{(red)} - \mathbf{T}_3^{(red)}\right) d\mathbf{r} = 0. \tag{8.34}$$

This integral is best solved by examining the inner product of the reducible partner functions first. The partner functions of the reducible representations are given by

$$\mathbf{T}_1^{(red)}(\mathbf{r}) = \begin{pmatrix} 0 \\ 1 \\ 0 \end{pmatrix} e^{i4\pi x/3a} \cos(k_z z), \tag{8.35}$$

$$\mathbf{T}_2^{(red)}(\mathbf{r}) = \begin{pmatrix} \sqrt{3} \\ 1 \\ 0 \end{pmatrix} e^{-i2\pi\left(x/3a - y/(\sqrt{3}a)\right)} \cos(k_z z), \tag{8.36}$$

$$\mathbf{T}_3^{(red)}(\mathbf{r}) = \begin{pmatrix} \sqrt{3} \\ -1 \\ 0 \end{pmatrix} e^{-i2\pi\left(x/3a + y/(\sqrt{3}a)\right)} \cos(k_z z). \tag{8.37}$$

If we examine the inner product of just two of the reducible partner functions we find:

$$\int_V \left\{\mathbf{T}_1^{(red)}(\mathbf{r})\right\}^* \cdot \mathbf{T}_2^{(red)}(\mathbf{r})\, d\mathbf{r} = \int_V \begin{pmatrix} 0 \\ 1 \\ 0 \end{pmatrix} e^{-i4\pi x/3a} \cos(k_z z) \cdot \begin{pmatrix} \sqrt{3} \\ 1 \\ 0 \end{pmatrix} e^{-i2\pi\left(x/3a - y/(\sqrt{3}a)\right)} \cos(k_z z)\, d\mathbf{r} = 0, \tag{8.38}$$

The inner product of $\mathbf{T}_1^{(red)}$ and $\mathbf{T}_2^{(red)}$ vanish, because any two different plane waves $e^{i4\pi x/3a}$ and $e^{-i2\pi\left(x/3a - y/(\sqrt{3}a)\right)}$ are orthogonal. Therefore we can state

$$\int_V \left\{\mathbf{T}_n^{(red)}(\mathbf{r})\right\}^* \cdot \mathbf{T}_m^{(red)}(\mathbf{r})\, d\mathbf{r} = V\delta_{n,m}. \tag{8.39}$$

Next, we examine the inner product when $n = m$

$$\int_V \left\{\mathbf{T}_2^{(red)}(\mathbf{r})\right\}^* \cdot \mathbf{T}_2^{(red)}(\mathbf{r})\, d\mathbf{r} = \int_V \begin{pmatrix} \sqrt{3} \\ 1 \\ 0 \end{pmatrix} e^{i2\pi\left(x/3a - y/(\sqrt{3}a)\right)} \cos(k_z z) \cdot \begin{pmatrix} \sqrt{3} \\ 1 \\ 0 \end{pmatrix} e^{-i2\pi\left(x/3a - y/(\sqrt{3}a)\right)} \cos(k_z z)\, d\mathbf{r} \tag{8.40}$$

The terms $e^{i2\pi\left(x/3a - y/(\sqrt{3}a)\right)}$ and $e^{-i2\pi\left(x/3a - y/(\sqrt{3}a)\right)}$ from Eq. (8.40) cancel as a results of

$$\left[e^{i2\pi\left(x/3a-y/\left(\sqrt{3}a\right)\right)}\right]e^{-i2\pi\left(x/3a-y/\left(\sqrt{3}a\right)\right)}=1 \tag{8.41}$$

Substitution of Eq. (8.41) back into Eq. (8.40) we find

$$\int_V\left\{\mathbf{T}_2^{(red)}(\mathbf{r})\right\}^*\cdot\mathbf{T}_2^{(red)}(\mathbf{r})\,d\mathbf{r}=\int_V\begin{pmatrix}\sqrt{3}\\1\\0\end{pmatrix}\cdot\begin{pmatrix}\sqrt{3}\\1\\0\end{pmatrix}\left(\cos\left(k_z z\right)\right)^2 d\mathbf{r}\,. \tag{8.42}$$

The dot product of the two vectors in Eq. (8.42) is

$$\begin{pmatrix}\sqrt{3}\\1\\0\end{pmatrix}\cdot\begin{pmatrix}\sqrt{3}\\1\\0\end{pmatrix}=\left(\sqrt{3}\right)\sqrt{3}+(1)1=4\,. \tag{8.43}$$

Substitute Eq. (8.43) into Eq. (8.42) we find

$$\int_V\left\{\mathbf{T}_2^{(red)}(\mathbf{r})\right\}^*\cdot\mathbf{T}_2^{(red)}(\mathbf{r})\,d\mathbf{r}=\int_V 4\left(\cos\left(k_z z\right)\right)^2 d\mathbf{r}\,. \tag{8.44}$$

The same exercise can be performed for the other partner functions and we find

$$\int_V\left\{\mathbf{T}_1^{(red)}(\mathbf{r})\right\}^*\cdot\mathbf{T}_1^{(red)}(\mathbf{r})\,d\mathbf{r}=\int_V\left(\cos\left(k_z z\right)\right)^2 d\mathbf{r}\,. \tag{8.45}$$

$$\int_V\left\{\mathbf{T}_3^{(red)}(\mathbf{r})\right\}^*\cdot\mathbf{T}_3^{(red)}(\mathbf{r})\,d\mathbf{r}=\int_V 4\left(\cos\left(k_z z\right)\right)^2 d\mathbf{r}\,. \tag{8.46}$$

Using the inner product rules established for the reducible partner functions $\mathbf{T}_m^{(red)}$, Eq. (8.39), and Eqs. (8.44)-(8.46), we now can easily evaluate the integral Eq. (8.34)

$$\int_V \frac{1}{6}\left(2\mathbf{T}_1^{(red)} - \mathbf{T}_2^{(red)} + \mathbf{T}_3^{(red)}\right)^* \cdot \frac{1}{6}\left(4\mathbf{T}_1^{(red)} + \mathbf{T}_2^{(red)} - \mathbf{T}_3^{(red)}\right) d\mathbf{r},$$

$$= \int_V \frac{1}{36}\left(8\left\{\mathbf{T}_1^{(red)}\right\}^* \cdot \mathbf{T}_1^{(red)} - \left\{\mathbf{T}_2^{(red)}\right\}^* \cdot \mathbf{T}_2^{(red)} - \left\{\mathbf{T}_3^{(red)}\right\}^* \cdot \mathbf{T}_3^{(red)}\right) d\mathbf{r}, \tag{8.47}$$

$$= \int_V \frac{1}{36}(8-4-4)\left(\cos(k_z z)\right)^2 d\mathbf{r} = 0.$$

Therefore, we have shown that

$$\int_V \mathbf{E}_{\mathbf{k}}^{(A_2)}(\mathbf{r}) \cdot \mathbf{E}_{\mathbf{k}1}^{(E)}(\mathbf{r}) d\mathbf{r} = 0, \tag{8.48}$$

and confirmed our initial assumption that Eq. (3.72) is the partner function of the E irreducible representation.

The second potential partner function of the E irreducible representation is

$$\mathbf{E}_{\mathbf{k}2}^{(E)}(\mathbf{r}) = P^{(E)}\mathbf{T}_2^{(red)} + P^{(E)}\mathbf{T}_3^{(red)}, \tag{8.49}$$

where

$$P^{(E)}\mathbf{T}_2^{(red)} = \frac{2}{6}\left(2\mathbf{T}_1^{(red)} + 2\mathbf{T}_2^{(red)} + \mathbf{T}_3^{(red)}\right), \tag{8.50}$$

$$P^{(E)}\mathbf{T}_3^{(red)} = \frac{2}{6}\left(-2\mathbf{T}_1^{(red)} + \mathbf{T}_2^{(red)} + 2\mathbf{T}_3^{(red)}\right). \tag{8.51}$$

Substituting Eqs. (8.50)-(8.51) into Eq. (8.49)

$$\mathbf{E}_{\mathbf{k}2}^{(E)}(\mathbf{r}) = \mathbf{T}_2^{(red)} + \mathbf{T}_3^{(red)}. \tag{8.52}$$

Then the inner product of

$$\int_V \left\{\mathbf{E}_{\mathbf{k}}^{(A_2)}(\mathbf{r})\right\}^* \cdot \mathbf{E}_{\mathbf{k}2}^{(E)}(\mathbf{r})\,d\mathbf{r} = \int_V \frac{1}{6}\left(2\mathbf{T}_1^{(red)} - \mathbf{T}_2^{(red)} + \mathbf{T}_3^{(red)}\right)^* \cdot \left(\mathbf{T}_2^{(red)} + \mathbf{T}_3^{(red)}\right) d\mathbf{r}. \quad (8.53)$$

Using the inner product rules established for the reducible partner functions $\mathbf{T}_m^{(red)}$, Eq. (8.39), and Eqs. (8.44)-(8.46), we now easily evaluate the integral Eq. (8.53)

$$\int_V \left\{\mathbf{E}_{\mathbf{k}}^{(A_2)}(\mathbf{r})\right\}^* \cdot \mathbf{E}_{\mathbf{k}2}^{(E)}(\mathbf{r})\,d\mathbf{r} = \int_V \frac{1}{6}(-4+4)\left(\cos(k_z z)\right)^2 d\mathbf{r} = 0. \quad (8.54)$$

Therefore the second partner function $\mathbf{E}_{\mathbf{k}2}^{(E)}(\mathbf{r})$ is also orthogonal to $\mathbf{E}_{\mathbf{k}}^{(A_2)}(\mathbf{r})$.

As a secondary check, we can determine the irreducible matrix representations $\ddot{D}^{(E)}(R)$, using the partner functions $\mathbf{E}_{\mathbf{k}1}^{(E)}(\mathbf{r})$ are $\mathbf{E}_{\mathbf{k}2}^{(E)}(\mathbf{r})$, and match the character of $\ddot{D}^{(E)}(R)$ to the C_{3v} character table. The irreducible matrix representation is defined by

$$R\mathbf{E}_{\mathbf{k}i}^{(E)}(\mathbf{r}) = \sum_j^l D_{ji}^{(red)}(R)\mathbf{E}_{\mathbf{k}j}^{(E)}(\mathbf{r}), \quad (8.55)$$

where $D_{ji}^{(E)}(R)$ is an element of the matrix $\ddot{D}^{(E)}(R)$, i denotes the degeneracy, l is the number of partner functions. For $R = C_3$ and $i = 1$ the left-hand side of Eq. (8.55) is

$$\begin{aligned} C_3\mathbf{E}_{\mathbf{k}1}^{(E)}(\mathbf{r}) &= \left(4C_3\mathbf{T}_1^{(red)} + C_3\mathbf{T}_2^{(red)} - C_3\mathbf{T}_3^{(red)}\right), \\ &= \left(2\mathbf{T}_3^{(red)} - 2\mathbf{T}_1^{(red)} + \mathbf{T}_2^{(red)}\right), \end{aligned} \quad (8.56)$$

where we have used the results of Table 3. Equation (8.56) is equal to the following linear combination of partner functions

$$\left(2\mathbf{T}_3^{(red)} - 2\mathbf{T}_1^{(red)} + \mathbf{T}_2^{(red)}\right) = -1/2\,\mathbf{E}_{\mathbf{k}1}^{(E)}(\mathbf{r}) + 2/3\,\mathbf{E}_{\mathbf{k}2}^{(E)}(\mathbf{r}). \quad (8.57)$$

The right-hand side of Eq. (8.55) is

$$D_{11}^{(E)}(C_3)\mathbf{E}_{\mathbf{k}1}^{(E)}(\mathbf{r})+D_{21}^{(E)}(C_3)\mathbf{E}_{\mathbf{k}2}^{(E)}(\mathbf{r}). \tag{8.58}$$

Comparing the Eq. (8.57) and Eq. (8.58), we can determine $D_{11}^{(E)}(C_3)=-1/2$ and $D_{21}^{(E)}(C_3)=3/2$. For $R=C_3$ and $i=2$ the left-hand side of Eq. (8.55) is

$$\begin{aligned} C_3\mathbf{E}_{\mathbf{k}2}^{(E)}(\mathbf{r}) &= \left(C_3\mathbf{T}_2^{(red)}+C_3\mathbf{T}_3^{(red)}\right), \\ &= \left(-2\mathbf{T}_1^{(red)}-\mathbf{T}_2^{(red)}\right). \end{aligned} \tag{8.59}$$

Equation (8.59) is equal to the following linear combination of partner functions

$$\left(-2\mathbf{T}_1^{(red)}-\mathbf{T}_2^{(red)}\right)=-1/2\,\mathbf{E}_{\mathbf{k}1}^{(E)}(\mathbf{r})-1/2\,\mathbf{E}_{\mathbf{k}2}^{(E)}(\mathbf{r}). \tag{8.60}$$

The right-hand side of Eq. (8.55) is

$$D_{12}^{(E)}(C_3)\mathbf{E}_{\mathbf{k}1}^{(E)}(\mathbf{r})+D_{22}^{(E)}(C_3)\mathbf{E}_{\mathbf{k}2}^{(E)}(\mathbf{r}). \tag{8.61}$$

Comparing the Eq. (8.60) and Eq. (8.61), we can determine $D_{12}^{(E)}(C_3)=-1/2$ and $D_{22}^{(E)}(C_3)=-1/2$. Then the final irreducible matrix representation is

$$\vec{D}^{(E)}(C_3)=\begin{pmatrix} -1/2 & -1/2 \\ 3/2 & -1/2 \end{pmatrix}. \tag{8.62}$$

We can repeat this process for the trivial operator $R=E$

$$\ddot{D}^{(E)}(E)=\begin{pmatrix}1 & 0\\ 0 & 1\end{pmatrix}. \tag{8.63}$$

and for the operator $R=\sigma_y$

$$\ddot{D}^{(E)}(\sigma_y)=\begin{pmatrix}-1 & 0\\ 0 & 1\end{pmatrix}. \tag{8.64}$$

Using Eq. (3.11), we can determine the characters of $\ddot{D}^{(E)}(E)$, $\ddot{D}^{(E)}(C_3)$ and $\ddot{D}^{(E)}(\sigma_y)$:

$$\chi_E^{(E)}=Tr\left\{\ddot{D}^{(E)}(E)\right\}=1+1=2. \tag{8.65}$$

$$\chi_{C_3}^{(E)}=Tr\left\{\ddot{D}^{(E)}(C_3)\right\}=-1/2-1/2=-1. \tag{8.66}$$

$$\chi_{\sigma_y}^{(E)}=Tr\left\{\ddot{D}^{(E)}(\sigma_y)\right\}=-1+1=0. \tag{8.67}$$

Checking the the C_{3v} character table (see Table 1), we find that Eqs. (8.65)-(8.67) match the characters from each of the three conjugacy classes. Therefore, we are sure that the partner functions of the E irreducible representation are

$$\mathbf{E}_{\mathbf{k}1}^{(E)}(\mathbf{r})=\frac{1}{6}\left(4\mathbf{T}_1^{(red)}+\mathbf{T}_2^{(red)}-\mathbf{T}_3^{(red)}\right), \tag{8.68}$$

$$\mathbf{E}_{\mathbf{k}2}^{(E)}(\mathbf{r})=\mathbf{T}_2^{(red)}+\mathbf{T}_3^{(red)}, \tag{8.69}$$

because the two functions are orthogonal to $\mathbf{E}_{\mathbf{k}}^{(A_2)}(\mathbf{r})$ and the character $\chi_{C_3}^{(E)}$ matches the expected value from the C_{3v} character table.

D. Optical forces and their relationship to optical singularities in purely two-dimensional photonic crystals

The significance of the optical vortex state in photonic crystals has implications for the robust generation of optical vortex arrays. Optical vortices have been shown to be intimately related to the orbital angular momentum of the light [60], and [73]. In other systems, such as Laguerre-Gaussian laser modes, it has been demonstrated that orbital angular momentum can be transferred to dielectric particles that are smaller than the wavelength of the light, which causes the particles to rotate within the optical vortex [78]-[79], and [84]. The following is a preliminary numerical investigation studying the optical forces generated within an optical Bloch mode containing optical vortices to determine if the same transfer of orbital angular momentum is possible. There have been previous studies of optical forces within photonic crystals, but they have not examined the effect of optical singularities [49]-[59], which makes this research unique. These numerical simulations have revealed the optical vortices within two-dimensional photonic crystals are not amenable to the transfer of orbital angular momentum to isotropic dielectric particles, as is the case for the Laguerre-Gaussian beams. However, it is shown that optical singularities form the focal points for the optical forces. This appendix represents unfinished work regarding the impact of optical singularities on the optical forces generated within photonic crystal structures. A full investigation needs to be conducted to explore the potential of this application of optical singularities. A possibility for future research is the manipulation of anisotropic particles, where it has been shown that circular polarized light can rotates these particles [118]-[119]. The complex states of local polarization discussed in Chapter 6 would provide very interesting for this work, where different particles would experience different rotational forces.

In order for dielectric particles to travel freely, they are normally suspended within a fluid. For this initial theoretical study, the impact of the dielectric materials and their effect on the movement of small dielectric particles were not considered. An important

future question is, therefore, what real dielectric materials are suitable for experimental realization? The optical forces are calculated using Lorentz force in the dipole approximation. In the dipole approximation, dielectric particles that are much smaller than the wavelength of the light $d \ll \lambda$ (where d is the particle radius) can be viewed as ideal charged dipoles within the electromagnetic field. Using the dipole approximation, the time-averaged optical forces are given by

$$\left\langle F_j(\mathbf{r})\right\rangle = (1/2)\,\mathrm{Re}\left[\alpha E_k(\mathbf{r})\partial E_k^*(\mathbf{r})/\partial x_j\right] \tag{8.70}$$

where $j,k = 1,2,3$ [120].

$$\alpha = \alpha_0 \big/ \left(1 - \tfrac{2}{3} ik^3 \alpha_0\right) \tag{8.71}$$

is the polarizability of the particle which includes a radiation reaction term, where $\alpha_0 = d^3(\varepsilon - 1)/(\varepsilon + 2)$ is the Claussius–Mossotti equation for static polarizability and $\varepsilon = \varepsilon_2/\varepsilon_1$, ε_2 is the dielectric permittivity of the small dielectric particle and ε_1 is the dielectric permittivity of the background material. The direction of the optical forces changes depending on the sign of the Claussius-Mossotti equation, where α_0 will be positive if $\varepsilon_2 > \varepsilon_1$ and negative if $\varepsilon_2 < \varepsilon_1$. In Eq. (8.71), the wave vector k is equal to an electric field of the form

$$\mathbf{E}(\mathbf{r}) = \mathbf{E}_0(\mathbf{r}) e^{i\mathbf{k}\cdot\mathbf{r}}. \tag{8.72}$$

Substituting Eq. (8.71) and Eq. (8.72) into Eq. (8.70), we can obtain

$$\left\langle \mathbf{F}(\mathbf{r})\right\rangle = 1/4\,\mathrm{Re}(\alpha)\nabla\left|\mathbf{E}_0(\mathbf{r})\right|^2 + 1/2\,\mathbf{k}\,\mathrm{Im}(\alpha)\left|\mathbf{E}_0(\mathbf{r})\right|^2 - 1/2\,\mathrm{Im}(\alpha)\,\mathrm{Im}\left(\mathbf{E}_0^*(\mathbf{r})\cdot\nabla\mathbf{E}_0(\mathbf{r})\right), \tag{8.73}$$

where the first term is the optical gradient force and the second term is the radiation-pressure force [121]. It is the second term radiation-pressure force that is associated with the transfer of orbital angular momentum to dielectric particles [84]. In Laguerre-Gaussian beams the optical forces that cause particles to rotate within the vortex structure are formed as follows: the optical gradient forces create a ring structure that forms a circular equal potential energy surface, where particles are free to move; then the radiation pressure move the particles around equal potential energy surface. The goal of this study is to determine if the photonic crystal electric fields (which contain optical vortices) form the same circular equal potential energy surfaces as the Laguerre-Gaussian beams and will the radiation pressure be able to move particles within these equal potential surfaces.

Examining the form of Eq. (8.72), we can see that it matches the form of the optical Bloch mode given by Eq. (2.15), where $\mathbf{k}$ is the Bloch wave vector and $\mathbf{E}_0(\mathbf{r}) = \mathbf{u}_{kn}(\mathbf{r})$. Substituting $\mathbf{E}_0(\mathbf{r}) = \mathbf{u}_{kn}(\mathbf{r})$ into Eq. (8.73) we obtain

$$\langle \mathbf{F}(\mathbf{r}) \rangle = 1/4\,\mathrm{Re}(\alpha)\nabla|\mathbf{u}_{kn}(\mathbf{r})|^2 + 1/2\,\mathrm{Im}(\alpha)\mathbf{k}|\mathbf{u}_{kn}(\mathbf{r})|^2 - 1/2\,\mathrm{Im}(\alpha)\,\mathrm{Im}\left(\mathbf{u}^*_{kn}(\mathbf{r})\cdot\nabla\mathbf{u}_{kn}(\mathbf{r})\right). \tag{8.74}$$

If we focus on the eigenmodes of a two-dimensional photonic crystal, then for the TM mode $\mathbf{E}_0(\mathbf{r}) = \hat{\mathbf{z}}u_{kn}(\mathbf{r})$ and Eq. (8.74) becomes

$$\langle \mathbf{F}(\mathbf{r}) \rangle = 1/4\,\mathrm{Re}(\alpha)\nabla|u_{kn}(\mathbf{r})|^2 + 1/2\,\mathrm{Im}(\alpha)\left\{\mathbf{k}|u_{kn}(\mathbf{r})|^2 - \mathrm{Im}\left(u^*_{kn}(\mathbf{r})\nabla u_{kn}(\mathbf{r})\right)\right\}. \tag{8.75}$$

In Section 2.4.1, we stated the form of the Poynting vector for the TM modes Eq. (2.32), restated here for the reader:

$$\mathbf{S}^{TM}_{kn}(\mathbf{r}) = \frac{1}{2\omega\mu_0}\left[\mathbf{k}|u_{kn}(\mathbf{r})|^2 - \mathrm{Im}\left[\left(u^*_{kn}(\mathbf{r})\nabla u_{kn}(\mathbf{r})\right)\right]\right]. \tag{8.76}$$

Comparing Eq. (8.75) and Eq. (8.76), we can see that the last two terms of Eq. (8.75) match the form of the Poynting vector. This result confirms the last two terms of Eq. (8.75) are both associated with the optical forces that are related to direction of energy flow (i.e., the Poynting vector). The significance of this result requires further investigation beyond this appendix.

To determine if the optical vortices discussed in Chapter 5 can rotate sub-wavelength dielectric particles, the optical forces within these Bloch modes were calculated using Eq. (8.74). The optical forces were considered for an isotropic dielectric particle ($\varepsilon_1 = 1.5$) within a two-dimensional hexagonal photonic crystal, where the Bloch wave vector is $\mathbf{k} = \hat{\mathbf{x}} 4\pi/(3a)$ for the first band 1. The TE and TM modes are both associated with the irreducible representations of the C_{3v} **k**-group, where in Chapter 5 we demonstrated that these modes must contain optical vortices.

In Figure 49(a) and (b), the simulation is of an array of dielectric columns $\varepsilon = 12$ in a background of air $\varepsilon = 1$, and in Figure 50(a) and (b), the simulation is of an array of air holes $\varepsilon = 1$ in a dielectric background $\varepsilon = 12$, where the TE and TM modes are considered in both cases. The optical forces are calculated for a dielectric particle with permittivity of $\varepsilon = 2.25$ and a diameter of $d = a/10$, where a is the lattice constant. They are denoted by black arrows (length proportional to magnitude) and the magnitude is given by the background colour. Figure 49(a) reveals that in the TE mode the optical forces are directed radially inward towards the centers of the dielectric columns. Similarly, Figure 49(b) reveals that in the TM mode the optical forces are directed radially, but now they are directed outward from the center of the dielectric column. In both cases, the center of the dielectric columns is the location of the principal axis. For the TE mode, the center of the dielectric columns is also the location of a polarization disclination, where the field vanishes (see Chapter 6, Figure 43 and Figure 44).

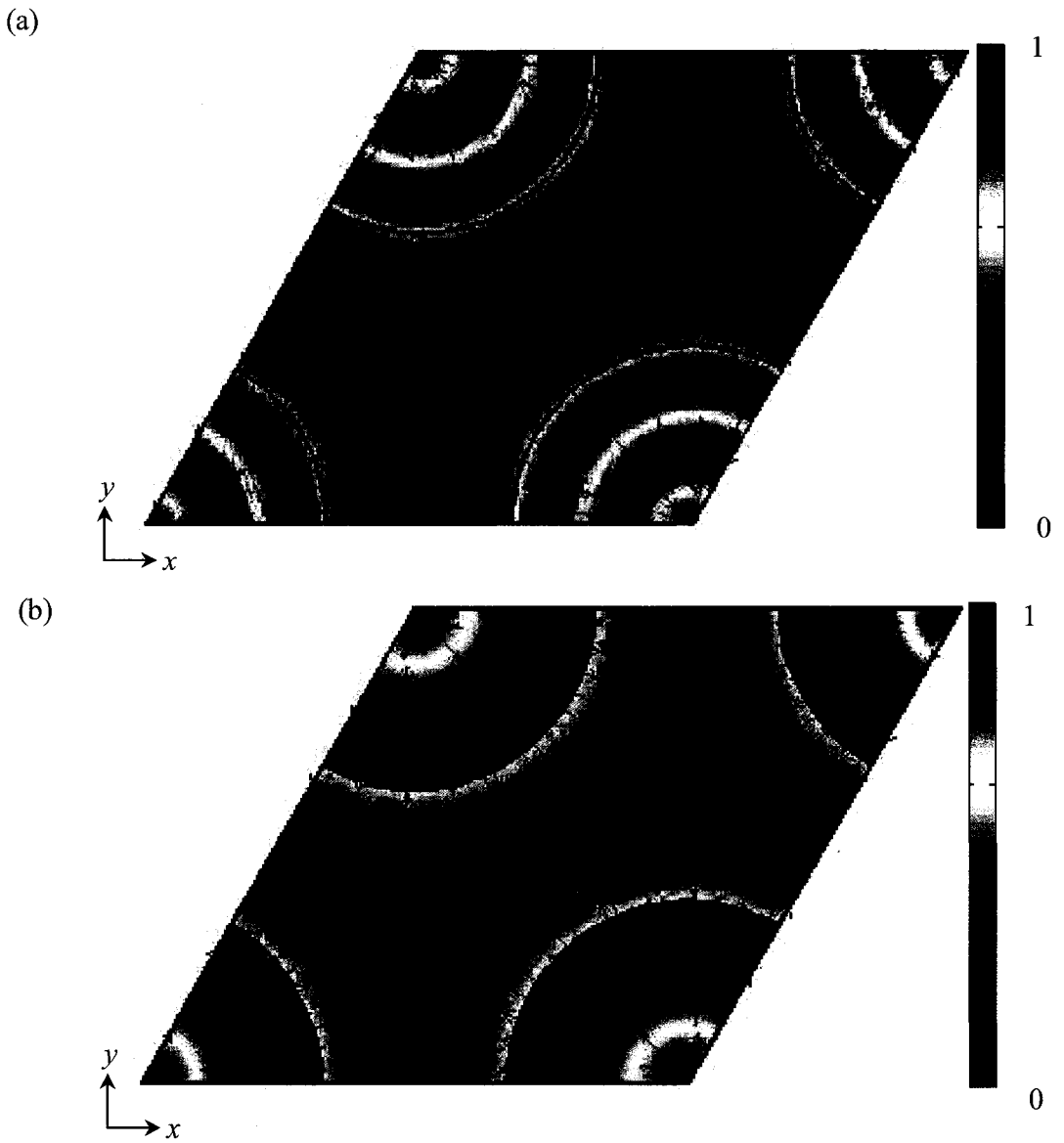

Figure 49. Hexagonal two-dimensional photonic crystal dielectric columns in a air background, $\varepsilon = 12$, Bloch mode, band 1, $\mathbf{k} = \hat{\mathbf{x}}\, 4\pi/(3a)$. Optical forces on a dielectric particle, $\varepsilon = 1.5$, black arrows (length proportional to magnitude) and magnitude back ground colour. (a) TE mode, where the electric field is associated with the A_2 irreducible representation of C_{3v} (b) TM mode, where the electric field is associated with the A_1 irreducible representation of C_{3v}. Bold black lines are edges of the unit cell and holes.

As a result, the optical gradient forces are directed inwards to create a stable equilibrium point. In contrast, the electric field of the TM has a maximum at the center of the dielectric column and thus the optical forces are directed outwards, creating an unstable equilibrium point. Stable equilibrium points are positions in space where a particle is at a local minimum of potential energy (e.g., a valley). Unstable equilibrium points are positions in space where a particle is at a local maximum of potential energy (e.g., hill top). The optical forces of the TE mode within a dielectric slab reveal no district symmetry (see Figure 50(a)). However, the optical forces of the TM modes within a dielectric slab are directed radially inward towards the centers of C_3 site symmetry (see Figure 50(b)). The electric field of the TM modes contains a phase singularity at this point and the field vanishes as a result. The phase singularities are located at the centers of C_3 site symmetry and form stable equilibrium positions.

Based on the examples presented, we can determine that locations where the electric field vanishes due to a phase singularity or a polarization disclination form stable equilibrium positions in the force fields. Note that these positions would change to unstable equilibrium positions if the dielectric permittivity of the particle was $\varepsilon_2 > \varepsilon_1$, because Eq. (8.71) would change sign and reverses the direction of the forces. In fact, it is at the special Wyckoff positions that equilibrium positions occur and the dielectric contrast between the particle and the background determine if the position is stable or unstable. This is no doubt due to the effect the local symmetry has the sub-wavelength features of the electromagnetic field. In all the cases considered, the dominant optical force, by several orders of magnitude, was the optical gradient force (the first term of Eq. (8.73)), which was directed radially from the positions of high symmetry within the unit cell. The radiation pressure which is required for the transfer of angular momentum was almost nonexistent. As a result there was no formation of circular equal potential surfaces. Therefore optical force patterns that would result in rotation of the dielectric particles within the optical vortices were not observed.

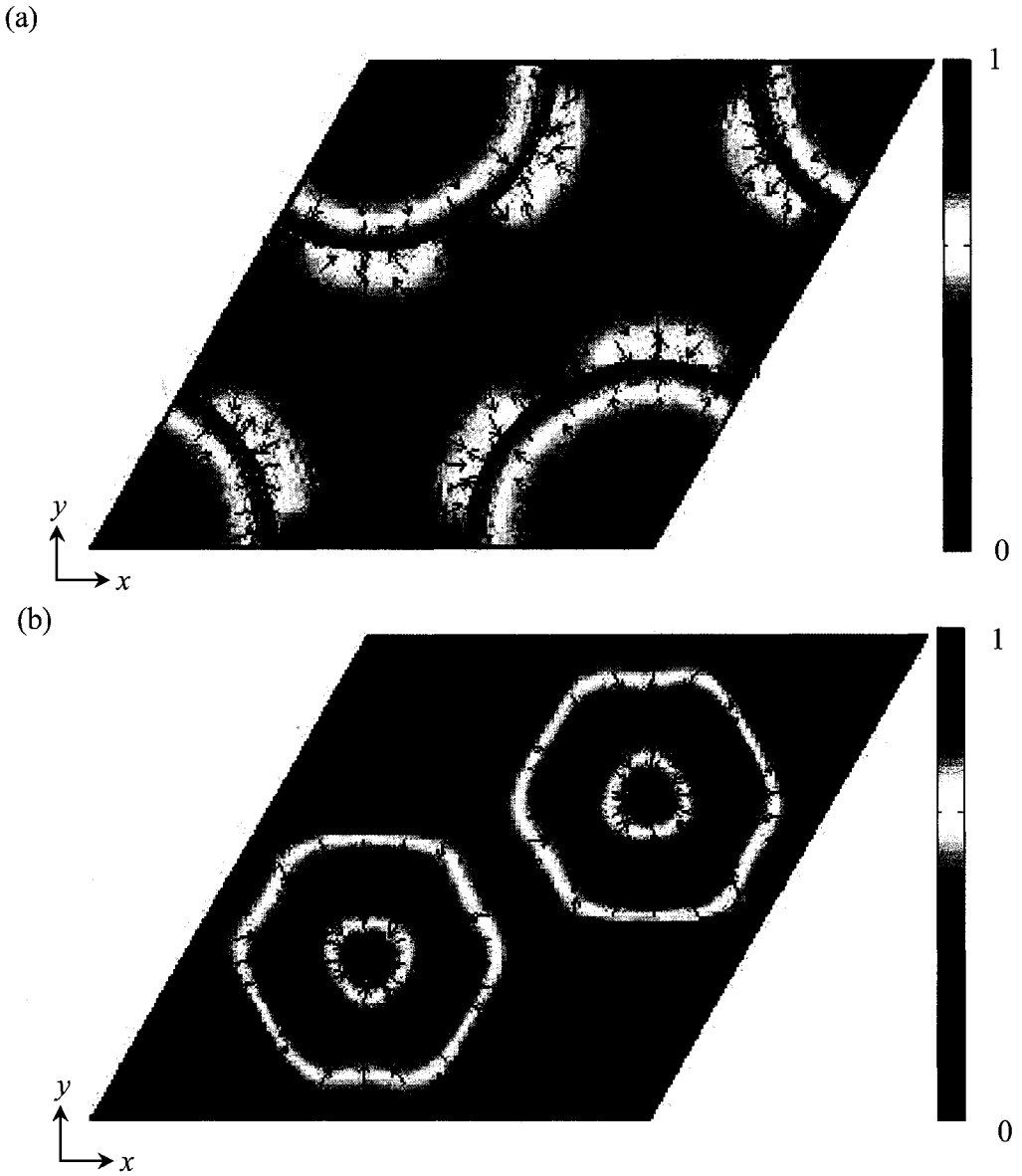

Figure 50. Hexagonal two-dimensional photonic crystal air holes in a dielectric background $\varepsilon = 12$, Bloch mode, band 1, $\mathbf{k} = \hat{\mathbf{x}} 4\pi/(3a)$. Optical forces on a dielectric particle, $\varepsilon = 1.5$, direction given by black arrows (length proportional to magnitude) and magnitude background colour. (a) TE mode, where the electric field is associated with the A_2 irreducible representation of C_{3v} (b) TM mode, where the electric field is associated with the A_1 irreducible representation of C_{3v}. Bold black lines are edges of the unit cell and holes.

E. Generation of Optical vortex modes in 2D photonic crystals

Central to the future experimental characterization of optical singularities, within photonic crystals, is the generation of the optical modes that contain vortex structures. This body of research has focused on the eigenmodes of photonic crystals, where they have been studied analytically and numerically, but there has been no mention of how to generate the eigenmodes. The following appendix is a preliminary study which seeks to address this issue, where we simulate the interaction of an electromagnetic source (an external plane wave) with a two-dimensional photonic crystal. The results are the following; we are able to excite an electromagnetic field within the photonic crystal that contains optical vortices and polarization singularities, which matches the symmetry vortices from Chapter 5 and the polarization singularities from Chapter 6.

These results are achieved using the finite element method set up as a driven problem. That is we solve Maxwell's equations for the TM case, but now we are including a source term. The source term is a plane wave, where the magnetic field is given by

$$\mathbf{H}(\mathbf{r}) = \hat{\mathbf{z}} H_{0z} e^{i\mathbf{k}\cdot\mathbf{r}-\omega t}, \tag{8.77}$$

which is polarized along the $\hat{\mathbf{z}}$ direction. This source originates from the left most edge of the simulation and spans the entire length of the edge. The parameters of the source term were chosen in an attempt to excite the hexagonal photonic crystal eigenmode at the K point, i.e. $\mathbf{k} = \hat{\mathbf{x}} 4\pi/(3a)$ for the first band 1 and $H_{0z} = 1.0\ A/m$ The frequency, ω, of the plane wave was set equal to the eigenvalue determined from Chapter 5, which simulated a unit cell with the same dielectric profile. The wave vector $\mathbf{k}$ was restricted to the $\hat{\mathbf{x}}$ direction. This was done in two stages: first, the confirmation of the numerical model by examining the propagation of the source plane wave in a uniform dielectric and second, the interaction of the plane wave source with a periodic dielectric structure. In each case the boundary conditions were set to scattering, where this boundary condition simulates a transparent interface on the edge of the solution space. This boundary

condition was not completely effective, which resulted in some back reflection from this interface. Figure 51 reveal the propagation of the source term in a uniform dielectric $\varepsilon = 12.11$, where we can see that the magnetic field is a perfect plane wave (background colour is the amplitude in the $\hat{\mathbf{z}}$ direction). In Figure 53, we can see the modal phase (determined by the arctangent of the ratio of the real to the imaginary parts of the field), which has parallel equi-phase planes as expected by Eq. (8.77) (background colour is the phase from π to $-\pi$). Consequently, we have verified the driven model in a uniform dielectric medium. Next, the hexagonal array of air holes in the same dielectric medium is simulated (i.e., a photonic crystal structure). Here we see that the external plane wave excites a magnetic field within the photonic crystal where the field has C_{3v} point symmetry (see Figure 53). The maximum amplitude of the magnetic field is 2.3, concentrated within certain air holes. To properly determine the coupling efficiency of the external plane wave to the photonic modes we would need to perform an average over a unit cell. However, visually we can see from the amplitude and distribution of the magnetic field within the photonic crystal that a significant percentage of energy is coupling from the external plane wave to the optical Bloch mode. In Figure 54, we see the modal phase of the magnetic field, which reveals the characteristic phase dislocations of optical vortices. Figure 56 displays the Poynting vector and confirms the appearance of optical vortices within the photonic crystal, where the arrows indicate direction (length proportional to magnitude and background colour is the magnitude). The model phase and the Poynting vector field present in Figure 54 and Figure 56 match the eigenmode that contains symmetry vortices discussed in Chapter 5 (see Figure 26 and Figure 27). Furthermore, the electric field of the Bloch mode demonstrates the characteristics of polarization singularities, such as the rotation of the electric field vectors about polarization disclinations within the field (see Figure 55, where the arrows indicate direction for $t = 0$ and the background colour is the field magnitude). The electric field pattern of Figure 55 matches the eigenmode from Chapter 6 that contain polarization singularities C points, disclinations and L lines (see Figure 43). Therefore, we can conclude that photonic crystal eigenmodes that contain optical vortices and polarization

singularities may be generated by an external electromagnetic source that is in the form of a plane wave.

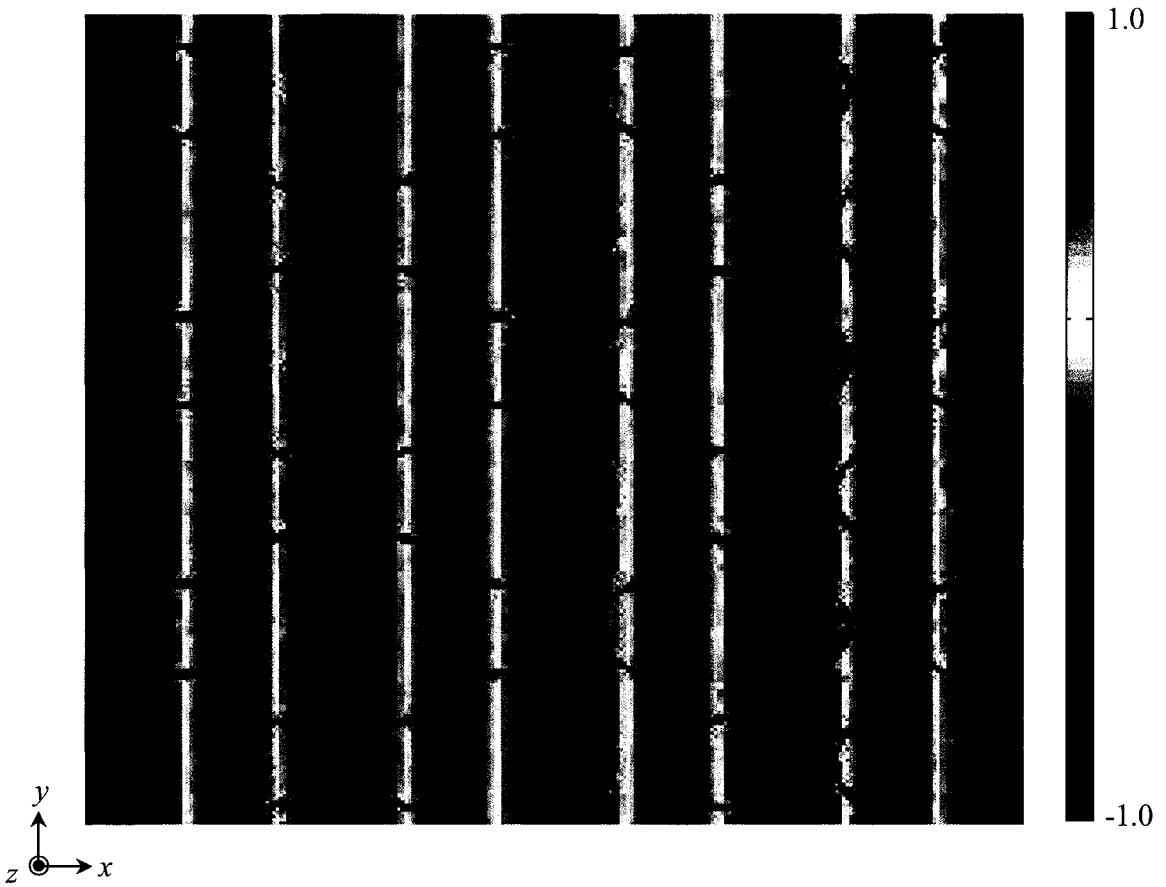

Figure 51. Uniform dielectric, where the holes and the background have been set to $\varepsilon = 12.11$. The magnetic field is polarized along the $\hat{\mathbf{z}}$ axis and the background colour is H_z component in units of $\mathrm{A/m}$. Bold black lines are edges of the holes.

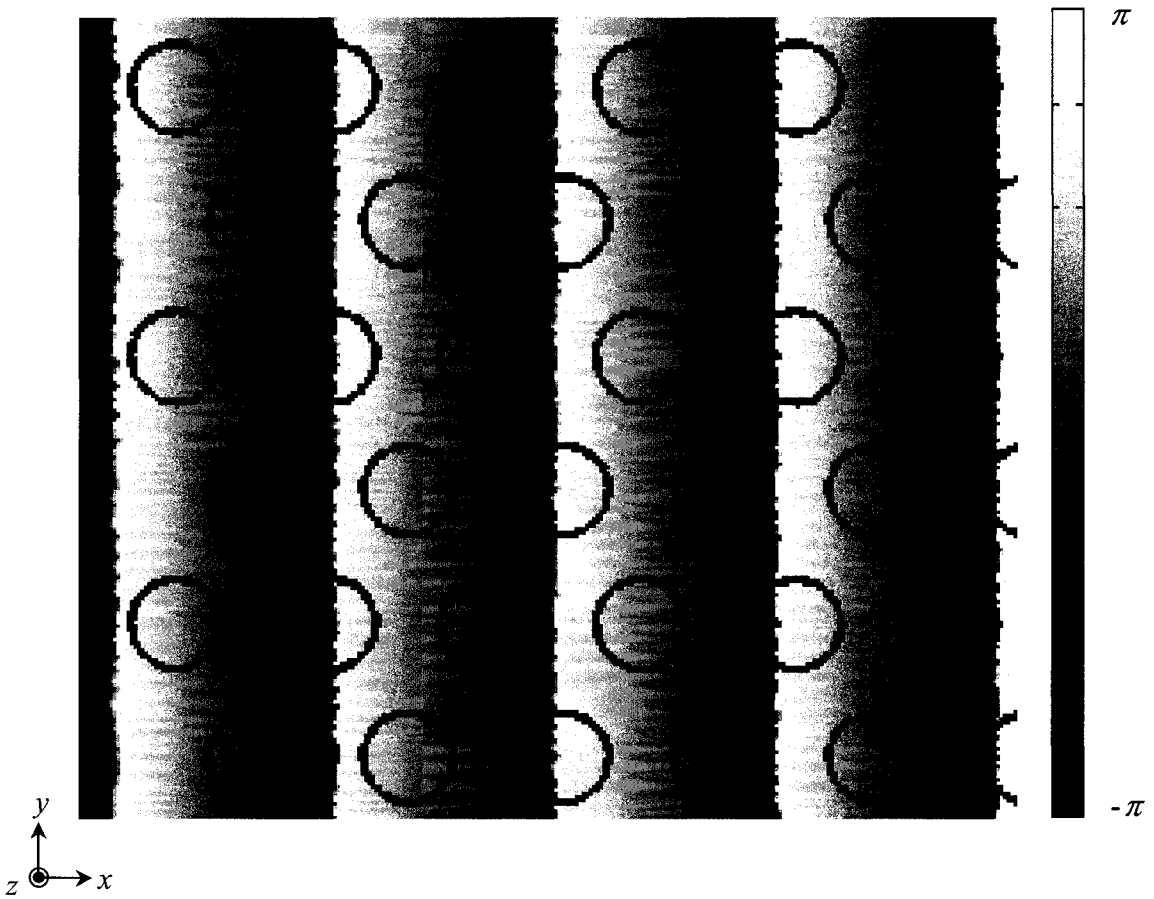

Figure 52. Uniform dielectric, where the holes and the background have been set to $\varepsilon = 12.11$. The model phase of the magnetic field polarized along $\hat{\mathbf{z}}$ axis and background colour is phase (π to $-\pi$). Bold black lines are edges of the holes.

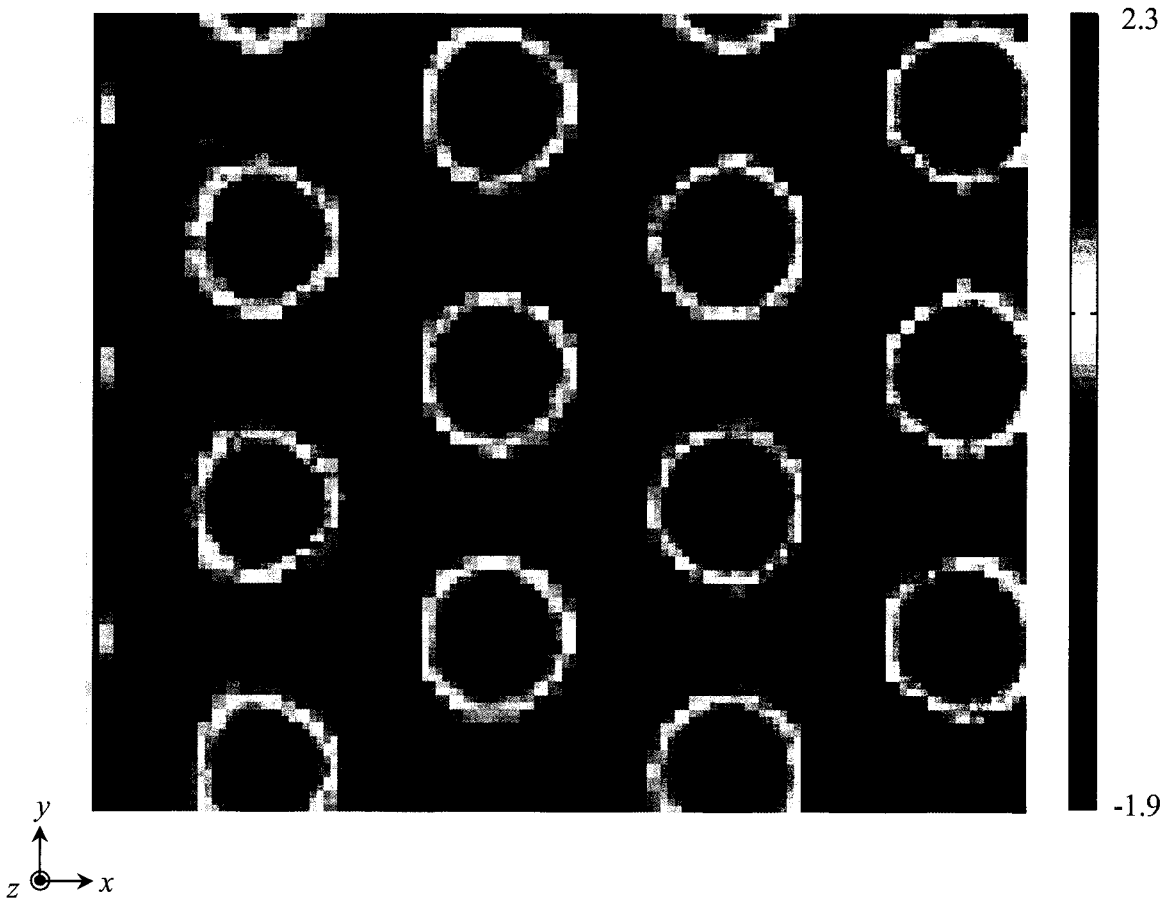

Figure 53. Hexagonal two-dimensional photonic crystal air holes in a dielectric background $\varepsilon = 12.11$, plane wave exciting the band 1 Bloch mode with wave vector $\mathbf{k} = \hat{\mathbf{x}}\, 4\pi/(3a)$. The magnetic field is polarized along the $\hat{\mathbf{z}}$ axis and the background colour is H_z component in units of $\mathrm{A/m}$. Bold black lines are edges of the air holes.

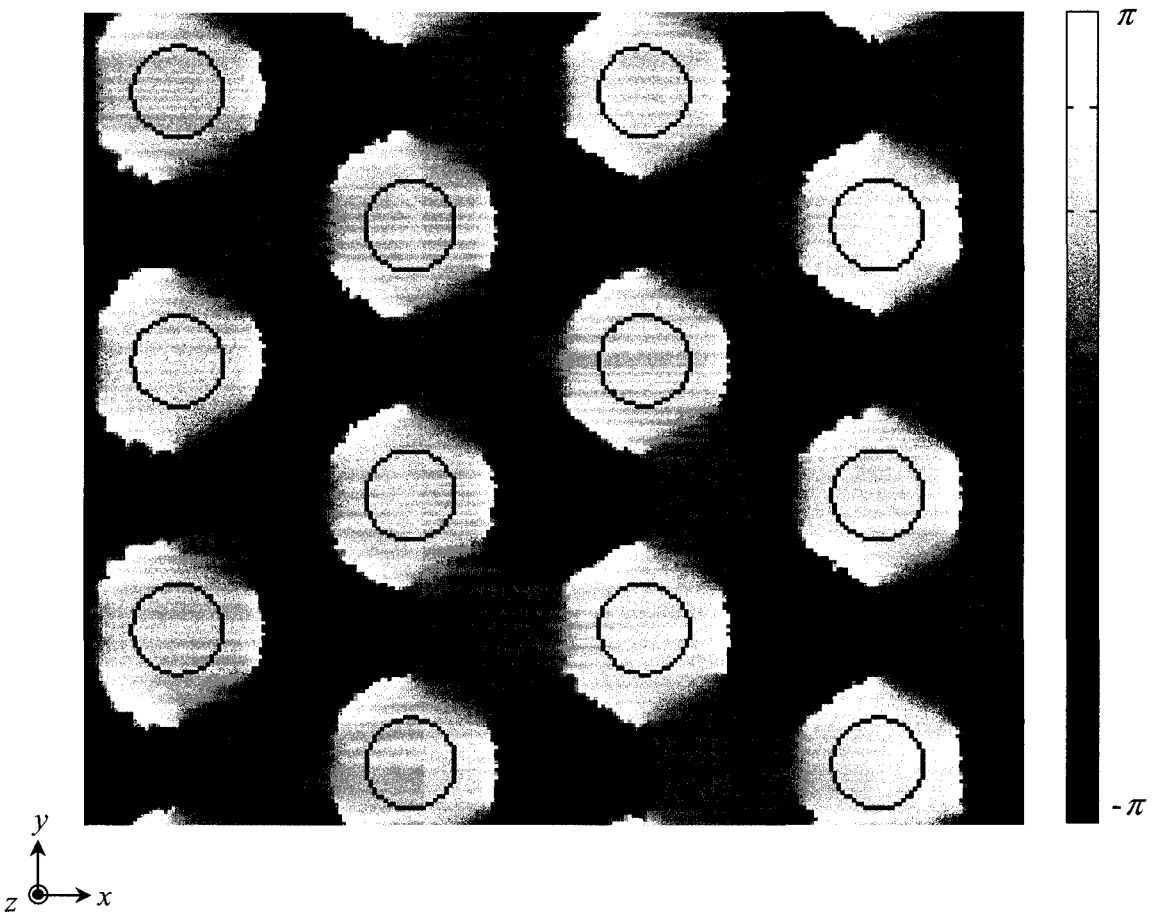

Figure 54. Hexagonal two-dimensional photonic crystal air holes in a dielectric background $\varepsilon = 12.11$, plane wave exciting the band 1Bloch mode with wave vector $\mathbf{k} = \hat{\mathbf{x}}\, 4\pi/(3a)$. The magnetic field is polarized along the $\hat{\mathbf{z}}$ axis and the background colour is model phase (π to -π). Bold black lines are edges of the air holes.

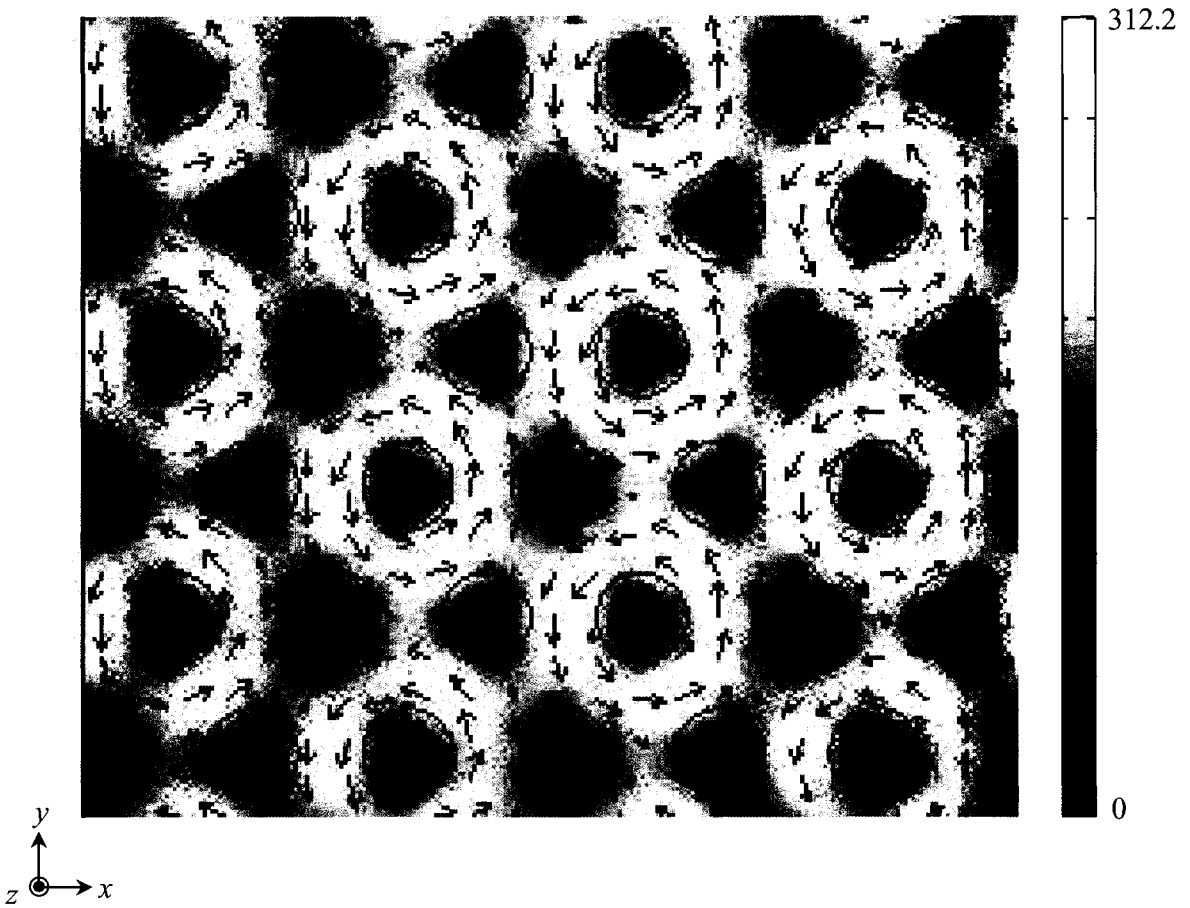

Figure 55. Hexagonal two-dimensional photonic crystal air holes in a dielectric background $\varepsilon = 12.11$, plane wave exciting the band 1 Bloch mode with wave vector $\mathbf{k} = \hat{\mathbf{x}} 4\pi/(3a)$. Electric field is polarized in the *x*-*y* plane at time zero, arrows denote direction (length proportional to vector components) and the background colour is $\sqrt{\mathbf{E} \cdot \mathbf{E}^*}$ time averaged magnitude in units of $\mathrm{V/m}$. Bold black lines are edges of the air holes.

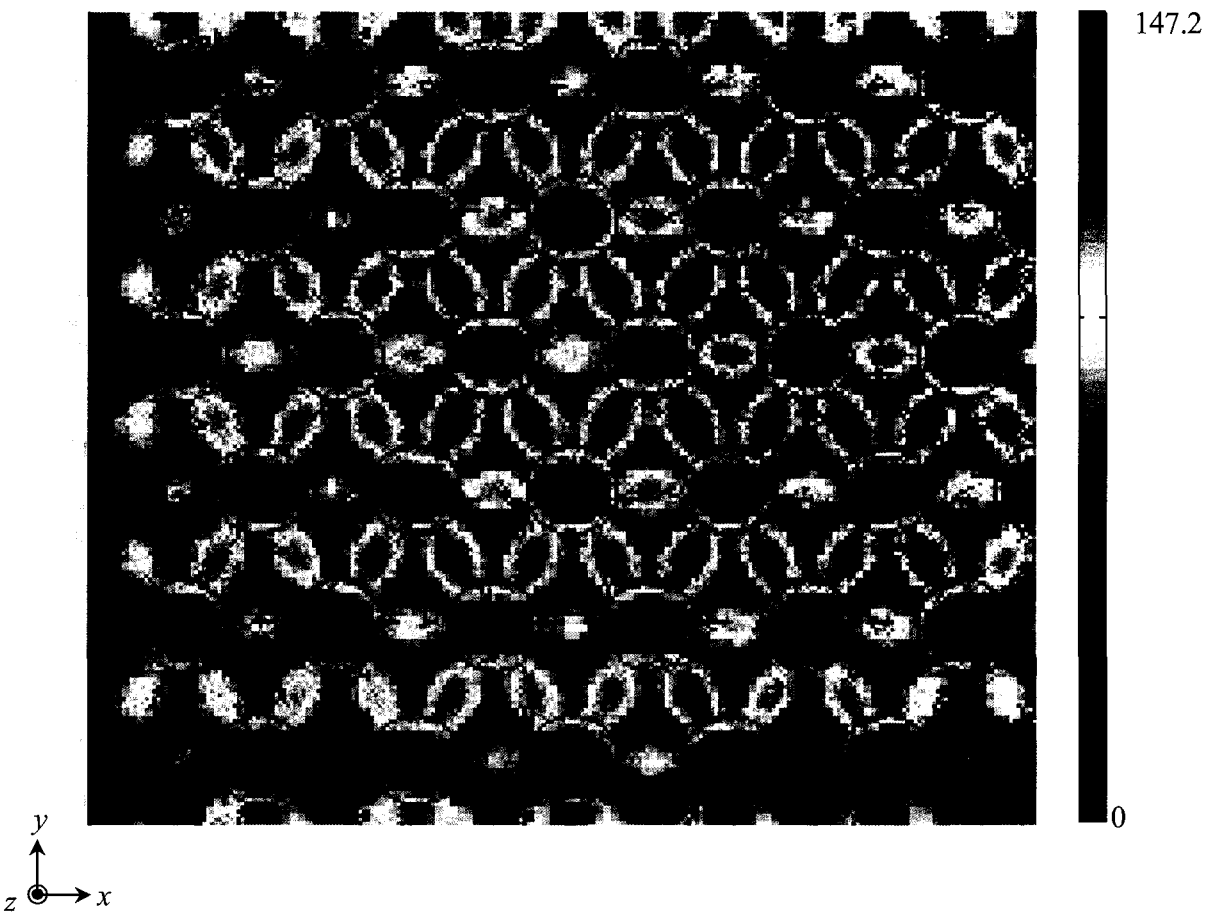

Figure 56. Hexagonal two-dimensional photonic crystal air holes in a dielectric background $\varepsilon = 12.11$, plane wave exciting the band 1Bloch mode with wave vector $\mathbf{k} = \hat{\mathbf{x}}\, 4\pi/(3a)$. Poynting vector, arrows denote direction (length proportional to magnitude) and background colour is the magnitude in units of $\mathrm{W/m^2}$. Bold black lines are edges of the air holes.

REFERENCES

[1] E. Yablonovitch, "Inhibited spontaneous emission in solid-state physics and electronics", Phys. Rev. Lett. **58**, 2059 (1987).

[2] S. John, "Electromagnetic absorption in a disordered medium near a photon mobility edge", Phys. Rev. Lett. **53**, 2169 (1984).

[3] S. John, "Strong localization of photons in certain disordered dielectric superlattices", Phys. Rev. Lett. **58**, 2486 (1987).

[4] J. D. Joannopoulos, P. R. Villeneuve, and S. Fan, "Photonic crystals: putting a new twist on light", Nature **386**, 143 (1997).

[5] K. Sakoda, *Optical properties of photonic crystals*, 2nd ed. (Springer-Verlag, Berlin Heidelberg, 2005).

[6] M. Soljacic and S. G. Johnson, "Photonic-crystal slow-light enhancement of nonlinear phase sensitivity", J.Opt. Soc. Am. B **19**, 2052 (2002).

[7] J. P. Dowling, M. Scalora, M. J. Bloemer, and C. M. Bowden, "The photonic band edge laser: A new approach to gain enhancement", J. Appl. Phys. **75**, 1897 (1994).

[8] M. Soljacic and J. D. Joannopoulos, "Enhancement of nonlinear effects using photonic crystals," Nature Materials **3**, 211 (2004).

[9] P. V. Parimi, W. T. Lu, P. Vodo, J. Sokoloff, J. S. Derov, and S. Sridhar, "Negative refraction and left-handed electromagnetism in microwave photonic crystals", Phys. Rev. Lett. **92**, 127401-1 (2004).

[10] M. Notomi, "Theory of light propagation in strongly modulated photonic crystals: Refractionlike behavior in the vicinity of the photonic band gap", Phys. Rev. B **62**, 10696 (2000).

[11] C. Luo, S. G. Johonson, J. D. Joannopoulos, and J. B. Pendry, "All-angle negative refraction without negative effective index", Phys. Rev. B **65**, 201104 (2002).

[12] S. Foteinopoulou, E. N. Economou, and C. M. Soukoulis, "Refraction in media with a negative refractive index", Phys. Rev. Lett. **90**, 107402 (2003).

[13] P. V. Parimi, W. T. T. Lu, P. Vodo, and S. Sridhar, "Photonic crystals – imaging by flat lens using negative refraction", Nature (London) **426**, 404 (2003).

[14] A. Berrier, M. Mulot, M. Swillo M. Qiu, L. Thylen, A. Talenau, and S. Anand, "Negative refraction at infrared wavelengths in a two-dimensional photonic crystal", Phys. Rev. Lett. **93**, 73902 (2004).

[15] H. Kosaka, T. Kawashima, A. Tomita, M. Notomi, T. Tamamura, T. Sato, and S. Kawakami, "Superprism phenomena in photonic crystals", Phys. Rev. B **58**, 10096R10098R (1998).

[16] H. Kosaka, T. Kawashima, A. Tomita, M. Notomi, T. Tamamura, T. Sato, and S. Kawakami, "Photonic crystals for micro lightwave circuits using wavelength-dependent angular beam steering," Appl. Phys. Lett. **74**, 1370 (1999).

[17] L. Wu, M. Mazilu, T. Karle, and T. F. Krauss, "Superprism phenomena in planar photonic crystals," IEEEJ. Quantum Electron. **38**, 915 (2002).

[18] H. Kosaka, T. Kawashima, A. Tomita, M. Notomi, T. Tamamura, T. Sato, and S. Kawakami, "Self-collimating phenomena in photonic crystals", Appl. Phys. Lett. **74**, 1212 (1999).

[19] J. Witzens, M. Loncar, and A. Scherer, "Self-collimation in planar photonic crystals", IEEE J. Sel. Top. Quantum Electron. **8**, 1246 (2002).

[20] J. Witzens and A. Scherer, "Efficient excitation of self-collimated beams and single Bloch modes in planar photonic crystals", J. Opt. Soc. Am. A **20**, 935 (2003).

[21] R. Meade, K. Brommer, A. Rappe, and J. Joannopoulos, "Nature of the photonic band gap: some insights from a field analysis." J. Opt. Soc. Am. B **10**, 328 (1993).

[22] R. Meade, K. Brommer, A. Rappe, and J. Joannopoulos, "Existence of a photonic band gap in two dimensions", Appl. Phys. Lett. **61**, 495 (1992).

[23] P. Villeneuve and M. Piché, "Photonic band gaps in two-dimensional square and hexagonal structures", Phys. Rev. B **46**, 4969 (1992).

[24] U. Grüning, V. Lehmann, S. Ottow, and K. Busch "Macroporous silicon with a complete two-dimensional photonic band gap centered at 5 μm" Appl. Phys. Lett. **68**, 747 (1996).

[25] D. Cassagne, C. Jouanin, and D. Bertho, "Hexagonal photonic-band-gap structures" Phys. Rev. B **53**, 7134 (1996).

[26] A. Mekis, "High transmission through sharp bends in photonic crystal waveguides" Phys. Rev. Lett. **77**, 3787 (1996).

[27] S. McCall, P. Platzman, R. Dalichaouch, D. Smith, and S. Schultz, "Microwave propagation in two-dimensional dielectric lattices" Phys. Rev. Lett. **67**, 2017 (1991).

[28] J. Chen, H. Haus, S. Fan, P. Villeneuve, and J. Joannopoulos, "Optical filters from photonic band gap air bridges", IEEE J. Lightwave Tech. **14**, 2575 (1996).

[29] C. Chan, K. Ho, and C. Soukoulis, "Photonic band-gaps in experimentally realizable periodic structures", Europhys. Lett. **16**, 563 (1991).

[30] H. Sözüer and J. Haus, "Photonic bands: simple-cubic lattice", J. Opt. Soc. Am. B **10**, 296 (1993).

[31] K. Ho, C. Chan, C. Soukoulis, R. Biswas, and M. Sigalas, "Photonic band gaps in three dimensions: new layer-by-layer periodic structures", Solid State Commnun. **89**, 413 (1994).

[32] H. Sözüer and J. Dowling, "Photonic band calculations for woodpile structures", J. Mod. Opt. **41**, 231 (1994).

[33] C. Cheng and A. Scherer, "Fabrication of photonic band-gap crystals", J. Vac. Sci. Technol. B **13**, 2696 (1995).

[34] M. Qiu, "Effective index method for heterostructure-slab-waveguide-based two-dimensional photonic crystals", App. Phy. Let. **81**, 1163 (2002).

[35] S. Fan and J. D. Joannopoulos, "Analysis of guided resonances in photonic crystal slabs", Phys. Rev. B **65**, 235112 (2002).

[36] N. Stefanou, V. Karathanos and A. Modinos, "Scattering of electromagnetic waves by periodic structures" J. Phys. Condens. Matter **4**, 7389 (1992).

[37] K. Sakoda, "Symmetry, degeneracy, and uncoupled modes in two-dimensional photonic lattice", Phys. Rev. B **52**, 7982 (1995).

[38] S. G. Johnson and J.D. Joannopoulos, "Block-iterative frequency-domain methods for Maxwell's equations in a planewave basis", Opt. Exp. **8**, 173 (2001).

[39] A. Taflove, S. C. Hagness, J. Maloney, and M. Kesler, *Computational electrodynamics the finite-difference time-domain method*, 3rd ed., (Artech House, Inc. Norwood, 2005), Chap. 13.

[40] W. Kuang, W. J. Kim, and J. D. O'Brien, "Finite-Difference time domain method for nonorthogonal unit-cell two-dimensional photonic crystals", J. of Light. Tech. **25**, 2612 (2007).

[41] J. Jin, *The finite-element method in electromagnetics* (Wiley, New York, 1993), Chap. 5.

[42] J. Lee, R. Lee, and A. Cangellaris, "Time-domain finite-element methods", IEEE Trans. On Ant and Prop. **45**, 430 (March 1997).

[43] T. F. Krauss, R. M. De La Rue, and S. Brand, "Two-dimensional photonic bandgap structures operating at near-infrared wavelengths ", Nature (London) **383**, 699 (1996).

[44] S. G. Johnson and J. D. Joannopoulos, *Photonic crystals: The road from theory to practice* (Kluwer Academic publishers, USA, 2003).

[45] H. Schriemer, J. Wheeldon, and T. Hall, "Transport Properties of Nonlinear Photonic Crystals", Photonics North 2005, Toronto, Canada (2005).

[46] J. Wheeldon, H. Schriemer, and T. Hall, "A nanoscale perspective of nonlinear optical tunability in two-dimensional photonics crystals in the superprism regime, Modelling", Simulation and Design of Dielectrics, Cambridge, UK (2005).

[47] T. Sondergaard and K. H. Dridi, "Energy flow in photonic crystal waveguides," Phys Rev. B **61**, 15688-15695 (2000).

[48] K. H. Dridi, "Mode dispersion and photonic storage in planar defects within Bragg stacks of photonic crystal stabs," J. Opt. Soc. Am. B **21**, 522 (2004).

[49] M. Barth and O. Benson, "Manipulation of dielectric particles using photonic crystal cavities", App. Phys. Lett. **89**, 253114 (2006).

[50] A. Rahmani and P. C. Chaumet, "Optical trapping near a photonic crystal", Opt. Express **14**, 6353 (2006).

[51] M. I. Antonoyiannakis and J. B. Pendry, "Electromagnetic forces in photonic crystals", Phys. Rev. B **60**, 2363 (1999).

[52] J. Wheeldon and H. Schriemer, "Symmetry transformation properties express polarization singularities in Bloch mode systems", Opt. Express (Submitted).

[53] O. Toader, S. John, and K. Busch, "Optical trapping, Field enhancement and Laser cooling in photonic crystals," Opt. Exp. Vol. 8, No. 8, 217(2001).

[54] J. Wheeldon and H. Schriemer, "Photonic crystals as a novel structure to generate optical vortices", CAP Congress 2008, Quebec City, Canada (2008).

[55] J. Wheeldon, T. Hall, and H. Schriemer, "Symmetry constraints and the existence of Bloch mode vortices in linear photonic crystals", Opt. Express **15**, 3531 (2007).

[56] J. Courtial, R. Zambrini, M. R. Dennis, and M. Vasnetsov, "Angular momentum of optical vortex arrays," Opt. Express **14**, 938 (2006).
[57] A. Ferrando, "Discrete-symmetry vortices as angular Bloch modes," Phys Rev. E **72**, 036612 (2005).
[58] D. Maystre and P. Vincent, "Phenomenological study of binding in optically trapped photonic crystals", J. Opt. Soc. Am. A **24**, 2383 (2007).
[59] D. Maystre and P. Vincent, "Making photonic crystals using trapping and binding optical forces on particles", J. Opt. A: Pure Appl. Opt. **8**, 1059 (2006).
[60] M. Berry, "Much ado about nothing: optical dislocation lines (phase singularities, zeros, vortices...)" in. Intl. Conf. on Singular Optics, M. S. Soskin, ed., Proc. SPIE **3487**, 1 (1998).
[61] M. V. Berry and M. R. Dennis, "Phase singularities in isotropic random waves", Proc. R. Soc. Lond. A **456**, 2059 (2000).
[62] J. V. Hajnal, "Singularities in the transverse field of electromagnetic waves. II. Observations on the electric field", Proc. R. Soc. Lond. A **414**, 447 (1987).
[63] M. V. Berry, "Index formulae for singular lines of polarization", J. Opt. A: Pure Appl. Opt. **6**, 675 (2004).
[64] M. V. Berry, "The electric and magnetic polarization singularities of paraxial waves", J. Opt. A: Pure App. Opt. **6**, 475 (2004).
[65] M. V. Berry and M. R. Dennis, "The optical singularities of birefringent dichroic chiral crystals", Proc. R. Soc. Lond. A **459**, 1261 (2003).
[66] J. V. Hajnal, "Observations of singularities in the electric and magnetic fields of freely propagating microwaves", Proc. R. Soc. Lond. A **430**, 413 (1990).
[67] I. Freund, "Coherency matrix description of optical polarization singularities", J. Opt. A: Pure Appl. Opt. **6**, S229 (2004).
[68] I. Freund, "Polarization singularity proliferation in three-dimensional ellipse fields", Opt. Lett. **30**, 433 (2005).
[69] I. Freund, "Emergent polarization singularities", Opt. Lett. **29**, 539 (2004).
[70] M. Dennis, "Local properties and statistics of phase singularities in generic wavefields", Second International Conference on Singular Optics (Optical Vortices): Fundamentals and Applications, Proceedings of SPIE **4403**, 13 (2001).
[71] J. F. Nye, "Local solutions for the interaction of wave dislocations", J. Opt. A: Pure Appl. Opt. **6**, S251 (2004).
[72] R. W. Schoonover and T. D. Visser, "Polarization singularities of focused, radially polarized fields", Opt. Express **14**, 5733 (2006).
[73] M. V. Berry, "Phase vortex spirals", J. Phys. A: Math. Gen. **38**, L745 (2005).
[74] M. V. Berry and M. R. Dennis, "Knotting and unknotting of phase singularities: Helmholtz waves, paraxial waves and waves in 2 + 1 spacetime", J. Phys. A: Math. Gen. **34**, 8877 (2001).
[75] I. Freund, "Cones, spirals, and Mobius strips, in elliptically polarized light", Science Direct Opt. Comm. **249**, 7 (2005).
[76] G. R. Fowles, *Introduction to modern optics*, 2nd ed. (Dover, USA, 1989).
[77] J. F. Nye and M. V. Berry, "Dislocations in wave trains", Proc. R. Soc. Lond. A **336**, 165 (1974).

[78] D. G. Grier, "A revolution in optical manipulation," Nature **424**, 21 (2006).
[79] K. Ladavac and D. G. Grier, "Microoptomechanical pumps assembled and driven by holographic optical vortex arrays," Opt. Express **12**, 1144 (2004).
[80] A. Ferrando, M. Zacares, and M. Garcia-March, "Vorticity cutoff in nonlinear photonic crystals," Phys. Rev. Lett. **95**, 043901 (2005).
[81] J. Masajada and B. Dubik, "Optical vortex generation by three plane wave interference," Opt. Commun. **198**, 21 (2001).
[82] K. O'Holleran, M. J. Padgett, and M. R. Dennis, "Topology of optical vortex lines formed by the interference of three, four, and five plane waves," Opt. Express **14**, 3039 (2006).
[83] J. Yang and Z. H. Musslimnai, "Fundamental and vortex solitons in a two-dimensional optical lattice," Opt. Lett. **28**, 2094 (2003).
[84] L. Allen, M. W. Beijersbergen, R. J. C. Spreeuw, and J. P. Woerdman, "Orbital angular momentum of light and the transformation of Laguerre-Gaussian laser modes," Phys. Rev. A **45**, 8185 (1992).
[85] J. F. Nye, *Natural focusing and the fine structure of light: caustics and wave dislocations* (IOP Publishing Ltd., Bristol ,1999).
[86] M. V. Berry and M. R. Dennis "Quantum cores of optical phase singularities," J. Opt. A: Pure Appl. Opt. **6**, S178 (2004).
[87] J. V. Hajnal, "Singularities in the transverse fields of electromagnetic waves. I. Theory," Proc. R. Soc. Lond. A **414**, 433 (1987).
[88] M. V. Berry and M. R. Dennis, "Singularities polarization singularities in isotropic random vector waves," Proc. R. Soc. Lond. A **457**, 141 (2001).
[89] Freund, "Polarization singularities in optical lattices," Opt. Let. Vol. 29, No. 8, 875 (2004).
[90] K. Inoue and K. Ohtaka, *Photonic crystals physics, fabrication and applications*, (Springer-Verlag, Berlin Heidelberg, 2004).
[91] W. M. Robertson, G. Arjavalingam, R. D. Meade, K. D. Brommer, A. M. Rappe, and J. D. Joannopoulos, "Measurement of photonic band structure in a two-dimensional periodic dielectric array", Phys. Rev. Lett. **68**, 2023 (1992).
[92] W. M. Robertson, G. Arjavalingam, R. D. Meade, K. D. Brommer, A. M. Rappe, and J. D. Joannopoulos, "Measurement of the photon dispersion relation in two-dimensional ordered dielectric arrays" J. Opt. Soc. Am. B **10**, 322 (1993).
[93] K. Busch, G. von Freymann, S. Linden, S. F. Mingaleev, L. Tkeshelashvili and M. Wegener,"Periodic nanostructures for photonics", ScienceDirect Phy. Rep. **444**, 101 (2007).
[94] H. Benisty, C. Weisbuch, D. Labilloy, M. Rattier, C. J. M. Smith, T. F. Krauss, R. M. De la Rue, R. Houdre, U. Oesterle, C. Jouanin, and D. Cassagne, "Optical and confinement properties of two-dimensional photonic crystals", J. Lightwave Technol. **17**, 2063 (1999).
[95] S. Olivier, H. Benisty, M. Rattier, C. Weisbuch, M. Qiu, A. Karlsson, C. J. M. Smith, R. Houdre, and U. Oesterle, "Resonant and nonresonant transmission through waveguide bends in a planar photonic crystal",Appl. Phys. Lett. **79**, 2514 (2001).

[96] N. W. Ashcroft and N. D. Mermin, *Solid state physics*, (Thomson Learning, USA, 1976).

[97] K. Okamoto, *Fundamentals of optical waveguides*, 2nd ed. (Academic Press, USA, 2006).

[98] K. Ohtaka and Y. Tanabe: "Photonic bands using vector spherical waves. I various properties of bloch electric fields and heavy Photons" J. Phys. Soc. Jpn. **65**, 2265 (1996).

[99] K. Ohtaka and Y. Tanabe, "Photonic bands using vector spherical waves. III. group-theoretical treatment" J. Phys. Soc. Jpn. **65**, 2670 (1996).

[100] M. Qiu, K. Azizi, A. Karlsson, M. Swillo, and B. Jaskorzynska, "Numerical studies of mode gaps and coupling efficiency for line-defect waveguides in two-dimensional photonic crystals" Phys. Rev. B **64**, 155113 (2001).

[101] S.G Johnson, S. Fan, P.R. Villeneuve, J.D. Joannopoulos, and L. A. Kolodziejski, "Guided modes in photonic crystal slabs," Phys. Rev. B **60**, 5751 (1999).

[102] M. Born and E. Wolf, *Principles of optics: electromagnetic theory of propagation, interference and diffraction of light*, 7th ed., (Cambridge University Press, Cambridge, 2003)

[103] J. D. Jackson, *Classical electrodynamics*, 3rd ed., (John Wiley and Sons, Inc., USA, 1999).

[104] H. J. Metcalf and P. van der Straten, *Laser cooling and trapping* (Springer-Verlag, New York, 1999).

[105] G. W. Bryant, E. L. Shirley, and L. S. Goldner, "Theory of probing a photonic crystal with transmission near-field optical microscopy", Phys. Rev. B **58**, 2131 (1998).

[106] S. Fan, I. Appelbaum, and J. D. Joannopoulos, "Near-field scanning optical microscopy as a simultaneous probe of fields and band structure of photonic crystals: A computational study", App. Phys. Lett. **75**, 3461 (1999).

[107] T. N. Oder, J. Shakya, J. Y. Lin, and H. X. Jiang, "III-nitride photonic crystals", App. Phys. Lett. **83**, 1231 (2003).

[108] H. Gersen, T. J. Karle, R. J. P. Engelen, W. Bogaerts, J. P. Korterik, N. F. van Hulst, T. F. Krauss, and L. Kuipers, "Real-space oberservation of ultraslow light in photonic crystal waveguides", Phys. Rev. Lett. **94**, 073903-1 (2005).

[109] K. Okamoto, M. Loncar, T. Yoshie, and A. Scherer, "Near-field scanning optical microscopy of photonic crystal nanocavities", App. Phys. Lett. **82**, 1676 (2003).

[110] P. T. Rakich, M. S. Dahlem, S. Tandon, M. Ibanescu, M. Soljacic, G. S. Petrich, J. D. Joannopoulos, L. A. Kolodziejski, and E. P. Ippen, "Achieving centimetre-scale supercollimation in a large-area two-dimensional photonic crystal", Nature Materials **5**, 93 (2006).

[111] H. Gersen, T. J. Karle, R. J. Engelen, W. Bogaerts, J. P. Korterik, N. F. van Hulst, T. F. Krauss, and L. Kuipers, "Direct observation of Bloch harmonics and negative phase velocity in photonic crystal waveguides", Phys. Rev. Lett. **94**, 123901-1 (2005).

[112] E. B. McDaniel and J. W. Hsu, "Local characterization of transmision properties of a two-dimensional photonic crsytal", Phys. Rev. B **55**, 10878 (1997).

[113] R. A. Evarestov and V. P. Smirnov, *Site symmetry in crystals theory and applications, Springer series in solid-state sciences 108*, (Springer-Verlag, New York, 1993).
[114] G. Arfken, *Mathematical methods for physicists*, 3rd ed., (Academic Press Inc., USA, 1985).
[115] M. Tinkham, *Group theory and quantum mechanics* (Dover Mineola, New York, 1992).
[116] D. M. Bishop, *Group theory and chemistry* (Dover New York 1973).
[117] T. Hahn, *International tables for crystallography: volume A space-group symmetry*, 4th ed., (The international union of crystallography, Kluwer Academic Publishers, London, 1995).
[118] R. A. Beth, "Mechanical detection and measurement of the angular momentum of light", Phys. Rev. **50**, 115 (1936).
[119] T. A. Nieminen, S. Parkin, N. R. Heckenberg, and H. Rubinsztein-Dunlop, "Optical torque and symmetry", Proc. SPIE **5514**, 254 (2004).
[120] P. C. Chaumet and M. Nieto-Vesperinas, "Time-averaged total force on a dipolar sphere in an electromagnetic field", Opt. Lett. **25**, 1065 (2000).
[121] M. Nieto-Vesperinas, P. C. Chaumet and A. Rahmani, "Near-field photonic forces", Phil. Trans. R. Soc. Lond. A **362**, 719 (2004).